STUDIES OF LASER ENERGY ABSORPTION AND X-RAY EMISSION IN PLASMAS PRODUCED BY ULTRAHIGH INTENSITY LASER PULSES

By

UDAY CHAKRAVARTY

PHYS 03 2008 04 001

Raja Ramanna Centre for Advanced Technology, Indore

A thesis submitted to the

Board of Studies in Physical Sciences

In partial fulfillment of requirements

for the Degree of

DOCTOR OF PHILOSOPHY

of

HOMI BHABHA NATIONAL INSTITUTE

August, 2013

HOMI BHABHA NATIONAL INSTITUTE

Recommendations of the Viva Voce Board

As members of the Viva Voce Committee, we certify that we have read the dissertation prepared by ***Shri Uday Chakravarty*** entitled : ***"Studies of laser energy absorption and x-ray emission in plasmas produced by ultrahigh intensity laser pulses"*** and recommend that it may be accepted as fulfilling the dissertation requirement for the degree of Doctor of Philosophy.

P. D. Gupta Date : 25-3-2014

Chairman : Prof. P.D. Gupta

Date : 25/3/2014

Guide : Prof. P.A. Naik

Date : 25/3/2014

Member-1 : Prof. N.K. Gupta

Date : 25/3/14

Member-2 : Prof. G.S. Lodha

Date : 25/3/14

Examiner: Prof. M. Krishnamurthy

Final approval and acceptance of this dissertation is contingent upon the candidate's submission of the final copies of the dissertation to HBNI.

I hereby certify that I have read this dissertation prepared under my direction and recommend that it may be accepted as fulfilling the dissertation requirement.

Date: March 25, 2014 **Guide:**

(Prof. P. A. Naik)

Place: RRCAT, Indore

STATEMENT BY AUTHOR

This dissertation has been submitted in partial fulfilment of requirements for an advanced degree at Homi Bhabha National Institute (HBNI) and is deposited in the Library to be made available to borrowers under rules of the HBNI.

Brief quotations from this dissertation are allowable without special permission, provided that accurate acknowledgement of source is made. Requests for permission for extended quotation from or reproduction of this manuscript in whole or in part may be granted by the Competent Authority of HBNI when in his or her judgment the proposed use of the material is in the interests of scholarship. In all other instances, however, permission must be obtained from the author.

Uday Chakravarty

Uday Chakravarty

DECLARATION

I, hereby, declare that the investigation presented in the thesis has been carried out by me. The work is original and has not been submitted earlier as a whole or in part for a degree / diploma at this or any other Institution / University.

Uday Chakravarty

Uday Chakravarty

List of Publications arising from the thesis

A Published papers

A.1 Publications in Journals (10)

1) Pulsed laser deposition of metal films and nano-particles in vacuum using sub nanosecond laser pulses
R. A. Ganeev, **U. Chakravarty**, P. A. Naik, H. Srivastava, C. Mukharjee, M. K. Tiwari, R. V. Nandedkar, and P. D. Gupta
Applied Optics **46**, 1205, 2007

2) Efficient keV X-ray generation from irradiation of *in-situ* produced silver clusters by Ti:sapphire laser pulses
U. Chakravarty, P.A. Naik, S.R. Kumbhare, and P.D. Gupta,
J. Opt. Soc. Korea **13**, 80, 2009

3) Formation of metal nano-particles of various sizes in plasma plumes produced by Ti:sapphire laser pulses,
U. Chakravarty, P. A. Naik, C. Mukherjee, S.R. Kumbhare, and P. D. Gupta.
J. Appl. Phys. **108**, 053107, 2010

4) Enhanced soft X-ray emission from carbon nano-fibers irradiated with ultra-short laser pulses
U. Chakravarty, P. A. Naik, B. S. Rao, V. Arora, H. Singhal, G. M. Bhalerao, A. K. Sinha, P. Tiwari and P. D. Gupta
Applied Physics B: Lasers and Optics , **103**, 571, 2011

5) X-ray enhancement in a nano-hole target irradiated by intense ultra-short laser pulses
U. Chakravarty, V. Arora, J. A. Chakera, P. A. Naik, H. Srivastava, P. Tiwari, A.Srivastava, and P. D Gupta.
J. Appl. Phys. **109**, 053301, 2011

6) Nano-ripple formation on different band-gap semiconductor surfaces using femtosecond pulses
U. Chakravarty, R. A. Ganeev, P. A. Naik, J. A. Chakera, M. Babu, and P. D. Gupta.
J. Appl. Phys. **109**, 084347, 2011

7) Electric field enhancement at multiple densities in laser irradiated nano-tube plasma
U. Chakravarty, P.A. Naik, and P.D. Gupta
Pramana J. Phys. **79**, 443, 2012

8) Enhancement of K_α emission through efficient hot electron generation in carbon nano-tubes on intense laser pulse irradiation
U. Chakravarty, V. Arora, P. A. Naik, J. A. Chakera, H. Srivastava, A. Srivastava, G. D. Varma, S. R Kumbhare, and P.D Gupta

J. Appl. Phys. **112**, 053301, 2012

9) Enhanced water window x-ray emission from *in situ* formed carbon clusters irradiated by intense ultra-short laser pulses
U. Chakravarty, B. S. Rao, V. Arora, A. Upadhyay, H. Singhal, P. A. Naik, J. A. Chakera, C. Mukharjee, and P.D. Gupta
Applied Physics Letters **103**, 054107, 2013

10) Estimation of electron density and temperature of semiconductor surfaces excited by ultra-short laser pulse
U. Chakravarty, P.A. Naik , J.A. Chakera, A. Upadhyay and P.D. Gupta
Applied Physics A Materials Science & Processing DOI 10.1007/s00339-013-8063-y

A.2 Selected thesis related publications in Conferences / symposia (18)

1) A novel method of intense keV x-ray generation from in-situ produced silver clusters using Ti: Sapphire laser pulses.
U Chakravarty, P.A Naik, R.A Khan and P.D. Gupta.

DAE-BRNS National Laser Symposium, Vadodara, 2007
Awarded Best Poster Award by the Indian Laser Association

2) Enhanced x-ray emission in water window region from ultra-short laser pulse irradiation of carbon nano-fibers
U. Chakravarty, P.A. Naik, B.S.Rao, V. Arora, H. Singhal, R.A. Khan, P.D. Gupta, G.M. Bhalerao, A.K.Sinha,
Fifth International Symposium on Modern Problems of Laser Physics, Novosibirsk, Russia, Aug. 2008

3) Enhanced x-ray emission in water window spectral region from ultra-short laser pulse irradiation of carbon nano-fibers
U.Chakravarty, P.A.Naik , B.S.Rao, V.Arora, H.Singhal, R.A.Khan, P.D.Gupta, G.M. Bhalerao and A.K.Sinha
Fifth International Symposium on Modern Problems in Laser Physics, Novosibirsk, Russia, Aug. 2008

4) X-ray emission enhancement in various forms of carbon target under irradiation by ultra-short laser pulses,
U.Chakravarty, P.A.Naik, R.K.Bhat, and P.D.Gupta,
Fourth Asian Symposium on Intense Laser Science, Gwangju, Korea, Nov. 2008

5) Efficient keV x-ray generation from irradiation of silver clusters by Ti:sapphire laser pulses
U.Chakravarty, P.A.Naik, S.R Kumbhare, and P.D.Gupta ,
Fourth Asian Symposium on Intense Laser Science, Gwangju, Korea, Nov. 2008

6) Multiple electric field resonances in laser irradiated nano-shells
U. Chakravarty, M. P. Singh, P. A. Naik, and P. D. Gupta
26th National Symposium on Plasma Science & Technology, Patna, Dec.2008

7) A comparative experimental study of the absorption of intense, short laser pulses in plasmas formed by planar solids and nano-form matter
U. Chakravarty, P. A. Naik, J. A. Chakera, V. Arora, R.A. Khan, H. Srivastava, A. Srivastava, P. Tiwari , G.D. Verma, and P.D Gupta
DAE-BRNS National Laser Symposium, Mumbai, January, 2009.

8) X-ray Emission Enhancement In Nano-hole Alumina Irradiated By Intense Ti: Sapphire Laser Pulses
U. Chakravarty, V Arora, J. A. Chakera, P. A. Naik, H. Srivastava, P. Tiwari, A. Srivastava, S.R.Kumbhare, and P.D Gupta.
24th National Symposium on Plasma Science & Technology , Hamirpur, Dec. 2009.

9) Metal Nano-particle Formation Of Various Sizes In Plasma Produced By Ti:sapphire Laser Pulses
U. Chakravarty, P.A. Naik, R.K. Bhat, C. Mukherjee, and P.D. Gupta
24th National Symposium on Plasma Science & Technology , Hamirpur, Dec. 2009.

10) Enhancement Of Characteristic Hard X-rays Emission From A Ultra-short Pulse Laser Produced Plasma Source
V. Arora, **U. Chakravarty**, J. A. Chakera, P. A. Naik, S. R Kumbhare, H. Srivastava, A. Srivastava, G. D. Verma, and P.D Gupta
24th National Symposium on Plasma Science & Technology, Hamirpur, Dec. 2009.

11) Electric Field Enhancement At Multiple Densities During Hydrodynamic Evolution Of Laser Irradiated Hollow Dielectric Nano-tubes
U. Chakravarty, P. A. Naik, and P. D. Gupta,
International symposium on waves turbulence and coherent structure in plasmas, Gandhinagar, Feb 2010

12) Nano-ripple formation on different band-gap semiconductor surfaces using femtosecond pulses
U. Chakravarty, R. A. Ganeev, J. A. Chakera, M. Babu, P. A. Naik, and P. D. Gupta
19th DAE-BRNS National Laser Symposium , Indore, December, 2010.

13) Electric Field Resonances in Laser Irradiated Nano-tube
U. Chakravarty, P. A. Naik, and P. D. Gupta
19th DAE-BRNS National Laser Symposium , Indore, December, 2010.

14) Enhanced water window X-ray emission from graphite target by dual time delayed Ti: Sapphire laser pulses

U. Chakravarty, B. S. Rao, V. Arora, H. Singhal, P. A. Naik, J. A. Chakera, and P.D. Gupta
25th National Symposium on Plasma Science & Technology, Guwahati, Dec. 2010.

15) Upshift of resonance density due to asymmetric expansion of laser irradiated nano-rods.
U. Chakravarty, P.A. Naik, P.D.Gupta
25th National Symposium on Plasma Science & Technology, Guwahati, Dec. 2010.

16) Resonant absorption and x-ray emission from nano-particles of various shapes irradiated by intense laser pulses
U. Chakravarty, P.A. Naik, V. Arora, J.A.Chakera, B.S. Rao, H. Singhal, S.R. Kumbhare, and P.D.Gupta
Topical Conference on EM radiation interaction with atom molecule and cluster, Indore, March 2010.

17) Hole size effect in hard x-ray emission from intense laser irradiated nano-holes
U. Chakravarty, V Arora, J. A. Chakera, P. A. Naik, H. Srivastava, P. Tiwari, A. Srivastava, and P.D Gupta
26th National Symposium on Plasma Science & Technology, Patna, Dec.2011.
Awarded Best Poster Award by **the Plasma Society of India**

18) A novel technique to obtain surface plasma electron density and temperature of semiconductor surfaces excited by ultra-short laser pulse
U. Chakravarty, P.A. Naik , J.A. Chakera and P.D. Gupta
27th National Symposium on Plasma Science & Technology, Puducherry, Dec.2012

Uday Chakravarty

Uday Chakravarty

DEDICATION

In what started as a sibling rivalry to seek everybody's appreciation was soon followed by a realization that it is futile to compete with perfection. This enlightenment was followed by ever-growing admiration to the extent of worship. I dedicate this thesis to my sister *Jhanjha Chakravarty* who is my ardent admirer, my fiercest critic, and my companion, with whom the hardest times of struggle seemed like a joy ride, the one person whose contribution is outstanding for my pursuit of academics and voyage of accomplishments.

ACKNOWLEDGEMENTS

First of all, I thank all my friends starting from good old school days, university, training school and many important persons whom I have come across. They gave me their valuable outlook and inspired me with their goodness and generosity, which has directly or indirectly helped me accomplish the present research work.

I am extremely thankful to my thesis guide *Dr. P. A. Naik,* for his continuous guidance and encouragement in carrying out the experiments, discussing and finding solution to physics aspects of the observations of the results. I owe a great deal to him for always being vigilant on my scientific progress and for his benevolence he has bestowed even when I made innumerable mistakes on countless occasions which he tried to eliminate forbearingly. Undeniably, he has been instrumental in my progression from the darkness of ignorance to come up to the level of the contemporary.

I am highly thankful to *Dr. P. D. Gupta*, Director RRCAT for his valuable guidance, constant support, encouragement, and motivation throughout the course of this work. I will always be indebted to him for tirelessly cultivating in me the skills of writing scientific manuscripts.

I am also thankful to *Dr. J. A. Chakera* for his valuable help in carrying out various experiments in the laboratory.

I am short of words to express my gratitude to *Shri Vipul Arora,* who has been a friend, philosopher and guide. His generous sharing of knowledge and experience has been a major contribution in my work. Apart from this, his wit and enjoyable company gives more reasons to look forward to come to the work place.

The present research work could not have been completed without the help of my exceptionally gifted colleagues who have been inspiring me with their scientific prowess and humanitarian approach. I consider it my fortune to have worked with *Dr. Himanshu Singhal* and *Dr. B. S. Rao.*

Special thanks to *Shri Mukund Kumar* for his help in the thesis compilation and *Dr. Ajit Upadhyay* for the simulation support .

I thank *Shri R. A. Khan, and R.K. Bhat* for the operation of the Ti:sapphire laser and for their zeal and enthusiasm in carrying out the experiments. I thank *Shri S. R. Kumbhare, Shri S. Sebastin* and *Shri R. P. Kushwaha* for providing the experimental support.

I wholeheartedly thank my collaborator *Dr. R. A. Ganeev* for leading by example in some very intuitive experiments. I also thank my other collaborators *Shri Himanshu Srivastava, Smt. Pragya Tiwari, Dr. Arvind Srivastava, Dr. Chandrachud Mukherjee* and *Shri Mahendra Babu* for their magnanimity for providing support, which was key to the success of the thesis work.

This work is a tribute to my mother *Mrs. Savita Chakraborty* who has been a pillar of strength and wisdom, who made sacrifices throughout her life so that her children get the best share in the toughest of times. She is an epitome of integrity and a role model of righteousness and sincerity.

The thesis has a major contribution from my wife *Usha Chakravarty* who has been omnipresent virtually throughout the work. It is a difficult life for working women to perfectly manage every sphere of life, which she has been doing with a radiant smile. I consider myself blessed for having a wise, bright and loving life partner who concedes to my eccentric disposition so well.

And last but definitely not the least, a big thank you to *Aalo(Samragyi),* my daughter who is the "*Light of my Life*" and my son Vilakshan.

Uday Chakravarty

Uday Chakravarty

CONTENTS

SYNOPSIS

In the recent times, there is a continued interest for enhancing the energy absorption of high intensity, ultra-short laser pulses in their interaction with matter. The enhanced absorption is manifested in the observation of energetic electrons, MeV ions and x-rays. The x-rays are useful as a micron sized point source which has many potential applications like time resolved x-ray diffraction studies, imaging of live biological specimen, mammography, radiography, and x-ray lithography. Since the absorption of the high intensity (~10^{17} W/cm^2) ultra-short (~100 fs) laser pulses by planar solid targets is low, various types of targets like gratings, structured targets, pre-deposited metal clusters, gas clusters, snow clusters etc. have been used to enhance the coupling of the laser energy in matter. The increased deposition of the femtosecond pulse energy in the grating targets and in pre-deposited metal clusters, has been achieved through plasmon resonance and field enhancement in protrusions. However, since the gratings are expensive, they are practically unusable on routine basis as targets for x-ray source. Next, high absorption (80-90%) of ultra-short laser pulses has been observed in gas atom clusters. The interest in the clusters stems from the fact that the electric field inside the cluster is highly enhanced at three times the critical density (n_c) and it is a debris-free source. However, there are few limitations on the use of gas atom clusters as an x-ray source, such as : only few noble gases or cryogenically cooled gases can be used for cluster formation and it is a low rep-rate source.

Solid clusters have also been used as targets for efficient laser energy absorption but this involves two steps, first depositing the clusters on a planar solid substrate, and then using it as a target for plasma formation. Recently, intense femtosecond laser irradiation of solid targets has been proposed as a simple means of synthesis of clusters. If the cluster formation can be done by an ultra-short laser pulse and then these generated clusters in the plasma plume are irradiated by a time delayed intense ultra-short laser pulse, it offers a lot of

advantages as an x-ray source. First and foremost, this gives an access to a wide range of materials from which clusters can be formed, and it also has the advantage of being a high rep-rate source.

Minimum debris is a must for applications using a solid target as an x-ray source. For example, in applications like lithography, one does not want to spoil a nano-structure by debris deposition. *In situ* formed clusters can help overcoming the debris problem if the delay between the cluster forming pulse and intense main pulse is so adjusted such that cluster density at the interaction zone is highest. We have explored this possibility of using the *in situ* formed clusters for absorption of the intense ultra-short pulse and the consequent x-ray emission.

Since the properties of nano-particles are highly size dependent, their size is a crucial factor in any area of application. Hence size control becomes a crucial parameter in their generation. We observed that the size of clusters/nano-particles produced by short pulse laser can be easily controlled by varying the incident laser pulse duration, or by varying incident laser light intensity. A high absorption of the intense 45 fs laser pulses and efficient x-ray conversion in both soft (water window) and hard x-ray region (> 1 keV) is observed from *in situ* formed clusters. We have also carried out experiments for finding the laser parameters and other factors for finding conditions for maximization of x-ray yield. Absorption and x-ray emission was studied as a function of pre-pulse intensity, main pulse intensity and main pulse duration and the delay between the pulses.

Other nano-structures are also used to study their interaction with intense ultra-short laser pulses. The laser energy absorption in nano-structures has a profound dependence on shape, surface morphology, and other geometric factors. Nano-structures in various shapes like elongated and pointed nano-structures have shown enhanced x-ray and energetic particle emission and this has been attributed to the enhanced electric field at the tip, also referred to

as the “Lightning rod effect”. It is desirable to design a nano-target with a geometry which will enable even higher field enhancement when irradiated by ultra-short laser pulses for efficient x-ray and energetic particle generation. Recently, some other kinds of nano-structures have been used for laser matter interaction studies, especially the ones which have a hollow structure for example fullerene, nano-hole alumina, carbon nano-tubes etc. They show efficient x-ray and hot electron generation, but their resonance densities have not been reported. In order to understand the reason for the x-ray enhancement from nano-tubes, we investigated both theoretically and experimentally the effect of the hollow structure on the field enhancement.

Experiments have shown that grating targets when irradiated with intense laser pulses lead to enhanced absorption, x-ray emission and high energy collimated electrons generation. Such grating-like surface structure may also be produced by ultra-short laser pulses on interaction with a solid surface and they are called nano-ripples. Nano-ripples can be another candidate of *in situ* formed nano-structured target. The laser energy absorption in such periodic structures depends primarily on the ripple width. We have explored the possibility of forming nano-ripples on semiconductors with different band gaps and to identify conditions which control the width of nano-ripples by varying the laser parameters and the ambient medium. The critical role of the surface plasmons in deciding ripple period is identified to help in controlling the ripple period. Considerably narrow ripple period was observed in high band gap materials as compared to that in low band gap semiconductors. These femtosecond laser modified structures are also interesting for applications like improving the response and conversion efficiency of photovoltaic devices.

A chapter wise summary of these studies is given below.

Chapter 1 begins with a brief introduction to plasma and laser produced plasma, followed by a brief presentation on various absorption processes relevant to the present thesis

work. Absorption processes like inverse bremsstrahlung, resonance absorption, vacuum heating, and J×B heating are described. A brief introduction to the laser energy absorption in clusters is given describing the electric field resonances in nanoparticles. Apart from this, the x-ray emision processes like bremsstrahlung emission, line emission, inner-shell line radiation in general are discussed with special emphasis on water-window x-ray emission and the 17.5 keV Mo K-α characteristic line emission.

Chapter 2 gives the description of the 10 TW, 45 fs Ti:sapphire laser system used for the experiments included in the thesis. The uncompressed sub-ns pulse from this high power femtosecond laser system is used for cluster generation. To study the absorption and x-ray emission from *in situ* formed clusters, various diagonistics were used for absorption and scattering measurements. The x-ray emission was monitored with calibrated x-ray p-i-n diodes and various spectrographs were used to record different spectral regions of the x-ray emission. A transmission grating spectrograph was used for sub-keV measurements and an x-ray CCD camera was used for measuring hard x-ray spectrum above 2 keV. These diagonistics are elaborated in this chapter.

Chapter 3 describes an experimental study on the generation of nano-particles of various sizes using Ti:sapphire laser pulses. Nano-particle formation in plasma plumes of metals like silver and copper, expanding in vacuum, has been studied using sub-ns stretched pulses and compared with that generated with the 45 fs compressed laser pulses. The description of the structural analysis of the nano-particle was done through AFM and SEM. Also, the visible light transmission and reflection from the nano-particle film of Ag and Cu on glass substrate showed surface plasmon resonance. It is shown that the 45 fs pulses form smaller sized particles, whereas on using the sub-ns pulses, larger particles are produced. Thus, it is shown that by controlling the laser pulse duration, one can control the size of the nano-particles formed.

Chapter 4 describes the utilization of the *in situ* formed clusters by a sub-ns pulse as a target for intense ultra-short laser pulse. Conditions for enhancing the absorption and x-ray emission were optimized by changing the pre-pulse intensity, main pulse intensity, and the delay between the two beams. Silver clusters produced by a sub-ns laser pulse were irradiated by a 70 mJ, 45 fs compressed laser pulses. An absorption of the laser light exceeding 70% was observed, resulting in an x-ray yield (>1 keV) of ~ 60 μJ/ pulse, which corresponds to a conversion efficiency of 8.5×10^{-2} %.

Chapter 5 describes the utilization of *in situ* formed carbon clusters in a different more-easy-to-use geometry compared to that described earlier. The water-window x-ray spectral measurements were done using a transmission grating spectrograph**.** Description of the experimental results and analysis of the carbon cluster characterization by AFM is presented. Optimization of the x-ray yield as a function of the delay and the main pulse duration is described. Simulations for pre-plasma characteristics are also described. It is shown that the technique leads to an enhanced water window x-ray emission (23-44 Å). The conversion efficiency of the laser energy converted to the water- window x-ray emission was also measured. For a 110 mJ, 45 fs laser pulse, the conversion efficiency in the water window was 5.8×10^{-2} % /sr from planar graphite. For the dual pulse configuration with 8 ns delay between the cluster forming pulse and ultra-short high intensity main pulse, the conversion efficiency from carbon clusters was estimated to be 0.54 % /sr. This x-ray source is an efficient, high repetition rate, and low debris x-ray generation alternative.

Chapter 6 describes a comparative experimental study on the x-ray emission in the water-window spectral region performed using carbon nano-fibers (CNF) of different sizes and graphite plate targets, irradiated with ultra-short (Ti:sapphire) laser pulses. The chapter includes description of the experimental set up. Soft **x**-ray yield dependence on target geometry, laser pulse intensity and pulse duration is presented. More than an order of

magnitude enhancement in the x-ray yield is observed from CNFs of 60 nm diameter with respect to graphite targets. The effect of the laser pulse duration on the x-ray emission from the CNFs was also studied by varying the pulse duration from 45 fs up to 3 ps and it was found that optimum laser pulse duration for maximum x-ray emission increases with the diameter of CNFs used. The results are explained from physical considerations of heating and hydrodynamic expansion of the CNF plasma in which resonance field enhancement takes place while passing through two-times the critical density.

Chapter 7 contains discussions of the experimental results on nano-hole alumina when irradiated with intense short pulses. The effect of laser pulse duration, chirp, and hole size on the hard x-ray yield was studied. The theoretical studies of laser nano-hole interaction is also presented. The x-ray yield enhancement from the nano-holes shows an increased coupling of the laser energy to the target. The effect of laser pulse duration on the x-ray emission was also studied, where a peaked behavior was observed. The results can be explained by considering the hydrodynamic expansion of the laser irradiated structure and field enhancement in the nano-holes.

Utilization of the target geometry for maximum field enhancement is crucial for laser energy coupling. In the quest for identifying a target with a geometry which causes high field enhancement and supports many resonances is done theoretically. The **Chapter 8** chapter describes intense laser pulse interaction with nano-tubes. Four specific nano-tubes are chosen viz. solid nano-rods, thin, ultra-thin, and resonant nano-tubes. The electric field in a nano-tube plasma is shown to be resonantly enhanced at multiple densities during the two phases of interaction, first the ionization phase and second the hydrodynamic expansion phase. It is further shown that by a proper choice of hollowness of the nano-tubes resonance can occur right at the solid density and also a continued occurrence of the resonance over a longer time can be achieved.

Chapter 9 describes nearly complete absorption and hard x-ray emission from carbon nano-tubes (CNT) irradiated by intense ultra-short pulses. The theoretical analysis done in chapter 8 is experimentally explored in this work. First, a description of the experimental set up and CNT characterization is given. Absorption studies in CNTs show near complete absorption of the energy of intense ultra-short laser pulses (45 fs, intensity ~1.6×10^{16} - 2.5 $\times 10^{17}$ W/cm^2) in carbon nano-tubes deposited on a planar molybdenum substrate. The hollow structure of the nano-tube plasma facilitates resonant electric field enhancement during its ionization phase. This resonantly enhanced localized field at a density much larger than the critical density n_c leads to efficient hot electron generation, which results in enhanced K_α emission of Mo at 17.5 keV.

As mentioned earlier, an experimental study of nano-ripple formation in various band-gap semiconductors was done. This study is described in **Chapter 10**. The effects of the number of laser shots, the angle of incidence, polarization, fluence and incident laser wavelength of the laser, band-gap, and ambient medium on the ripple period, have been studied. Depending upon the experimental parameters, nano-ripple sizes varied in the range of ~ (0.1-1) λ. The observed results are explained considering the transient metallic nature of the semiconductor surface on irradiation with intense femtosecond pulse which excites surface plasmon leading to the nano-ripple formation. It is also proposed to use nano-ripples in future as an alternative target that can be generated *in situ*.

Chapter 11 gives a summary of the results in the thesis, and conclusions derived from the presented work. The future proposed works for extension of the present work is also outlined.

List of figures

List of tables

Chapter 1

Introduction

One of the most important inventions of this century is unquestionably the invention of LASER, which has led to the exploration of a plethora of phenomena in physical, chemical, and biological sciences [1,2], apart from its innumerable applications in medicine, material processing, defense, and entertainment, etc. Using lasers, it is now possible to study matter in its fourth state (i.e. plasma state) at extremely high temperature (~ tens of keV) and density (higher than solid density), thanks to the rapid developments in the technology of ultra-intense, ultra-short pulse lasers [3]. In particular, with the advent of chirped pulse amplification technique [4] one can obtain few optical cycle pulses with focused intensity reaching as high as ~ 10^{22} W/cm^2 [5]. This has opened a very wide range of research and developmental activities where the ultra-short, ultra-intense laser produced plasma becomes relevant as a high peak brilliance table-top source of high energy charged particles [6-13] and x-rays [14-17]. Most importantly, these lasers now have the capability to deliver a large amount of energy in a hot spot in a compressed core of deuterium and tritium, in order to ignite a fusion pellet in the inertial confinement fusion fast ignition scheme.

This thesis work is on the absorption laser light and subsequent x-ray emission from the interaction of ultra-short laser pulses (10 TW, 45 fs Ti:sapphire) with planar solid and nano-structured targets. The thesis begins with a brief description of the basic concepts of plasma and laser-plasma interaction involving laser energy coupling to the plasma, and emission of radiation from the heated plasma. Different absorption mechanisms possible in the laser-plasma interactions are discussed, starting with inverse bremstrahlung and standard resonance absorption. The other important absorption mechanisms for ultra-short, ultra-intense laser plasma

interactions known as “not-so-resonant” resonance absorption or vacuum heating and JXB heating are also be discussed briefly, followed by some description of laser-nano-particle interaction and various models that are used to understand the underlying physics. The x-ray emission process are also covered briefly, primarily focusing on the water window x-ray emission and characteristic K-α line emission. In the quest for finding better targets and techniques for enhancing the laser energy coupling in plasma, various techniques have been proposed and demonstrated, which are described in detail in this thesis.

1.1 Basic plasma parameters

1.1.1 Plasma : Definition

The word “plasma” describes a *quasi-neutral* assembly of charged and neutral particles, which exhibits *collective behaviour*. The term “quasi-neutrality” implies that the plasma is neutral on a macroscopic scale so that the overall charge of the electron and the ions can be taken as equal and opposite [18]. However, on microscopic scale, the charge in a given small volume need not be not completely neutral. The term “collective behavior” implies the existence of long range Coulomb force on large number of particles, as a result of which particles of a particular species (electrons or ions) tend to behave like a single entity, giving rise to several interesting phenomena. The terms quasi-neutrality and collective behavior can be further elaborated in terms of the following parameters which are characteristics of any plasma:

1.1.2 Debye length (λ_D) : The length over which the field of an individual charge is shielded out by the response of surrounding particles, is called the *Debye length*. If one puts an electric field inside the plasma, say by inserting an electrode connected to a battery, the electrode will

attract the particles of opposite charge and a sheath would be formed around the electrode to shield its electric field. The thickness of this charge-non-neutral layer surrounding the electrode (or a test charge) is called the Debye length. Physically, the Debye length is the distance over which the charge non-neutrality can exist in the plasma. Mathematically, the Debye length is given by [18],

$$\lambda_D \approx 7430 \sqrt{\frac{T_e(eV)}{n_e}} \text{ m} \qquad (1.1)$$

where, T_e is the plasma temperature in eV, and n_e is the plasma electron density in m^{-3}. Since the plasma is quasi-neutral, it is required that length of plasma (L) must be greater than the Debye length, as within λ_D the plasma can be non-neutral (i.e. $L >> \lambda_D$). Further, for the Debye shielding to be statistically meaningful and effective, the number of particles (N_D) in the Debye sphere should be large (i.e. $N_D = n_e \lambda_D^3 >> 1$)

1.1.3 Plasma frequency (ω_{pe}) : If the electrons in the plasma are displaced from a uniform background of ions, an electric field will be set up in a direction so as to restore the neutrality of the plasma by pulling the electrons back to their original position. However, due to their inertia, the electrons will overshoot and oscillate around their original position, with a characteristic frequency known as the *"plasma frequency".* It is denoted by ω_{pe} and it characterizes the response of plasma to the external time varying fields. Mathematically, the plasma frequency is given by [18]

$$\omega_{pe} = 56.4 \sqrt{(n_e)} \text{ rad/s} \qquad (1.2)$$

where n_e is the electron density in m^{-3}. Since ω_{pe} is the characteristic frequency of the collective oscillation of the electrons, it is required that it should be more than the frequency of collisions, so that the collective behavior can be sustained. This means

$$\omega_{pe}\tau >> 1 \qquad (1.3)$$

where τ is the mean time between collisions.

In short, for a quasi-neutral ensemble of charge particles to be called a plasma, it has to satisfy the following three criteria :

1) $L >> \lambda_D$; 2) $N_D = n_e \lambda_D^3 >> 1$; and 3) $\omega_{pe}\tau >> 1$

1.1.4 Waves in non-magnetized plasmas :

In general, a plasma can be a magnetized plasma (e.g. Tokamak plasma) or a non-magnetized plasma (e.g. laser produced plasma). As the present thesis work is related to laser produced plasmas, we shall discuss here only the waves which a possible in a non-magnetized plasma.

a) Electron Plasma waves : The plasma oscillations are electrostatic oscillations and do not propagate. However, plasma oscillation can propagate due to the thermal motion of electrons. Electrons streaming into adjacent layers of plasma with their thermal velocities will carry information about what is happening in the oscillating region. In this case, the plasma oscillations can be called a "*plasma wave*" or "*electron plasma wave*" or "*Langmuir wave*". The electron plasma wave dispersion relation (i.e. the energy-momentum relation) is given by

$$\omega^2 = \omega_p^2 + \frac{3}{2}k^2 v_{th}^2, \qquad \text{where } v_{th}^2 \equiv \frac{2KT_e}{m} \qquad (1.4)$$

b) Ion acoustic waves : Just as acoustic waves propagate from one layer to the next by collisions among the air molecules, in the plasma, an analogous phenomenon occurs. This is called an "*ion acoustic wave*". Ordinary sound waves cannot occur in the absence of collisions, but ions can still transmit vibrations to each other because of their charge; and acoustic waves can occur through the intermediary of an electric field. Since the motion of massive ions is involved, these waves have low oscillation frequency. The dispersion relation for an ion acoustic wave is given as [18]

$$\frac{\omega}{k} = \sqrt{\frac{KT_e + \gamma_i KT_i}{M}} \cong v_s \quad \text{where } v_s \text{ is the sound speed in a plasma.} \qquad (1.5)$$

It may be noted that whereas the plasma oscillations are basically "*constant-frequency* waves" with a correction due to thermal motion, the ion acoustic waves are basically "*constant-velocity* waves", and exist only when there is thermal motion.

c) Propagation of electromagnetic waves in plasma : For an electromagnetic (e.m.) wave of frequency ω_L propagating in plasma, the dispersion relation gets modified from $\omega_L = kc$ in vacuum to [18]

$$\omega_L^2 = \omega_p^2 + k^2c^2 \qquad (1.6)$$

where, ω_p is the plasma frequency, k is the wave propagation vector and c is the velocity of light. The refractive index (μ) of plasma varies as

$$\mu = \sqrt{1 - \frac{\omega_p^2}{\omega^2}} \quad . \qquad (1.7)$$

It may be noted from the above expression that the light wave propagates in plasma only if the refractive index is real i.e. when $\omega_L \geq \omega_p$.

1.2 Plasma production with lasers

Although 99% of the matter in the universe is said to be in the plasma state (the fourth state of matter), on the Earth, very little matter can be found in plasma state. However, plasma can be created artificially by several methods such as electrical discharge (DC), radio frequency (RF) discharge, ohmic heating, heating by particle beams, pinch devices etc. Plasma created with these methods give access to matter over an enormous range of temperature and densities [18]. One of the most important categories of plasma is the *"Laser-produced plasma*". On account of its high temperature and high density, is relevant for research investigations such as inertial confinement fusion [19] and x-ray lasers [20]. Laser produced plasma is a very small sized, high brightness source of short duration x-rays, which has many interesting applications such as in time resolved diffraction studies [21,22]. Further, the plasma produced by a high intensity laser is recognized as one of the most promising field of study due to its potential to accelerate ions [23] and electrons [24] to GeV energies on a small scale length, and for generating coherent x-rays [25].

When a high power laser beam is focused on a target (solid, liquid, gas), if the intensity is high enough, plasma is produced. The electric field associated with an electromagnetic wave of intensity I is E_o (V/cm) = 27.5 $\sqrt{}$ I (W/cm^2) [18] and at high intensities it can be higher than the atomic fields. Moreover, the oscillatory energy (*quiver* energy) of electron in the linearly polarized laser field $\{\varepsilon = e^2 E_o^2 / 4 m \omega^2 = 9.33 I_{14} \lambda(\mu m)^2 \ (I_{14} = I /10^{14} \text{ W/cm}^2) \}$ can become tens to hundreds of keV at moderate intensity of $10^{16\text{-}18}$ W/cm^2 . Even at lower laser intensities ~ 10^{11} W/cm^2, plasma is formed on the target surface (this intensity depends on the laser pulse duration). The physical process through which initial ionization takes place depends upon the intensity and temporal profile of the laser beam. For instance, at intensities $10^{12\text{-}14}$ W/cm^2, the

ionization of atoms is through nonlinear process of multi-photon ionization [26]. When the single laser photon energy is less than the ionization energy of the atom, simultaneous absorption of many photons can give a bound electron energy sufficient to cross the ionization barrier. For higher intensities (~$10^{14\text{-}15}$ W/cm^2) the laser electric field is strong enough to cause the distortion of the atomic potential and gives the electron a finite probability of tunnel ionization, provided the tunneling occurs before the field polarity reverses to increase the potential barrier [27,28]. Further increase of intensity distorts the atomic potential so much that the atoms are ionized through optical field ionization [29]. The above mentioned mechanisms causes the generation of free electrons and ions during the initial portion of an ultra-intense, ultra-short laser pulse and the subsequent laser pulse interacts with and gets absorbed in this plasma. Large spatial gradients in plasma density and temperature exist inside the plasma. Generally, the density decreases approximately exponentially with the distance away from target surface. One important parameter of laser-produced plasma is the density scale length (L). It is defined as the distance over which the density of the plasma decreases by a factor of 1/e [30]. For the case of an exponentially decreasing density profile of the type

$$n = n_o \exp(-x / L) \qquad (1.8)$$

the density scale length {given by n / (dn/dx) } is equal to L. However, the hot plasma expands during the laser pulse itself and results in a decrease in density with the distance away from the target surface. This decrease in density essentially depends on the laser pulse duration τ_L. In laser irradiated planer targets with finite spot size R, the plasma expansion may be considered to be nearly planar to an expansion distance of an order of focal spot radius R. The density scale length depends on laser pulse duration.

1) For laser pulse duration τ ~ few nano-seconds, the density scale length can be taken equal to focal spot radius [31].

2) For sub-nano-second (ps to fs) laser pulse duration τ, the density scale length is given by $c_S\tau$, where c_S is the plasma sound speed and is given by $c_S = (z\, k\, T_e/M_i)^{1/2}$. c_S is typically ~ $10^{4\text{-}5}$ m/s. Therefore, for τ ~ 100 ps, L ~ = 1-10μm ~ > λ_L and for τ ~ 100 fs, L ~ = 1-10 nm << λ_L For τ ~ 100 ps, L ~ 1μm ~ λ_L. For τ ~ 100 fs, L ~ 1 nm << λ_L. The density scale length and the laser pulse intensity are the key to various absorption process be it collisional or non collisional in nature. In the following we discuss some important laser energy absorption processes typically in the moderate intensity range of 10^{15}-^{18} W/cm^2.

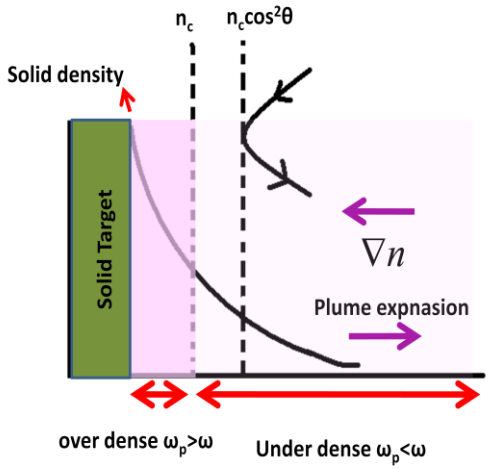

Fig. 1.1 The density profile of laser produced plasma and the trajectory of light in such plasmas.

Figure 1.1 shows a typical density profile of laser produced plasma. Since the laser-produced plasma has outward decreasing density profile, hence ω_p will increase in the inward direction (i.e. the direction of propagation of light). So at normal incidence, the laser light will penetrate only up to the density at which the frequency of laser light will become equal to the frequency of the plasma. This density at which $\omega_L = \omega_p$ is called the "*critical density*" and is represented by n_{cr}, and can be calculated as

$$\omega_L = \sqrt{\frac{n_c e^2}{\varepsilon_0 m}}\,. \tag{1.9}$$

In the terms of the wavelength of the e. m. wave, the critical density is given by

$$n_C = 1.1\times 10^{21}/\lambda(\mu m)^2 cm^{-3} \tag{1.10}$$

It is at this density, that the laser light undergoes total internal reflection. If the plasma has lower density than the critical density i.e. when the time period of electromagnetic oscillation is smaller than the response time of plasma electrons ($\omega_L \geq \omega_p$) the plasma will allow the electromagnetic wave to propagate through it. However, if the plasma density is high such that $\omega_L < \omega_p$, then the plasma electrons respond fast enough and reflect the electromagnetic wave. Such a plasma is called *over dense* plasma.

1.3 Absorption processes in laser produced plasma

Any absorption process of the electromagnetic interaction with matter should obey the Poynting theorem [32]. The theorem is basically about the electromagnetic energy conservation and, in a general form, is given by

$$\frac{\partial U}{\partial t} + \nabla.\vec{S} = -\vec{J}.\vec{E} \tag{1.11}$$

where $U = (1/2\varepsilon_0 E^2 + 1/2B^2/\mu_0)$ represents the energy density of the laser electromagnetic fields, S is the Poynting vector defined as $\vec{S} = c^2\varepsilon_0 \cdot \vec{E} \times \vec{B}$ and J is the electric current density. The rate of change of energy density is due to the energy flow expressed by the divergence of the Poynting vector and is due to the work done by the electromagnetic field onto matter [33]. In

steady-state conditions, averaging over the laser period *T*, the first term of the above equation becomes zero. Consequently $\langle \nabla.\vec{S} \rangle = \langle -\vec{J}.\vec{E} \rangle$ which implies that the averaged divergence of the Poynting vector is the dot product of the current density and the electric field of the electromagnetic wave.

For free electrons oscillating in an electric field, $\vec{E}$ and $\vec{J}$ (=ne$\vec{V}$) are out of phase by $\pi/2$. In this case, as expected, there is no absorption as $\vec{J}.\vec{E} = 0$. For absorption to occur, the phase of $\vec{J}$ and $\vec{E}$ have to differ from $\pi/2$, i.e. dephasing is required [34]. This can happen if there are collisions, which change the phase of $\vec{J}$ (or velocity) w.r.t. the external electric field $\vec{E}$. The random direction of the electron velocity (and its magnitude, as the collision can happen at any instant) after collision means *heating of the plasma*. Thus the energy gets transferred (*absorbed*) from the applied electric field of the electromagnetic wave (laser) to the plasma via collisions. Details of this mechanism are given in the next section (1.3.1).

The other way of coupling of the laser energy in plasma is through the processes of collision less absorption. This mechanism is discussed in detail later in section 1.3.2. Here, the electromagnetic wave excites plasma wave at the critical density and damping of this plasma wave couples the energy of the laser to the plasma.

We now describe in detail the various mechanisms of absorption of laser light into plasma.

1.3.1 Collisional absorption (Inverse bremsstrahlung absorption)

Inverse bremsstrahlung is one of the most common and well-understood absorption mechanisms of laser-matter interaction. It arises from electrons that have gained energy from the laser field and lose this energy in collisions with the ions. In this way, the light wave is effectively damped by the plasma, and the plasma correspondingly heats up [35-37].

The electron ion collision frequency determines the absorption and is given by [30,31]

$$\nu_{ei} \propto n_i \left(\frac{2ze^2}{m_e v_{te}^{\,2}} \right)^2 v_{te} \propto \frac{n_i z^2}{T_e^{3/2}} \propto \frac{n_e z}{T_e^{3/2}} \tag{1.12}$$

The electric field of the laser is E =E_O exp i(kz-ωt). In the presence of electron-ion collision frequency ν_{ei}, the wave vector k gets modified to

$$k = \left[\frac{\omega_L}{c} \right] \sqrt{1 - \frac{\omega_P^{\,2}}{\omega_L^{\,2}} \left[1 - i \left(\frac{\omega_P^{\,2}}{\omega_L^{\,2}} \right) \frac{\nu_{ei}}{\omega_L \times 2\left(1 - \omega_P / \ \omega_L^{\,2}\right)} \right]} \tag{1.13}$$

$k = k_{real} + k_{imag}$, which gives k_{imag} as

$$k_{img} = \frac{1}{2} \left(\frac{\omega_P^{\,2}}{\omega_L^{\,2}} \right) \left(\frac{\nu_{ei}}{c\left(1 - \omega_P^{\,2} / \omega_L^{\,2}\right)^{1/2}} \right) \quad . \tag{1.14}$$

The imaginary part of the wave-vector is responsible for the absorption and, since $k_{img} \propto \nu_{e,i}$, it means that laser absorption by the inverse bremsstrahlung process can take place only in presence of the electron-ion collisions. This mechanism takes place in the under-dense plasma region. The electron-ion collision frequency which describes the damping of the high frequency wave in a plasma is given by

$$\nu_{e,i} \approx 3 \times 10^{-6} \ln \Lambda n_e \left(\frac{Z}{T_e^{3/2}} \right) \tag{1.15}$$

where lnΛ is the Coulomb logarithm. The Coulomb logarithm, which is the ratio of maximum and minimum impact parameters, the maximum being the Debye length (λ_D) and minimum being the inter-atomic distance [31]. The minimum for the Coulomb logarithm is the 90 degree collision cross-section of the electron or the deBroglie wavelenglh of the electron, whichever is larger [31]. Its value is not very sensitive to the density and temperature and varies from 5-10 for a wide range of plasma parameters [18]. In eqn. 1.15, the electron density is in cm^{-3} and the electron temperature in eV. This expression also indicates that the inverse bremsstrahlung absorption will be stronger for lower temperatures, higher densities, and for high Z-target material. Moreover, it will be more for long density scale length plasmas [38].

At higher intensities, i.e. $I > 10^{17}$ W/cm^2, the inverse bremsstrahlung absorption gets reduced due to the decrease in collision frequency [39]. The electron temperature and the density scale length dependence on laser intensity is given by Riley *et al* as [40] for a laser pulse duration of 12 ps and a wavelength of 268 nm

$$T\,(eV) = 9.05 \times 10^{-7} [I_{abs}(W\ cm^{-2})]^{0.615} \quad (1.16)$$

$$L\,(m) = 4.28 \times 10^{-11} [I_{abs}(W\ cm^{-2})]^{0.306} \quad (1.17)$$

It must be noted that the temperature and scale length will be different at different times for another laser system depending on its wavelengths and pulse duration. Though, in general, it is concluded that at higher intensities, the electron temperature is higher and hence the collisional frequency decreases, as a result of which, the inverse bremsstrahlung absorption decrease on increasing intensity [38].

1.3.1.a Absorption by inverse bremsstrahlung of laser light incident normally

When the laser light is incident normally on the plasma, it travels up to the critical density n_c at which the laser light propagation stops and the e.m. wave gets reflected. The

absorption of the laser light in the under dense region can be estimated from the imaginary part of the wave vector (k_{img}). The absorption of laser light into the plasma also depends upon the density profile. The absorption can be estimated for linear and exponential density profiles as below [31]

i) For linear density profile*:*

$$n = n_c\left(1-\frac{x}{L}\right) \tag{1.18}$$

Absorption in length L is given by

$$A = 1-\exp\left[\int -\beta dx\right] \tag{1.19}$$

$$2k_{img} = \beta = \alpha\frac{n_e^{\,2}}{n_{cr}^{\,2}\sqrt{1-n_e/n_{cr}}} \tag{1.20}$$

where $\alpha = \nu_{ei}(n_{cr})/c$. On solving this, one gets the absorption factor A as

$$A = 1-\exp\left\{-\left(\frac{16}{15}\right)\alpha L\right\} \tag{1.21}$$

ii) For exponential density profile

$$n = n_{cr}\exp\left(-\frac{x}{L}\right) \tag{1.22}$$

$$\text{Absorption} = 1-\exp\left\{-\left(\frac{4}{3}\right)\alpha L\right\} \tag{1.23}$$

Based on the above equations, the absorption due to inverse bremsstrahlung can be estimated for linear (eqn. 1.21) and exponential (eqn. 1.23) density profiles. The values of α and $\nu_{e,i}$ depend on the density and temperature of the plasma.

1.3.1.b Absorption by inverse bremsstrahlung of laser light incident obliquely

When the laser light is incident obliquely on a target, the absorption due to inverse bremsstrahlung process decreases sharply with increasing angle. This is because the laser light gets reflected at $n_c\cos^2\theta$ (which is less than the critical density). Here θ is the angle of incidence of laser light from target normal [30,31]. Since the inverse bremsstrahlung absorption depends on the density, at larger angles of incidence, it is lesser in comparison to that at normal incidence [40,41]. It can be shown that in this case,

$$A = 1 - \exp\left(-\frac{32\nu_{e,i}L}{15c}\cos^5\theta\right) \tag{1.24}$$

and for an exponential density profile,

$$A = 1 - \exp\left(-\frac{8\nu_{e,i}L}{3c}\cos^3\theta\right) \tag{1.25}$$

For both these profiles, the absorption of laser light by inverse bremsstrahlung process decreases with increase in the incidence angle. At oblique incidence, the inverse bremsstrahlung absorption is estimated by assuming a density profile using the above relations. Thus, the following conditions are favorable for better inverse bremsstrahlung absorption

1) Short wavelength of laser light is better for inverse bremsstrahlung process. The shorter wavelength laser light penetrates up to a much higher density in the plasma. The corresponding collision frequency is also higher. Since the absorption of laser light by inverse bremsstrahlung process depends upon the collision frequency, *inverse bremsstrahlung absorption is higher for shorter wavelength lasers.*

2) The second important parameter for inverse bremsstrahlung process is the pulse duration of the laser light. For the long duration pulses, the density scale length is large (~focal spot). For the short duration pulses, the density scale length is proportional to the pulse duration

($c_S\tau$). Therefore, the absorption of laser light by inverse bremsstrahlung process increases with increase in the pulse duration. Thus, *long duration pulse is favorable for inverse bremsstrahlung process.*

3) Lower laser intensity is also more favourable for inverse bremsstrahlung absorption. At higher intensity, the temperature is also higher. The collision frequency decreases with increase in the temperature and hence with intensity. Hence *low intensity (or low temperature) is favorable for absorption by the inverse bremsstrahlung process.*

4) High density and high atomic number (Z) plasma are favourable for the absorption of laser light by inverse bremsstrahlung process, because the collision frequency increases with an increase in density and atomic number, as seen from eqn. 1.15. Thus, *higher density and higher atomic number are more favourable for the inverse bremsstrahlung absorption.*

1.3. 2 Resonance absorption

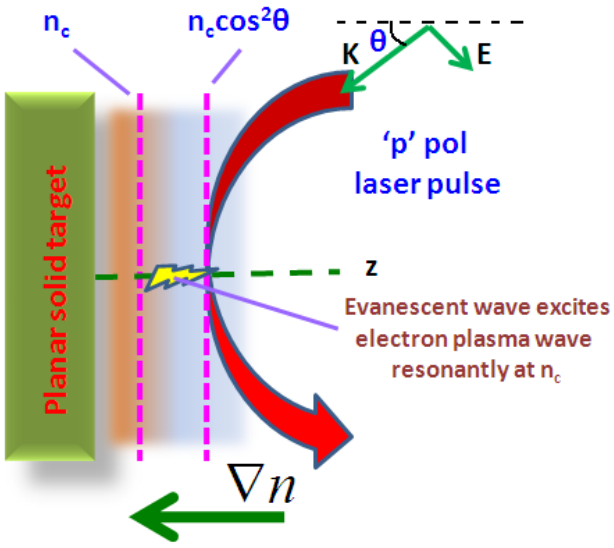

Fig. 1.2: Mechanism of resonance absorption

When a p-polarized laser light is obliquely incident on a plasma having density gradient, the laser is reflected from the $n_c\cos^2\theta$ surface and the evanescent wave excites the plasma waves as shown in Fig. 1.2 [30,31]. The evanescent wave amplitude decreases exponentially with distance from the reflecting interface. The evanescent wave has both transverse and longitudinal components. The longitudinal component resonantly excites oscillations at the critical surface, where the plasma frequency matches with the frequency of oscillation of the driving evanescent wave (i.e. the laser frequency). Therefore, the energy of the laser wave is coupled to the plasma by resonant excitation of electron-plasma wave at the critical density [42-46]. The driven electrostatic plasma oscillations are damped either by collisions or by collisionless process. The energy is, in effect, transferred from the laser electric field to the plasma. This process takes place only if the electric field has a component in the direction of density gradient [18,30,31].

The resonance absorption depends upon the polarization of electric field E. For s-polarization, the electric field is perpendicular to the plane of incidence, which means that there is no E field component in the direction of density gradient. Hence the evanescent wave does not have any longitudinal component. As a result, no resonance absorption should take place for the s-polarized laser light. However, finite resonance absorption is still reported due to surface roughness [47], rippling of critical density surface [48,49], polarization rotation due to self generated magnetic field in plasma [50,51], and the finite "p" component due to focusing geometry.

1.3.2.a Landau damping

As mentioned earlier, a collisionless damping of the electron plasma wave excited by the resonance absorption takes place by Landau damping. This damping mechanism can be explained using the simplistic picture below (it can be also explained by rigorous mathematics). A wave will exchange its energy with the particles traveling with a velocity close to the phase velocity of the wave. If the particle has higher velocity than the wave velocity, it will overshoot the wave and get slowed down to the wave velocity and if its velocity is lower, it will gain energy from wave. So in plasma, the electrons with slightly higher velocity than the plasma wave velocity will lose their energy to the plasma wave and those with slightly lower velocity will gain energy from the plasma wave [30,31]. A Maxwellian distribution has, for any wave velocity, more slower electrons than faster ones i.e. the number of electrons having velocity slightly greater than the phase velocity of plasma wave is always lesser than the number of electrons having velocity slightly smaller than the phase velocity of plasma wave [18]. Therefore the electrons will gain net energy from the wave i.e. wave always gets damped. The temperature of these "hot electrons" (T_{hot}) produced due to resonance absorption is given by T_{hot} (keV) $\approx 10 (T_{keV} I_{15} \lambda^2)^{1/3}$ [52], where T_{keV} is the background electron temperature.

The resonance absorption is critically dependent on the incidence angle of the laser. If the incidence angle θ is small, then the component E $\sin\theta$ along the density gradient small, and therefore small density fluctuation takes place. Hence resonance absorption is low. If θ is large, then the total internal reflection takes place at lower densities and hence the turning point is at a larger distance from $n_{cr.}$ Hence evanescent field does not reach the critical density surface efficiently. Hence the resonance absorption is less. Thus, there exists an optimum angle of

incidence where the resonance absorption reaches a maximum. For a linear density profile, the optimum angle θ is given by [31]

$$[k_L L]^{1/3} \sin\theta = 0.8 \qquad (1.26)$$

For $L >> \lambda_L$, the resonance absorption occurs in small range of angles around θ given above. However, for $L << \lambda_L$, the laser light is practically close to the critical density for large range of angles, and there is no sharp maximum angle.

For effective resonance absorption, the following conditions of the laser are favorable:

1) P-polarized light is necessary because it light has a component of the electric field vector is in the direction of the density gradient, which produces the plasma wave at the critical density.
2) Higher laser intensity is favorable for resonance absorption because at high intensities the electric field being large, for a given angle of incidence, the component of electric field E sinθ along the density gradient is also high, so that it excites the plasma wave effectively.
3) Short laser pulse is favourable for resonance absorption, because for a short pulse, the density scale length is short ($L=c_s\tau$). Hence, the distance of critical surface from reflected surface is small. Therefore, the evanescent field of the reflected laser light reaches the critical density properly. Therefore resonance absorption is high for short laser pulse.

1.3.3 Vacuum heating

This absorption mechanism was first discussed by Brunel [53] and is also known as *Brunel heating.* The electric field of laser light drives electrons across a density gradient which is much smaller than the wavelength of laser light [54-57]. Consider a resonantly driven plasma

wave at the critical density with a field amplitude E_P. In a sharp edged profile, E_P will be roughly same as incident laser field E_o. The electrons will undergo oscillation along the density gradient with amplitude

$$X_P = \frac{eE_0}{m_e\omega_0^{\,2}} = \frac{v_{0S}}{\omega_0} \tag{1.27}$$

The resonance breaks down if this amplitude exceeds the density scale length L, i.e. if

$$\frac{v_{0S}}{\omega_0} > \text{L}. \tag{1.28}$$

Under this condition, the electrons are not heated by a plasma wave, since this wave is destroyed and rebuilt afresh each cycle. Brunel proposed that here the electrons are directly heated by the p-polarized component of the laser field. According to the Brunel model, electrons are dragged away from the target surface, turned around and accelerated back into the solid all within half a laser cycle. The laser field only penetrates to a skin depth or so. Assuming that the electrons gain a velocity v_{os} during their vacuum orbit, the absorption fraction has been estimated as [52]

$$f_{vh} = (8/c)v_{osc}\sin^3\theta \tag{2.29}$$

As expected, the absorption fraction of the laser light by the vacuum heating process increases with increasing the incidence angle, since the component of the electric field of the laser in the direction of target normal increases with increase in angle of incidence. Brunel heating absorption is proportional to $\sqrt{(I\lambda^2)}$ therefore it is dominant absorption mechanism for intense few cycle laser pulses [58].

1.3.4 J×B heating

Plasma heating mechanisms like resonance absorption and vacuum heating can occur only for oblique laser incidence with p-polarization. However for high intensity pulses, high absorption is recorded even at normal incidence and s-polarization [59]. At high intensities the

electric field of laser is strong enough to drive the electrons relativistically, then the magnetic term of the Lorentz force is not negligible and makes the electrons undergo "figure-of-eight" motion. The longitudinal component of this motion can drive longitudinal plasma oscillations leading to heating of plasma by the damping of the plasma oscillations. Heating by such mechanism is referred to be JX B heating [60]. For intense light, the plasma density is steepened because of the ponderomotive force (due to longitudinal component of electron motion). The driving term is the high frequency v×B component of the Lorentz force, which oscillates the electron undergoing figure-of-eight motion at twice the laser frequency. A wave $E = E_o(x) \sin\omega t$ gives rise to a longitudinal pondermotive force term given by [60]

$$f_x = -\frac{m}{4}\frac{\partial v_{os}^{\ 2}}{\partial x}(1 - Cos2\omega t) \tag{1.30}$$

If the magnitude of the force is large enough, all the electrons at the boundary will oscillate in the direction of the k vector of the laser. From this expression, it is clear that this force is proportional to v_{os} and the spatial gradient of v_{os} , both of which become high for ultra-short ultra-high intensity pulses [60]. The fraction of electrons escaping as hot electrons depends on the strength of the oscillating force and laser energy is directly coupled to the hot electrons. If the energy associated with the electrons is given by the potential they feel during the interaction, then an effective "temperature" of the "hot" electrons is given by [52]

$$T_{hot} \approx \left(\sqrt{1 + \frac{I\lambda^2}{2.8\text{x}10^{18}}} - 1 \right) 511\, keV \tag{1.31}$$

To summarize, the absorption mechanisms involved in the laser plasma interaction depends on the laser intensity, pulse duration, polarization, and incidence angle. One can find out which absorption mechanism is dominant in a given plasma condition, with the help of

polarization, incident angle, and emission characteristics of electrons [59,61,62]. Resonance absorption and vacuum heating takes place only for p-polarized light. By measuring the absorption before and after changing the polarization, one can distinguish between these two groups. By changing the laser polarization from s to p, if the absorption increases, the possible absorption mechanism could be resonance absorption or vacuum heating. To distinguish between resonance absorption and vacuum heating, one needs to change the angle of incidence of the laser as vacuum heating keeps on increasing with increasing angle of incidence. If for a given angle of incidence, by changing polarization from s to p, the absorption does not change, the possible absorption mechanism could be inverse bremsstrahlung absorption or J×B heating, as they are independent of laser polarization. By varying the incident laser intensity, one can distinguish between inverse bremsstrahlung and J×B heating. On increasing the intensity, the inverse bremsstrahlung absorption decreases as the hotter plasma becomes more and more collisionless. On the other hand, with increasing intensity, the J×B force increases, as the ponderomotive force is higher at higher intensities. In general, the inverse bremsstrahlung absorption dominates up to 10^{17} W-cm^{-2}. Beyond this intensity, J×B heating dominates over the inverse bremsstrahlung absorption. The hot electron emission characteristics also shed some light on the absorption process. In the case of resonance absorption, or vacuum heating, the hot electrons comes out normal to the target surface [55,63]. In J×B heating, if the magnitude of the J×B forces increases, then the electrons go in the direction of the laser [59,61,62].

1.4 Absorption in gas clusters / nano-particles

The absorption of the high intensity (~10^{17} W/cm^2) ultra-short laser pulses (~100 fs) by planar solid targets is quite low (~10-20% at near normal incidence) [39, 64]. At an oblique

incidence of 45^0 and similar intensity range, Borghesi *et al* have measured ~ 10% absorption for s-polarized light and ~ 30% for p-polarized light [65]. At even higher intensities the absorption varied from 10-40% for a large range of incidence angle and showed very less dependence of absorption for s and p-polarized light [66]. This low absorption at moderate intensities ~$10^{16\text{-}17}$ W/cm^2 is because the short scale length of the ultra-short laser produced plasma offers a negligible collisional absorption, especially at higher intensities, due to the decrease in collision frequency [39,40]. Resonance absorption also requires an optimum scale length which is achieved by either changing the angle of incidence [40,45] or by introducing a prepulse which creates a pre-plasma of the desired scale length [67,68]. For pulses < 100 fs, the scale length becomes too small for excitation of plasma wave and vacuum heating is considered as the major absorption mechanism, though this process of heating is more effective at intensities >10^{17} W/cm^2 [59]. Therefore, it becomes important to find targets offering a high absorption of the laser energy. Hence experimental investigations on interaction of intense ultra-short laser pulse with gas clusters and nano-structured targets are being widely pursued for enhanced energy coupling [69-71] leading to bright x-ray emission [72], generation of MeV ions [73], fusion neutrons [74], and hot electrons [75]. Nano-structures with pointed and elongated shapes have shown enhanced x-ray and energetic particle emission and this has been attributed to the enhanced electric field at the tip, also referred to as the "Lightning rod effect" [76-78]. Some other kinds of nano-structures have been used for laser matter interaction studies, especially the ones which have a hollow structure [79-86]. They show efficient high x-ray generation and hot electron generation [79-86]. To name a few, the hollow nano-targets that have been used for experiments with intense short pulses include: fullerene [79], nano-hole alumina [80], foam [81], nano-brush [82], carbon nano-tubes (CNTs) [83,84] etc. The enhanced field and surface

currents in hollow structures are believed to support hot electron generation and transport [82-86] necessary for the fast ignition scheme of inertial confinement fusion, and also for efficient x-ray generation. The electric field enhancement in the nano-structures make the effective laser intensity on the target very high, and consequently, it leads to x-ray yield enhancement that is proportional to the rescaled enhanced intensity [87]. Similarly a lot of work has been done on laser gas atom cluster interaction [88,91]. These clusters created by expanding a jet of gas in vacuum are Van der Waal bonded. The cooling associated with the adiabatic expansion causes the gas to supersaturate and the atoms nucleate into clusters. The size of these cluster depends on the nozzle diameter, expansion half angle, backing pressure, and stagnation temperature of the gas being used [92]. To explain the enhanced absorption in clusters, a variety of models of the laser–cluster interaction have been put forward. These include: inner shell excitation [91], ionization ignition [93], collective electron dynamics [94], Coulomb explosion [95], and nano-plasma model [96]. The last one explains the maximization of the absorption cross-section and the electric field in the vicinity of Mie resonance at $3n_c$ in spherical clusters. A large number of experimental results concerning laser energy absorption and spectral emission characteristics [97-100] are observed to be consistent with this model. Various models of laser cluster / nano-particle interaction are briefly described in the following sub-sections.

1.4.1 Nano-plasma model (uniform density)

The interaction of a laser pulse with a cluster can be understood as that of laser interacting with a small ball of high density plasma. This picture is valid when the cluster dimension is significantly larger than the plasma Debye length. When high intensity laser interacts with a cluster, two important processes take place. First, the ionization takes place,

which is followed by heating during cluster expansion [96-100]. According to uniform density model, heating of the cluster volume occurs uniformly. Since light penetrates into solid to a depth of about a wavelength, when the size of the cluster is very small compared to the laser wavelength, the cluster sees uniform electric field inside. The field inside a dielectric sphere kept in uniform electric field E_o is given by [96-100]

$$E = 3 E_o / (\varepsilon + 2). \qquad (1.32)$$

When $(\varepsilon + 2) \rightarrow 0$, the field inside gets highly enhanced. For plasma, $\varepsilon = 1 - n_e/n_c$. Hence the condition $\varepsilon + 2 = 0$ means $n_e/n_c = 3$ or $n_e = 3 n_c$. This means that as a cluster is heated from solid density, it will start expanding and as the density reaches three times the critical density, the laser field inside the cluster gets highly enhanced and the light gets strongly absorbed. The absorption cross-section for a cluster is given by

$$\sigma_{abs.} = 4\pi k r^3 \,\mathrm{Im}\left(\frac{\varepsilon - 1}{\varepsilon + 2}\right) \qquad (1.33)$$

which also has the same inverse $\varepsilon + 2$ dependence and gets enhanced at $n_e = 3 n_c$. In a practical situation, ε depends on the collision frequency also and the expression gets modified to, $\varepsilon = 1 - \frac{\omega_p^2}{\omega_L(\omega_L + i\nu)}$ which gives the absorption a finite width and finite peak, instead of being a Dirac delta function.

Figure 1.3 describes the absorption process of ultra-short laser pulse in a cluster. There exists an optimal pulse duration for maximum laser energy absorption [97]. If the pulse width is too small (<100 fs), the cluster absorbs energy and expands, but by the time it reaches $3n_c$ the laser pulse is over. If the pulse is too long, then the $3n_c$ condition is reached before the arrival of the peak of the laser electric field [96,97]. It is therefore desirable for maximum absorption and

x-ray generation that the resonance condition is met at or near the peak of the ultra-short laser pulse [96,97,101]. Therefore, for meeting this requirement, the laser pulse is generally stretched and there exists an optimum pulse duration for a given size of a cluster. The expansion time of the cluster to reach the resonance density is given by [97],

$$\tau = \left(\frac{r_0}{c_s}\right)\left[\left(\frac{n_e}{3n_c}\right)^{1/3} - 1\right]. \qquad (1.34)$$

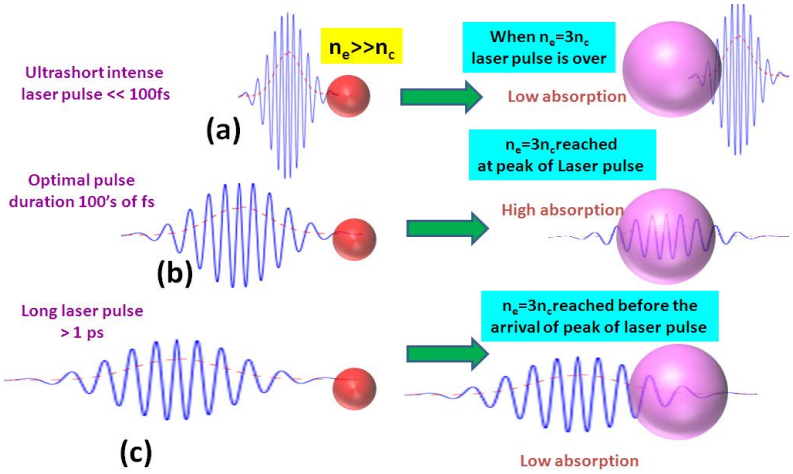

Fig. 1.3 Pictorial depiction of uniform density nano-plasma model a) for pulses < 100 fs b) optimal pulse for maximum absorption c) Long laser pulses > 1 ps

Cluster expansion can be attributed to two process. First one is the hydrodynamic pressure ($n_e kT$). Since in an expanding cluster, $n_e \alpha 1/r^3$, the hydrodynamic pressure also decrease with increase in the cluster radius. The other mechanism of cluster expansion is the Coulomb pressure due to the cluster ionization and it has a variation $\alpha 1/r^4$. The Coulomb pressure is more dominant for smaller clusters [96]. When the resonance condition is reached in a cluster, the field inside becomes extremely high due to field enhancement. This field gives a oscillates the electrons at a high amplitude, driving them out of the cluster. Once the electron is out of the cluster, it sees the actual electric field of the laser which is much lower than the inside field. As a result, the electrons which come out of the cluster tend to fly off (as the field outside

is too low to push them back into the cluster), leaving a cluster of positively charged ions. Due to the strong Coulomb repulsion, this cluster expands with a high velocity (i.e. explodes). This phenomenon is called *Coulomb Explosion*.

1.4.2 Non-uniform density model

This is an extension and improvement of the uniform density nano-plasma model. In the non-uniform density model, one considers the radial non-uniformities during cluster expansion in the laser interaction with atomic clusters [102]. Holkundkar *et al* [103] have calculated the laser absorption by solving the Helmholtz equation for a stratified sphere using a recursive algorithm. They include three types of ionization mechanisms, namely: tunnelling ionization, collisional ionization and ponderomotive ionization Furthermore, the collisional ionization is calculated by using a numerically fitted formula for the gases of low atomic numbers ($Z < 28$), while Lotz formula is used for higher-Z elements. The hydrodynamics is treated by solving the conservation of mass, momentum and energy equations in 1D Lagrangian geometry. The uniform density

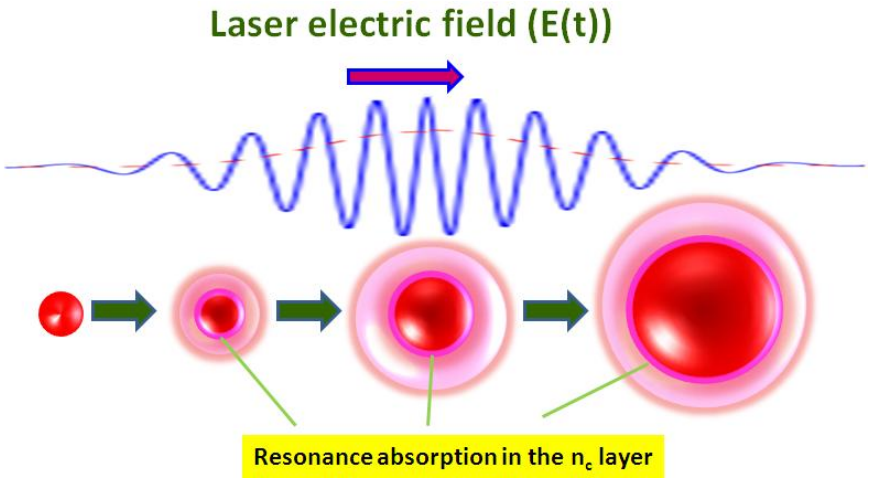

Fig. 1.4 Pictorial depiction of non-uniform density model. As time progresses, the n_c layer keeps evolving giving rise to high absorption during the entire hydrodynamic expansion of cluster

model, where the cluster is considered as a one region sphere, is a particular case of this general model. It is shown that the spatial non-uniformities play a vital role in the absorption dynamics.

In the case of the uniform density model, the resonance occurs only once , but here the resonance point keeps moving in space and time giving higher absorption as depicted in the Fig. 1.4. For a laser intensity of $5x10^{15}$ W/cm^2, the laser absorption increases by a factor of 40 as compared to the uniform density model. Study of the effect of the pulse duration of the laser revealed that in this model also, there is an optimum pulse duration for maximum absorption.

1.4.3 Oscillator model and nonlinear collisionless absorption.

In the first stage of irradiation of a cluster, the generation of free electrons by laser field takes place. This is referred to as "*inner ionization"*. With increasing laser intensity, few electrons may leave the cluster. This is referred to as "outer ionization". The laser field displaces the electron cloud, and the ions being massive are considered stationary. The separation of the charged spheres causes the setting of space charge fields which provides the restoring force and causes the oscillation of the electron cloud about the ion sphere, as shown in Fig. 1.5. The problem has been modeled by Saalmann *et al* [104] considering a damped driven harmonic oscillator. The linear resonance is met when the $\omega=\omega_p/\sqrt{3}$, where ω is the laser frequency and $\omega_p/\sqrt{3}$ is the natural frequency of cluster oscillation. The cluster oscillation frequency is very high initially due to the solid density plasma created in the foot of the intense laser pulse. Therefore, for linear resonance, the cluster has to expand sufficiently so that the cluster oscillation frequency is reduced to become equal to the laser frequency.

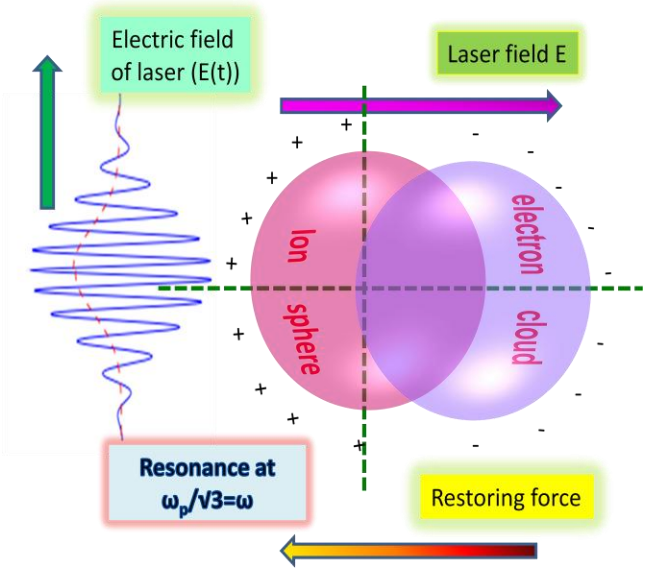

Fig. 1.5 Depiction of oscillator model of laser cluster interaction where the electron cloud is displaced with respect to ion sphere, the restoring force is provided by the Coloumb attraction

If the electron sphere is displaced to a very large extent, the restoring force is reduced, which leads to the reduction of the instantaneous oscillation frequency. Like in other nonlinear oscillations, here also the instantaneous frequency of oscillation depends on the instantaneous amplitude [105,106]. The instantaneous oscillation frequency is given by

$$\omega(t)=\frac{\omega_p(t)}{\sqrt{3}}\left(1-\left(\frac{9}{16}\right)\Delta(t)\right) \tag{1.35}$$

where Δ is the amplitude of the electron cloud displacement per unit cluster radius. Nonlinearity starts playing an important role only when the displacement Δ becomes large and hence there exist a threshold intensity that depends on the cluster size and density [107]. The resonance condition can be met during every cycle and even without considering cluster expansion, high absorption is likely to occur.

1.5 X-ray Emission Processes in Plasma

The absorption processes described above cause heating of the plasma and a hot dense ionized matter is created, which emits radiation right up to the x-ray region. The spectrum of x-ray emission from plasma is an envelope of the radiation emitted from a) free-free, b) free-bound, and c) bound-bound transitions in various ionization species present in the plasma. The spectrum is therefore a superposition of the line radiation on a broad continuum. The x-ray emission from laser produced plasma (LPP) is determined by the charge state distribution as well as the excited level population of different ions [108]. This in turn depends on the hydrodynamic parameters viz. plasma temperature and the electron density.

1.5.1 Free-free radiation

This radiation is emitted when a charged particle is accelerated or retarded in the Coulomb field of another charged particle. Here as the particle emitting radiation is free before and after the emission, it is called *free-free* radiation. It is also called *bremsstrahlung* (braking radiation). In a hot plasma, when an energetic electron comes in the Coulomb field of an ion, it gets deflected, undergoes acceleration and emits radiation. The emitted photon energy has the following dependence:

$$\Delta\varepsilon \propto Z^2 / b^3 v \qquad (1.36)$$

where v is the velocity of the electron, b is the impact parameter, and Z is the ion charge. Along with the electrons, the ions also gets deflected but being massive the acceleration is negligible and hence they do not make a significant contribution in the emission. The interactions between ion-ion and electron-electron do not result in the emission of radiation (except at relativistic velocities). This is because when two identical particles of equal charge and mass interact, they

produce equal and opposite acceleration and the radiation emitted by both the particles cancels out. Thus for plasma, the bremsstrahlung radiation is primarily due to the deflection of electrons in the field of ions. The power emitted/volume of bremsstrahlung radiation (W_B) is proportional to $\sqrt{T_e}$, and the power emitted per unit volume per wavelength is given by the expression

$$W_B^{\lambda} = 2.2 \times 10^{-27} Z n_e^2 [T_e]^{-1/2} [(1/\lambda^2) \exp{-(hc/\lambda k T_e)}] \text{ erg sec}^{-1} \text{ cm}^{-4} \quad (1.37)$$

1.5.2 Free-bound radiation

This radiation is emitted when a free electron is captured in the bound state of an ion. Since the electron is free before emission and bound after emission, this radiation is called free-bound radiation. The radiation is emitted in the form of photon of energy $h\nu = KE + E$, where KE is the kinetic energy of the free electron and E is the ionization potential of the recombining level of the ion. $h\nu = E$ is called the recombination edge. The recombination spectrum is continuous as the free electrons have a continuous energy distribution (Maxwellian distribution). However, since the recombination can occur in various shells with different values of E, the overall spectrum is quasi–continuous showing discontinuities at various shell energies. The emitted power/ volume (W_R) of the recombination radiation is given by

$$W_R = 2.4 \, W_B \, [Z^2 E / kT_e] \quad (1.38)$$

The continuum x-ray emission spectrum from a plasma consists of both free-free radiation and free-bound radiation. Power emitted as recombination may exceed that of bremsstrahlung at low temperatures and high ionization potentials. At very high temperatures, the free-free radiation dominates as ions become completely stripped.

1.5.3 Bound-bound radiation

Bound-bound radiation or line radiation is emitted as a result of transition between two bound states of an ion or an atom. The spectrum of the emitted radiation therefore consists of line at discrete wavelength rather than being continuous. Power emitted per unit volume (P_{bb}) as line radiation from plasma is given by

$$P_{bb} = 3.5 \text{ X } 10^{-25}(kT_e)^{-1/2} N_e \Sigma N_{i+1} \exp(-E_i / kT_e) \text{ W/cm}^3 \qquad (1.39)$$

where E_i is the energy of radiation emitted by an ion of charge i. The line radiation can be put into three different categories as described below:

a) Resonance lines: These are the transitions from excited states to the ground state of partially ionized species. The selection rules followed by these transitions are same as those for the optical transitions. Resonance lines play an important role in the diagnostics of plasma. Intensity ratio of the two resonance lines can be used for temperature estimation and these lines with the combination of other lines can be used for density and temperature estimation in plasmas. Since the oscillator strength of resonance transition is very high, such lines are quite likely to be reabsorbed in dense plasma and thus the opacity of such radiation should be taken into account for quantitative analysis.

b) Intercombination lines: The intensity of the optically allowed transition of same multiplicity is very high (as in the case of resonance transitions). Relatively weaker lines which arise due to transitions between states of different multiplicities, are called intercombination transitions. The energy of an intercombination line is slightly less than that of the corresponding resonance line. These weaker lines thus appear as satellites of the resonance lines on the higher wavelength side. The ratio of the intensity intercombination lines to that of the resonance line can be used for the density estimation of plasmas.

c) Dielectronic satellite lines: In an x-ray spectrum, the dielectronic satellite lines arise as a result of transitions originating from doubly excited states of multiply charged ions. Due to the presence of an additional electron, called the spectator electron, the Coulomb shielding decreases, this results in transitions occurring at slightly lower energy than that of resonance line. Depending on the excited state of the additional electron, there can be a number of satellites but the most distant from the resonance lines and at the same time the strongest are those corresponding to the transitions in the presence of an additional electron in the state of lowest quantum number n=2. The ratio of intensities of dielectronic satellites can be used for density estimation.

1.5.4 Characteristic line radiation

The characteristic line radiation is generated by a two stage process, first the generation of vacancy in the atomic (or ionic) inner shell (K, L, M etc.) and second is lowering of the energy by the atom by one of its outer shell electron jumping to the inner shell, emitting a photon having energy equal to the difference energy. The filling of a vacant K-shell by an L-shell electron results in K-α radiation. The inner shell vacancies are mostly created by external energetic free electrons, like the hot electrons in the plasma. Hence, the K-α yield essentially depends on the energy distribution of the hot electrons and the K-shell ionization cross-section σ_K for electron impact. It is assumed that: i) the hot electron energy distribution is Maxwellian; and ii) the K-α photons generated by the hot electrons with certain energy are emitted at some mean depth. Reich *et al* [109] predicted existence of an optimum laser intensity for the K-α yield as a result of equilibrium between the K-α production and the re-absorption in bulk targets. It

occurs when the mean emission depth is comparable to the absorption length for K-α. It is found that there is both an optimal target thickness and hot-electron temperature for forward emission. This temperature has been shown to be six times the K-shell ionization energy and it was independent Z of the target [109]. As the hot electron temperature is related to the laser absorption mechanism, it is important to optimize the energy distribution of the hot electrons in experimental conditions to achieve high conversion efficiency of the K-α line radiation.

1.5.5 Water window x-rays

Pulsed soft x-ray from laser produced plasmas offers a chance to study living cells with a time resolution sufficient to capture dynamical processes on a sub-nano-second or even sub-picosecond time scale. Although electron microscopy can provide high resolution, it requires dehydration of the sample and its treatment before analysis. X-ray microscopy using x-rays in the "*water-window*" spectral region (2.3– 4.4 nm) from laser produced plasma allows imaging of live biological samples [108]. This is the x-ray region between the K-edge of carbon and the K-edge of oxygen. In this region, carbon has high absorption and water has low absorption, so that there is no need to dehydrate the biological specimen. This region allows transmission of the probe beam through the live sample while providing natural contrast between proteins (i.e. carbon, nitrogen and oxygen) and water (oxygen), which can yield information on protein structures, since water present in the live samples has a very low absorption coefficients compared to proteins as shown in Fig. 1.6.

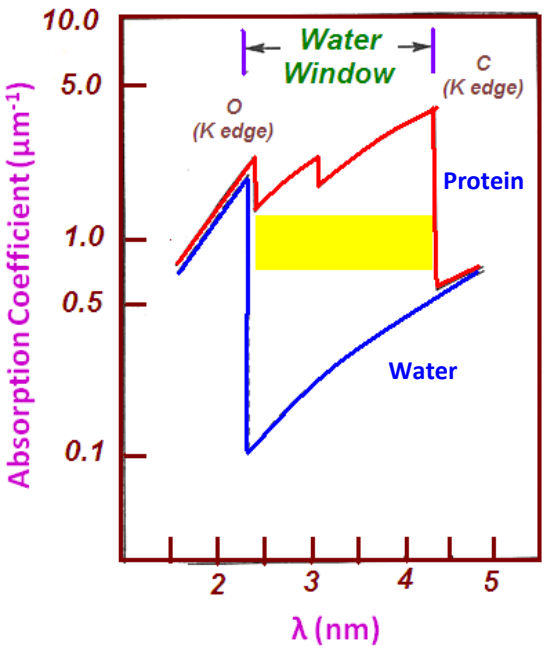

Fig.1.6 Absorption in protein and water in the "water window" spectral region

Chapter 2

Laser System and Various Diagnostics

The laser used in the various studies reported in this thesis was a 10 TW, 45 fs, 10 Hz Ti:sapphire laser system. In this chapter, a brief description of this laser is given, along with the characterization of its pulse duration. This is followed by a general description of the experimental arrangement for absorption and x-ray measurements. Various diagnostics that have been used to carried out x-ray emission measurement like : x-ray pin diodes, x-ray CCD camera working as a dispersion less spectrograph, and transmission grating spectrograph are described in detail. The nano-particles / cluster used in various experiments and also those formed *in situ* by the laser pulses were characterized by various microscopic techniques like scanning electron or scanning tunnel microscopy. A brief discussion on these is given, along with that of the atomic force microscope used to study the surface morphology of the nano-structured targets and nano-ripples.

2.1 10 TW, 45fs Ti: sapphire laser system

This is a commercial system supplied by Thales Laser, France. This system, like any chirped pulse amplification (CPA) based laser system consists of the following main components:

1) Oscillator (which provides the ultra-short pulses for amplification).
2) Stretcher (which temporally stretches the pulses to be amplified).
3) Amplifiers (which amplify the stretched pulses).

a) Regenerative amplifier (pumped by a frequency doubled Nd:YAG laser) followed by pulse cleaner and pre-amplifier.

b) Main amplifier (pumped by two frequency doubled Nd:YAG lasers)

4) Pulse compressor (which compresses the amplified pulses to generate the ultra-short pulses).

A block-diagram of the laser system is shown in Fig 2.1.

The output characteristics of the laser system are shown in Table 2.1.

Parameter	Measured value
Pulse duration	~ 45 fs
Wavelength	~ 800 nm
Bandwidth	~ 50 nm
Repetition rate	2, 5, 10 Hz
Energy/pulse	~ 450 mJ
Peak power	10 TW

Table : 2.1

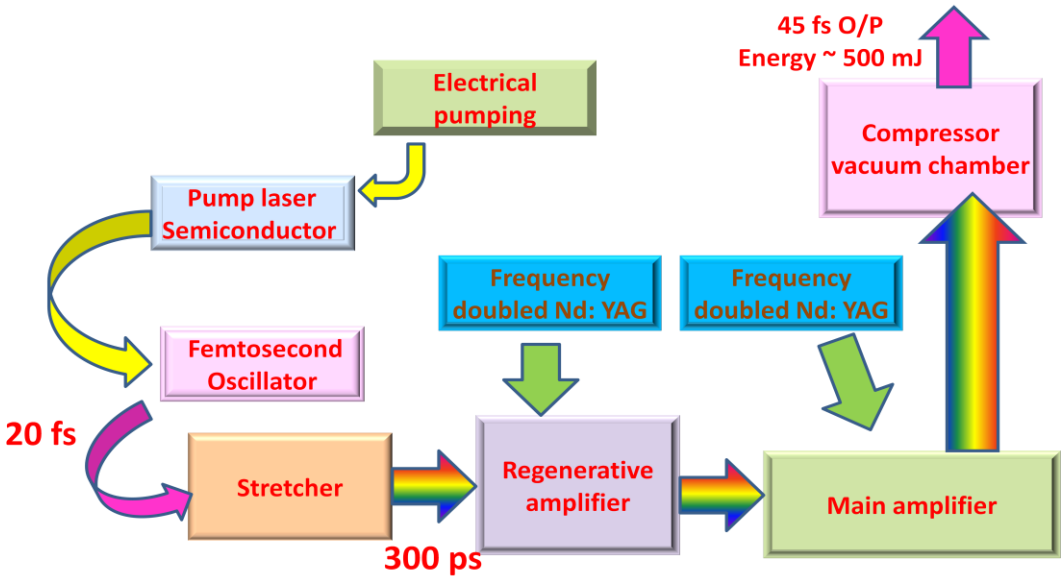

Fig. 2.1 A block diagram of the 10 TW Ti:sapphire laser system

A brief description of the various components of the laser system is as follows

2.1.1 Oscillator

It is a "Kerr lens mode locked Ti:sapphire Oscillator" whose output characteristics are shown in Table 2.2 .

Pulse duration	< 20fs
Spectral width	> 50 nm
Average output power	> 300 mW
O/P energy @ 75 MHz	> 4 nJ
Pump beam diameter($1/e^2$)	2 mm, TEM_{00}
Pump power @ 532 nm	5 W

Table 2.2

This oscillator uses a Ti:sapphire crystal as the gain medium. Ti:sapphire exhibit a broad absorption band in the blue-green region of the visible spectrum with a peak around 490 nm and a broad vibronic fluorescence band which can allow tunable laser output between 670-1070 nm, with the peak of gain curve around 800 nm. Also it has high thermal conductivity, good optical quality, and mechanical rigidity. It is commercially available in large sizes. This crystal has a high damage threshold (~5GW/cm^2) and hence used in amplifiers also. In the oscillator, this crystal is end-pumped by the p-polarized 532nm, 5W laser (Model: Verdi) which is a compact solid state, diode pumped, frequency doubled Nd:vanadate laser that provides single frequency green (532nm) output at power level 5-6 W with vertical linear polarization. The oscillator cavity is a long cavity so that a large number of modes can fall within the broad gain profile of Ti:sapphire. These modes are locked using the Kerr lens mode locking technique [110] with soft aperture, where the Ti:sapphire crystal itself acts as the Kerr lens. This oscillator gives mode-locked ~20fs, ~ 4 nJ energy pulses of nearly transform-limited nature at 76 MHz. These pulses are sent to the stretcher.

2.1.2 Stretcher

For amplification of ultra-short pulses it is mandatory that the laser power above the damage threshold of crystals or any optical component in the amplifier chain is never exceeded. Therefore, the short laser pulse has to be stretched in time. In our laser system, an all reflective type of stretcher called *Offner Pulse Stretcher* is used. The Offner pulse stretcher uses only one grating, which serves the role of the two gratings. In it, a pair of a concave mirror and a convex mirror is used. The Offner pulse-stretcher has another advantage that it is totally based on reflection. So the group delay dispersion generates linear chirp only, which can be reversibly

compensated. As the 20 fs pulse has a broad spectral width (50 nm), hence the pulse gets stretched to ~300 ps. This stretched pulse is then sent to the amplifiers.

2.1.3 Regenerative amplifier, pulse-cleaner, and pre-amplifier

The regenerative (regen) amplifier is a Q-switched, cavity dumped, seeded oscillator. It is end pumped by a frequency doubled Nd:YAG laser. The pulses coming from the stretcher are horizontally polarized. A half wave plate and a Faraday rotator together shift the horizontal polarization to vertical. There is a Pockels cell (PC) which changes its polarization to horizontal and injects the laser pulse into the cavity. The injected laser seed pulse makes about 15 round trips in the cavity and is amplified by passing through the Ti:sapphire crystal. A voltage pulse is applied on the PC to change polarization to vertical and amplified pulse is ejected from the cavity. The gain of the regen amplifier is around 10^5. The vertically polarized pulse coming out of the cavity goes through a pulse cleaner. A small part of the amplified beam can be transmitted (leaked) by the polarizer at each round trip of the cavity. When these pulses get amplified in the multi-pass amplifiers, they reduce the nano-second replica contrast of the main compressed pulse. The pulse cleaner is used to transmit only one pulse from the cavity and block the rest. The selected pulse is sent to the multi-pass pre-amplifier. It is a 4 pass bow-tie amplifier, pumped at both ends by the same frequency doubled Nd:YAG laser. At the end of this stage, one gets 40 mJ, 300 ps laser pulses at the set rep-rate. These pulses are then sent to the Main amplifier.

2.1.4 Main amplifier

The main amplifier is based on the same principle as the pre-amplifier. It is a four pass bow-tie amplifier having a bigger Ti:sapphire crystal as the gain medium, with both sides

symmetrically end-pumped by two frequency doubled Nd:YAG lasers. It has a gain ~ 5-6. Here one gets ~600 mJ, 300 ps laser pulses. These amplified pulses are sent to the pulse compressor which is kept in vacuum as the intensity of the compressed 45 fs laser pulse can damage the gratings (in air) and it also picks up phase distortion (B-integral) when transmitted in air.

2.1.5 Pulse Compressor

It utilizes the dispersive property of the grating pair kept parallel to each other. In this configuration, shorter wavelengths travel shorter path than the longer ones. Hence negative dispersion takes place. Thus the positively chirped stretched pulse gets compressed. The grating separation and parallelism has to be precisely adjusted to get shortest pulse. Due to loss in bandwidth in the amplifiers, one can never get back the pulse duration one started with. After the pulse compressor, we get as output 450mJ, ~45 fs pulses at 10 Hz rep-rate.

2.2 Pulse duration measurements

Intensity autocorrelation method [111] is used to measure the duration of ultra-short laser pulses. In the second order autocorrelator, a beam splitter splits the incoming laser beam into two, which are then passed through a nonlinear crystal for second harmonic generation. If the two beams overlap, both in space and time, a second harmonic beam is generated in the direction mid-way between the two beams (non-collinear phase matching). The temporal overlap of the two beams is achieved by adjusting the delay line of one arm of the autocorrelator. The angle between two beams and the spatial width of the second harmonic correlated beam together give the laser pulse duration.

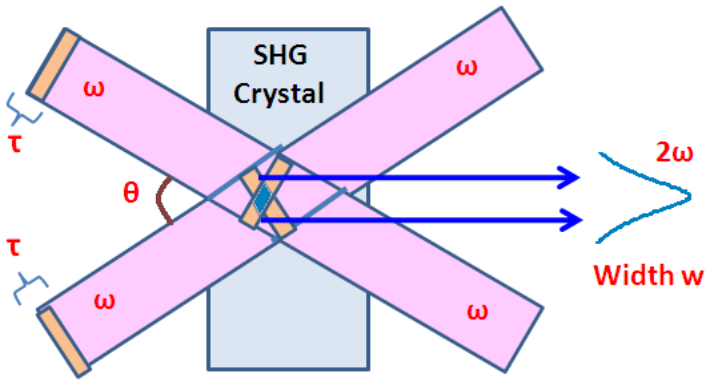

Fig. 2.2 A schematic diagram of the autocorrelator setup

A schematic ray diagram of the intensity autocorrelator is shown in Fig. 2.2. The detector shown is a space resolved detector like a CCD camera. Only in the case of spatial and temporal overlap of two beams, the central second harmonic beam, known as the autocorrelator trace, is generated. As mentioned earlier, the width of the central trace depends on the duration of the laser pulse and the temporal profile of the laser pulse. In a way, the measurement of the autocorrelation trace width does not give full information about the ultra-short pulse, as one has to know (or assume) the shape of the laser pulse in order to know the exact duration of the pulse. The width of the autocorrelator trace (W) is related to the pulse width τ (FWHM) of the laser pulse and the cross-over angle θ between the two overlapping beams (see Fig. 2.2) by the relation [111]

$$\tau = [2W \sin(\theta/2)]/ Kc \qquad (2.1)$$

where K is a constant which depends on the exact temporal shape of the laser pulse, and c is the velocity of light. For a hyperbolic secant squared ($sech^2$) pulse, K = 1.55 . Figure 2.3 shows a typical autocorrelator signal and its trace.

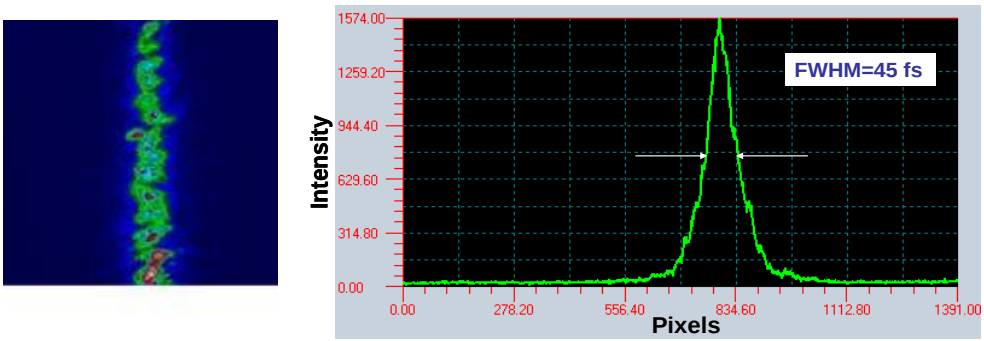

Fig. 2.3 (a) Autocorrelator signal, and (b) its trace

One way to study the dynamics of laser-solid or laser-nano-structure interaction is by changing the laser pulse duration, while keeping the fluence same. This variation of the laser pulse duration can be easily done by changing the grating separation in compressor chamber of the Ti:sapphire laser system. The stretching of pulse duration was done by changing the separation between the compressor gratings. In the case when the grating separation was increased, the pulse gets negatively chirped i.e. the higher frequencies precede the lower frequencies temporally in the laser pulse. On the other hand, in the case when the grating separation was decreased the pulse gets positively chirped i.e. the lower frequencies precede the higher frequencies temporally in the laser pulse. The temporal feature of a stretched pulse directly translates in to the spatial features of the autocorrelator trace recorded in the CCD. Figure 2.4 shows the laser pulse duration measured experimentally as a function of the grating separation. It is seen that the curve is symmetrical about the mean position of the grating where the shortest pulse duration of 45 fs was recorded.

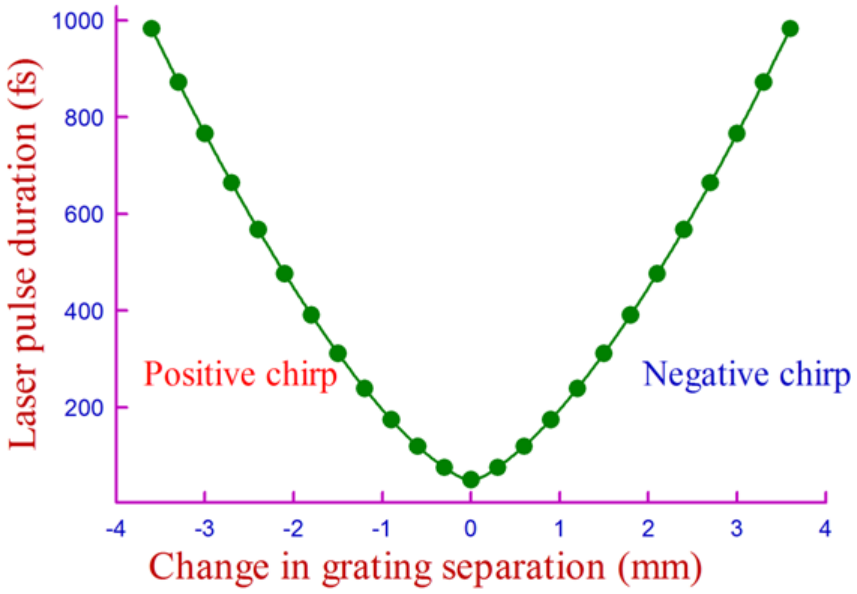

Fig. 2.4 The variation of laser pulse duration by changing the grating separation in compressor chamber of the Ti:sapphire laser system

2.3 Experimental setups for various experiments

2.3.1 Absorption measurement in solids and nano-structures

The absorption of laser light by the plasma formed from planar solids and various nano-structured targets like carbon nano-tubes, nano-hole alumina etc. was estimated by measuring the reflected energy of the laser light from the target. Measurement of the input and reflected energy collected by a large aperture lens was done using two pyro-electric (Model: Gentec-ε) energy meters. The basic working principle of an energy meter is that the coating on the pyro-electric crystal absorbs the incident radiation and gets heated up. The pyroelectric crystal releases charge upon heating and absorbs charge upon cooling. The electrical pulse generated is displayed on an oscilloscope as voltage pulse. From the known calibration factor, the incident energy can be measured. The energy meter used in our experiment is shown schematically in Fig.2.5. The rise time of this energy meter is the order of millisecond and has a calibration factor of 3 V/J.

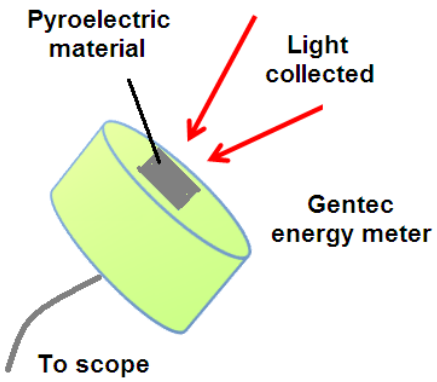

Fig 2.5: "Gentec-ε" energy meter

The absorption was estimated as follows: first the energy incident was recorded and then the energy reflected was found by taking transmission of all optical components like lenses and windows coming before collection of the reflected light. The scattered signal was integrated over a large solid angle to find the total energy scattered and this was taken in to account to estimate absorption. To collect the side-scattered light, a sensitive energy meter with conversion factor 164 V/J was used. The scattering percentage was estimated by assuming isotropic scattering distribution. The absorption fraction was calculated as {Energy incident - Energy reflected - Energy Scattered}/ Energy Incident.

2.3.2 Absorption measurement in solids and nano-structures

The laser energy measurement from *in situ* formed clusters was done in the following configuration. Details of the cluster formation by uncompressed stretched sub-ns pulses of the Ti:sapphire laser is given in Chapters 3, 4 and 5. Clusters formed by the sub-ns prepulse were irradiated by intense ultra-short laser pulses. Figure 2.6 shows the setup for measurement of absorption in the *in situ* formed clusters / nano-particles. Figure 2.6a shows the clusters formed by the stretched sub-ns pulses from the Ti:sapphire laser system. Figure 2.6b shows the

transmitted light from the cluster containing plasma plume collected using a large aperture lens and made incident on an energy meter. The clusters formed move away from the target surface with a typical speed of 0.1-10 km/s and optimization of delay for getting maximum cluster in the intense beam is needed. More details will be given in the subsequent chapters.

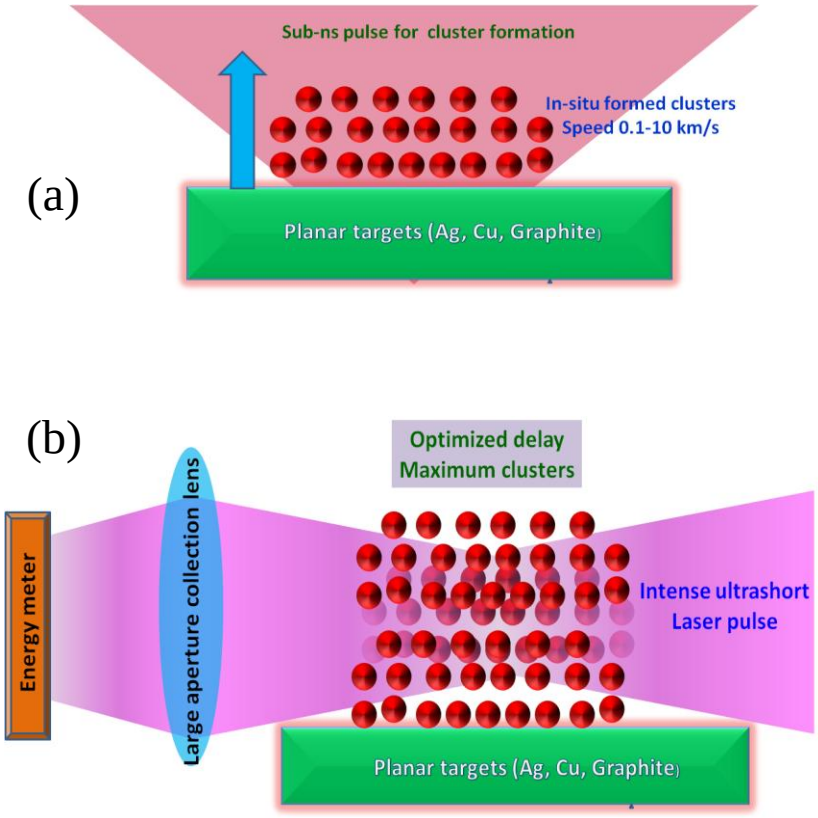

Fig. 2.6 : a) Cluster generation from sub-ns pulses of Ti:sapphire; b) Absorption measurement setup

2.3.3 Nano-ripple formation using Ti:sapphire laser

Using the same Ti:sapphire laser, we studied nano-ripple formation on different band gap semiconductors. Multiple laser shots were fired on the semiconductor surface (InAs, InP, GaAs, GaP, SiC etc.) to perform a parametric study of the nano-ripple formation with different laser parameters and ambient media . Nano-ripples were formed using the Ti-sapphire laser with 8 mJ energy, 45 fs pulse duration, and 800 nm wavelength (1.56 eV) at a fluence in the range of ~ 100

mJ/cm^2 – 1J/cm^2. The effect of the number of laser shots, the angle of incidence, polarization of the laser, fluence, incident laser wavelength, band gap and ambient medium was studied. Schematic diagram of the setup used for experiments in air and water are shown in Figs. 2.7a and 2.7b.

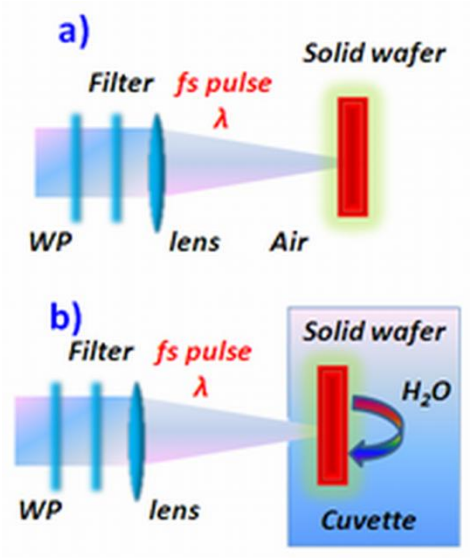

Fig 2.7: a) nano-ripple formation in air; b) in water. WP is wave plate used to change the polarization, filters are neutral density filters to vary the laser energy.

2.4 Dispersion-less spectrograph

High energy x-rays spectrum generated from laser produced plasma can be easily monitored online using as dispersion-less spectrograph [112-116]. Such a spectrograph can be designed using the x-ray CCD camera working on single photon counting principle. The x-ray CCD used for this purpose was a 16 bit, back illuminated, two stage cooled camera (4 M Reflex SRO). The active image area was 27.6 x 27.6 mm^2, the pixel size : 13.5 x 13.5μm^2, and the image readout speed > 25 kilo pixel per second. Single photon counting condition was ensured while recording the x-ray emission spectrum by eliminating low energy photons by appropriate material filters. The high energy photon density can be reduced by increasing the distance between the x-ray source and the detector. The spectrum in the 2-20 keV region was recorded in

single shot mode using the dispersion-less spectrograph. A 25 μm thick Ni foil (cut-off at 7.9 keV) was put before the CCD for cutting off the low energy x-rays. A magnet of 0.085 T (850 G) field was kept in front of the x-ray CCD camera. This field was sufficient to deflect even the most energetic hot electrons, to avoid the x-ray contribution from the hot electrons striking the filter foil in front of the CCD camera. If an x-ray photon of energy E is absorbed completely, it will produce a photo-electron having energy almost equal to that of the incident photon. This electron will lose its energy in the detector medium by producing several electron-hole (e-h) pairs. If ε is the average energy required for e-h pair creation (e.g. ~3.7 eV in silicon) and E is the energy of incident photon, then the average number of the e-h pair produced is approximately E/ε. The charge generated by the x-ray photon is collected and transported to the output amplifier. The availability of x-ray sensitive CCD with large number of pixels (typically four million) allows one to record the entire x-ray spectrum in a single shot, by simultaneous detection of a large number of single photon counting events [114-117]. This is equivalent of capturing events equal to the number of pixels, in a single shot, and subsequently construction the spectrum from these events. Histogram of the pixel values gives the incident x-ray spectrum Pixel value is converted into incident photon energy through a calibration curve. Dispersion-less spectrograph has advantage over wavelength dispersive spectrometers such as crystal spectrometers. The advantages are: 1) large spectral range, 2) single shot operation, 3) independent of dispersive element characteristics (such as reflectivity of crystal). Although different types of high energy x-ray spectrographs have been reported in literature for measurements of emission from laser-produced plasmas, the dispersion-less spectrograph is simple to operate x-ray spectrograph for quantitative, single shot measurements and processing of the data. Further it is easy in alignment and provides absolute x-ray flux information.

2.5 Transmission Grating Spectrograph

In our experiment, a transmission grating soft x-ray spectrograph (TGS) was used for the measurement of x-ray yield in the water-window region {23 A- 44 A} [118,119]. It had a gold bar grating of 5000 lines per mm. The detector was a multi-channel plate (MCP) detector, with its output imaged onto a CCD camera connected to a PC. Transmission grating spectrographs are based on diffraction of soft x-ray radiation from free-standing gold microstructure with period of sub-micron order. The grating may either be mounted on a slit or on a pin-hole aperture. The simplest form of these spectrographs involves a grating in normal incidence geometry [119, 120]. A transmission grating spectrograph (TGS) has been used for measurements of soft x-ray radiation spectrum from plasma produced carbon nano-fibers, carbon clusters, nano-hole alumina, graphite and aluminum, as will be described in chapter 5, 6 and 7. A brief description of the design principle and operating characteristics of this spectrograph is given here.

Figure 2.8 shows the basic geometry of a TGS in normal incidence mode. X-rays from a laser produced plasma source incident on the grating are diffracted into the zeroth and higher orders (on either side of the zeroth order) according to the standard grating equation

$$d \sin\theta = n \lambda, \qquad 2.2$$

where d is the grating period and n is the diffraction order number. The maximum wavelength that can be detected is given by the theoretical grating cut-off at $\lambda = d$, but in practical cases is limited by the spatial extent of the detector along the dispersion axis. The minimum wavelength detectable is limited by the spectral resolution or the overlap of the first order with the zeroth order.

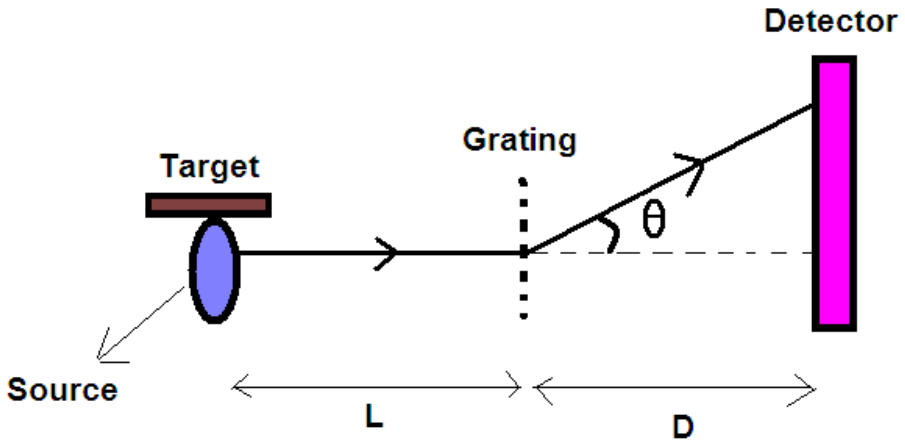

Fig. 2.8: Geometry of TGS spectrograph operation.

Spectral resolution $\Delta\lambda_D$ is governed by the dispersive resolution of the grating, and the geometrical resolution $\Delta\lambda_G$ on account of spectral blurring due to finite source size Δs, and the slit/pin-hole aperture A. The dispersive resolution is given by

$$\Delta\lambda_D = \frac{\lambda}{Nn} = \frac{\lambda d}{nA} \qquad 2.3$$

where N is the number of grating bars in the pin-hole or slit. The geometrical resolution is

$$\Delta\lambda_G = \left(\frac{d}{n}\right)\left[\frac{\Delta S + A}{L} + \frac{A}{D}\right] \qquad 2.4$$

where L and D are the source-to-grating and grating-to-detector distances respectively. The overall spectral resolution $\Delta\lambda$ is then given by

$$\Delta\lambda = \sqrt{\Delta\lambda_D^2 + \Delta\lambda_G^2} \qquad 2.5$$

In our experiments, L and D were 65 and 77 cm respectively, n=1, A= 150 μm, and the source size was assumed to be ~ 100 μm. The spectral range detected was ~ 15 Å to 50 Å with a spectral resolution ~1 Å in this wavelength region, with the above mentioned configuration.

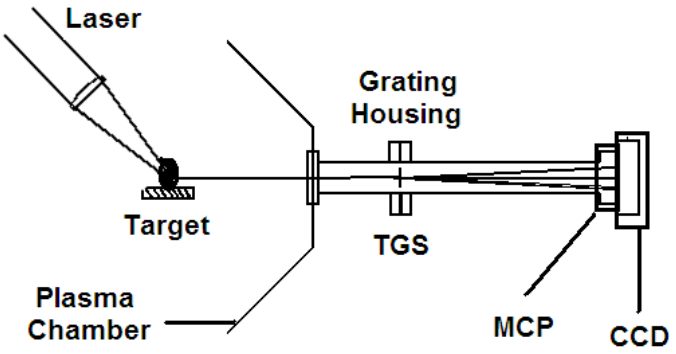

Fig. 2.9: A schematic diagram of the transmission grating spectrograph setup

Figure 2.9 shows a schematic diagram of the TGS setup for recording the x-ray emission from plasma produced by an obliquely incident focused laser beam. The grating was mounted in a long tubular housing connected to the plasma chamber. Spectrum was recorded on the MCP - CCD system placed on a flange at the end of another long tubular housing.

2.6 X-ray p-i-n diodes

For the measurement of spectrally integrated x-ray intensity from the plasma, p-i-n x-ray diodes have been used. These diodes consist of an active intrinsic (i) region sandwiched between p and n type semiconductor layers. Hence the name "p-i-n" diode. The incident x-ray photons are absorbed in the active region, resulting in a current proportional to the incident flux or energy. Almost all the energy of x-ray photons is used to generate electron-hole pairs. About 3.6 eV is required to generate one electron hole pair.

In our experiment, we have used several p-i-n diodes (Quantrad) each seeing a different spectral region. They have sensitivity above 0.8 keV and have a large detection area of 1 cm^2. The rise time of diodes was ~3 ns and fall time ~5 ns and quantum efficiency was about 0.2 C/J for 1 keV x-rays. 300 V reverse bias voltage was applied. X-ray pulse energy was measured from the x-ray p-i-n diode signal obtained using a biasing circuit shown in Fig. 2.10. The signal from the p-i-n diodes was recorded on an oscilloscope.

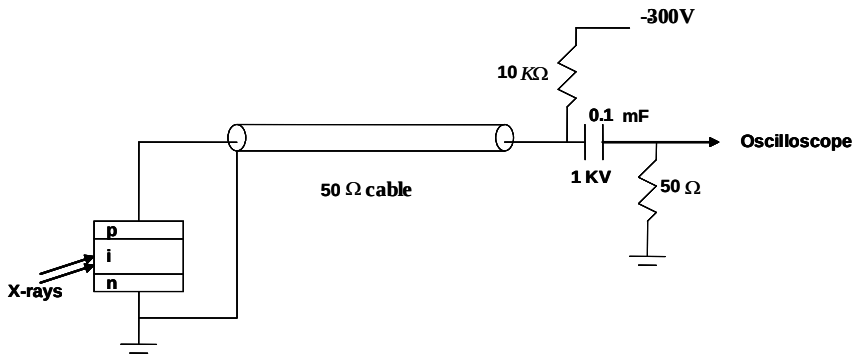

Fig 2.10 : Circuit configuration used with the p-i-n diode.

Three p-i-n x-ray diodes were used to estimate the x-ray energy yield in different x-ray photon energy ranges. A magnet of 0.15 tesla field was also kept in front of p-i-n diode to avoid the hot electrons, emitted normal to the target, colliding with the filter foils of the p-i-n diodes to generate x-rays, which can be misinterpreted as x-ray signal from the target. For cutting off the low energy x-rays, a filter of 75 μm Be was used, which has a cut-off at ~ 2 keV. For monitoring the hard x-ray spectral region, two filters : 25 μm Ni and 25 μm Ag were used with the remaining two diodes. The cut-offs for Ni and Ag are about 7 keV and 16 keV respectively. Aluminized polycarbonate foil (B-10, atomic composition: aluminium : 0.05 mg/cm^2, oxygen : 0.0375 mg/cm^2 and carbon : 0.15 mg/cm^2) was also used as a filter. The cut-off energy of two B-10 foils is ~ 0.9 keV.

2.7 Microscopic investigations

Nano-structures are characterized by various techniques like electron microscopy (SEM, TEM), using AFM, x-ray diffraction etc. The technique to be used depends on the type of material and information one needs to know. Properties like size, shape, abundance, crystalline

type, composition are easily retrieved. In the electron microscope, electrons are used instead of electromagnetic radiation. When electrons interact with sample, they are scattered. The scattered electrons from the specimen are detected using a system of electrostatic and magnetic lenses. Advantage of electron microscopy is that the probe wavelength can be tuned to a very small value by changing the electron energy so that resolution can be increased. There are two types of electron microscopes 1) Scanning Electron Microscope and 2) Transmission Electron Microscope

2.7.1 Scanning Electron Microscope (SEM)

We have extensively used an SEM (Model : Philips XL30CP) for characterizing the nano-particles formed by sub-ns and fs laser pulse. It was also used to study the nano-structured targets like nano-holes, nano-fibers where the surface morphology, fill fraction, size and shape information become clearly evident. Since the SEM has advantage of scanning a large area, many samples of nano-ripples formed on various band gap semiconductors in different laser focusing condition were also characterized by this method.

In an SEM, backscattered electrons from sample are used for imaging the sample. It can be used to image the surface of a thick sample also. The electrons emitted from a hot filament cathode are focused with the help of electrostatic or magnetic lenses. The focused beam is scanned on the sample surface with the help of scan generator and the backscattered electrons are collected by a detector. The signal from the scan generator, along with the amplified signal from the electron collector, generates the image of sample surface. One disadvantage of an SEM is that insulating samples cannot be analyzed directly because they get charged due to incident electrons, leading to a blurred image. To avoid this, insulating materials have to be coated with a

very thin metal film like gold or platinum (<10 nm) making them conducting, without altering the details of the sample.

2.7.2 Transmission electron microscope (TEM)

TEM is ideally suitable for investigating the nano-structures as it can give very high resolution (better than 0.5 nm). Since it works in a transmission mode, it is the best tool to see whether a nano-structure is hollow from inside, which cannot be done using AFM or SEM. In our experiments, we have used a TEM (Model : Philips CM200) for studying nano-fibers and nano-tubes. The carbon nano-tubes clearly showed a hollow structure and the inner and outer diameters of CNTs could be easily measured. In a TEM, an energetic electron beam (energy >50 keV) passes through a series of magnetic lenses (of variable focal lengths), and is made incident on a thin sample. The electrons transmitted and diffracted through the sample are imaged onto a detector. Additional lenses are used to improve the image quality and resolution.

2.7.3 Atomic force microscope (AFM)

We have also extensively used an AFM for characterizing the nano-particles of Ag, Cu and C formed by sub-ns and fs laser pulses. The AFM (Model: SOLVER PRO, NT-MDT) measurements were carried out in noncontact mode under an ambient environment. Silicon cantilever tips of resonant frequency 180 kHz and spring constant 5.5 N/m were used. The AFM has a very high resolution of fraction of a nano-meter. The surface characterization is carried out by sensing the surface with a mechanical probe comprising of a cantilever (silicon or silicon nitride) with a sharp tip at its end. When the tip is brought close to the sample surface, forces between the tip and the sample lead to a deflection of the cantilever according to Hooke's law. Depending on the situation, forces that are measured in an AFM include mechanical contact force, Van der Waals forces, capillary forces, chemical bonding, electrostatic forces etc.

Typically, the deflection is measured using a laser spot reflected from the top surface of the cantilever into an array of photodiodes. As the tip at has an associated risk of striking the surface and causing damage to the sample as well as the tip, a feedback mechanism is included for adjusting the tip-to-sample distance while maintaining a constant force between them. An AFM has a better resolution than an SEM, and in addition it provides a three dimensional topography of the surface, and does not need a vacuum operation. Further, the samples do not require any metal coating that would irreversibly change or damage the sample. A major disadvantage of AFM as compared to an SEM is the image size. The SEM can image large area of dimension of ~ 1 mm^2 but AFM can only image a maximum height on the order of μm and a maximum scanning area of around ~ 100 μm x 100 μm.

2.8 Surface plasmon resonance of the nano-particle containing films

Nano-particles of silver and copper are known to exhibit absorption associated with the surface plasmons. Surface plasmons are the longitudinal oscillations of free electrons on interaction with an electromagnetic wave. The resonance occurs when the cluster polarizability maximizes at a particular frequency of the light. Surface plasmons are a perfect example of a optical, electrical, and mechanical effect of light and nano-scale matter interaction. Although one can characterize the nano-particles by SEM, TEM or AFM, it is a lengthy process. One quick method to instantly infer the generation of nano-particles is depositing the plasma debris on a glass slide and measuring the reflection and transmission of the deposited film. Reflection and transmission characteristics of the deposited films of silver and copper also gives some preliminary indication of the size of the nano-particle by observing the surface plasmon resonance absorption peaks. The analysis and inference is based on the standard light interaction with nano-scale matter. The variation of the reflection and transmission from the nano-particle

containing film deposits on glass slides was studied by us using a spectrophotometer (CARY 50). It is a Czerny- Turner monochromator based spectrometer with an holographic grating of 1200 lines/ mm. It works in the wavelength range of 190-1100 nm and has an accuracy of ± 0.07 nm at 541 nm. The broadband light source used is xenon lamp and it has two silicon photodiode detectors. The optical properties of noble metal nano-particles are understood by invoking Mie theory in the dipole approximation or the quasi-static approximation [121-123]. By measuring the reflectivity or transmission or absorption due to the surface plasmon resonance (SPR), one can get some idea of the size of the particles. The absorption is proportional to the volume of particle and therefore the transmission and reflectivity is expected to be less for larger nano-particles. Another aspect is the width of the SPR in the deposited films. The width is expected to be independent of the resonance frequency and is directly related to the damping processes in the nano-particle [124]. As smaller nano-particles have a higher damping because of scattering at the surface. Therefore, the SPR width in the case of smaller nano-particles will be large. In addition, due to the higher absorption, both the reflectivity and transmission are expected to be less for smaller particles.

Chapter 3

Nano-particle formation in laser produced plasmas

In recent years, there has been a considerable scientific interest in the area of growth of nano-particles, as nano-science offers a great scope for technological advancement [125-128]. Conventionally nano-particles and their films are produced either by arc discharge [129], or by vapor and electrochemical deposition [130,131]. Of late, pulsed laser deposition (PLD) has been an attractive alternative due to the number of advantages it has over the conventional processes, such as the possibility of producing materials with a complex stoichiometry [132], and a narrower size distribution [133] of the nano-particles. PLD technique based on ablation of solid targets using femtosecond laser pulse, has been used as a means for the synthesis of nano-particles [134-140]. Recent theoretical studies have suggested that a rapid expansion and cooling of solid density matter irradiated by an fs laser pulse may result in nano-particle generation via liquid phase ejection and fragmentation, homogeneous nucleation, and decomposition [141-145]. This technique of using fs laser ablation for nano-particle synthesis in vacuum is different compared to that using ns laser pulses, since the fs pulses do not interact with the ejected material thereby avoiding complicated secondary laser interactions [146]. Moreover, the fs laser pulses heat a solid to higher temperature and pressure than the longer pulses of comparable fluence, since in the fs irradiation, the energy is delivered to the target before significant thermal conduction can occur. Therefore, a fs laser pulse can heat any material to a state with temperature and pressure above the critical point, and is thus ideal for studying the fundamental properties of matter under extreme conditions. Finally, since the plasma plume expansion takes place into vacuum, all the complications introduced by the presence of a background gas (which

is normally used with ns laser PLD) are avoided. In continuation with this trend of laser ablation with femtosecond pulses, it has been recently shown that focusing of sub-ns pulses in vacuum, is also a viable and attractive technique for the production of nano-particles of various materials, but only at higher irradiation intensity conditions [147]. It has been shown that these nano-particles, produced *in situ* using sub-ns laser pulses, are a promising target for intense short pulse laser plasma experiments [148].

Since the properties of nano-particles are highly size dependent [149], their size is a crucial factor in any area of application. Hence control on the size becomes a crucial parameter in their generation. Typically, ns PLD is carried out in an ambient gas used to quench the ablated plume, for controlling the mean particle size [150]. This technique, however, presents the disadvantage of requiring optimization of the background gas pressure, and a good understanding of the complex aspects of the expansion of the plume into the ambient gas, such as its gas dynamics, and "in-flight" chemical kinetics [151]. The general route of nano-particle size variation using the ultra-short pulse irradiation technique is by using time delayed pulse fs laser pulses [152], or using lasers of different wavelengths [153]. In generation of size-controlled semiconductor nano-particle formation under gas phase conditions, it has been shown that the size distribution can be changed if picosecond pulse sequence of tailored ultra- short laser pulses (< 200 fs) is used [154]. The dependence of size of nano-particles on laser wavelength has also been investigated both experimentally and theoretically. A study [153] carried out with Ni target by using laser pulses of $\approx$300 fs duration at two different laser wavelengths : green (λ = 527 nm) and ultra-violet (λ = 263 nm), showed that the size distribution of the nano-particles, which is quite broad in the case of green light, becomes significantly narrower and slightly shifts towards smaller sizes for ultra-violet light. Amourso *et al* [155] have shown that the dependence of nano-

particle size on laser fluence is very weak. The nano-particles generated in their experimental conditions were independent of the laser pulse duration and fluence. Therefore, a simple method to control the size of the laser generated nano-particles is required for their usability in various practical applications.

It must be mentioned here that there is a special interest in silver and copper nano-particles due to their potential applications. Silver nano-particles are widely used for surface-enhanced Raman scattering as the position of the Surface Plasmon Resonance (SPR) of silver nano-particles is far from the inter-band transition energy. This enables one to investigate the optical and nonlinear optical effects in the silver nano-particles by focusing on the surface plasmon contribution. In general, highly dispersed metals have a much higher surface area for a given volume, and hence they can be useful for efficient catalytic conversion example copper nano-particles [156,157]. Here we describe an experimental study on generation of nano-particle of various sizes using femtosecond and sub-ns laser pulses. Formation of nano-particles of metals like Ag and Cu was studied using stretched pulses of 300 ps (sub-ns) duration from a Ti:sapphire laser, in vacuum ($< 10^{-5}$ mbar pressure). It was compared with nano-particle formation of the same materials when compressed pulses of 45 fs duration were used under similar focusing conditions. Both, the sub-ns and fs pulses, had the same energy of 30 mJ, and were focused at a fluence of 10^3 J/cm^2. It is observed that using ultra-short pulses, smaller particles with average size ~ 20 nm are generated in comparison to those generated with sub-ns pulses (~40-60 nm). The structural and optical analyses also confirm this observation.

3.1 Nano-particle formation with different pulse duration of the laser

The following section describes the experimental details and results on nano-particles generation and their properties under various laser irradiation conditions. The ablation of polished Ag and Cu planar targets was carried out in vacuum using 45 fs pulses (referred to as fs pulse) and was compared with the deposition made using uncompressed pulses (300 ps duration: referred to as sub-ns pulse) from the same chirped pulse amplification based Ti:sapphire laser system. Variation of the pulse duration from 45 fs to 300 ps was done simply by changing the separation of the two gratings in the pulse compressor. The deposition was carried out in vacuum 10^{-5} mbar pressure and at room temperature using the setup shown in Fig.3.1.

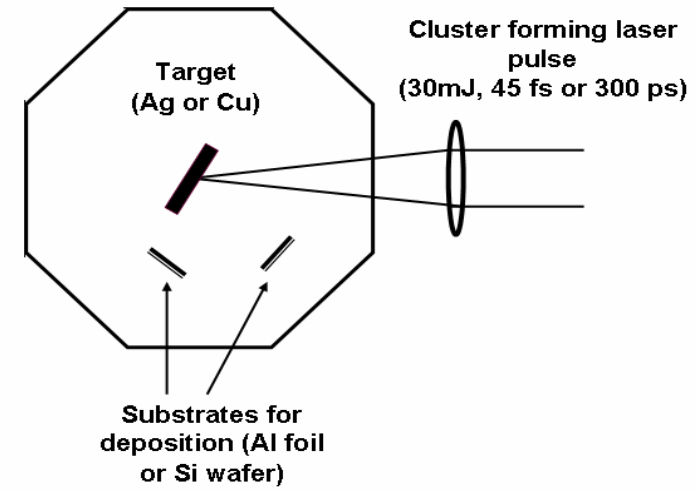

Fig.3.1: A schematic diagram of the experimental setup

Ti:sapphire laser pulses (λ=793 nm, E =30 mJ, 10 Hz pulse repetition rate) were focused on planar targets at 45 degree incidence (p-polarized). The target was mounted on a raster scan setup to avoid overlap of laser shots at the plasma formation spot on the target. The deposition was collected on glass slides, silicon wafer, and Al foil, placed at a distance of 50 mm from the target. The substrates for collecting deposition were placed at the same distance but at different

angular positions, to determine the spatial evolution of the generated particles. In both the cases of deposition, whether using the fs pulse or the sub-ns pulse, the laser fluence was same (~10^3 J/cm^2), only the pulse duration was different. One hundred laser shots were fired to collect the deposit for spatial and spectral analysis.

The presence of nano-particles was inferred by analyzing the spatial characteristics and the spectral analysis of the deposited material. The variation of the reflection and transmission from the nano-particle containing film deposits on glass slides was studied using a spectrophotometer (CARY 50). The optical properties of the films deposited in different conditions were studied in the wavelength region 300-800 nm. The analysis of the sizes and structural properties of deposited nano-particles was carried out using an atomic force microscope (AFM : SOLVER PRO, NT-MDT). The AFM measurements were carried out in noncontact mode under an ambient environment. Silicon cantilever tips of resonant frequency 180 kHz and spring constant 5.5 N/m were used.

Figure 3.2 shows the AFM images and corresponding size histograms of the silver nano-particles deposited on silicon substrate, using the 45 fs and 300 ps pulses. The average size of Ag nano-particles generated by 45 fs pulses was 25 nm and of those produced with 300 ps pulse was 40 nm. Fig.3.3 shows the AFM images and size histograms of the films of copper nano-particles in same conditions. They also show that smaller particles (average diameter 20 nm) are produced by the fs pulses, and bigger particles (50 nm) are produced by the sub-ns pulses.

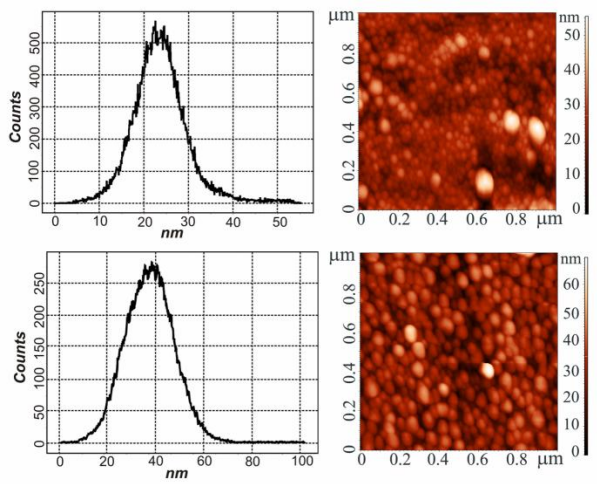

Fig.3.2: Silver nano-particles formed by 45 fs pulses showing mean particle size of 25 nm (Top) and those formed with sub-ns pulses (Bottom) showing a mean particle size of 40 nm. The focused laser energy in both the pulses was 30 mJ, with a fluence of 10^3 J/cm^2.

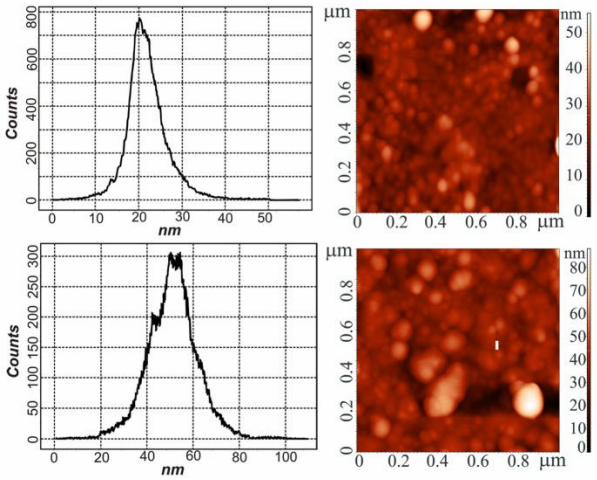

Fig.3.3: Copper nano-particles formed by 45 fs pulses (Top) showing mean particle size of 20 nm and those formed with sub-ns pulses (Bottom) showing a mean particle size of 50 nm. The focused laser energy in both the pulses was 30 mJ, with a fluence of 10^3 J/cm^2

The presence of nano-particles was also inferred from the appearance of strong absorption bands associated with surface plasmon resonance (SPR). Transparent substrates (glass slides) were used to determine the presence or absence of nano-particles by studying the SPR in the transmission spectrum. Fig.3.4 shows the transmission curves for the silver

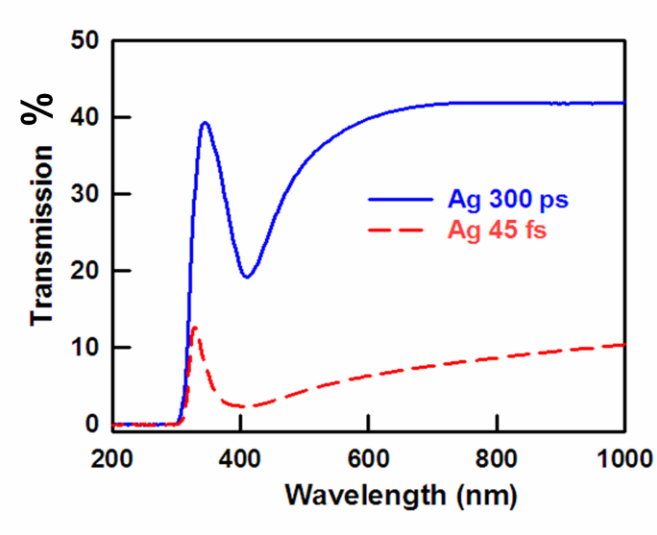

Fig.3.4: Transmission spectrum for the silver nano-particle films formed by 1) fs pulses and 2) sub-ns pulses. SPR is observed at ~410 nm for both the films.

nano-particle films deposited with fs and sub-ns pulses. In this case, it is observed that : 1) the transmission from the film deposited using fs pulses is lower at all wavelengths, 2) the dip associated with SPR both the films is at around 410 nm, and 3) the width of this dip is slightly more for the film deposited using fs pulses

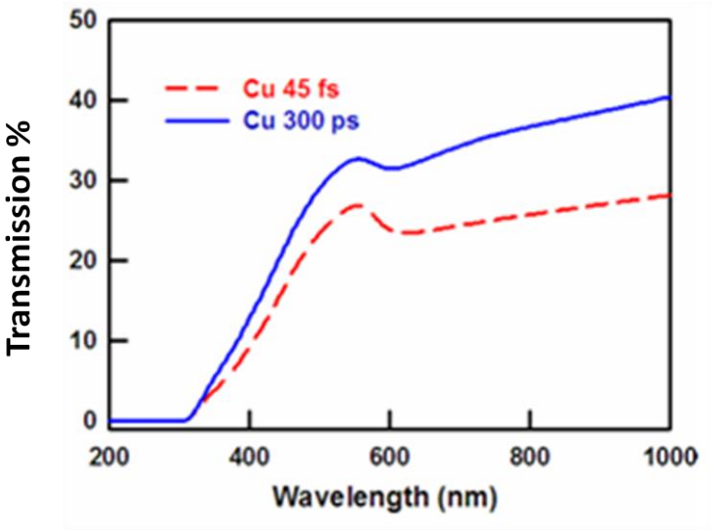

Fig.3.5: Transmission spectrum for copper nano-particle films formed by 1) fs pulses and 2) sub-ns pulses. SPR is observed at ~610 nm for both the films.

Fig.3.5 shows the transmission from the copper nano-particle films deposited using the fs and sub-ns pulses, showing similar behaviour. In this case, 1) as in the case of silver, the transmission from the film deposited using fs pulses is lower at all wavelengths, 2) the dip associated with SPR both the films is at 610 nm, and 3) the width of this dip is slightly more for the film deposited using fs pulses (as in the case of silver).

The reflection measurements were also carried out in silver and copper nano-particle films deposited on glass substrates using the fs and sub-ns pulses. The reflection curves obtained using the spectrophotometer, for the silver nano-particle films formed in the two pulse duration regimes, are shown in Fig.3.6. Three points are noticed from the reflection curves of the two samples: 1) the reflection from the fs pulse deposited film is lower at all wavelengths, 2) the dip associated with SPR is at 380 nm (c/f 410 nm in transmission mode) for both the films, and 3) the width of this dip is slightly more for the film deposited using fs pulses.

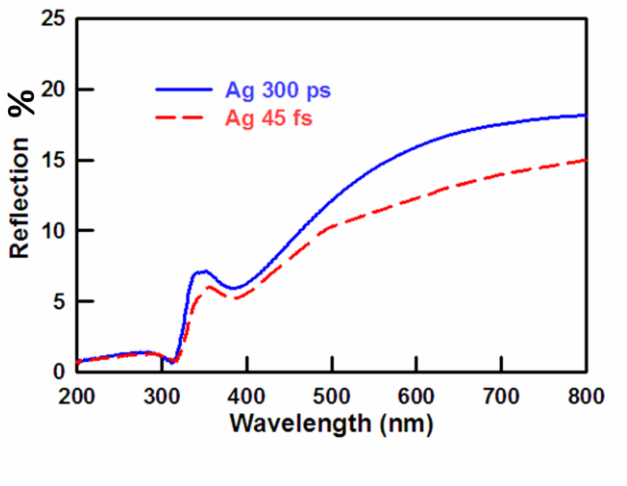

Fig.3.6: Reflection spectrum from Ag nano-particle films formed by 1) fs pulses and 2) sub-ns pulses. SPR is observed at ~380 nm for both the films

Similarly, the reflection curves for the copper nano-particle films formed in the two pulse duration regimes, are shown in Fig.3.7. The reflection curves have similar trends as recorded

for the Ag film, i.e. 1) the reflection from the fs pulse deposited film is lower at all wavelengths, 2) the dip associated with SPR is at 490 nm (c/f 610 nm in transmission mode) for both the films, and 3) the width of this dip is slightly more for the film deposited using fs pulses.

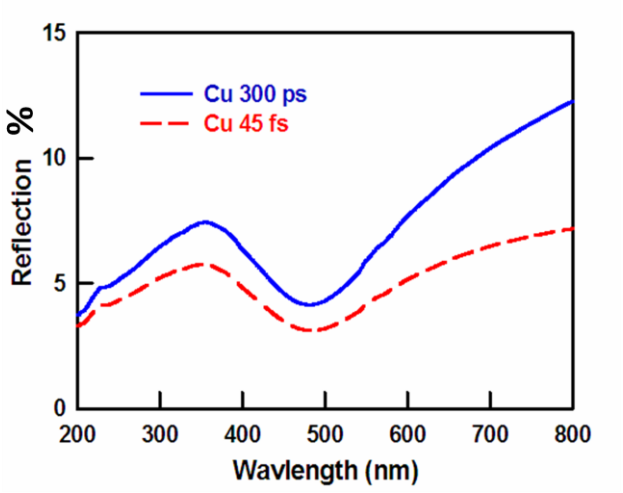

Fig.3.7: Reflection spectrum from Cu nano-particle films formed by 1) fs pulses and 2) sub-ns pulses. SPR is observed at ~490 nm for both the films

3.2 Study of nano-particle formation at different focusing conditions

The laser ablation of various materials was carried out in vacuum using uncompressed pulses (of 300 picosecond duration) from the chirped pulse amplification based Ti:sapphire laser system described in Chapter 2. The samples were placed inside a vacuum chamber. Uncompressed pulses from the Ti:sapphire laser (λ = 793 nm, τ = 300 ps, E = 30 mJ, 10 Hz pulse repetition rate) were focused on a bulk target at two regimes of focusing. In the first case (referred to as tight focusing), the intensity of laser radiation was in the range of 2×10^{12} W-cm^{-2}, and in the second case (referred to as weak focusing), the intensity was considerably lower (4×10^{10} W cm^{-2}). Silver, indium, copper, chromium, and some other metals were used as targets. Float glass, silicon wafer, and various metal strips (silver, copper, aluminum) were used as the

substrates, and were placed at a distance of 50 mm from the targets. The deposition was carried out in oil-free vacuum (≈1×10^{-4} mbar) at room temperature.

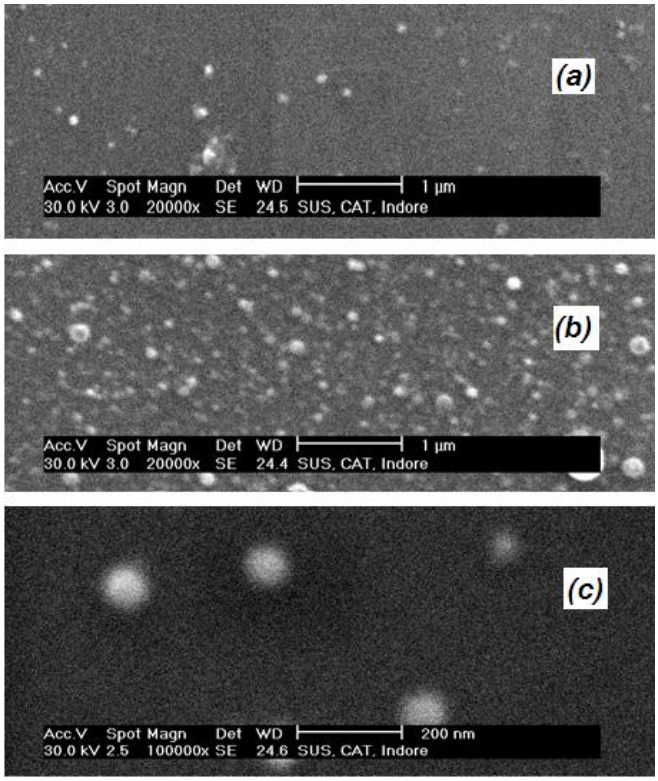

Fig. 3.8. SEM images of the nano-particles deposited on the surface of a silicon wafer. These images were obtained at a) weak (chromium nano-particles) and b) tight (stainless steel nano-particles) focusing conditions. c) High magnification of SEM image of the silver nano-particles

Our SEM studies of the structural properties of the deposited films showed that, in the tight focusing conditions, these films contain a lot of nano-particles with variable sizes. In the weak focusing conditions, the concentration of nano-particles was considerably smaller compared to the tight focusing conditions.

Figure 3.8 shows the SEM images of the deposited nano-particles on the surface of a silicon wafer. In the case of weak focusing, the deposited film was almost homogeneous with a few nano-particles appearing in the SEM images (see Fig. 3.8a showing the deposition of chromium), while, at tight focusing conditions, plenty of the nano-particles ranging from 30 to

100 nm appeared in the SEM images (see Fig. 3.8b showing the deposition of stainless steel). The enlarged SEM image of the silver nano-particles prepared at the tight focusing conditions is presented in Fig. 3.8 c. The average size of these spherical nano-particles was measured to be 60 nm.

The same behavior was observed in the case of silver target also. Figure 3.9 shows the SEM images of silver deposited on a silicon wafer. One can see a considerable difference in the concentrations of nano-particles in the cases of weak (Fig 3.9a) and tight focusing conditions (Fig. 3.9b) respectively.

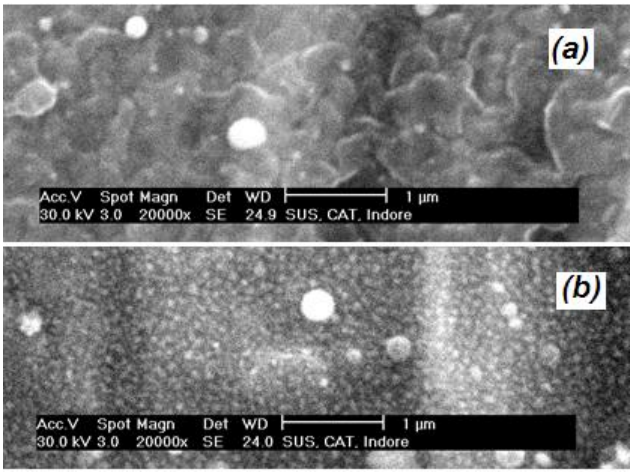

Fig. 3.9. SEM images of the silver nano-particles deposited at the (a) weak focusing conditions and (b) tight focusing conditions.

Further studies on the characteristics of nano-sized structures of the deposited materials were carried out using the atomic force microscopy. Figure 3.10 shows the AFM image of the silver nano-particles deposited on the surface of a copper strip. The average size of silver nano-particles was 65 nm. In contrast to this, the AFM images obtained from the deposited films prepared at the weak focusing condition (Fig. 3.10 b) showed considerably smaller number of nano-particles compared to that obtained at tight focusing conditions (Fig. 3.10 a).

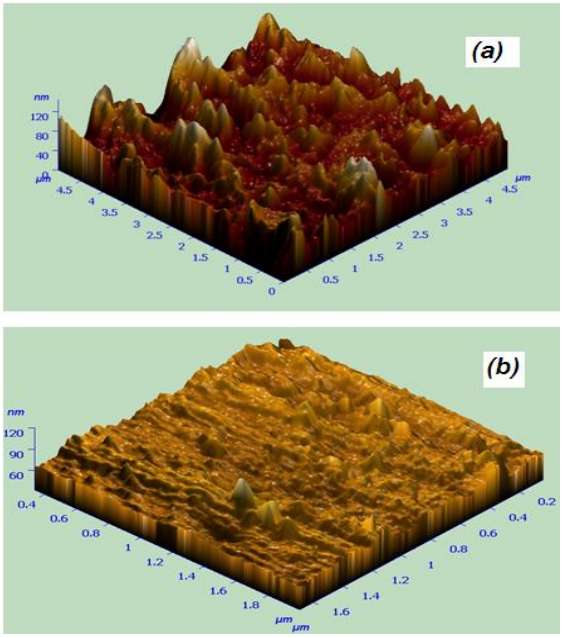

Fig. 3.10 a) AFM image of the silver nano-particles deposited on a copper strip prepared tight focusing. b) on a aluminium strip at the conditions of weak focusing.

The absorption spectra of the materials deposited on transparent substrates (float glass) were used to determine the presence or absence of nano-particles. The presence of nano-particles was inferred from the appearance of strong absorption bands associated with surface plasmon resonance (SPR). The peaks of SPR were centered in the range of 440 to 490 nm but in the case of the deposition of silver film at the weak focusing conditions, no absorption peaks were observed in this region, indicating the absence of nano-particles.

Thus it is observed that using ultra-short pulses, smaller size (~ 20 nm average diameter) nano-particles are generated in comparison with the sub-ns pulses (~40-60 nm average diameter). Therefore by controlling the laser pulse duration one can control the size of the nano-particles formed. The study of the metal nano-particle deposition by laser ablation in vacuum using sub-nano-second laser pulses showed a considerable difference in the structural properties of the films deposited under different focusing conditions. In the case of weak focusing, concentration of nano-particles was considerably smaller compared to that in the tight focusing case where

nano-particles were generated efficiently. Our study suggests that nano-particles are predominantly formed near the target surface as a result of the fast non-thermal melting and consequent vacuum expansion of the material heated to high temperatures by the intense laser pulse. The present work shows that by laser ablation of the bulk material in vacuum, under appropriate focusing condition, one can obtain stable nano-particles of defined sizes. It is also shown that for ablation using sub-nano-second pulses is a general rote of nano-particle formation, irrespective of the target material.

3.3 Analysis of the results

a) Resonance in nano-particles : The experimental observations can be understood considering the optical properties of noble metal nano-particles. The theory is simplified by invoking the dipole approximation or the quasi-static approximation [121,122]. The optical absorption and scattering of a homogeneous metal nano-sphere of radius R embedded in an optically homogeneous matrix has been modeled by Mie [123]. For 2R << λ (i.e. : in dipole approximation), the Mie theory predicted optical extinction (i.e.: scattering + absorption) of homogenous spherical particles. In this small size approximation, the extinction and absorption cross-sections are identical (i.e. $\sigma_{extinction} = \sigma_{absorption}$), since for particle size << λ, the scattering can be neglected [121, 122]. The absorption cross-section is given by

$$\sigma_{abs} = \frac{9.V.\varepsilon_m^{3/2}}{c}\left(\frac{\omega.\varepsilon_2(\omega)}{[\varepsilon_1(\omega)+2\varepsilon_m]^2+\varepsilon_2(\omega)^2}\right) \qquad \text{.....(3.1)}$$

where V is the particle volume, ω is frequency of the incident light, ε_m dielectric functions of surrounding medium (matrix), and $\varepsilon_1(\omega)$ and $\varepsilon_2(\omega)$ are the real and imaginary parts of the dielectric function of the metal nano-particle. Thus, the SPR wavelength λ_R (minimizing the

denominator of equation 3.1) is determined by the particle properties {ε(ω)}, and by its local environment {ε_m}. For a small value of $\varepsilon_2(\omega)$ or if it is weakly dispersed in the SPR spectral region (i.e. $\varepsilon_2(\omega)$ constant), λ_R is determined by the simple condition [121,122]

$$\varepsilon_1(\lambda_R) + 2\varepsilon_m = 0 \qquad \text{……(3.2)}$$

For noble metals, the relaxation time of electrons is on the order of several fs [121,158], which makes the SPR wavelength nearly size independent. Thus, the wavelength of surface plasmon resonance is given by the relation

$$\lambda_R = \frac{2\pi * c\sqrt{1+2\varepsilon_m}}{\omega_p} \; . \qquad \text{…… (3.3)}$$

In the reflection mode ε_m is 1 (i.e. air), but in the transmission mode ε_m ~2.13 for glass (μ=1.5). Thus, from the equation 3.3, a red-shift in the SPR wavelength is expected in transmitted light from the films, compared to that for the reflected spectrum. Accordingly, the SPR for silver nano-particle films which is at 410 nm for spectrum transmitted through glass (Fig.3.4) becomes 380 nm in reflection (Fig.3.6). The above shift of 30 nm is less than the shift expected using the relation defined by equation 3.3. Exact validation of the Mie theory in the deposited films will require the inclusion of nano-particle size, shape, exact environment, and various statistical effects. Similarly, the SPR for copper nano-particle films which is at 610 nm for spectrum transmitted through glass (Fig.3.5) becomes 490 nm in the reflected spectrum (Fig.3.7) because of the same reason.

Now consider the width of the SPR in the deposited films. The width is expected to be independent of the resonance frequency and is directly related to the damping processes in the nano-particle [124]. Since the sizes of the nano-particles deposited using fs pulses on Ag and

Cu are smaller, hence the damping in them is high. If γ is the overall damping term in nano-particles, γ_b is the bulk damping term, and v_F/is the Fermi velocity of the electrons in the metal, then $\gamma = \gamma_b + v_F/R$, implying that due to additional scattering at surface the damping term is increased in nano-particles [124]. Therefore, the SPR width in them is comparatively more than for the nano-particles produced by sub-ns pulses.

b) Formation of nano-particles : Next, the main observation that the size of the nano-particles formed by fs pulse ablation of solids is always smaller compared to the nano-particles formed with sub-ns pulses at similar fluence condition, can be qualitatively understood by the fragmentation model proposed by Glover *et al* [144]. They estimated the mean particle size and its dependence on the initial temperature. In femtosecond ablation, the laser energy is rapidly deposited in the target, causing lattice heating under conditions of approximately constant volume (isochoric heating), creating an energetic and highly pressurized fluid. This fluid expands into vacuum, and the strain associated with the expansion leads to breaking of the mechanical bonds and results in fluid fragmentation. By minimizing the total surface energy and kinetic energy of the expanding fluid w.r.to surface to volume ratio of the fragments, mean size of the fragment is obtained [159]. The previous studies, done using ultra-short pulses [133,134,151] as well as those done using sub-ns pulses [147], suggest that nano-particles are generated as a result of some relaxation processes of the extreme material state reached by the irradiated target surface. This stands in stark contrast to the formation of nano-particles during nano-second laser ablation in a background gas, where vapor condensation is considered to be the most important mechanism. In the case of sub-ns pulses also, the energy deposited on the target surface at high fluence leads to formation of a high temperature strained fluid. Thus, similar to the ultra-short pulse nano-particle formation, for sub-ns pulses focused at high intensity, fragmentation of the

heated and strained molten target material takes place during hydrodynamic evolution. The initial lattice temperature would be lower in the sub-ns pulse case, compared to intense fs pulse case, because the irradiation intensity is much higher in the latter case. In addition, there would be significant thermal conduction during the sub-ns pulse, lowering the temperature further. A lower initial lattice temperature leads to lower initial strain and hence larger fragments [144]. This explains the observation of smaller size nano-particles with fs pulses than with sub-ns pulses. The experimental observations also brings out an interesting fact that nano-particle generation using ultra-short pulses take place for a wide range of intensities. Efficient nano-particle formation with ultra-short laser pulses has been observed even at intensities as high as $2x10^{16}$ W/cm^2. This intensity is much higher than $5x10^{14}$ W/cm^2, which was considered as the upper limit of intensity for nano-particle production using 50 fs pulses [160].

Chapter 4

Absorption of ultra-short laser pulses in *in situ* formed clusters

Coupling of intense ultra-short laser pulse energy on interaction with matter is a very important aspect [71,91, 161], since the enhanced absorption leads to generation of energetic electrons, MeV ions, and x-rays. The x-rays produced by ultra-short ultra-intense laser have high peak brilliance, short pulse duration, and micron scale size. This makes it a potential source for various applications like time resolved x ray diffraction, imaging of live biological specimen etc. At moderate intensities (~10^{17} W/cm^2) absorption of ultra-short laser pulses (~100 fs) by planar solid targets is quite low, as described in Chapter 1 [39,59,64,65]. Various types of targets like gratings [162], structured targets [80], pre-deposited metal clusters [76], gas clusters [96], snow clusters [69] etc. have been used to enhance the coupling of the laser energy in matter. However, since the gratings are expensive, they are practically unusable on routine basis as targets for x-ray source. Next, high absorption (80-90%) of ultra-short laser pulses has been observed in gas atom clusters [88,163]. The interest in the clusters stems from the fact that the electric field inside the cluster is highly enhanced at three times the critical density (n_c) [97,98] as mentioned in Chapter 1. As the clusters (at near solid density) absorb the laser energy, they get heated up and start expanding. During expansion, the density decreases. When the density approaches $3n_c$, the absorption increases rapidly due to the enhancement of the electric field inside the clusters [96]. Although gas clusters offer a debris-less source of x-rays, the keV x-ray conversion from gas clusters is rather small (~0.01%) and it is a low repetition rate source, with a further

limitation that there are few option of available gases. This limits the use of gas atom clusters as an x-ray source.

Metal clusters have also been used as targets for efficient laser energy absorption. They can be produced by high pressure dc sputtering on polished disks, or by magnetron gas aggregation. They can also be produced by atom pick-up method. All these methods involve two steps, first depositing the clusters on a planar solid substrate, and then using them as target for plasma formation [76]. As mentioned in Chapter 3, intense femtosecond laser irradiation of solid targets is a simple method of synthesis of clusters with few tens of nm diameter [134,160]. We also observed that a sub-ns pulse focused to high intensity can also do the same as observed in materials like Ag, In, Cu etc [147,164]. As mentioned in Chapter 3, the SEM pictures of the deposit taken at two pre-pulse intensities, one at a high intensity of $3x10^{12}$ W/cm^2 and the other at a low intensity 10^{10} W/cm^2, clearly revealed a much higher cluster density corresponding to the deposition taken at the higher intensity of the sub-ns pulse. The particle density in this case ($I = 3x10^{12}$ W/cm^2) was estimated to be ~100 particles/μm^2 from the SEM pictures [147,164].

We have explored the possibility whether the *in situ* formed clusters/nano-particles can be used as targets for enhanced absorption of fs laser light and consequently higher x-ray generation. Silver clusters produced by a 30 mJ, 300 ps laser pulse were irradiated up to an intensity of $3x10^{17}$ W/cm^2 by a 70 mJ, 45 fs compressed laser pulse from the same Ti:sapphire laser. Absorption of the laser light exceeding 70% was observed, resulting in an x-ray yield (>1 keV) of ~ 60μJ/ pulse. This may constitute a much simpler means of intense x-ray generation using ultra-short laser pulses as compared to the irradiation of structured / pre-deposited cluster targets. Moreover, it offers higher x-ray conversion efficiency than that from gas clusters and planar solid targets.

4.1 Description of the experiment

The absorption measurements of intense femtosecond laser pulses by the *in situ* produced clusters/nano-particles, were carried out using the experimental setup shown in Fig. 4.1. The stretched 300 ps laser pulse, before the grating compressor, was split by a pellicle

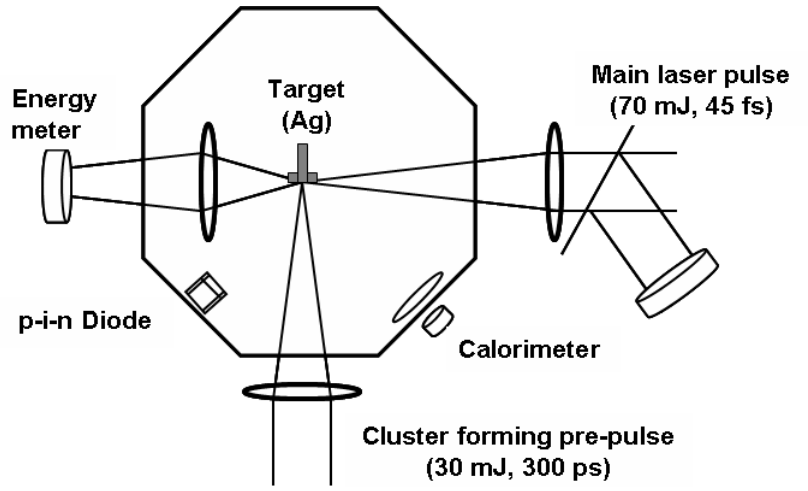

Fig.4.1 : A schematic diagram of the experimental setup

beam splitter and was used to produce silver clusters by focusing it on a planar solid target of silver, in normal incidence geometry. This pulse will be henceforth referred to as the cluster forming "pre-pulse". The focused intensity of the pre-pulse beam was varied between 10^{10} – $4x10^{12}$ W/cm^2. The transmitted part of the uncompressed beam (through a pellicle beam splitter) was time delayed through a delay setup and then compressed for getting a pulse of 45 fs duration (referred to as the "main pulse" or the "main beam"). This main beam (70 mJ, 45 fs) was focused very close to the target, at a distance of ~30 μm from the target surface (See Fig.4.1). This beam propagated parallel to the target surface and irradiated the clusters emanating from the pre-pulse

beam irradiating target. For absorption measurements, the main beam energy was measured with and without pre-pulse produced plasma in its path, to get normalized transmission through the plasma plume. After the main beam propagated through the plasma, the transmitted light was collected using a large diameter lens (75 mm diameter, 100 mm focal length) and made incident on a pyro-electric detector (Gentec, sensitivity 3V/J) for energy measurement. Another more sensitive calorimeter (Gentec, sensitivity 164 V/J) was placed outside the chamber to sample the scattered light collected by another lens of focal length 50 mm placed on the plasma chamber wall window in a direction of 45^{o} w.r.t. the target. The scattering signal was very low and the angle integrated scattered laser light intensity, normalized to the incident beam, was estimated to be $\leq$1%. Thus, the reduction in transmission of the main pulse beam was predominantly due to its absorption by clusters. Next, an x-ray p-i-n diode (Quantrad) filtered with two aluminized polycarbonate filters having cut-off (1/e transmission) at 0.9 keV, was used to measure the x-ray radiation emitted by the laser irradiated clusters. The detector subtended a solid angle of 410 μ sr at the source and was kept at 45^{0} angle from the target.

4.2 Optimization of absorption in the in-situ formed clusters

Once confirmed that efficient production of cluster is taking place then conditions of maximum absorption and x-ray emission from in-situ formed clusters has to be found. For this intensity of pre-pulse beam and main pulse beam has to be varied but first the delay must be optimized. It is expected that the pre-pulse intensity must be high such that efficient cluster production take place.

a) Effect of delay and cluster forming laser pulse intensity : Absorption measurements of the main laser beam were carried out at the maximum main beam intensity of

$3x10^{17}$ W/cm^2, for different intensities of the pre-pulse beam. First, a small delay of 10 ns was kept between the cluster forming pre-pulse and the main pulse. A low absorption was observed as shown in Fig.4.2.

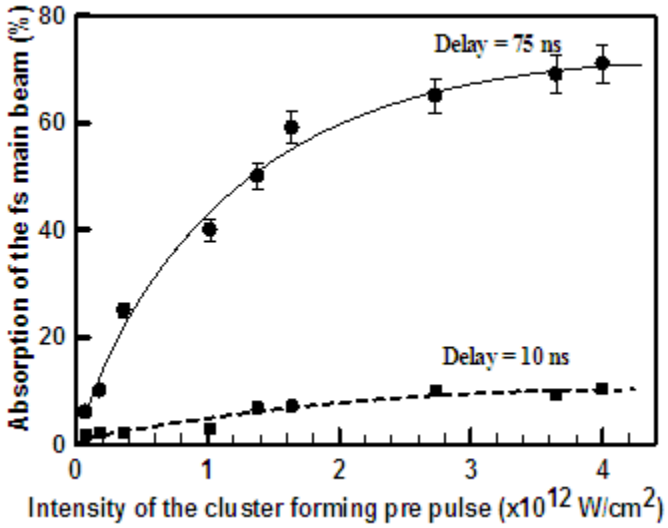

Fig.4.2 : The variation of the main pulse absorption as a function of the pre-pulse laser intensity at a main beam intensity of $3x10^{17}$ W/cm^2. The absorption is studied at two delays of 10 ns and 75 ns between the pre-pulse and the main pulse.

Despite the increase in absorption with pre-pulse energy, the absorption did not increase much (<10%) even when the pre-pulse was focused at higher intensities >10^{12} W/cm^2, where a larger amount of cluster formation is expected. The delay was then increased to 75 ns. From Fig.4.2 it is seen that at this delay, there is a low absorption of ~10% recorded for intensity around 10^{10} W/cm^2. As the pre-pulse intensity is increased, the absorption increases rapidly up to 10^{12} W/cm^2, and thereafter, it shows saturation in the range (1-4)x10^{12} W/cm^2, corresponding to a high absorption of ~70% .

The above observations can be understood as follows. At the delay of 10 ns, even at the highest pre-pulse intensity of $4x10^{12}$ W/cm^2, the large clusters of size ~10 - 40 nm (radius)

having a typical velocity ~10^2-10^3 m/s [135,152, 155] will travel a distance of only ~ 1-10 μm from the target surface and hence will not reach the interaction volume of the main pulse, passing 30 μm away from the surface. Thus, the main beam will interact with only the plasma produced by the pre-pulse beam (and perhaps some very small clusters traveling with a higher velocity), resulting in the observed low absorption. Increasing the delay results in the arrival of more and more clusters in the region of main beam. The observed increase in absorption with increasing pre-pulse intensity is then simply understood from the increase in number as well as the velocity of clusters produced at higher pre-pulse intensity [147,164].

b) Effect of laser pulse intensity on absorption :

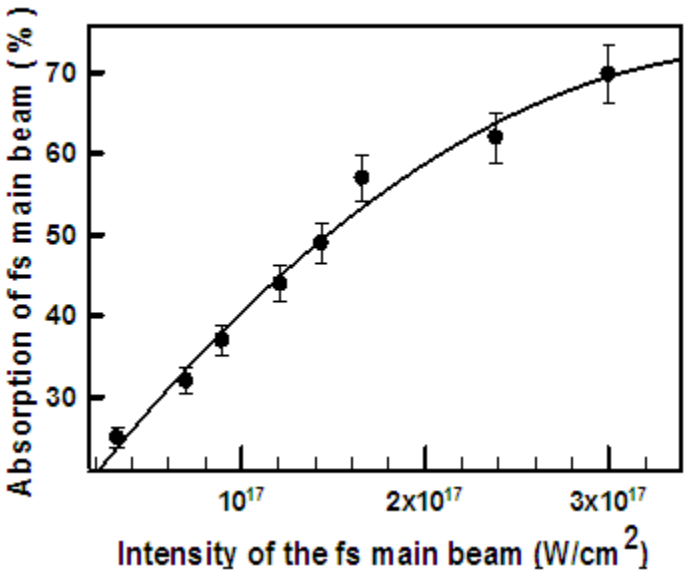

Fig. 4.3: Variation of the main beam absorption as a function of its intensity. The pre-pulse beam intensity is fixed at $4x10^{12}$ W/cm^2.

Next, the absorption of the main beam was studied as a function of its intensity, at a fixed pre-pulse intensity of $4x10^{12}$ W/cm^2. For this purpose, calibrated neutral density filters were used to attenuate the main beam energy, starting from the highest value. The neutral density filters were put before the compressor in the path of the uncompressed beam thereby eliminating the pulse

spreading and additional B integral issues. The absorption variation for silver target is shown in Fig.4.3, where the intensity of the main beam was varied in the range of $3x10^{16}$ – $3x10^{17}$ W/cm^2. When the intensity was increased by one order of magnitude (from ~$3x10^{16}$ W/cm^2 to $3x10^{17}$ W/cm^2), the absorption increased from ~ 25% to 70%. The increase in absorption was initially fast and at higher intensities the increase in absorption was slow.

At a fixed pre-pulse beam intensity of $4x10^{12}$ W/cm^2, the increase in absorption with increase in the main pulse intensity can also be understood in terms of the $3n_c$ resonance absorption in clusters [88,97,98]. As a cluster absorbs the laser energy and gets heated up, it starts expanding and the density decreases from near solid density and approaches $3n_c$. The absorption increases rapidly due to the rapid enhancement of the laser electric field inside the cluster at this density, when the dielectric constant of the cluster approaches a value of –2 at $3n_c$ [97-99]. The clusters irradiated at higher laser intensity will be at higher temperature and will expand faster. Hence they will reach comparatively closer to $3n_c$ during the laser pulse (resulting in higher absorption) than those irradiated at lower intensity [88,98]. As a result, one gets lower absorption at lower intensities as seen in Fig.3. Moreover, the rate of change of electron density in a cluster after irradiation is expected to be fast initially for smaller radius (as $dn_e/dR \alpha R^{-4}$), hence with increasing intensity of main pulse, a slower change in electron density is expected as most of the expansion occurs during the initial part of the pulse. This explains qualitatively the fast rise in absorption followed by a slower increase of absorption when the main pulse intensity is increased.

c) Effect of multiple shots : It may be relevant to point out that a high absorption was observed only when fresh surface of the target was irradiated. When the pre-pulse laser beam was incident on a previously irradiated spot on the target, the absorption decreased. Fig.4.4

shows the main pulse absorption after a number of pre-pulse shots were fired at the same place. It is seen that the absorption decreases with the number of pre-pulse shots.

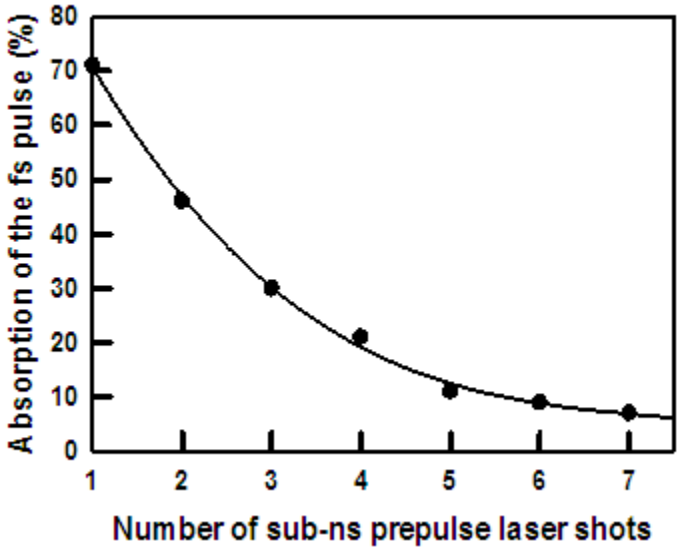

Fig.4.4 : Variation of the absorption of the main beam with n^{th} pre-pulse shot fired at the same place in silver target. The fitted curve is only guide to the eyes

The above behavior may be understood as follows. When the pre-pulse irradiates a solid surface it forms a crater. On subsequent laser irradiation at the same spot, there will be a recession of the crater surface as more and more material ablates out. Thus the clusters produced from irradiation of crater region will take a longer time to reach the interaction region and would increasingly miss interaction with the main beam. This inference is also supported from the observation that when the target, after few shot irradiation, was brought slightly closer (~10 μm) to the main beam, the absorption showed a slight increase compared to that in the unshifted position. Next, as stated above, the absorption did not reduce to zero even after a number of shots were fired at the same place. This may be due to arrival of some smaller clusters in the interaction region even after crater formation.

4.3 KeV x-ray emission measurements

Now, we present the results of the x-ray emission measurements from the *in situ* produced clusters by irradiation of 45 fs laser pulse heating. Fig.4.5 shows the intensity of x-ray emission as a function of the pre-pulse beam intensity at the 45 fs heating pulse of maximum intensity of $3x10^{17}$ W/cm^2. It is seen that the x-ray intensity increases with pre-pulse beam intensity. This behavior is consistent with our measurements of a higher absorption of the main beam at high pre-pulse intensity (shown in Fig.4.2). With increase in pre-pulse intensity, the number of clusters interacting with the main pulse increases. As a result, the absorption increases and the x-ray yield also increases, showing a variation somewhat similar to that of the absorption.

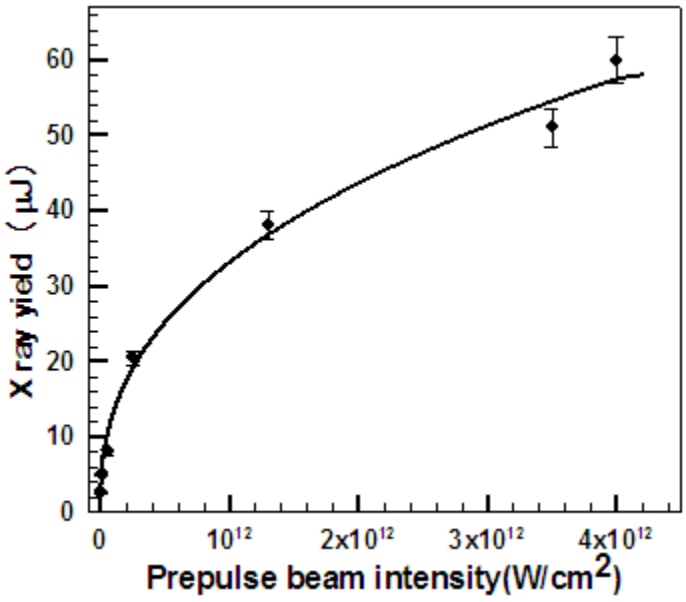

Fig.4.5 : X-rays emission intensity from silver clusters as a function of the pre-pulse intensity, for main beam intensity of $3x10^{17}$ W/cm^2.

The spectrally and temporally integrated x-ray yield (for hν ≥ 1 keV and up to 10 keV beyond which the response of p-i-n diode drops due to finite detector layer thickness) at the main beam intensity of $3x10^{17}$ W/cm^2 and the pre-pulse intensity of $4x10^{12}$ W/cm^2, was measured to

be ~ 60 μJ, assuming isotropic emission. For the above condition of the pre-pulse and the main pulse, the recorded absorption of the high intensity 45 fs pulses was ~ 70%. Thus, the percentage conversion efficiency of the laser energy into x-rays is ~ 8.5×10^{-2} %.

The above high yield of the x-rays achieved from silver clusters can be due to several reasons. Irradiation of the metal cluster with intense femtosecond pulses leads to enhanced absorption. Due to the enhanced field inside the clusters, highly charged ion species are produced [165-167]. Therefore, the clusters give a high x-ray output due to increased collisionality, and higher ionization and excitation inside the clusters caused by laser heating [163,166,167]. Due to the above reasons, a high percentage conversion efficiency of laser energy into x-rays is observed. In conventional Xe gas cluster targets, the percentage conversion efficiency of laser energy into x-rays ($h\nu > 1$ keV) is reported to be between 1.7- 4.2×10^{-3} % [163]. Nickel target in various forms, when irradiated with 1 ps pulse of 10^{17} W/cm^2, produces efficient x-rays above 900 eV [70]. The reported percentage conversion efficiency of 70 mJ laser energy in to x-rays ($h\nu > 900$ eV) from flat nickel target is 2.8×10^{-3} %, for Ni nano-groove target it is 2.8×10^{-2} % , for Ni "smoke" targets it is 1.3×10^{-1} %, and for Ni black target it is 1.4×10^{-1}% [70]. This suggests that the silver clusters produced *in situ* is a better source of x-rays than the gas clusters and solids. Moreover, it offers a simple single step method for keV x-ray generation than the structured targets which are difficult to fabricate and are expensive.

Next, the x-ray emission in directions making large angle with target normal is nearly debris free. This is because, while the x-ray emission from the *in situ* produced clusters is expected to be isotropic, the debris expand predominantly in a direction normal to the target, making it practically a debris-free source in a direction perpendicular to the target normal. The present scheme of cluster formation has also the advantage that the interaction of the generated

clusters with the main beam is slightly away from the solid target. This prevents heat conduction from clusters to the cold target substrate, leading to enhanced plasma temperature and increased x-ray emission, than in the case of metal clusters pre-deposited on a planar target.

Thus we have observed a high absorption of ~ 70% of high intensity ultra-short laser pulses in silver clusters *in situ* produced by a sub-ns pre-pulse. Effect of temporal delay (between the pre-pulse and the main pulse) and the pre-pulse intensity was studied to achieve high absorption of the fs pulses in these clusters. The high laser light absorption resulted in an efficient keV x-ray generation. A high conversion efficiency of $\sim 8.5 \times 10^{-2}$ % of the laser energy into x-rays ($h\nu \geq 0.9$ keV) is observed. Moreover, the x-ray source is practically debris-free.

Chapter 5

Water window x-ray emission from *in situ* formed carbon clusters.

As mentioned earlier, one of the areas of continuing interest in ultra-short laser pulse interaction with matter is on enhancing the laser energy absorption for energetic particle and x-ray generation suitable for various applications [69-86, 168,169]. In particular, imaging of live biological samples with high contrast requires a point x-ray source in the water-window spectral region (23 - 44 Å) [170,171]. Ultra-short laser pulse produced plasma from solid targets can be an x-ray source for such applications. The problem of inefficient laser energy coupling in planar solid target is normally overcome by using structured targets like gratings, pre-deposited nano-particles like nano-tubes or metal clusters but such targets have their own merits and demerits as described in Chapter 4 [71,162,172]. A high absorption (80-90%) of the ultra-short laser pulses has been observed in gas atom clusters [88] and it is demonstrated as a debris-free source of short duration x-rays [90], although this is a low repetition rate source and is limited by the number of gases available. It is therefore desirable to devise techniques for generation of an efficient x-ray source that involves a simple, single step method, works at a high repetition rate, and also has low debris.

As mentioned in Chapter 3, short pulse laser irradiation of solid targets is a simple means of synthesis of clusters [133,134,144,147]. The clusters are formed in a time scale of < 1ns [44] after laser irradiation and travel typically at a speed of 0.1-10 km/s, depending on cluster forming laser parameters and the target material [173]. The clusters can be produced in situ using the sub-ns stretched pulse from a chirped pulse amplification based Ti:sapphire laser system. The cluster production by this method can be at a high rep-rate (unlike in the case of gas clusters). These in situ produced clusters may then be used as a target for efficient x-ray

generation by irradiating them with a time delayed fs (compressed) laser pulse [148]. Recently, a few experiments on laser energy absorption [148] have shown that such in situ produced clusters from various material like silver, carbon etc., when irradiated with a fs pulse (after a delay of few tens of ns) offer high energy absorption [148]. Such clusters also give higher high-harmonic conversion [174,175]. To study the interaction of intense ultra-short pulse laser with the in situ formed clusters, one needs to characterize the size of these clusters and also optimize the delay between the pre-pulse (i.e. the stretched pulse producing clusters) and the main pulse (i.e. the compressed pulse interacting with the clusters), so that efficient laser energy absorption (of the main pulse) takes place in the cluster-filled low-density pre-plasma. This approach is somewhat similar to the dual pulse technique used for increasing the laser energy absorption by increasing the density scale length using a controlled pre-pulse to create preformed plasma before the arrival of the main laser pulse [176]. In this method, both the pre-pulse and the main pulse, are of femtosecond duration and the delay between them is sub-ns, in general [68,176]. In this technique, for enhancing the x-ray emission, one needs to optimize various parameters such as the intensity ratio of the pre-pulse and main pulse, the time delays between the two pulses etc. However, it must be noted that these experiments were done at a lower main pulse intensity of 10^{15}-10^{16} W/cm^2 and the soft x-ray enhancement was more pronounced at lower intensity of the main pulse and the enhancement decreased considerably at higher laser pulse intensity [68,176].

In this chapter we describe the demonstration of enhanced water window x-ray emission (23-44 Å) from carbon clusters, formed in situ using a pre-pulse, irradiated by intense (I >10^{17} W/cm^2) ultra-short laser pulse. An order of magnitude x-ray enhancement over planar graphite target is observed in carbon clusters, formed by a sub-ns pre-pulse, interacting with intense main pulse after a delay. The effect of the delay and the duration of the main pulse has been studied

for optimizing the x-ray emission in the water window region. The conversion efficiency of the laser energy converted to the water- window x-ray emission was also measured. For a 110 mJ, 45 fs laser pulse, the conversion efficiency in the water window, from a planar graphite target, was 5.8×10^{-2} % /sr. For the dual pulse configuration with 8 ns delay between the cluster forming pulse and ultra-short high intensity main pulse, the conversion efficiency from carbon clusters was estimated to be 0.54 % /sr. This method has added advantages of being an efficient, high repetition rate, and low debris x-ray source.

5.1 Description of the experiment

The experimental setup used in the present experiment is shown in Fig. 5.1. The plasma was produced using the pre-pulse (30 mJ, 300 ps) focused to an intensity of 10^{12} W/cm^2. The pre-formed plasma was then heated by the time delayed main pulse (110 mJ, 45 fs) focused to an intensity of 3×10^{17} W/cm^2. Both the laser beams were incident at 45^o with respect to the target normal as shown in Fig.5.1. The main beam was p-polarized for better resonance absorption. The x-ray emission spectra from the target surface were recorded using a transmission grating spectrograph kept along the target surface, at 90^o to the target normal. The spectrum was recorded "on-line" using an MCP- CCD camera combination. A calibrated delay line was set up for providing a known delay between the pre-pulse and main pulse in two regimes, first in the sub-ns range and then in few tens of ns range. To obtain the conversion efficiency, which is defined as the fraction of the laser energy converted to the water- window (23-44 Å) x-ray emission, a soft x-ray CCD camera (X-Vision M 25) was used to record the spectrum. The obtained spectrum was corrected for the transmission grating diffraction efficiency [120] and the

quantum efficiency of the CCD [117] for estimation of the integrated water window x-ray emission.

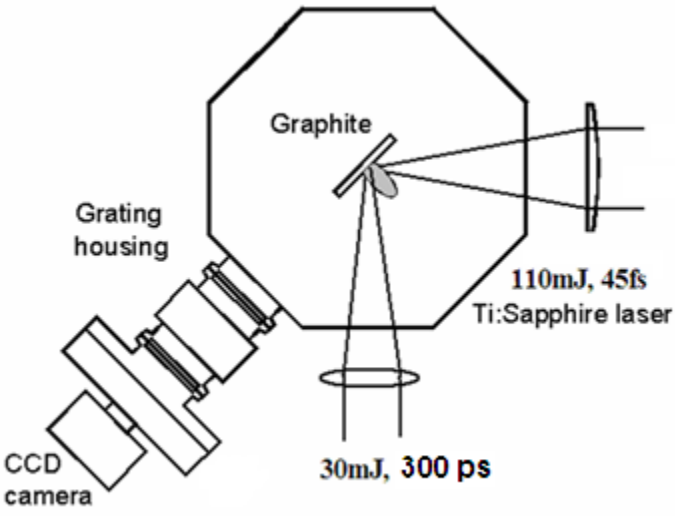

Fig.5.1: A schematic diagram of the experimental setup

Graphite was used as the target because carbon has resonance line emission (from H-like and He-like ions) in the water-window region. More x-ray emission compared to that from planar graphite may be expected if carbon clusters are formed by a pre-pulse, and are then irradiated after a suitably time delayed fs pulse.

5.2 Cluster formation and characterization

To check whether clusters of carbon can be formed by irradiation of graphite by a 30 mJ, 300 ps uncompressed pulse from a Ti:sapphire laser focused at an intensity of 10^{12} W/cm^2, the deposited plasma debris was collected on a silicon wafer kept at a distance of 5 cm from the ablation spot, at 45^o angle with respect to target normal and an analysis of the sizes and

structural properties of deposits was carried out using an atomic force microscope (AFM : SOLVER PRO, NT-MDT).

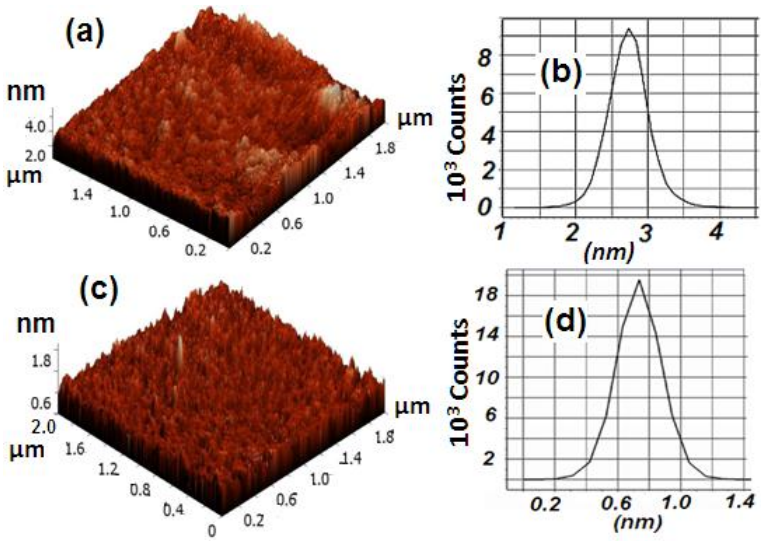

Fig.5.2 : a) AFM images of carbon clusters b) average size of 2.8 nm formed at 10^{12} W/cm^2 intensity of the 300 ps pre-pulse; c)The corresponding AFM image at a pre-pulse intensity of 10^{10} W/cm^2 d) fullerene of size 0.7 nm.

Figure 5.2a shows the AFM image of carbon clusters deposited in 10^3 laser shots on Si wafer. Figure 5.2b shows the size distribution and number of clusters deposited on a ~ 2 µm x 2 µm area of the sample. It is seen from Fig. 5.2b that ~ 9 x 10^3 clusters of average size of 2.8 nm were deposited over 4 µm^2 area in 10^3 laser shots when the 300 ps pulse (referred to as pre-pulse) was focused at an intensity of 10^{12} W/cm^2. Smaller clusters are formed when the intensity was reduced to 10^{10} W/cm^2 by defocusing the cluster forming pulse, as seen from the AFM image Fig.5.2c. The size of the deposited particles in this case was 0.7 nm (the size of fullerenes) as seen from Fig. 5.2d. Some smaller clusters like fullerenes can be formed at high intensity of pre-pulse as well due to temporal and spatial intensity variation of the prepulse. After

confirming and characterizing the clusters formed by the pre-pulse, the delay was optimized for maximizing the x-ray emission.

5.3 Results of x-ray emission with 45 fs laser

a) X-ray spectra at various delays : First, the effect of the delay between the two pulses was investigated for obtaining the condition for maximum x-ray emission. Figure 5.3 shows the x-ray emission spectra from plasmas produced from planar graphite using single fs pulse, and dual pulses at different delays of 0, 5 ns and 8 ns. The zero delay is defined as the one when the peaks of the pre-pulse and main pulse coincide temporally. The x-ray emission is in the water-window region, with intense lines from carbon plasma viz. He-α (C V) $1s^2$-1s2p (λ =40.3Å) and Ly-α (C VI) 1s-2p (λ = 33.7Å), ride over a strong continuum.

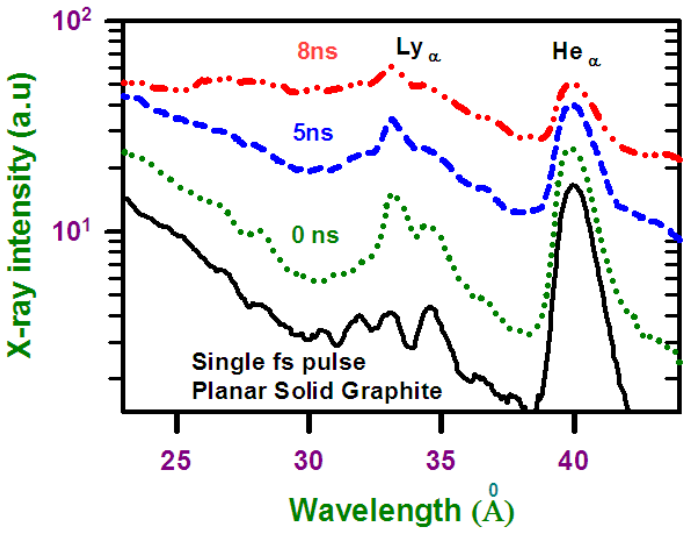

Fig. 5.3 : Water window x-ray emission spectra from plasma produced from single fs pulse irradiating planar graphite, and using dual pulses at a delay of 0 ns, 5ns and 8 ns. The pre-pulse intensity was 10^{12} W/cm^2, and the main pulse intensity was $3x10^{17}$ W/cm^2. In the 0 delay case, the enhancement in the x-rays is due to laser interaction with long scale length plasma, and at 8 ns delay, it is due to laser-cluster interaction.

It may be noted that the x-ray emission from planar graphite irradiation from single fs pulse irradiation is 2.5 times higher compared to polyethylene target, as observed in one of our

earlier experiments, which was assigned to the pitted surface structure of the graphite target seen in its SEM image [177]. The maximum x-ray enhancement was seen at a delay of 8 ns.

b) X-ray yield at various delays *:* Figures 5.4a and 5.4b show the conversion efficiency (CE) given in % / sr obtained after integrating the x-ray emission in the water window spectral region from plasma produced from planar graphite using single 45 fs

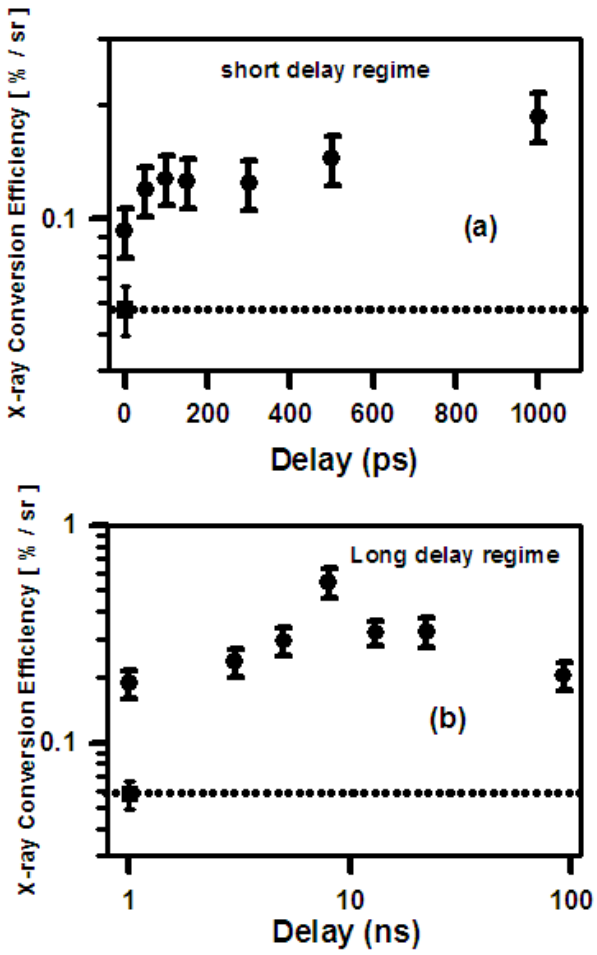

Fig. 5.4. Integrated water window x-ray emission spectra using dual pulses as function of delay. The pre-pulse(30 mJ, 300 ps at I ≈ 10^{12} W/cm^2), main pulse (110 mJ, 45 fs, I= 3x10^{17} W/cm^2). a) For short delay regime, and b) For long delay regime . The dashed line in the two figures is the x-ray output using single fs pulse irradiating planar graphite.

pulse (dashed line) and dual pulses at different (short and long) delays. Interestingly, there was an enhancement of the x-ray emission in the water window spectral region in both the delay regimes, as compared to the x-ray output using single 45 fs pulse.

5.4 Discussion of the results of x-ray emission with 45 fs laser

In the short delay regime (Fig. 5.4a), the absorption processes in the plasma is governed by the density scale length "L" of the plasma [31,52] given by $L = c_s\tau$, where c_s is plasma expansion velocity $\{c_s = Z\ kT_e/M_i)^{1/2}$, M_i is the ion mass)}, and τ is the delay between the two pulses [52,176]. With increasing delay, L increases and so does the absorption since the absorption by inverse bremsstrahlung is $A_{col} = 1 - \exp\left(-32\nu_{ei} L\cos^5\theta\ /15c\right)$ where ν_{ei} is the collision frequency given by $\nu_{ei} = 2.91\text{x}10^{-6}\ Z\ n_e\ T_e^{-3/2}\ \ln\Lambda$, where Z is number of free electrons per atom, n_e is the electron density in cm^{-3}, T_e is electron temperature of the plasma in eV, and $\ln\Lambda$ is the Coulomb logarithm [52]. It may be noted that this expression for L is applicable for shorter delays, since at longer delays (> 1 ns) L becomes equal to the laser pre-pulse beam focal spot which is ≈100μm in our experiments [52]. In this case, the expansion is no longer 1D and there is a faster decrease of the plasma density due to 3D expansion. Hence, one does not expect the absorption to increase further with increasing delay. However, the experimental observation in Fig.5.4b shows that the x-ray emission keeps on increasing for delays >> 1 ns. From Fig. 5.4b, it is seen that after 1 ns, the x-ray emission gradually increases, peaks at 8 ns and then gradually drops but still remaining high at 22 ns delay, and eventually the enhancement reduces (but not very significantly) at a delay of 92 ns.

The observation of peaking of the absorption at 8 ns delay is quite different from the general dual pulse experiments [68,176] where the x-ray emission was found to maximize up to

1 ns. Our experimental results of high x-ray enhancement at longer delays cannot be attributed to an extended under dense plasma [68,176] or formation of crater by the pre-pulse, although both these reasons have been shown to enhance the laser energy absorption, leading to x-ray enhancement [178]. The x-ray enhancement due to crater formation can be ruled out in our case since the x-ray emission is monitored along the target surface at 90^o to the target normal. The x-ray emission coming from within crater will not be recorded by the spectrograph looking at the focal spot along the target surface. The observation of enhanced x-ray emission at longer delay can be explained if one assumes that the cluster produced by the pre-pulse start coming into the fs main pulse interaction zone at longer delays. When an obliquely incident laser interacts with the preformed plasma at lower delays (< 1ns), the laser light propagates up to $n_c\cos^2\theta$ (i.e. $n_c/2$ at 45^o incidence). At longer delays (>> 1ns), the clusters, which move at a speed much slower than that of the plasma, start crossing the laser turning point ($n_c\cos^2\theta$) to come in the interaction zone of the fs main pulse, giving rise to the possibility of high laser absorption in the clusters. At longer delays (> 1ns), the fraction of the clusters will increase with increasing delay as more and more clusters start arriving the main pulse interaction zone. To explain this clearly a schematic diagram is given Fig. 5.5a which shows the pre-pulse which forms the plasma which expands. In short delay regime, clusters are behind the critical density surface and the main pulse interacts with the expanding under dense plasma. Fig 5.5b shows the prepulse forms plasma the clusters cross the critical density surface and main pulse interacts with clusters.

It appears that at 8 ns delay, the fill fraction of the clusters occupying the main pulse interaction zone peaks and gradually their number density reduces at longer delays when they start moving out of the interaction zone of the main laser pulse. This explains the peak x-ray emission at 8 ns delay followed by a gradual decrease.

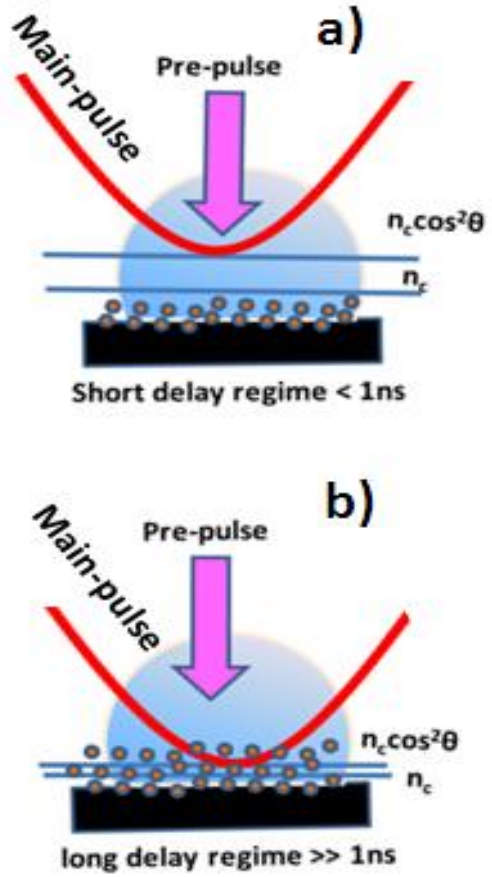

Fig. 5.5. A schematic diagram showing laser plasma interaction at two delay regimes: a) For short delay regime, the main pulse interacts with plasma, and b) For long delay, the main pulse interacts with clusters.

Thus, one can conclude that the x-ray enhancement at longer delays is due to high absorption in the carbon clusters which leads to higher x-ray yield than obtained from planar graphite irradiated with as single 45 fs pulse. As seen from the Fig 5.4a and 5.4b, the conversion efficiency of 110 mJ, 45 fs laser pulse in the water window is 5.8×10^{-2} % / sr from planar graphite, which is similar to the conversion obtained from planar carbon target reported by Nishikawa et al [83]. The x-ray CE from carbon clusters is estimated to be 0.54 % / sr from dual pulses with 8 ns delay (Fig. 5.4 b) between them. This CE is similar to the conversion reported from ultra-short laser pulse irradiation of carbon nanotubes by Nishikawa et al [83]. It may be

noted that the x-ray conversion in all the above cases is estimated assuming isotropic x-ray emission from the plasma volume.

5.5 Simulation of pre-plasma conditions using Multi-1D

To investigate the role of under dense plasma in x-ray enhancement at long delays, simulation of the interaction of a 300 ps laser pulse of intensity 10^{12} W/cm^2 with a planar carbon target was carried out using a 1D hydrodynamic code (Multi-1D) [179] to evaluate the plasma density scale length at the critical density n_c (L=n/(dn/dx) at n_c). The density scale length "L" is one of the most important parameters that determine the absorption processes in the plasma [31,52]. As mentioned earlier, it is given by $L= c_s\tau$. In the present case, τ is the delay between the two pulses [52,176]. This expression for L is applicable for shorter delays since at longer delays (much larger than a ns), L becomes equal to the laser focal spot, as the expansion is no longer 1D. Further, Multi-1D was used in the planar expansion case. This helps in qualitative understanding the reason of the observed x-ray enhancement at longer delays. Considering spherical expansion will lead to even faster decrease of scale length for longer delays once 3D expansion sets in.

Figure 5.6a shows the time evolution of the estimated density scale length. One can see that upto few hundred picoseconds (laser pulse duration is 300 ps), the density scale length increases and after the pulse is over, the density scale length starts decreasing rapidly with time, becoming even sub-λ after 1 ns. Figure 5.6b shows the calculated distance of the critical density and half critical density layer from the target surface as a function of time. The n_c and $n_c/2$ surfaces move ahead initially but eventually at longer interval of time these layers become closer to the target surface, when the cluster can cross the laser turning / reflection surface and interact

with the fs main pulse. Thus the possibility of clusters crossing the n_c and $n_c/2$ surface at long delays is supported by simulations also.

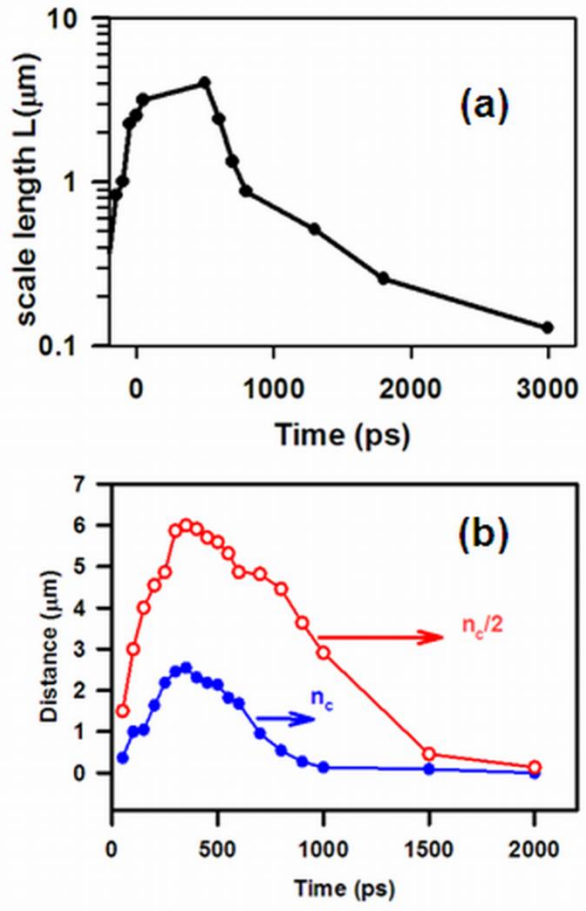

Fig.5. 6 : a) The estimated evolution of the plasma density scale length (at n_c) of the plasma formed by the pre-pulse as a function of time, b) The calculated distance of critical density and half critical density layer from the solid target surface as a function of time.

5.6 Results on x-ray yield variation with main pulse duration

The effect of the duration of the main laser pulse on the x-ray yield was also studied. The results are shown in Fig 5.7. In this study, the main pulse duration was varied from 45 fs to 5 ps, at a fixed fluence of ~ $2x10^4$ J/cm^2. While the x-ray emission from graphite target showed a slow

monotonic increase with the main pulse duration for the case of no pre-pulse, the x-ray emission from dual pulses showed a peaked behavior. As the laser pulse duration is increased, plasma of a longer scale length is produced, leading to an increase in the collisional absorption and corresponding increase in the x-ray emission. In the dual pulse case (delay 8 ns), an optimum x-ray yield was observed for a pulse duration ≥ 400 fs, the CE for this case is 0.98 % / sr, which is the highest yield recorded in the current experiment. A similar observation was made at a delay of 22 ns, where the optimum laser pulse duration for maximum x-ray emission was ~ 1 ps.

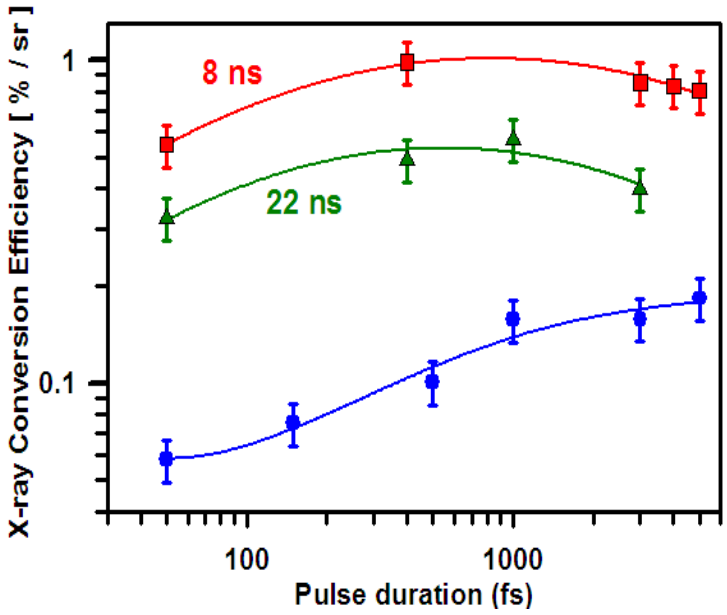

Fig5.7 : Variation of x-ray yield with main laser pulse duration for : no pre-pulse (closed circles), and dual pulses with a fixed delay of : 8 ns (closed squares) and 22 ns (closed triangles). The main pulse duration was varied from 45 fs to 5 ps, at a fixed fluence of ~2x10^4 J/cm^2.

5.7 Discussion of results on x-ray yield variation with pulse duration

The peaking of the x-ray yield at longer pulse duration can be attributed to the presence of carbon clusters going into resonant phase (i.e. reaching a density of $3n_c$) during the (main) laser pulse, resulting in higher absorption of the laser, leading to enhanced x-ray emission. As

the carbon clusters (at near solid density) absorb the laser energy, they get heated up and start expanding. During the expansion, the density decreases, and when it approaches $3n_c$, the absorption cross-section $\sigma_{abs} = \frac{8\pi kr^3}{3}\mathrm{Im}\left(\frac{\varepsilon\text{-}1}{\varepsilon+2}\right)$ increases rapidly due to the enhancement of the electric field inside the clusters $\frac{E_{in}}{E_L} = \frac{3}{\varepsilon+2}$ at $3n_c$, which corresponds to $\varepsilon = -2$ [96].

It may be noted that we have measured the x-ray emission along the target surface, since the plasma debris from the laser-irradiated target is minimal in this direction, which is highly desirable for applications like lithography, where one does not want to spoil a nano-structure by debris deposition. The irradiation of the in situ formed clusters by a time delayed fs pulse at a delay of 8 ns (when the cluster density at the interaction zone is maximum) ensures the maximum annihilation of the clusters, thereby reducing the debris further [180].

Thus, we have demonstrated enhanced water window x-ray emission from *in situ* formed carbon clusters irradiated by laser pulse at $I > 10^{17}$ W/cm^2 after a delay of few ns and obtained the condition for maximum x-ray emission at 8 ns. For this delay, the x-ray conversion efficiency from carbon clusters was estimated to be 0.54 % /sr. At the same delay of 8 ns the optimal pulse duration for maximizing the x-ray emission is found to be 400 fs and for this case the conversion was found to be as high as 0.98%/sr. This provides an alternative, simple, single step method for studying laser cluster interaction with the added advantages of being an efficient, high repetition rate, and of low debris x-ray source.

Chapter 6

Soft x-ray emission from carbon nano-fibers

As mentioned in Chapter 5, point-like x-ray sources in the water-window spectral region (23-44 Å), emitting ultra-short pulses, are of particular interest for ultra-fast imaging of live biological samples with high contrast [108,171]. Plasma produced by intense ultra-short laser pulses from solid targets can serve as a compact and low-cost source for the above application [181-183]. As we have shown that the *in situ* formed targets are very attractive for overcoming the problem of low absorption of high-intensity, ultra-short laser pulses in plasma produced on solid targets. As mentioned in Chapters 1, 4 and 5, various other forms of solid targets like gratings, structured targets, metal clusters, nano-fibers etc. [69-86, 168,169] have been used by various experimental groups to enhance the laser energy absorption, production of energetic particles, and improving the x-ray conversion efficiency. In this and the following chapters, experiments on absorption and x-ray emission from intense laser irradiated nano-structures will be described. The aim is to study the effect of geometrical shape, size, fill fraction, and topography of the target on the absorption of intense ultra-short laser pulses. Another aspect is the dynamics of the laser irradiated nano-structures and resonances occurring in them, which can be manipulated for a higher absorption and the consequent x-ray conversion.

In this chapter, we describe an experimental study of the x-ray emission in the water-window region from carbon nano-fibers (CNFs) irradiated with ultra-short laser pulses. Since carbon also has intense resonance lines (from H-like and He-like ions) in the water-window region, graphite has been used as a target [184]. An increase in the x-ray emission may be expected by coupling intense short laser pulses to carbon based nano-structures [83,84,185-187]

instead of carbon-containing planar targets. CNFs, which can be produced easily in different sizes at low cost, are one such potential candidate.

We have observed that CNFs of different diameters show an order of magnitude enhancement of x-ray emission intensity over that for planar graphite target. The effect of laser pulse duration and the intensity scaling of the integrated x-ray yield are studied for CNFs of 60 nm and 160 nm diameters. The integrated x-ray yield of these carbon based targets is observed to scale with the laser intensity (I_L) as $I_L^{\sim 1.3\text{-}1.4}$ in the intensity range of 4 x10^{16} – 4 x10^{17} W/cm^2. The effect of the laser pulse duration on the x-ray emission from the CNFs has been also studied by varying the pulse duration from 45 fs up to 3 ps, at a constant fluence of 2 x10^4 J/cm^2. The optimum laser pulse duration for maximum x-ray emission increases with the diameter of CNFs used. The results are explained from the physical considerations of heating and hydrodynamic expansion of the CNF plasma in which resonance field enhancement takes place while passing through two times the critical density. The results add to the efforts towards achieving an efficient low-cost water-window x-ray source for microscopy.

6.1 Description of the experiment

First a description of the processes used for CNF fabrication is given and also the characterization by a scanning electron microscope (SEM) is presented. The SEM is used to ascertain the CNF diameter and the inter fiber separation, as these factors determine the laser energy absorption.

6.1.1 Preparation and characterization of CNFs

CNFs of two different diameters were used. The 60 nm CNFs were prepared by spray pyrolysis of a mixture of ferrocene and benzene [188]. They had a size variation with a standard deviation of ~20 nm. The length distribution of the CNFs could not be determined because viewing the ends of the spaghetti-like CNFs turned out to be prohibitive. The thickness of the CNF deposition on the substrate was ~20-50 μm. Visual observation of a 5x7-μm² area of the sample suggested that about 30% of the area was free from CNFs in the deposited layer. The 160 nm CNFs were grown by thermal decomposition of a precursor mixture of acetylene and hydrogen (1:5). The growth was done on a strip of iron coated with its nitrite.

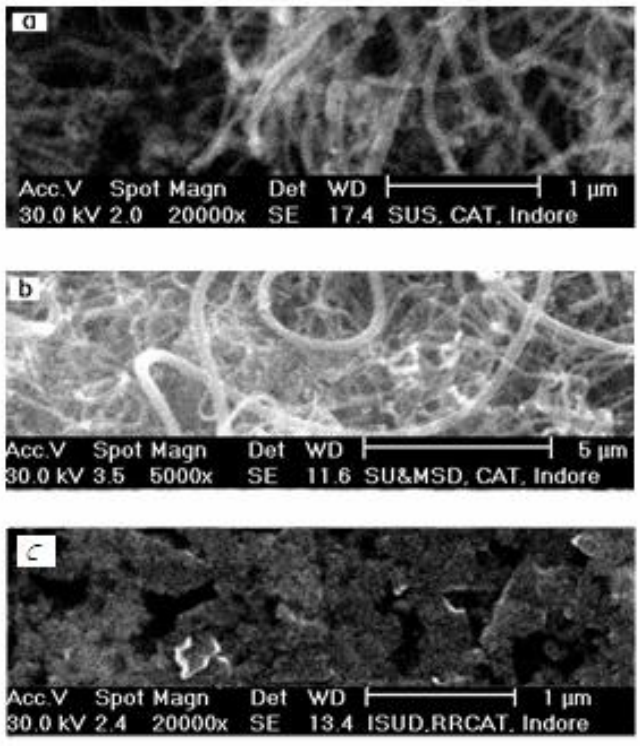

FIG.6.1 : SEM images of (a) 60 nm CNFs, (b) 160 nm CNFs and (c) graphite plate

Figure 6.1 shows the images of CNFs deposited on graphite plates, observed with an SEM (Philips XL30CP; ~3.5 nm instrumental resolution). It is noted from Fig. 6.1a that the

CNFs of 60 nm diameter have gaps between them of upto a few times their average diameter though the exact estimation of the intra-fiber spacing is difficult as it is non-uniform but it appears to be ~ 300-500 nm on an average. On the other hand, the larger diameter CNFs (see Fig.6.1b) are more closely packed and the average spacing between the fibers appears to be smaller than the intra-fiber spacing of the smaller nano-fiber target. The planar graphite target was porous in nature with many craters of nano-meter scale as seen from the SEM image shown in Fig.6.1c. Since porous targets are also efficient absorbers of ultra-short intense laser pulses, a planar polyethylene target free of porosity was also used for comparison.

6.1.2 Experimental setup

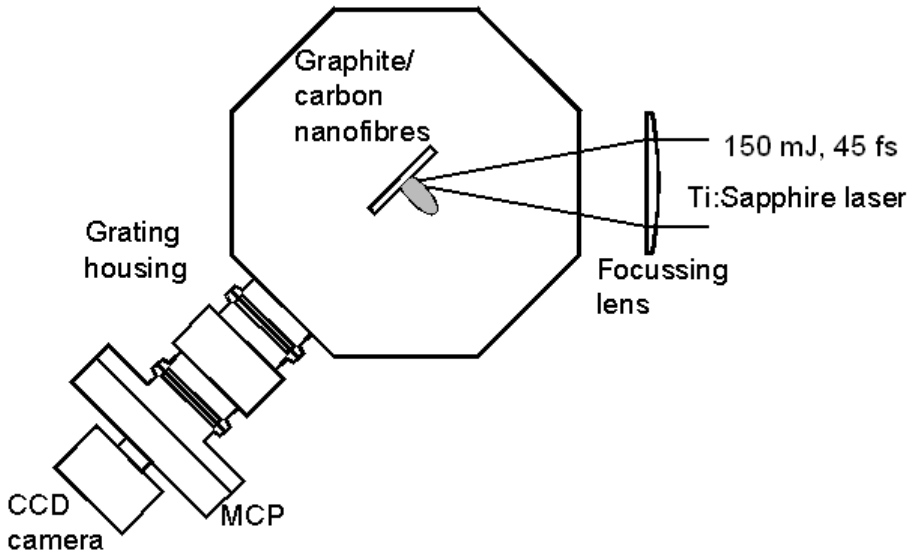

FIG.6.2 : A schematic diagram of the experimental setup

Figure 6.2 shows the schematic of experimental setup used in the current study. Plasma was produced by focusing 150 mJ, 45 fs (FWHM) Ti-sapphire laser pulses (λ = 790 nm) on a planar graphite target with / without pre-deposited carbon nano-fibers. The p-polarized laser

beam was made incident on the target at an angle of 45^{o} with respect to the target normal, at a maximum intensity of ~ 4 $x10^{17}$ W/cm^2. The oblique incidence geometry was used so that the plasma produced from the planar targets was predominantly by the resonance absorption mechanism of laser light absorption [40,44]. The ns pre-pulse intensity contrast was better than 10^6. The x-ray emission spectra were recorded with a spectral resolution of ~ 1 Å, using a micro-channel plate - CCD camera based on-line transmission grating spectrograph [119]. The laser intensity was varied by using calibrated neutral density filters. To study the effect of the laser pulse duration on the x-ray yield, the former was varied by changing the grating pair separation in the optical compressor, from 45 fs to 3 ps, at a fixed fluence of ~ $2x10^4$ J/cm^2. The stretching of the pulse duration by increasing the separation between the compressor gratings introduces negative chirp in the laser pulse i.e. the higher frequencies precede the lower frequencies temporally in the laser pulse.

6.2 Experimental Results

6.2.1 X-ray spectra from CNFs

Figure 6.3 shows the x-ray emission spectra from plasmas produced from polyethylene, graphite, and CNFs (60 nm and 160 nm) deposited on a graphite substrate. The x-ray emission in the water-window region has intense lines from carbon plasma, viz. C V $1s^2$-1s2p (λ=40.3Å) and C VI 1s-2p (λ=33.7 Å) riding over a strong continuum.

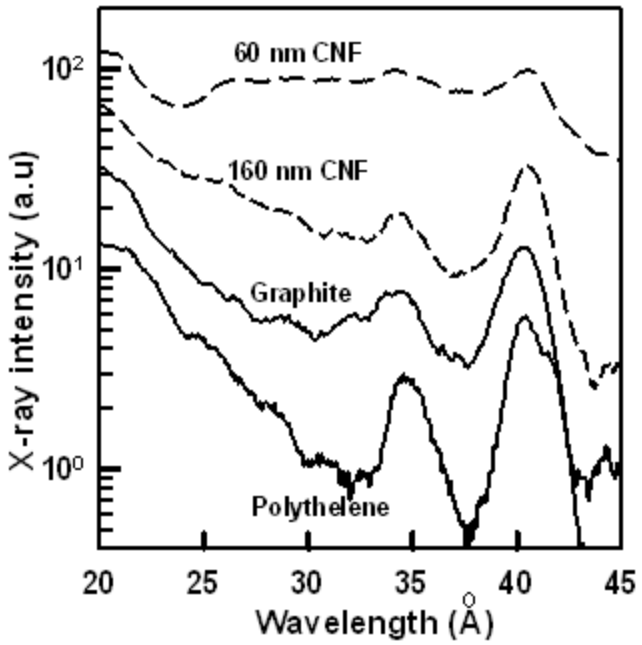

FIG.6.3: X-ray emission spectra from plasma produced from CNFs, graphite, and polyethylene targets.

The x-ray intensity is much higher for 60 nm and 160 nm CNFs compared to that for graphite and polyethylene targets. It is also observed that the CNFs with the smaller diameter are more efficient x-ray emitters in the water window. The integrated x-ray intensity over the water-window spectral region for the 60 nm CNFs was ~ 18 times higher than that with planar graphite and ~45 times higher than that of the polyethylene target. The corresponding x-ray intensity enhancement for the 160 nm CNF target was ~2.5 and 7.5 times higher, respectively.

Although the enhancement of the x-ray emission from the CNFs over the planar graphite target was recorded along the target surface only, the x-ray intensity enhancement as compared to planar target is also expected at other angles. This is because the x-ray emission from plasma produced by the irradiation of a planar target with intense short laser pulses has a more isotropic distribution [15] than that generated through the irradiation with longer pulses of ps or ns duration. Since locally the carbon nano-fibers are at solid density, the x-ray emission from them is likely to show a behavior similar to that known from solids. In ref.13, the x-ray emission from

carbon nano-tubes in the water window was studied under similar experimental conditions like us. They recorded the x-ray emission at 45^o with respect to the target normal (instead of 90^o in the present work). A higher x-ray emission from carbon nano-tubes as compared to planar carbon was observed by them in that direction. Therefore, it appears that x-ray enhancement will occur in other directions as well. We have measured the x-ray emission along the target surface since the plasma debris from the laser-irradiated target is minimal in this direction. Therefore, the x-ray enhancement in that direction is more important and desirable for applications (like microscopy, lithography etc).

6.2.2 X-ray yield study with intensity and pulse duration.

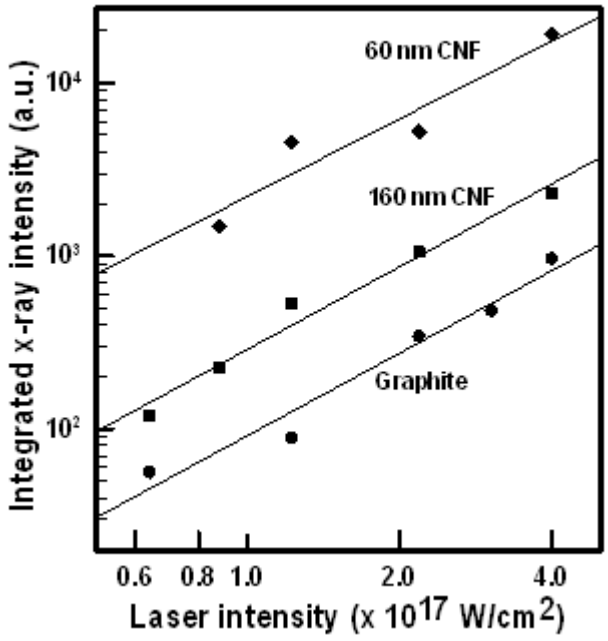

FIG.6.4 : Dependence of the integrated x-ray intensity from CNFs and graphite target plasma on laser intensity (45 fs pulse duration).

Figure 6.4 shows the dependence of the integrated x-ray yield (in the 23-44 Å water window range) from graphite and CNF targets on the laser intensity I_L. The x-ray yield increases as $I_L^{\sim 1.3-}$

$^{1.4}$ for the two CNFs and the graphite as well. Fig. 6.4 also reveals that the enhancement factor for the CNF targets does not vary much with I_L. The emission from the 60 nm CNF target was highest in the entire range of laser intensities used in the experiment

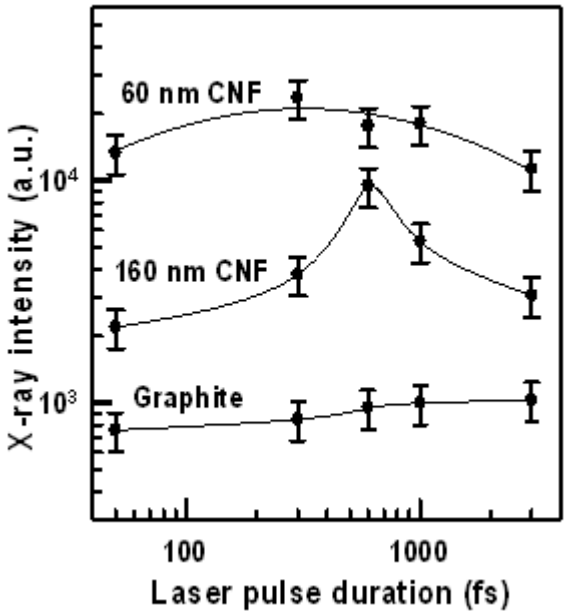

FIG.6.5 : Integrated x-ray intensity from plasma produced from CNFs and graphite targets as a function of laser pulse duration, at a constant laser fluence of 2 x10^4 J/cm^2.

Figure 6.5 shows the dependence of the integrated x-ray yield in the water-window spectral region on the laser pulse duration, at a constant fluence of 2 x10^4 J/cm^2 for the graphite and the 60 nm and 160 nm diameter CNFs as well. While the x-ray intensity from the graphite target shows a small monotonic increase with the laser pulse duration, the 60 nm and 160 nm diameter CNFs exhibit a peak. The emission from the 60 nm CNF target is highest in the entire range of laser pulse duration used in the experiment. The x-ray yield for the 60 nm diameter CNF is maximal at 300 fs and thereafter gradually decreases till 3 ps. For 160 nm CNFs, the peak behavior is more pronounced, a distinct peak occurs at the laser pulse duration of 700 fs.

The x-ray intensity enhancement factor for the two CNFs of different diameters with respect to the graphite target, as a function of the laser pulse duration, is shown in Fig. 6.6. The enhancement factor increases from 18 to 27 when the laser pulse duration is changed from 45 to 300 fs. For larger pulse durations, the enhancement factor decreases gradually. However, even for irradiation of the 60 nm CNFs with 3 ps laser pulses, there is a considerable enhancement factor of ~10. In the case of the 160 nm CNFs, a similar behavior is observed, where the enhancement first gradually increases, peaks at 700 fs (peak value ~ 10), and then smoothly declines when the laser pulse duration increases.

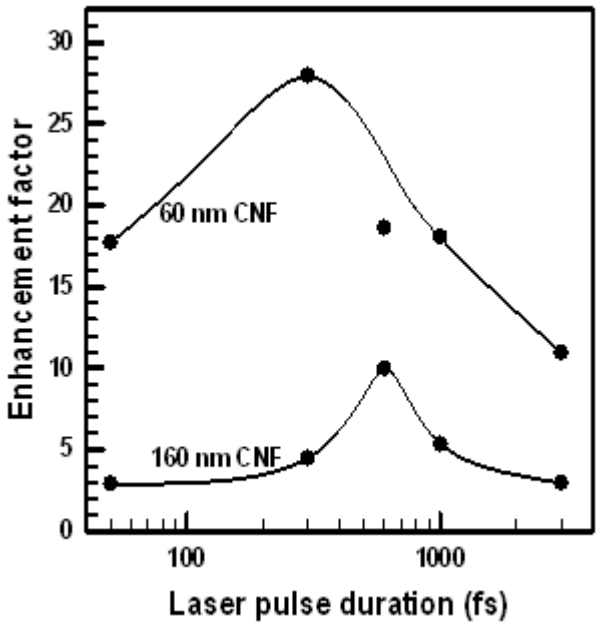

FIG.6.6 : Enhancement of water-window x-ray yield from CNFs w.r.to graphite target as a function of laser pulse duration, at a constant fluence of $2x10^4$ *J/cm*^{2}.

It is important to mention here that for applications like contact microscopy of biological specimen, the x-ray pulse duration should be sub-ns, so that image blurring due to hydrodynamic motion is negligible. Since we did not measure the x-ray pulse duration of the emission from graphite and CNFs, we refer in this context to the work of Nishikawa *et al.* [13] who measured

the pulse duration of the x-rays (in the water window region) from laser-irradiated carbon nano-tubes using a streak camera with 3 ps time resolution. The x-ray pulse durations for planar solid carbon and carbon nano-tubes were 8 and 26 ps, respectively. Thus, even though the x-ray pulse duration from the CNFs is likely to be larger than the laser pulse duration, the CNF-based source is still attractive for many applications.

6.3 Application of the nano-plasma model for x-ray enhancement

The x-ray intensity enhancement observed for CNF targets is basically due to higher laser energy absorption in the CNF plasma compared to that occurring in plasma from planar solid targets. The absorption of a high-intensity ($I\lambda^2 > 10^{17}$ W/cm^2) p-polarized laser pulse obliquely incident on a planar solid surface is mostly by resonance absorption, vacuum heating, and $\vec{J} X \vec{B}$ heating, whereas at lower laser intensities ($I\lambda^2 < 10^{17}$ W/cm^2), inverse bremsstrahlung absorption is more dominant [52]. A major difference in the absorption by a bulk target and a nano-size target (like gas clusters or CNF) is that the laser field gets strongly enhanced inside a nano-particle for certain values of the dielectric constant and this forms the basis of the nano-plasma model [96-98]. We have applied this model to explain our results since the model successfully explains various experimental results with clusters concerning laser energy absorption [88,96-99], x-ray emission [101], electron emission [75] and ion emission [95].

The nano-plasma model considers the irradiation of a cluster by an intense short pulse laser which results in the initial ionization of the cluster by the optical field. The free electrons thus produced oscillate under the laser electric field and collide with the surrounding ions (at near solid density) and transfer their energy collisionally to the ions. This raises the temperature of the nano-plasma cluster ball which subsequently expands due to a combined Coulomb and

hydrodynamic pressure. Although such a simple model successfully explains the numerous experimental observations, the notion of hydrodynamic expansion of a cluster on 100 fs time scale is debatable, as the typical time scale for energy transfer from electron to ion is few ps. Hence, the efficient absorption of ultra-short laser pulse (< 100 fs) by clusters has been attributed to the non-collisional process [105-107]. Nevertheless, as the laser irradiated clusters have locally solid density and are highly ionized, the plasma is highly collisional [96]. Invoking this aspect, the nano-plasma model justifies efficient absorption even for ultra-short pulses ~ 100 fs where the hydrodynamic motion may be negligible. Several authors have carried out numerical simulations on the clusters hydrodynamic expansion in the nano-plasma[96,102,189]. The simulations show the time evolution of the electric field, the plasma temperature, and the hydrodynamic pressure inside the cluster, which causes cluster expansion and density dilution. Subsequently the electron density starts approaching $3n_c$ near the peak of the laser pulse [94-99,189]. Therefore, although the cluster does not expand sufficiently to arrive at the resonance condition at the peak of laser pulse, still high electric field, temperature and pressure are attained. The simulations further show that the cluster electrons density eventually becomes $3n_c$ on a time scale of few 100 fs away from the peak of the ultra-short laser pulse (~ 100 fs) [94-99]. This implies that there is further scope for even higher absorption if the laser pulse is stretched to be > 100 fs, so that the cluster density passes through $3n_c$ at the peak of the pulse [97]. It has been experimentally verified that stretched pulses lead to the best x-ray output because for a cluster of given size there exists an optimum pulse duration for maximum absorption which may vary from ~ 100 fs to ~ 1 ps [97,101].

In the present context, the nano-fiber target used in our experiments has a resemblance with the generally used spherical metal and gas clusters, and the major difference is that it has a

cylindrical shape due to which they show resonance at $2n_c$ [190] instead of $3n_c$. The CNFs are like cylindrical nano-particles (nano-rod) and to study their interaction with intense laser pulses it can be considered as a cylindrical dielectric placed in the laser field, in a treatment similar to clusters. The experimental observations can be explained by extending the nano-plasma model from a spherical to a cylindrical geometry.

When an external electric field E_0 is applied perpendicular to the axis of a cylindrical nano-particle (having a very large length in comparison to its diameter), the inside field E_{in} is given by the relation [190]

$$E_{in} = \frac{2}{\varepsilon + 1} E_0 \quad . \qquad \text{....6.1}$$

The inside field becomes very large when the dielectric constant ε approaches -1. For heated nano-fiber plasma, ε shows a transient behavior because the rapid heating is followed by a density reduction due to hydrodynamic expansion. For plasma the dependence of ε on density has the form

$$\varepsilon = 1 - n_e/n_c \qquad \text{....6.2}$$

where n_e is the electron density and n_c is the critical density. It follows from Eqns.6.1 and 6.2 that the inside field becomes very large in the vicinity of $n_e = 2n_c$. However, when the applied field is parallel to the axis of a nano-cylinder, due to the long extent of the cylinder (compared to the laser wavelength), there will be no field enhancement. An electric field applied to an unaligned CNF will have field components perpendicular and parallel to the fibre axis. When the plasma density approaches $2n_c$, there will be a large enhancement of the radial component of the electric field, leading to strong inverse bremsstrahlung absorption of the laser light. The time τ_R taken for reaching this condition depends on the initial radius r_o, the initial density n_o, and the

expansion speed c_s. The expression for τ_R of CNFs is similar to that for clusters [97] and is given by

$$\tau_R = (r_0/c_s)\left(\sqrt{\frac{n_0}{2n_c}} - 1 \right) . \qquad \text{....6.3}$$

As seen from Eq.6.3, the resonance condition for larger diameter nano-fibers is attained later in time, in comparison to the smaller diameter nano-fibers. Since the diameters of the CNFs vary in a given target sample and the hydrodynamic expansion may also be non-uniform, and hence the resonance condition is expected to occur over a period of time. It may also be noted that for spherical nano-plasma, due to 3-D expansion, the resonance condition is reached earlier in time than for cylindrical nano-plasma which undergoes 2-D expansion.

Despite the fact that the irradiation of the nano-fibers with ultra-short duration pulses (~45 fs) will not cause expansion sufficient enough to reach the resonance condition, a significant absorption of the ultra-short pulses is still observed in nano-particles. This has been explained by various models which consider the collective electron dynamics and nonlinear resonances [104-107]. Moreover, due to the collisions present within a cluster, the resonance gets broadened over a larger range of densities and pulse duration [96]. In addition to this, the collision frequency of large sized cluster is known to be inversely related to its size [191]. This explains the observed higher x-ray enhancement in the case of the smaller diameter nano-fibers (60 nm) as compared to the larger 160 nm fibers because of the higher collisionality in the former. Hence, even for the smallest pulse duration, the x-ray yield is not negligible compared to the peak value at some higher pulse duration. Moreover, the 60 nm CNF absorbs more laser energy than the 160 nm CNF, as the density of the former approaches $2n_c$ earlier in time [148,

166,167] as the rate of decrease of electron density with the instantaneous radius (r) is inversely proportional to the cube of r i.e. $dn/dr \propto 1/r^3$ (*as for cylindrical nano-fibers* $n \propto 1/r^2$).

On the basis of the above physical picture, one can explain the results shown in Figs. 6.3-6.6. As stated earlier, the resonance field enhancement in nano-fiber plasma in the vicinity of $2n_c$ will result in strong absorption of laser energy to increase the nano-plasma temperature. This is responsible for the large enhancement factor in the x-ray yield for CNF plasma as compared to the carbon-containing planar solid targets. First, we discuss the dependence of the integrated x-ray yield on laser intensity for CNF and graphite targets. All three targets showed almost the same scaling $I_L^{\sim 1.3\text{-}1.4}$. The spaghetti-like structure of the nano-fibers (Fig.6.1) has nano-meter sized spaces (voids). Due to these voids, the incident laser light gets multiply reflected from one fiber to another and thus gets better absorbed (by being trapped in the voids). This would also enhance the x-ray emission compared to a planar target. The SEM image of the graphite target (Fig.6.1c) clearly shows nano-sized pits on its surface, which, due to multiple reflections, may lead to a better absorption of laser energy. This is also consistent with the observation of a much smaller x-ray yield from the polyethylene target which had no porosity.

6.4 Resonance in nano-fibers

Now we come to the variation of the x-ray yield with the laser pulse duration. As observed from Fig.6.5, the x-ray yield for CNF targets first increases with laser pulse duration, reaches a peak at a certain value and then decreases. As the laser pulse duration is increased, plasma of a longer scale length is produced, leading to an increase in the collisional absorption. Secondly, the increase in x-ray emission can also be due to a larger volume of the expanded

plasma and longer emission time. Also, there is a slower decrease of the electron temperature with time due to larger density scale length. Thus the plasma emission time is also longer, which can explain the increase in x-ray yield [184] with increase in laser pulse duration. However, as the laser pulse duration is further increased, the resonance condition would progressively occur in the initial part of the laser pulse. Due to the continued plasma expansion during the remaining laser pulse, the laser energy absorption would occur at lower plasma density (away from $2n_c$). This would result in less effective heating of the plasma and thereby providing a lower x-ray yield.

The above qualitative picture is also consistent with the observation of different values of laser pulse duration for peak enhancement for the two different diameters of CNFs used (Fig. 6.6). As the smaller diameter nano-fibers (60 nm) will reach resonance earlier than the larger ones (160 nm), the x-ray yield in the former case peaks at a smaller pulse duration of ~300 fs while the latter showed a maximum at a laser pulse duration of ~700 fs (since τ_R is proportional to r_0 as seen from Eq. 6.3).

To substantiate the time scales for the resonance (τ_R), we estimate the expected τ_R for the nano-fibers taking the typical laser parameters, plasma temperature and density and the targets geometrical parameter r_0. To estimate τ_R, we first estimate the plasma expansion speed $c_s = \sqrt{\frac{ZkT_e}{M_i}}$ where M_i is the ion mass. Since c_s is temperature dependent, we take temperature value from the work of Issac *et al* [192] who have done experiments using very similar laser parameters, with the shortest pulse duration of 60 fs and worked at a fluence of 8 kJ/cm^2, which in our experiments was 20 kJ/cm^2. They have estimated the electron temperature at various pulse durations from 60 fs to 2.2 ps which is again very similar to pulse duration range covered in our

experiments, while keeping the fluence unchanged. Their electron temperature varied from ~1.5 keV to 2 keV. In this temperature range c_s varies from 2.7-3.2 x10^7 cm/s. The value of n_0/n_c for carbon nano-fiber irradiated with Ti:sapphire laser at 800 nm is taken to be 40. The time for occurrence of resonance τ_R can be found using Eq.6.3. For a 60 nm fiber, the resonance would occur at 320-380 fs (considering the range of speed of expansion). Similarly, the resonance is expected to occur between 850 fs- 1ps for the 160 nm fiber. The observed resonance for smaller diameter nano-fibers (60 nm) ~300 fs and the observed peak for larger diameter nano-fibers (160 nm) ~700 are in close agreement with the predicted values and hence substantiate the claim of resonance absorption occurring in the nano-fibers.

Void closure may also be a factor in governing laser energy absorption in the nano-fiber targets. For the 60 nm CNFs, the void closure can occur over a 1-2 ps time scale. This is because, considering the intra-fiber distance to be 300-500 nm and the plasma of ~1.5-2 keV temperature expanding at the rate of ~2-3x 10^7 cm/s will take about a picosecond time for void closure, which is also similar to the time scales reported by Gibbon *et al* [193]. Thus, in the case of the smaller diameter fibers, the void closure will occur after the resonance is reached. However, for the 160 nm CNFs, the average intra-fiber spacing is of smaller magnitude compared to that for the 60 nm diameter nano-fibers. In this case, there is a possibility that void closure may occur on a sub-ps time scale, even before reaching resonance. Thus, smaller laser energy absorption may occur for the larger diameter (160 nm) CNFs in comparison to the 60 nm diameter CNFs.

Lastly, we consider the effect of pre-pulse associated with the laser pulse which can damage the nano-structure prior to the arrival of the main pulse. The pre-pulse can form a pre-plasma making the geometrical shape of the nano-structure not effective. In addition to this, the

field enhancement occurring in the nano-fiber will make the effective intensity of the pre-pulse interacting with the nano-fiber further higher. However, we believe that the pre-pulse did not contribute in the present experiment due to the following reasons. The contrast ratio of the pre-pulse before 8 ns (replica contrast) was better than 10^{-6} and the contrast ratio of ns-pedestal due to amplified spontaneous emission (ASE contrast) was also about 10^{-6}. Therefore, the pre-pulse intensity is less than $4x10^{11}$ W/cm^2. As for the replica pre-pulse (the one 8 ns before the main pulse), its duration being short (same as that of the main pulse), it has a large threshold to produce plasma. Rajeev *et al* [194] have experimentally measured the plasma formation threshold intensity for solid copper and copper nano-particles containing target using 100 fs laser pulses. The threshold intensity for plasma formation was found to be about 10^{14} W/cm^2 for both the targets. Since the highest intensity of the pre-pulse in our experiments ($4x10^{11}$W/cm^2) is much smaller than the value of plasma formation threshold by more than two orders of magnitude, one can assume that even the effect of field enhancement facilitated by the nano-fiber will not lead to any pre-plasma formation due to the replica pre-pulse. This argument is strengthened by the observation of Dorchies *et al* [101] who conclude that the pre-pulse contrast should be better than 2 $x10^{-6}$ so as to prevent the cluster from any modification prior to the arrival of main pulse. As for the ASE foot, the focused intensity is much smaller due to its larger divergence to cause any significant heating. Moreover, the ASE intensity does not vary with change of laser pulse duration, and hence had ASE been the dominant factor, one would not see any variation with the laser pulse duration observed in the experiment (Fig. 6.5).

Thus, we have demonstrated that CNFs irradiated with ultra-short laser pulses show more than one order of magnitude enhancement in x-ray yield in the water-window x-ray emission from for 60 nm diameter CNF compared to graphite and polyethylene targets. The higher x-ray

yield, the scaling of the x-ray yield with laser intensity, and the dependence of the x-ray yield enhancement on laser pulse duration are explained by higher absorption due to the occurrence of resonance field enhancement at two times the critical density in nano-fiber plasma during its hydrodynamic evolution. The results may be helpful in determining the optimum parameters of nano-fiber targets and laser pulses to achieve high x-ray yield in the water-window spectral region for x-ray microscopy.

Chapter 7

Enhancement of x-ray emission from nano-hole alumina.

As elaborated in the previous chapters, the inefficient deposition of the laser energy in solids can be improved by using nano-structure targets. The nano-structures offer a high absorption due to several reasons : 1) average mass density of a surface with nano-structure is lesser than a solid, implying a greater energy deposition depth ("Light trapping") [70] 2) greater surface to volume ratio also leads to enhanced interaction volume [71], 3) the protrusions of some nano-structures like, nano-wire, or metal nano-particles lead to efficient resonance absorption, because of the curvature of the structure, due to which the optimum angle for resonance absorption may be met locally [47]. Efficient absorption in nano-structured surface can also be achieved through excitation of surface plasma waves which are absent in planar solids [195]. Moreover, the electric field enhancement ("Lightning rod effect") [87] and linear [96-98] and nonlinear resonances [105-107] in nano-particles make them competitive as an efficient electron, ions and x-ray source [69-91]. They can be easily characterized by microscopic techniques, which gives them an edge over gas clusters whose characterization is difficult and indirect [92].

One can say that a nano-structured target should have the following characteristics for practical usability : i) it should be easy to produce in bulk quantity, ii) it should have a highly regular nano-structure, and iii) it should be cost effective. Nano-structured target like nano-hole alumina is a very promising laser-plasma x-ray source because of all the above mentioned characteristics present in it [196]. It consists of arrays of nano-holes which are perpendicular to the target surface. The target is easy to make with a large area, with a narrow hole size

distribution, by anodic oxidation of an aluminum plate. This target is also very useful to study the dynamics of ultra-short intense laser pulses with nano-structured targets owing to its regular arrangements of nano-holes.

The interaction of intense light with holes of few tens of nano-meters is also interesting for studying the electric field generated inside them after irradiation. Since, the nano-structured targets exhibit shape and size dependent field enhancement, which is evident from the hard x-ray emission from these targets, therefore nano-holes are also worth pursuing for study as target for the possibility of high fields in them. Nano-hole is a different type of structure. It is interesting to study the electric field inside the nano-holes, its hydrodynamic evolution, and its effect on x-ray emission. Although, nano-hole targets have been studied in the past for soft x-ray generation and the soft x-ray yield dependence on the nano-hole diameter [80,197], there is no study, on the hard x-ray emission and its dependence on laser pulse duration. Moreover, a clear understanding of the mechanism of x-ray enhancement in nano-holes is lacking.

In this chapter, we describe a comparative study of the laser energy absorption, soft x-ray emission (in the water window region : 2.3-4.4 nm), and hard x-ray emission (2-20 keV range) from planar aluminum and nano-hole alumina of various average diameters, when irradiated by Ti:sapphire laser pulses. The x-ray yield from the nano-holes was enhanced clearly showing an increased coupling of the laser energy to the target. The laser pulse duration was varied from 45 fs to 500 fs, and the focused intensity on the target ranged from ~3×10^{16} W/cm^2 to 3×10^{17} W/cm^2. The x-ray yield enhancement from the nano-holes shows an increased coupling of the laser energy to the target. The effect of laser pulse duration on the x-ray emission was also studied, where a resonance like phenomenon was observed. The laser energy absorption measurements in the nano-holes showed a marginal enhancement in absorption as compared to

planar Al. The integrated keV x-ray yield, from nano-hole alumina and planar Al, at an intensity of 3×10^{17} W/cm^2, was 25 μJ and 3.5 μJ respectively. The results can be explained by considering the hydrodynamic expansion of the laser irradiated structure and field enhancement in the nano-holes.

7.1 Description of the experiment

7.1.1 Experimental setup

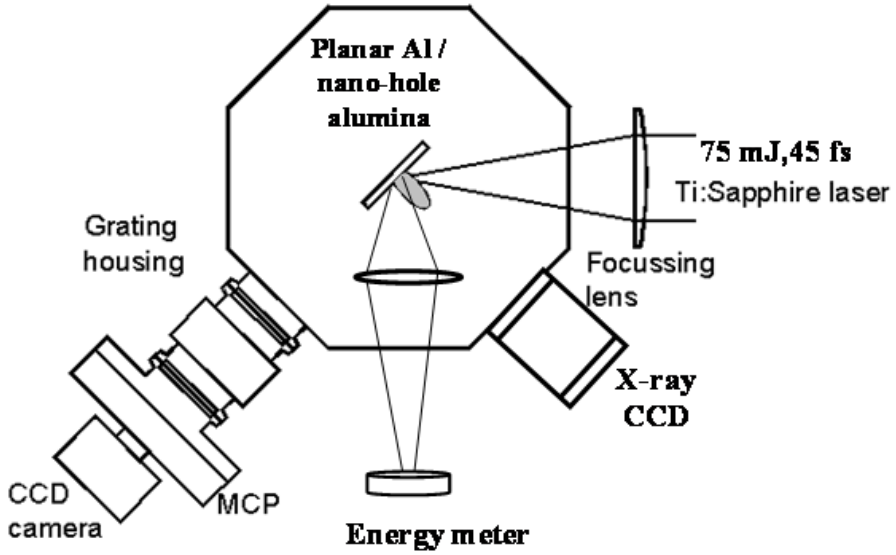

Fig.7.1: Experimental setup for absorption and x-ray measurements

The experimental setup for the study of absorption and x-ray emission from planar Al and nano-hole alumina, is shown in the Fig.7.1. Ti:sapphire laser pulses, with 75 mJ energy and 45 fs pulse duration, were focused on the target to a spot of 20 μm diameter, using a convex lens having a focal length of 500 mm. The p-polarized laser beam, with nanosecond intensity contrast ~ 10^6, was incident on the target at an angle of 45^o with respect to the target normal. The intensity on the target surface was upto ~3×10^{17} W/cm^2. The laser energy absorption was studied

from the measurement of the reflected and scattered laser light energy as a percentage of the incident laser light energy. A convex lens was used to collect the reflected light onto an energy meter. The collection solid angle of the lens was kept large enough to ensure that any reflected light from the plasma was collected by the lens. Another convex lens (not shown in Fig.7.1), also kept at 45^0 to the laser beam axis, and was used to collect the side-scattered light, which was monitored using a sensitive calorimeter having sensitivity of 164 V/J. The scattering percentage was estimated by assuming isotropic scattering. The pulse duration was varied from 45 fs to 500 fs, by changing the grating pair separation, for studying its effect on the x-ray emission and absorption.

7.1.2 X-ray diagnostics

To estimate the x-ray yield in plasma produced by the planar and nano-structured targets, three diagnostics were used : 1) Transmission grating spectrograph (TGS), 2) Dispersion-less spectrograph (as shown in Fig 7.1) and 3) X-ray p-i-n diodes (not shown in Fig.7.1). These diagnostics were set up to measure the x-ray signal simultaneously from different ports of the diagnostics chamber along with the absorption measurements. In this setup, the TGS was mounted along the target surface. It was used for the measurement of the x-ray yield in the soft x-ray region, particularly in the water-window region (23Å - 44Å). The x-ray emission spectrum was recorded using an MCP with CCD camera-PC based on-line measurement system. To maintain the MCP at proper vacuum, an additional vacuum system was used.

An x-ray p-i-n diode (Quantrad) was used with a 75 μm Be filter to estimate the x-ray energy yield above 2 keV. It was kept in the plane containing the target normal and laser beam axis. A permanent magnet of 0.15 tesla field was also kept in front of the x-ray diode to prevent

the hot electrons, emitted normal to the target, from colliding with the filter foils of the p-i-n diode and generating x-rays, which can be misinterpreted as x-ray signal from the target.

The spectrum in the 2-20 keV region was recorded in single shot mode using the dispersion-less spectrograph. The spectrograph was mounted on the 22.5^0 port, below the x-ray p-i-n detectors, as shown in Fig.7.1 (p-i-n diodes not shown for clarity). The x-ray CCD camera of the dispersion-less spectrograph had $4x10^6$ pixels. A 25 μm thick Ni foil (cut-off at 7.9 keV) was put before the CCD for cutting off the low energy x-rays. Another magnet of 0.085 tesla field was kept in front of the x-ray CCD camera. This field was sufficient to deflect even the most energetic hot electrons, to avoid the x-ray contribution from the hot electrons striking the filter foil in front of the CCD camera.

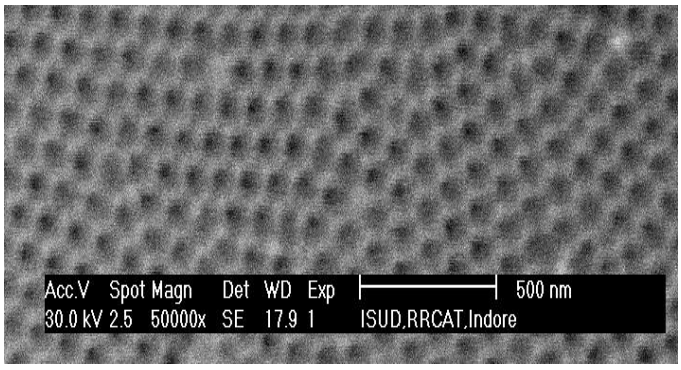

Fig.7.2 : SEM image of nano-hole alumina showing hole size of ~ 40 nm.

Figure 7.2 shows the SEM micrograph of nano-hole alumina. It shows that the nano-holes have a uniform size distribution of average diameter 40 nm.

7.2 Experimental Results

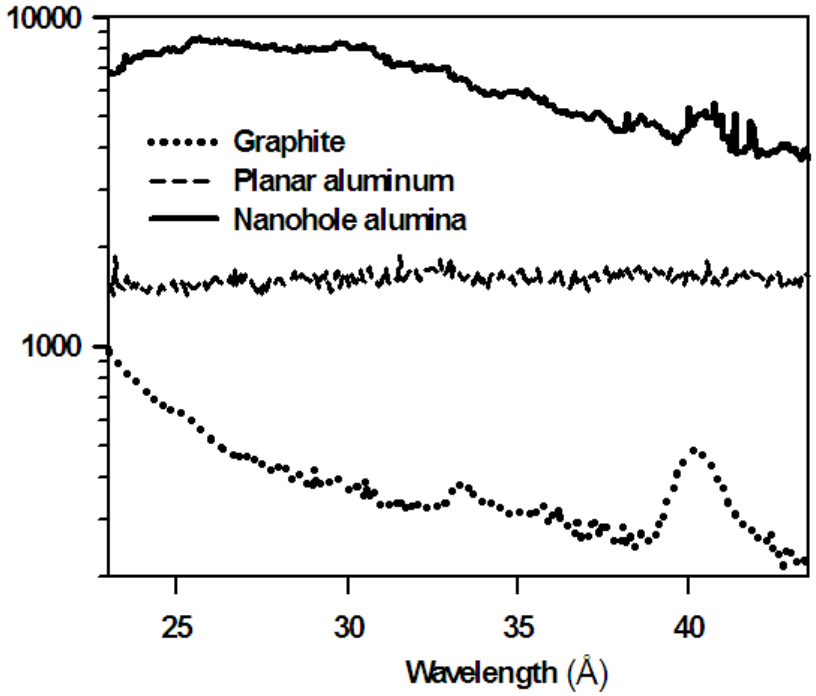

Fig.7.3: X-ray spectra of carbon, planar aluminum, and nano-hole alumina, in the water window region.

The soft x-ray emission spectrum was recorded using the TGS, from targets irradiated by Ti:sapphire laser beam at an intensity of ~3×10^{17} W/cm^2. Figure 7.3 shows the x-ray spectra obtained from carbon, aluminum and nano-hole alumina. The carbon spectrum shows two peaks corresponding to He-α and Ly-α at wavelength λ = 40.7 Å and 33.7 Å. These intense lines were used as reference for the x-ray emission spectra of Al and nano-hole alumina targets. Fig.7.3 also shows that in the soft x-ray region, the x-ray yield is ~4 times higher for nano-hole alumina compared to that for planar aluminum target. Due to the poor resolution of this spectrograph, Al lines from the targets were not seen. A nano-hole target offers a larger surface area that interacts with the fs-laser pulses leading to whole volume heating of the material by the laser. This observation is similar to that of Nishikawa *et al* [80,197] showing nano-hole alumina as a good soft x-ray source.

Figure 7.4 shows the x-ray spectra recorded using the x-ray CCD working as a spectrograph in the single photon counting regime (i.e. as a dispersion-less spectrograph). It clearly shows a high enhancement in the 1-10 keV range. Beyond 10 keV, the increase was not significant. The value of the enhancement varied between 6 to 8 in the above spectral range. More error is likely in the higher energy range than in lower energy range due to poor signal to noise ratio.

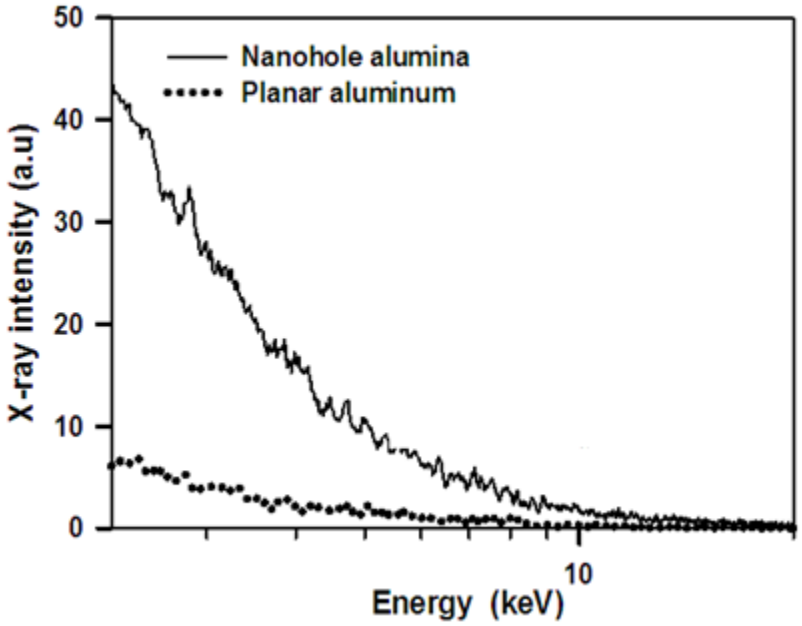

Fig.7.4 X-ray spectra for planar aluminum (lower) and nano-hole alumina (upper)

7.2.1 Effect of pulse duration

Figure 7.5 shows the pulse duration dependence of integrated yield of x-ray emission in the energy range of 2.2 keV to 20 keV region, recorded using the dispersion less spectrograph. Planar Al and nano-hole alumina targets were irradiated by laser pulses with variable pulse duration, at a fixed fluence of $\sim 10^4$ J/cm^2. The pulse duration was varied by changing the grating pair separation in the laser pulse compressor.

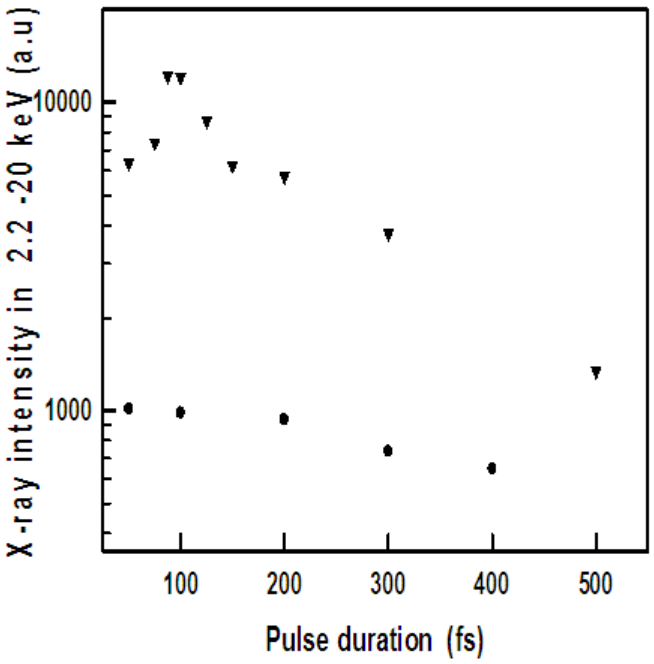

Fig.7.5: X-ray intensity vs. pulse duration for planar aluminum (circles) and nano-hole alumina (inverted triangles)

It was observed that for the planar aluminum, the x-ray yield (denoted by circles) decreased monotonically with increasing the pulse duration, but for the case of nano-hole alumina, the x-ray yield (denoted by inverted triangles) increased with pulse duration, reaching a maximum at ~100 fs, and then decreased with increasing pulse duration. The enhancement of the x-ray yield in the above mentioned range for the shortest pulse duration (45 fs) was 7 times. The maximum x-ray yield (at 100 fs) was 12 times higher than that for planar Al target, followed by a gradual decrease at higher pulse duration. At an intensity of 3×10^{17} W/cm^2 for 45 fs pulses, the integrated x-ray yield above 2 keV from planar Al was 3.5 μJ and that from nano-hole alumina was 25 μJ measured using the p-i-n diode. The x-ray yield from nano-hole target was somewhat higher than the x-ray yield reported using Al coated grating target, where 20 μJ yield was achieved under similar conditions [161]. On stretching the pulse to 100 fs, the intensity was

~1.5×10^{17} W/cm^2, and the x-ray yield above 2 keV from nano-hole alumina was 43 μJ, whereas from planar Al it was 3.2 μJ.

7.2.2 Absorption studies

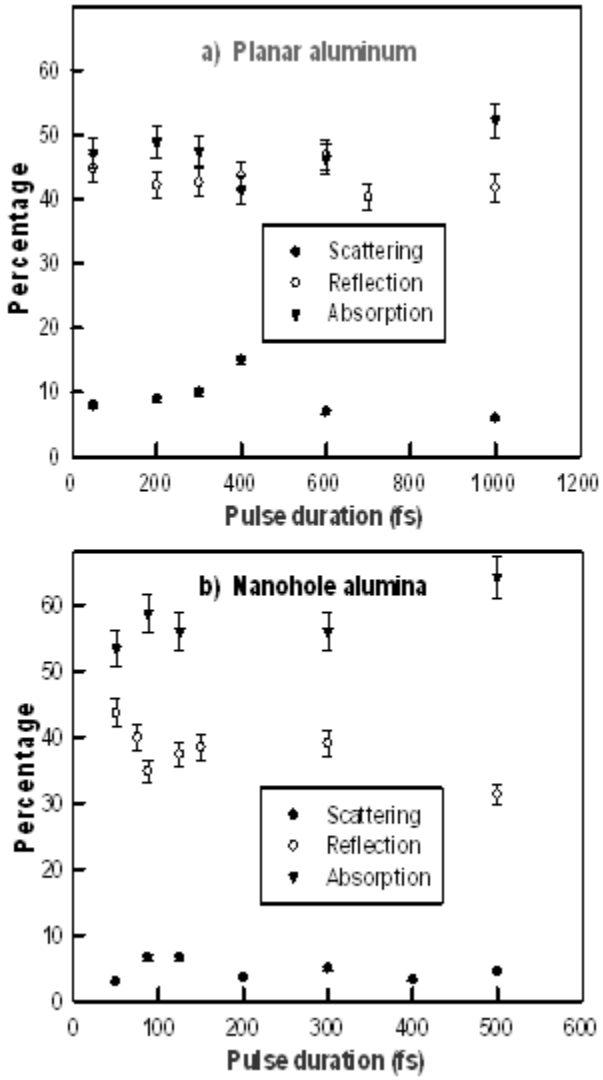

Fig. 7.6: Percentage of absorption, reflectivity and scattering vs. pulse duration, for : a) planar aluminum, and b) nano-hole alumina

The laser energy absorption in both the targets was also studied and estimated by monitoring the specularly reflected light along with the scattering measurement at 45^o angle of incidence. Figures 7.6a and 7.6b show the variation of the percentage of absorption, reflectivity, and scattering, as a function of the pulse duration, for planar Al and nano-hole alumina targets,

respectively. The absorption measurements were made simultaneously with the x-ray measurements at a fixed fluence of ~10^4 J/cm^2. The data of scattering and reflectivity was averaged over 3 shots. Comparing the two graphs, one can see a nominal increase of absorption in nano-hole targets compared to the planar Al. Quantitatively, for the nano-hole alumina, the absorption was about 10-15 % higher in comparison to that in planar Al. It is also observed that, for the nano-hole alumina target, scattering is less than that for planar Al, perhaps due to light trapping in the holes. Planar Al had absorption between 38 to 53%, whereas for nano-hole alumina, it was between 52 to 69%.

7.3 Analysis of the results

To investigate the reason for a large enhancement in the x-ray yield despite just a marginal increase in the absorption, the electric field inside these nano-holes was calculated. The details of the calculation are given below and the results of the calculations of electric field for nano-holes and nano-wires are shown in Fig.7.7. It shows that the field inside a nano-cylindrical hole can be very high (i.e. holes inside a dielectric medium can be very effective for field enhancement). The calculation is done for the electric field inside a solid nano-cylinder (nano-wire or nano-rod) and compared with a cylindrical hole in a dielectric (nano-hole), to study the interaction of these targets with intense short pulses. Although we have not done experiments with aluminum based nano-wires, for the sake of completeness, the case of solid nano-wire is also discussed along with other targets. It may be noted that in some other experiment on studying x-ray emission (not reported here) from planar zinc and zinc oxide nano-wires, the hard x-ray enhancement was only moderate (2-3 times), although a very high absorption of 90% was recorded in the ZnO nano-wire target. The strikingly less efficient x-ray generation from nano-

wire in comparison to a nano-hole structure brings out the importance of spatial feature of nano-structure for field enhancement in them.

For the case of a nano-cylinder, when the laser light having electric field E_0 is incident on it, two cases arise :

In the first case**,** when the applied electric field is *parallel* to the cylindrical axis, the electric field inside the cylinder is given by $E_{in} = E_0$ [190]. This is because the length of the cylinder in this direction is much longer than the light wavelength, and there is no enhancement of the field.

In the second case, when the electric field is *perpendicular* to cylindrical axis, the electric field magnitude inside the cylinder is given by the relation [190]

$$E_{in} = \frac{2}{\varepsilon + 1} E_0 \qquad \text{.....(7.1)}$$

where the dielectric constant of plasma is given by

$$\varepsilon = 1 - \frac{n_e}{n_c(1 + i\nu/\omega)} \qquad \text{.....(7.2)}$$

where n_c is the critical density corresponding to the laser wavelength (ν/ω is the ratio of collision frequency and the laser frequency). Equation 7.1 gives enhancement in the field inside the nano-cylinder at a density $n_e = 2n_c$, after ignoring the collision term [190]. This is similar to the enhancement observed at $3n_c$ in gas clusters ($E_{in} = \frac{3}{\varepsilon + 2} E_0$ in spherical geometry) and n_c in planar solid ($E_{in} = \frac{1}{\varepsilon} E_0$ in slab geometry) [190].

In general, for the laser electric field applied at some angle with the cylinder axis, the electric field will have two component, one along the cylindrical axis and the other perpendicular

to it. This perpendicular component is the one which gives the enhancement in electric field inside cylinder as per Eq. 7.1.

For the case of a nano-hole of radius "*a*" inside a dielectric medium, the expression for electric field inside the hole can be easily calculated by replacing ε by 1/ε in Eq. 7.1 (similar to the treatment for uniform density nano-plasma model for the case of nano-sphere for spherical cavity in a dielectric). Therefore, the magnitude of the field inside the nano-hole can be found by replacing ε by 1/ε in equation 7.1 as [198]

$$E_{in} = \frac{2\varepsilon}{\varepsilon+1} E_0 \qquad \text{…..(7.3)}$$

As seen from this equation, the magnitude of the internal field is independent of *r* and θ, and the direction is along the applied field. However, the electric field outside the hole, i.e. at $r > a$, has a radial field component ($E_{r\,out}$) given by

$$E_{r\,out} = \left(\frac{a^2}{r^2} \frac{1-\varepsilon}{\varepsilon+1} + 1 \right) E_0 \cos\theta \qquad \text{.....(7.4)}$$

and an azimuthal component ($E_{\theta\,\mathrm{out}}$) given by

$$E_{\theta\,out} = \left(\frac{a^2}{r^2} \frac{1-\varepsilon}{\varepsilon+1} - 1 \right) E_0 \sin\theta . \qquad \text{.....(7.5)}$$

The magnitude of this external field ($E_{\,out}$) is given by $\sqrt{E_r^{\,2} + E_\theta^{\,2}}$ and it is a function of both *r* and θ. The electric field value just at the hole-boundary (i.e. at r = a) is given by

$$E_{out} = \frac{2\sqrt{\cos^2\theta + \varepsilon^2 \sin^2\theta}}{1+\varepsilon} \mathrm{E}_0 \quad . \qquad \text{.....(7.6)}$$

The spatial average of the electric field magnitude taken over 2π is given by the expression

$$E_{rms\ \ out} = \quad \frac{2\sqrt{1+\varepsilon^2}}{1+\varepsilon} \frac{\mathrm{E}_0}{\sqrt{4\pi}} \qquad \text{…….(7.7)}$$

Equations 7.1, 7.3-7.7 show that resonant enhancement occurs in the field inside the nano-hole as well as outside it, at $2n_c$.

In a practical situation, when an intense ultra-short pulse irradiates a nano-wire or a nano-hole, the foot of the intense laser pulse ionizes the matter and the subsequent pulse interacts with the plasma electrons which oscillate under the applied field and collide with the ions to deposit their energy. The initial density of the electrons in both cases (nano-wire or nano-hole) will be equal to solid density, which is ~ 100 n_c in the beginning. The energy deposition leads to the enhancement of the temperature and this causes the density of the electrons in the nano-particle to evolve hydrodynamically, i.e. the nano-hole will decrease its radius (ultimately leading to void closure) and the nano-wire will increase its radius. In both the cases, the electron density will decrease because of the volume expansion. However, there is a difference in the electric field value inside the nano-wire and the nano-hole as shown in Fig.7.7a which summarizes the field enhancement factor in planar solid, solid nano-wire, outside nano-hole, and inside nano-hole (using equations 7.1, 7.3, 7.7).

The field enhancement factor mentioned here is defined as the magnitude of the ratio of the electric field inside the nano-structure to the applied laser electric field strength, that is $\left| E / E_0 \right|$. Initially the electron density is ~100 n_c which keeps decreasing with time. The maximum field enhancement take place at $2n_c$ for both the cylindrical targets (nano-wire and nano-hole), and at n_c for planar solid. When the electron density surrounding the nano-hole is high ($n_e >> 2n_c$), Fig.7.7a shows that the field inside the nano-hole is twice high as compared to the applied field. As the heated nano-holes expand, the density reduces and there is further field enhancement. When the density reduces to two times of critical density, the electric field inside the nano-hole

is resonantly enhanced compared to the applied field. The enhancement value remains above a factor of 2 till the density falls to less than 1.5 n_c.

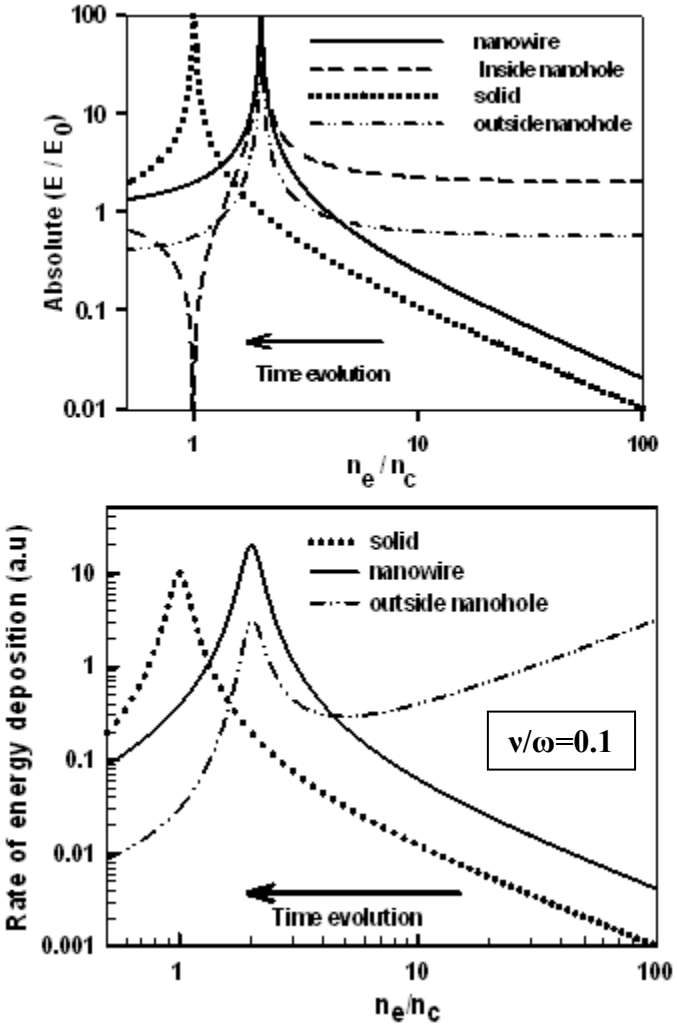

Fig. 7.7 : a) Electric field evolution with density for inside and outside nano-holes, solid nano-wires, and planar solid for comparison. b) Rate of deposition of energy in planar solid, nano-wire, and region outside the nano-hole. v/ω is taken as 0.1 for all the plots.

As explained in the next section, this field enhancement in the nano-hole exists over a very large range of densities, and results in higher x-ray emission, as seen in Figs. 7.3, 7.4, and 7.5. In comparison, the resonant field enhancement in the case of a planar target occurs only at the critical density, and therefore the x-ray emission in this case remains much below that in the

case of the nano-holes. In addition, the field outside the nano-hole is also high as compared to the planar solid and solid nano-wire for most of the range of electron density. The electric field inside a nano-structure governs the ionization and energy deposition processes in the plasma. The laser primarily deposits its energy into the free electrons through inverse bremsstrahlung. The rate of deposition of energy in the target is the heating rate ($\frac{\partial U}{\partial t}$) and it can be found by considering dielectric constant (ε) of plasma and the electric field inside the irradiated nano-structure . The energy deposited per unit volume in the plasma is given by [199]

$$\frac{\partial U}{\partial t} = \frac{1}{4\pi} E.\frac{\partial D}{\partial t} \qquad \text{……..(7.8)}$$

where E and D are the electric field and the electric displacement vector inside the plasma dielectric material, and ε is the dielectric constant of plasma given by Eq. 7.2. The heating rate time averaged over a cycle becomes [96]

$$\frac{\partial U}{\partial t} = \frac{\omega}{8\pi} \mathrm{Im}\varepsilon.\left| E^2 \right| \qquad \text{…….(7.9)}$$

The rate of heating described in equation 7.9 has a resonant phase when the electric field maximizes while the electron density passes through $2n_c$, for cylindrical geometry targets. It is important to note here that the expression of electric field 'E' inside the plasma from equations 7.1, 7.3-7.7 is dependent on the dielectric constant 'ε' which also contains the term ν/ω (which is the ratio of collision frequency and the laser frequency). The relative height and width of this resonance is dependent on the collision frequency ν. The collision frequency in turn depends on the electron density of the plasma and the temperature of the plasma as $\nu = 2.91\text{x}10^{-6}\ Z\ n_e\ T_e^{-3/2}$

ln Λ, where Z is number of free electrons per atom, n_e is the electron density in cm^{-3}, T_e is electron temperature of the plasma in eV, and lnΛ is the Coulomb logarithm. Assuming Z=5 and T_e= 1 keV and lnΛ=10, the value of ν/ω varies from 0.004 to 0.4 in the density range from n_c to $100n_c$. We assume an intermediate fixed value of the term ν/ω to be equal to 0.1 to bring out qualitatively the difference of the energy deposition rate in planar solid, nano-wire and region around nano-hole. Taking this collision frequency parameter into account, and using equations 7.1, 7.2, 7.7 and 7.9, the rate of heating, which is proportional to $\mathrm{Im}(\varepsilon)|E|^2$ [96], is shown for various targets in Fig.7.7b. It is clearly seen that the rate of energy deposition is higher in a nano-hole structure as compared to planar solid or a nano-wire as seen from Fig.7.7b. This leads to an efficient heating of the nano-hole alumina material and results in enhanced temperature of the hot plasma and hence efficient x-ray emission is observed from them.

The question that remains is how the electric field enhancement inside the nano-holes, where there are no ions to absorb the laser energy, helps in x-ray emission enhancement. As mentioned earlier, the absorption of laser energy in 40 nm nano-holes alumina was slightly higher (by 10-15%) than that in planar Al target. However, although the ions are absent in the nano-holes, the electrons oscillating in the applied electric field will still be present. For example, at an intensity of $3x10^{17}$/W/cm^2, the excursion peak amplitude of the electrons ($eE_0 / m\omega_L^2$) will be ~ 60 nm, which is of the order of the diameter of the nano-holes. With enhanced field, the excursion length is going to be even higher. This will force the electrons ejected from one side of the nano-hole penetrate into the other side of the nano-hole. These energetic electrons colliding with the ions can give rise to enhanced x-ray emission, as observed experimentally.

The increase of x-ray emission in nano-hole targets on stretching the laser pulse (as seen in Fig.7.5) is perhaps because a longer laser pulse will see higher field enhancement. Assuming that the density reduction due to expansion takes place at a certain rate, a longer pulse will reach closer to $2n_c$ before it dies out, than a shorter laser pulse. As a result, the x-ray emission will show increase with pulse duration. However, as the laser pulse duration is increased, the electric field of the laser reduces. Moreover, as the plasma expands, the nano-holes will get filled up (void closure). Once this happens, one has almost uniform density plasma all over, like in a planar target, and there is no field enhancement. As a result of both these effects, the x-ray emission will start decreasing to reach the value for a planar target, at large pulse widths. Thus, there will be a maximum at some pulse duration. Experimentally, for 40 nm nano-holes, the optimum pulse duration is observed to be about 100 fs (Fig.7.5).

Finally, it is necessary to mention here that the observed x-ray enhancement from a nano-hole target has been explained invoking basic electromagnetic theory in a very idealized geometry. In reality, the length of the cylinder (hole depth) in the direction parallel to the cylindrical axis is finite and in some cases may not be much longer than the light wavelength. For example, the SEM image of the cross-section of the nano-hole alumina target used in our experiments shows the depth of the nano-hole target was ~2 μm, which is not large enough to be considered as much larger than the light wavelength. Consequently, such a structure should be considered as a cone-shape cavity rather than a cylinder. Then, certain resonant electromagnetic modes other than the mode located in the density $n_e=2n_c$ may be excited, as evident in detailed numerical simulations available on such cavity structures. For example, Huang *et al* [200] have shown through simulations that surface-plasmon-related electromagnetic modes can be excited in the cavity nano-structures irradiated by intense ultra-short pulse laser, which would induce

strong localized field enhancement in the cavity. Excitation of these surface plasmons need free electrons which are readily available in metallic medium. When the nano-hole alumina surface is irradiated by an intense ultra-short pulse, free electrons are generated instantaneously and therefore the dielectric constant of nano-hole alumina transforms from being dielectric to metallic, and the plasmonic effect can be activated [201]. Thus for a complete understanding of the observed experimental results, such detailed simulations [200,201] would be very important. Nevertheless, the simple analytical analysis described in this paper broadly helps in understanding the x-ray enhancement from nano-hole target

7.4 Hole size effect

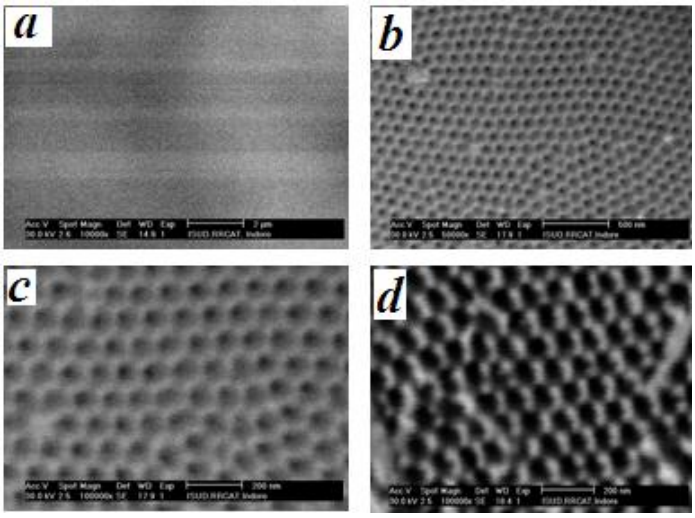

Fig.7.8 : SEM image of a) Planar aluminum, rest are nano-hole alumina showing hole size b) ~ 40 nm. b) ~60 nm, d) 90 nm.

We also studied the hard x-ray emission (in the 2-20 keV range) from planar aluminium and nano-hole alumina of various hole diameters. Figure 7.8 shows the SEM micrograph of a) Planar aluminum, rest are nano-hole alumina showing hole size b) ~ 40 nm. b) ~60 nm, d) 90 nm.

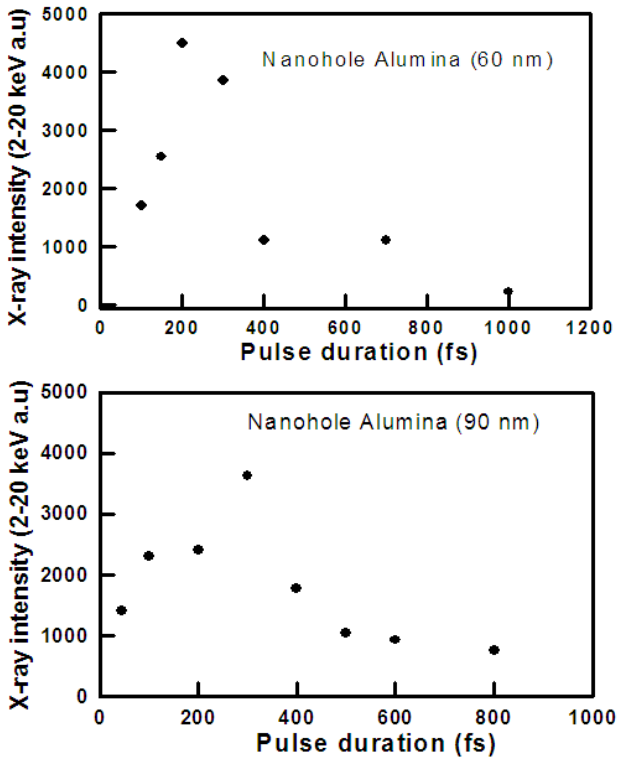

Fig. 7.9 X-ray intensity vs. pulse duration for nano-holes of various diameters ~60nm (above) and ~90 nm (below))

The effect of laser pulse duration on the x-ray emission was also studied, where the x-rays showed a peak behavior in all the cases for nano-hole targets. The pulse duration was varied by changing the compressor grating separation. Both positive and negative chirped pulses were used and chirp had no effect on the x-ray peak and x-ray yield, as the yield was similar in both cases of the chirp. The peaking time was observed to be proportional to the hole diameter. For instance, nano-holes of hole diameter 40 nm (see Fig. 7.5), 60 nm and 90 nm exhibit peaks in x-ray yield at 100 fs, 200 fs and 300 fs respectively as seen from Fig. 7.9. The results can be explained by considering the hydrodynamic expansion of the laser irradiated structure and field enhancement in the nano-holes.

The nano-hole target plasma does not possibly reach the resonance ($2n_c$) before the void closure. The x-ray peak is therefore observed due to absence of field enhancement on void

closure. Void closure time is observed to be proportional to the hole diameter. The nano-holes of diameter 40 nm, 60 nm and 90 nm exhibit peaks in x-ray yield at 100 fs, 200 fs and 300 fs respectively. From the void closure time, it is concluded that for the 40, 60 and 90 nm sized holes Cs= 200 nm/ps (for 40 nm nano-holes) and Cs= 150 nm/ps for the others. In summary, the nano-hole alumina target exhibit enhancement in the water window region and the hard x-ray (2-20 keV region) over planar aluminum. The observations of higher x-ray yield in the nano-hole targets (c/f planar target) and peaking of the x-ray yield in nano-hole targets is explained considering the electric field enhancement and void closure during hydrodynamic expansion..

Chapter 8

Electric field enhancement in nano-tubes.

As discussed in the previous chapters, various novel targets are studied as alternative to planar targets in the quest for achieving high absorption of intense ultra-short laser pulses for energetic particle and radiation generation [69-85]. To explain interaction of laser with spherical gas clusters, a variety of models of the laser–cluster interaction have been put forward including inner shell excitation [75], ionization ignition [93], collective electron dynamics [104], Coulomb explosion [95], and nano-plasma model [96]. The last one explains the maximization of the absorption cross-section and the electric field in the vicinity of Mie resonance at $3n_c$ in spherical clusters. This is also supported by a large number of experiments [96-100] which are consistent with this model. For cylindrical nano-structures, this maximization occurs when the electron density passes through $2n_c$ [17-19, 177, 190, 202]. Nano-structures in other shapes like elongated and pointed nano-structures (nano-protrusions and nano-rods) have shown enhanced x-ray and energetic particle emission and this has been attributed to the enhanced electric field at the tip, also referred to as the "Lightning rod effect" [76, 78, 87]. It is desirable to design a nano-target with a geometry which will enable even higher field enhancement when irradiated by ultra-short laser pulses for efficient x-ray and energetic particle generation [203]. Unfortunately, the field enhancement in nano-structures discussed above is limited by their geometry and dielectric properties. Although the field is resonantly enhanced at Mie resonance in spherical clusters and nano-rods at $3n_c$ and $2n_c$ respectively during the ionization and expansion phase, the limitation is that this resonance is at a density much lower than the solid density and the resonance condition is also short lived (~ a few fs) [96, 102]. Even more importantly, as the high density laser heated

cluster plasma expands, the electric field inside the cluster is shielded i.e. the field inside the cluster is actually less than the applied laser field strength, and the field enhancement occurs only when the electron density is near to the resonance condition [96, 177,190, 202, 204]. Further, a lower resonance electron density requires the laser heated cluster to expand sufficiently long for the electron density to decrease and approach the resonance condition. This time required is typically ~100 fs to 1 ps [97, 101, 189, 202]. For ultra-short pulses of duration < 100 fs, the clusters do not expand enough during the laser pulse to reach resonance at the peak of the pulse [97, 101]. It is therefore desirable for maximum absorption and x-ray generation that the resonance condition is met at the peak of the ultra-short laser pulse [96, 177, 190, 202, 204]. Therefore, for meeting this requirement, the laser pulse is generally stretched and there exists an optimum pulse duration for a given size of a cluster [96, 177, 190, 202, 204]. However, stretching of the pulse is not very desirable since it compromises the laser intensity as well as the resultant x-ray emission duration. In the light of the above facts, it would be ideal to have a structure that has resonance density close to the solid density, which will result in more absorption, electron generation, and x-ray emission, as now more electrons would interact with the enhanced field. Moreover, a high resonance density means the resonance condition can be met even for pulses shorter than 100 fs, since now the nano-structure does not have to expand much to reach the resonance condition. It is further desirable that the chosen nano-structure has an extended resonance in time, so that the field enhancement continues during most of the entire hydrodynamic evolution.

Although a target with the above mentioned features will be highly desirable, little work has been done for designing such nano-structure targets. Nevertheless, recently, some other kinds of nano-structures have been used for laser matter interaction studies, especially the ones which

have a hollow structure [79-85]. They show efficiently high x-ray generation and hot electron generation, but their resonance densities have not been reported [79-85]. To name a few, the hollow nano-targets that have been used for experiments with intense short pulses are: fullerene [79], nano-hole alumina [80], foam [81], nano-brush [82], carbon nano-tubes (CNTs) [83-85,187] etc. The enhanced field and surface currents in hollow structures are believed to support hot electron generation and transport [83-85,187] necessary for fast ignition scheme in inertial confinement fusion, and also for efficient x-ray generation. The electric field enhancement in the nano-structures make the effective laser intensity on the target very high, and consequently, it leads to x-ray yield enhancement that is proportional to the rescaled enhanced intensity [87]. In the class of hollow targets, CNTs are very attractive for ultra-short laser-plasma interaction [83-85, 187] as they are easily produced in bulk quantities with controllable inner and outer diameters [205]. To understand the reason for the x-ray enhancement from nano-tubes (as reported in references [83-85, 187]), it is necessary to investigate the effect of the hollow structure on the field enhancement and to determine the optimum geometric parameters of the nano-tubes for efficient absorption of ultra-short laser pulses (<< 1 ps).

Here we calculate the electric field enhancement inside a nano-tube plasma, and find out the plasma density at which the field enhancement occurs. We find that nano-tube has resonance density higher than a nano-rod and it can even be tuned to be close to the solid density. Therefore, a hollow structure helps in overcoming the limitation of a solid cluster or a nano-rod whose resonance densities are much smaller than the solid density. Moreover, it is observed that instead of a single resonance density (e.g. $3n_c$ in spherical clusters [96], or $2n_c$ in a solid nano-cylinder [177, 190, 202]), a nano-tube shows field enhancement at two densities : $n_H = \frac{2n_c}{1-\left(\frac{a}{b}\right)}$

and $n_L = \frac{2n_c}{1+\left(\frac{a}{b}\right)}$, where *a* and *b* are the instantaneous inner and outer radii. The high density resonance (n_H) occurs at a progressively higher density as one chooses nano-tubes of increasing degree of hollowness (*a/b*). Multiple resonances can occur in hollow nano-structures during the ionization and hydrodynamic expansion phases. Another interesting feature arises from the fact that in an expanding heated nano-tube, the plasma density as well as high resonance density (n_H) decrease with time. Simultaneous decrease in these two densities for nano-tubes of certain degree of hollowness may allow continued occurrence of resonance for a much longer time.

8.1 Theoretical considerations

The interaction of ultra-short laser pulses with spherical clusters/ nano-rods is calculated considering it as a nano-plasma [96-100]. The cluster dipole moment and the internal electric field can be easily evaluated under the quasi-static approximation (The cluster size being much smaller than the incident laser wavelength) [96-100]. The Laplace equation is solved taking the Drude dielectric function [87, 96-100] and Mie theory in dipole limit to obtain the resonance condition and the internal electric field distribution.

We now proceed on similar lines to calculate the electric field inside a laser irradiated hydrodynamically evolving nano-tube. Consider a nano-tube with inner and outer radii a_o and b_o in an applied laser field of strength E_L ($E_L = \frac{\hat{x}}{2}\left(Ee^{i\omega t} + c.c\right)$). Let the laser field be oriented perpendicular to the axis of the nano-tube. A field applied on a nano-tube at any arbitrary direction can be resolved into two components, one parallel to the axis and the other perpendicular to the axis. The component of electric field applied parallel to the nano-tube axis is

not enhanced [177, 190, 202]. The enhancement in the perpendicular component depends on the geometric and dielectric parameters of the nano-tube.

Laser - nano-tube interaction can be studied in two phases, the first being the ionization phase and the second being the hydrodynamic expansion phase. In the ionization phase, at the onset of the interaction of the nano-tube with intense ultra-short laser pulse, there is plasma formation. The threshold of plasma formation is typically 10^{14} W/cm^2 for 100 fs pulse for planar solid and nano-structures [194]. This threshold is crossed near the foot of the intense pulse. Therefore the dielectric constant of the nano-tubes instantaneously modifies and becomes metal-like or plasma-like because of the generation of free electrons [200, 201]. The subsequent pulse further ionizes the nano-structure by optical field ionization and tunnel ionization, leading to creation of a solid density plasma of density n_0 [96, 97, 202]. In the ionization phase, the nano-tube's geometry is almost preserved during interaction of the intense short pulse with the nano-tubes since the temperature rise is not enough to cause sufficient hydrodynamic expansion for the structure to get modified in such short time scales [96, 177, 190, 202, 204]. The nano-tube's expansion is thus expected to be extremely slow during the ionization phase at the beginning of interaction and subsequently the temperature rises very quickly due to collisional absorption and maximum electron density is achieved near the peak of the pulse [96, 204]. In the hydrodynamic expansion phase, the energy absorption and the consequent sharp rise of the plasma temperature causes the expansion of the nano-plasma, and the electron density of the cluster starts to decrease monotonically [96, 204]. Since the plasma expansion takes place along the density gradient, the inner radius starts decreasing while the outer radius increases. Therefore, the expansion leads to modification of the inner and outer radii to some instantaneous value *a* and *b*. It must be noted that during the ionization phase, the electron density increase monotonically (under the

assumption that target geometry and inner and outer radii remain fixed). On the other hand, when the nano-tube expands in the hydrodynamic expansion phase [102, 206], the electron density decreases monotonically (under the assumption that no further ionization or recombination takes place) [97, 202]. This modifies the dielectric constant ($\varepsilon = 1 - n_e/n_c$) of the nano-tubes plasma [97, 202] during both the phases of interaction. Here n_e is the instantaneous electron density and n_c is the critical density for the laser.

Like in the case of a nano-cluster or nano-rod, the electric field inside the hollow nano-tube is calculated using the Laplace equation $\nabla^2 V = 0$ solved under the above mentioned quasi-static approximation, where the outer radius considered is much smaller than the applied laser wavelength (i.e. $b << \lambda$). Solving this equation, one finds the dependence of the electric field in the nano-tube on the instantaneous value of a, b, ε and E_L. Expanding in cylindrical coordinates and neglecting the Z variation (as the length of the cylinder is much larger compared to its outer diameter), the general solution is

$$V = K + \ln r + \sum_{n=1}^{\infty} (A_n r^n + B_n r^{-n}) \cos n\theta + (C_n r^n + D_n r^{-n}) \sin n\theta \qquad \ldots\ldots\ldots (8.1)$$

Applying appropriate boundary conditions, the potential can be shown to be

$$V_{\mathrm{I}} = A_1 r \cos\theta \qquad \text{for } (\ r \le a \quad \text{Region I}) \qquad \ldots\ldots\ldots (8.2)$$

$$V_{\mathrm{II}} = (A_2 r + \frac{B_2}{r}) \cos\theta \qquad \text{for } (\ a \le r \le b \quad \text{Region II}) \qquad \ldots\ldots\ldots (8.3)$$

$$V_{\mathrm{III}} = -E_L r \cos\theta + \frac{B_3}{r} \cos\theta \qquad \text{for } (\ r \ge b \quad \text{Region III}) \qquad \ldots\ldots\ldots\ldots\ldots (8.4)$$

Using the continuity of D_n, E_t and potential V, one gets the four unknowns A_1, A_2, B_2, B_3 (all other A_i, B_i being zero) in terms of a, b and ε as

$$A_1 = \frac{-4E_L\varepsilon}{(\varepsilon+1)^2 - \left(\frac{a}{b}\right)^2(\varepsilon-1)^2} \quad \text{.....8.5(a)}$$

$$A_2 = \frac{-2E_L(\varepsilon+1)}{(\varepsilon+1)^2 - \left(\frac{a}{b}\right)^2(\varepsilon-1)^2} \quad \text{.....8.5(b)}$$

$$B_2 = \frac{-2E_L a^2(\varepsilon-1)}{(\varepsilon+1)^2 - \left(\frac{a}{b}\right)^2(\varepsilon-1)^2} \quad \text{.....8.5(c)}$$

$$B_3 = \frac{E_L b^2(1-\frac{a^2}{b^2})(\varepsilon^2-1)}{(\varepsilon+1)^2 - \left(\frac{a}{b}\right)^2(\varepsilon-1)^2} \quad \text{.....8.5(d)}$$

The radial and azimuthal components of the electric field $\left(E_r = -\frac{\partial V}{\partial r} \text{ and } E_\theta = -\frac{1}{r}\frac{\partial V}{\partial \theta}\right)$ in the three regions can be derived from equation 8.2, 8.3 and 8.4. The magnitude of electric field ($\sqrt{E_r^{\,2} + E_\theta^{\,2}}$) in the three regions is thus given by

$$E_I = A_1 \quad \text{..... 8.6(a)}$$

$$E_{II} = \sqrt{A_2^{\,2} + \frac{B_2^{\,2}}{r^4} - \frac{2A_2B_2}{r^2}\cos 2\theta} \quad \text{.....8.6(b)}$$

$$E_{III} = \sqrt{E_L^{\,2} + \frac{B_3^{\,2}}{r^4} + \frac{2E_LB_3}{r^2}\cos 2\theta} \quad \text{.....8.6(c)}$$

We now calculate the electric field enhancement in laser irradiated nano-tube plasma. In region I, the electric field is given by equation 8.6(a), and it is independent of r and θ. For region

II, one may define the root mean square (R.M.S.) electric field enhancement by taking the spatial average of the magnitude of field enhancement as

$$< E_{II}/E_L > = \frac{1}{\pi(b^2-a^2)}\sqrt{\int_0^{2\pi}\int_a^b \left(\frac{E_{II}}{E_L}\right)^2 r dr d\theta} \qquad \text{……...8.7(a)}$$

$$= \frac{1}{E_L}\sqrt{A_2^{\,2} + \frac{B_2^{\,2}}{a^2 b^2}} \qquad \text{.....8.7(b)}$$

For the case of a nano-rod (a=0), the above equations provide the electric field inside the nano-rod to be $\frac{2E_L}{\varepsilon+1}$, as expected [177, 190, 202]. By using the value of $\varepsilon = 1 - n_e/n_c$ (where n_e is the electron density and n_c is the critical density), it is seen that the resonant field enhancement occurs at $2n_c$, in agreement with earlier reported result [177, 190, 202].

Next, we may note from equations 8.6(a) and 8.7(b), together with equations 8.5(a) – 8.5(c), that the electric field in region I and region II will peak for certain values of $\left(\frac{a}{b}\right)$ given by

$$\frac{a}{b} = \pm\left(\frac{\varepsilon+1}{\varepsilon-1}\right). \qquad \text{……..(8.8)}$$

Therefore, the field enhancement in the case of nano-tube plasma occurs at two densities

$$n_H = \frac{2n_c}{1-\left(\frac{a}{b}\right)} \qquad \text{……(8.9)}$$

$$n_L = \frac{2n_c}{1+\left(\frac{a}{b}\right)} \qquad \text{.....(8.10)}$$

It may be seen from equation 8.9 that the higher resonance density (n_H) can be increased by choosing a nano-tube of smaller wall thickness. This is in contrast to the case of solid clusters

and nano-rods, where the field enhancement occurs only in the vicinity of $3n_c$, and $2n_c$ respectively.

8.2 Results and Discussion

From the preceding section, it is clear that the field enhancement depends on the ratio of the instantaneous inner and outer radii of the laser irradiated nano-tubes and the instantaneous dielectric constant of the plasma. First, one calculates the field enhancement factor during the ionization phase of laser nano-tube interaction where the electron density of the nano-tube plasma monotonically increases as the laser pulse intensity increases. The nano-tube gets ionized up to the solid density with no expansion (i.e. the initial inner and outer radii are at a_0 and b_0) [97, 202, 207]. This is a valid assumption since the optical field ionization and tunnel ionization are instantaneous processes.

Figure 8.1 shows the root mean square (R.M.S.) field enhancement during the ionization phase of laser irradiated nano-tubes of different degrees of hollowness (which is defined as the ratio of the initial inner and outer radii) subject to the condition that $b_0 << \lambda$, the assumption under which the Laplace equation was solved. For this calculation, one uses equation 8.7(b) and the value of ε is varied since n_e/n_c varies from 0 to 40 (n_o/n_c is taken as 40 for Ti:sapphire laser (800 nm) irradiation of CNTs). Four values of degree of hollowness (0, 0.5, 0.75, and 0.95) were chosen.

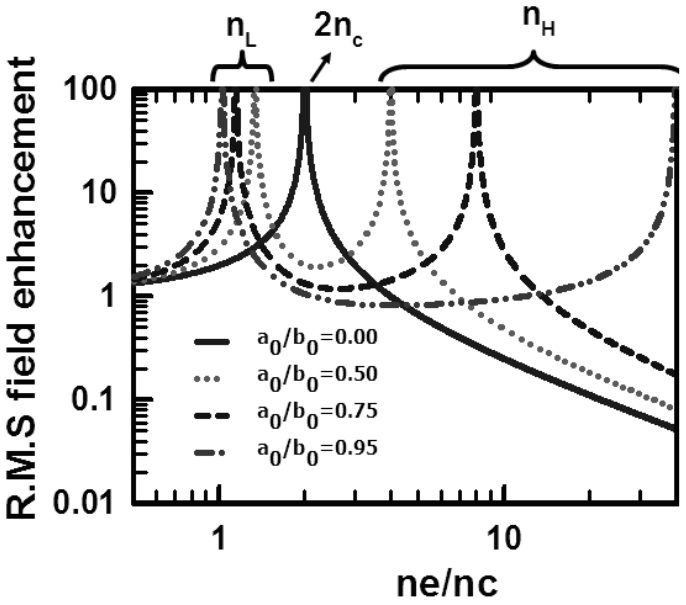

FIG.8.1 : R.M.S. field enhancement during the ionization phase of laser irradiated nano-tube plasma for fixed inner to outer radii nano-tubes of different degrees of hollowness (a_0/b_0)

It is seen from Fig. 8.1 that for a nano-rod, there is a single resonance at $2n_c$, also the electric field is highly shielded as the electron density increases and approaches the solid density. It can also be seen that nano-tubes show two resonances during ionization. To obtain a high electric field enhancement at a higher electron density, it is desirable to choose a nano-tube with greater degree of hollowness. This brings out an important point in the perspective of the spherical clusters and nano-rods where the resonance condition ($3n_c$, $2n_c$) is met near the foot of laser pulse during the ionization phase. However, since the resonance is reached at low laser intensity (near the foot of the pulse), this resonance is of less significance [96-100]. It is desirable to meet the resonance condition at the peak of the laser pulse. If the resonance density is enhanced by choosing a hollow nano-structure, the resonance condition could be met when the applied field is also high [79-85] . Therefore, even in the ionization phase, one can make the resonance happen near the peak of the pulse so that it will have a significant role in the interaction with nano-tube.

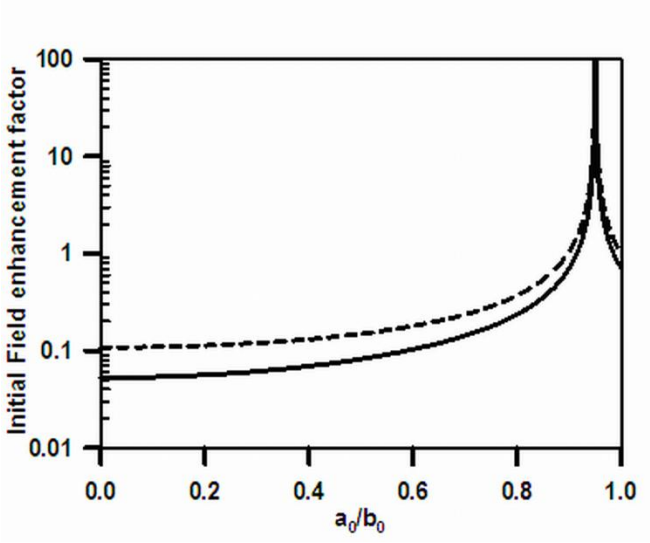

FIG.8.2: Initial field enhancement factor as a function of a_0/b_0 in two regions of the nano-tube: dotted curve $r<a_0$ Region I, solid curve $a_0<r<b_0$ Region II. Maximum initial field enhancement occurs for

$$\frac{a_0}{b_0} = \frac{n_0 - 2n_c}{n_0}.$$

Next, for the other phase of laser nano-tube interaction where one considers the hydrodynamic evolution, one can consider a zero time to mark the onset of expansion and variation of nano-tube inner and outer radii with time. One can define the zero time as the time when the nano-tube plasma is ionized up to the solid density n_0 assuming no expansion has occurred (i.e. the initial inner and outer radii are at a_0 and b_0) [97, 204, 207]. For calculating the initial value of ε, n_o/n_c is taken as 40. This will help in identifying the class of nano-tubes with same degree of hollowness (a_0/b_0) for maximum initial field enhancement. Figure 8.2 shows the variation of initial field enhancement factor with the degree of hollowness (a_0/b_0) in region I and II. The value of a_0/b_0 lies between 0 and 1. For a nano-rod a_0/b_0=0. It is clearly seen that for a nano-rod the field is highly shielded. It is also seen that the field in region I is higher than that in region II. Further, for smaller values of a_0/b_0, there is a shielding of the applied electric field. However, as the degree of hollowness increases, field enhancement occurs. The maximum enhancement occurs for

$$\frac{a_0}{b_0} = \frac{n_0 - 2n_c}{n_0} \qquad \text{.....(8.11)}$$

As may be seen from equation 8.9, this condition corresponds to the occurrence of the high density resonance at the solid density n_0. Beyond this value of a_0/b_0, the field enhancement starts reducing.

Now we examine the temporal evolution of the R.M.S. electric field during the expansion phase in the nano-tube plasma and also estimate the time scales of resonance, as done for clusters or nano-fibers [177, 204, 207]. This is done under a simplifying assumption of a constant temperature. As the plasma expands along the density gradient (perpendicular to the nano-tube axis), the instantaneous inner radius a decreases and is a_0-$c_s t$ and outer radius b increases and is b_0+$c_s t$, where $c_s = \sqrt{\frac{ZkT_e}{M_i}}$ is the plasma expansion speed, where M_i is the ion mass. The value of c_s can be estimated from the work of Issac *et al* [192] who have done experiments on gas cluster using Ti:Sapphire laser with the duration ranging from 60 fs to 2 ps, and intensity up to 10^{18} W/cm^2. They have predicted a nearly constant electron temperature (between 1-2 keV) from experiments and simulations for the range of pulse duration in their experiments. Taking the typical value of plasma temperature of ~ 1 keV from their work, we estimate c_s to be ~100 nm/ps [177]. Of course, c_s will have some variation during the hydrodynamic expansion, but a constant value of c_s for a given average electron temperature helps in predicting the time scale at which the resonance would occur. For example, various experiments on spherical clusters and nano-fibers have shown that an assumption of constant c_s helps in predicting the resonance time scales quite accurately [97, 177]. Moreover, the simulations done by Ditmire *et al* [95] and Liu *et al* [204] show that the ion velocity c_s is extremely low initially during the ionization phase and after that it increases very rapidly when the electron density become close to solid density (this

happens approximately near the peak of the laser pulse), after this c_s is almost constant. The electron density gradually decreases as the cluster expands with a variation discussed in the following text. On the basis of this picture, it is a good approximation to consider the zero time as that time when the nano-tube plasma is at solid density n_0 with a given inner and outer radii a_0 and b_0 and then it starts expanding eventually leading to the monotonic decrease of the electron density [177, 204, 207].

An important point during the hydrodynamic expansion of the nano-tube plasma is the "void closure", i.e. when $a = 0$. The time required for void closure (t_v) is a_0/c_s. If the void closure occurs before the condition for high density resonance is reached, one may term the nano-tube as a "thick" nano-tube. On the other hand, if the void closure takes place after the occurrence of high density resonance, the nano-tube may be referred to as a "thin" nano-tube. We first consider a thick nano-tube. Before the void closure, the plasma density varies with time as $n_e = \frac{n_0(b_0 - a_0)}{b_0 - a_0 + 2c_s t}$, and after the void closure, it varies as $n_e = \frac{n_0(b_0^2 - a_0^2)}{(a_0 + b_0 + c_s\tau)^2}$ (where τ in the last expression is the time after void closure). Once the void closure occurs, the nano-tube plasma behaves like a nano-rod which will show resonance at $2n_c$. Next, in the case of a thin nano-tube, the time taken by the nano-tube plasma to reach the high density (n_H) resonance is $t_H = \frac{1}{c_s}\left[(b_0 - a_0)\frac{n_0}{2n_c} - b_0\right]$. By comparing this time with the time of void closure, it is easily seen that the high density resonance will occur before void closure if $\frac{a_0}{b_0} > \frac{n_0 - 2n_c}{n_0 + 2n_c}$. Further, in a real situation, $t_H > 0$. This implies that $\frac{a_0}{b_0} < \frac{n_0 - 2n_c}{n_0}$. It can be shown that if this condition is

satisfied, then the low density (n_L) resonance also occurs before the void closure. Therefore two resonances occur only when $\frac{n_0-2n_c}{n_0+2n_c}<\frac{a_0}{b_0}<\frac{n_0-2n_c}{n_0}$.

In the thin nano-tube category, we may identify two particular situations, viz. $\frac{a_0}{b_0}=\frac{n_0-2n_c}{n_0}$ as in equation 8.11, and the other being $\frac{a_0}{b_0}>\frac{n_0-2n_c}{n_0}$. As seen from Fig. 8.2 and discussed earlier, the first condition $\frac{a_0}{b_0}=\frac{n_0-2n_c}{n_0}$ corresponds to occurrence of high density resonance at the solid density. Such a nano-tube may be referred to as "resonant" nano-tube. Finally when $\frac{a_0}{b_0}>\frac{n_0-2n_c}{n_0}$, the high density resonance does not occur at all, and only the low density resonance condition is fulfilled. We may refer to such a nano-tube as "ultra-thin". Thus, the nano-tubes can be categorized as

Thick nano-tube : $0<\frac{a_0}{b_0}<\frac{n_0-2n_c}{n_0+2n_c}$ .....(8.12)

Thin nano-tube : $\frac{n_0-2n_c}{n_0+2n_c}<\frac{a_0}{b_0}<\frac{n_0-2n_c}{n_0}$ .....(8.13)

Ultra- thin nano-tube : $\frac{a_0}{b_0}>\frac{n_0-2n_c}{n_0}$ .....(8.14)

Resonant nano-tube : $\frac{a_0}{b_0}=\frac{n_0-2n_c}{n_0}$ .....(8.15)

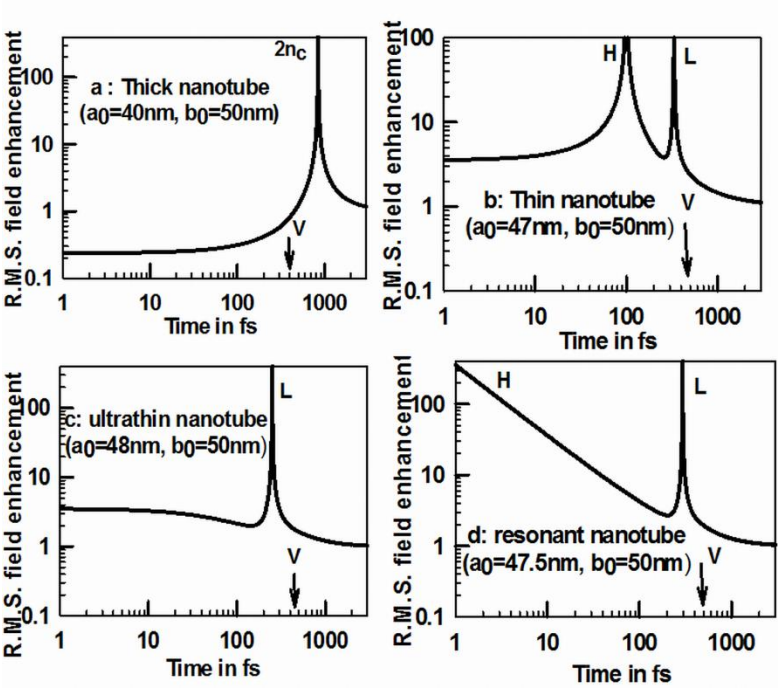

FIG.8.3 : Time evolution of the electric field in various size nano-tubes : (a) Thin nano-tube, (b) Thick nano-tube, (c) Ultra-thin nano-tube, and (d) Resonant nano-tube {all for $n_0/n_c = 40$, $c_s = 100$ nm/ps}. The points H, L and V indicate the time corresponding to occurrence of higher density resonance, lower density resonance, and void closure respectively

Using equations 8.5(b), 8.5(c) and 8.7(b), one can plot the R.M.S. electric field enhancement evolution for nano-tubes with initial inner and outer radii a_0 and b_0 respectively, while they expand after being irradiated by an intense ultra-short laser pulse. The initial maximum plasma electron density is chosen as $n_o/n_c = 40$ and the expansion speed c_s =100 nm/ps [192]. We also take into account that the fact that hydrodynamic evolution causes the instantaneous inner radius a to decrease as a_0-c_st and outer radius b increases as b_0+c_st and this causes the decrease of electron density and the dielectric constant (ε) modifies accordingly. Figure 8.3 shows the calculated variation of the R.M.S. electric field enhancement in region II for thick and thin carbon nano-tubes. Figure 8.3a depicts the case of a thick nano-tube (a_0 = 40 nm, b_0 = 50 nm), showing the occurrence of void closure at 400 fs, followed by $2n_c$ resonance at 840 fs. Figure 8.3b shows the electric field evolution for a thin nano-tube (a_0 = 47 nm, b_0 = 50

nm). It is noted that while for the thick nano-tube there was an initial field shielding and the field enhancement occurred only near $2n_c$, the field inside the thin nano-tube is highly enhanced from the very beginning of heating and expansion and the enhancement takes place throughout the expansion of the nano-tube. The high (H) and low (L) density resonances are observed at 100 fs and 335 fs respectively, prior to the void closure (V) at 470 fs. Next, Fig. 8.3c shows the electric field evolution for ultra-thin nano-tube (a_0 = 48 nm, b_0 = 50 nm). It shows the occurrence of the low density resonance (L) at 250 fs, while the void closure (V) occurs at 480 fs. Like the thin nano-tube, even in the case of the ultra-thin nano-tube the field enhancement exists at all instants of the expansion. Finally, Fig.8.3d shows the electric field evolution of a resonant nano-tube (a_0 = 47.5 nm, b_0 = 50). It is seen that the high density resonance (H) occurs over an extended time period from the beginning. The low density resonance (L) occurs at 295 fs and void closure at 475 fs. Thus, in all the cases of thin nano-tube, there is a greater field enhancement compared to the thick nano-tube.

An important aspect of the nano-tube - laser interaction arises from the fact that as the nano-tube (with appropriate choice of a_0, and b_0) expands, the higher density resonance will progressively occur at lower densities, so that the resonance condition can be sustained over a longer time. This is clearly seen from Fig. 8.4 which depicts the time evolution of the resonance densities of different nano-tubes (thick, thin, ultra-thin and resonant), plotted along with their density evolution for n_o/n_c = 40 and c_s = 100 nm/ps. The point of intersection of the decreasing nano-tube density with evolving resonance density gives the time of occurrence of resonance.

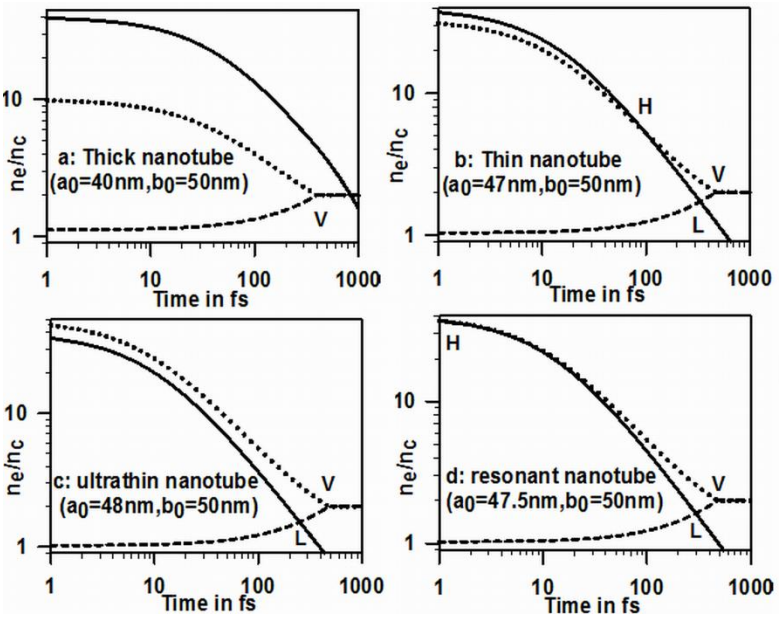

FIG.8.4 : Time evolution of the nano-tube density (solid curve) along with that of the higher resonance density (dotted curve) and the lower resonance density (dashed curve) for (a) thick, (b) thin, (c) ultra-thin, and (d) resonant nano-tubes. The points H, L and V indicate the time corresponding to occurrence of higher density resonance, lower density resonance, and void closure respectively.

Figure 8.4a shows that the void closure (V) in the case of thick nano-tube (a_0 = 40 nm, b_0 = 50 nm) takes place before the occurrence of the resonance condition and the resonant density becomes $2n_{c,}$ like in a solid nano-rod. In addition, the time duration over which the nano-tube plasma density is close to the resonance density is small. Figure 8.4b for the case of thin nano-tube (a_0 = 47 nm, b_0 = 50 nm) shows the occurrence of both higher and lower density resonances (H,L) before the void closure (V) occurs. In this case, the plasma density remains in the vicinity of the high resonance density for a longer time. Figure 8.4c shows that in the case of ultra-thin nano-tube (a_0 = 48 nm, b_0 = 50 nm), only the low density resonance (L) takes place before void closure (V) and the resonance condition is met over a small time. Figure 8.4d shows that in the case of "resonant" nano-tube (a_0 = 47.5 nm, b_0 = 50 nm) the high density resonance starts from the very onset of expansion, and the resonance continues for a very long time compared to the other categories of nano-tubes. These figures (Figs. 8.4a, b, c) also show the number of

resonances shown by thick, thin and ultra-thin tubes, as were seen earlier in Figs 8.3a-c. The overall analysis brings out the fact that the hollow structure has various advantages over clusters or nano-rods as resonance density of a nano-tube can be tuned close to the solid density and the resonance condition can be met for pulses shorter than 100 fs. In addition to this, there are resonances during the ionization and expansion phase, along with continued occurrence of high density resonance for a nano-tube with a particular degree of hollowness. Finally, since the electric field inside a structure governs the absorption, electron, ion and x-ray generation, therefore large field enhancement in laser irradiated nano-tubes make them very interesting target from application point of view.

To summarize, we have studied the evolution of the electric field enhancement inside the nano-tube plasma irradiated with intense short pulse laser. The hollowness of the nano-tubes determines the field enhancement and the electron density at which such structures exhibit resonance. It is found that a nano-tube exhibits two resonance at two electron densities during the ionization phase. During the hydrodynamic expansion phase also, a thin nano-tube exhibits resonant field enhancement at two densities (depending on its inner and outer radii). There exists a particular ratio of the inner to outer radii of the nano-tube where the field enhancement starts right at the solid density which may continue for a much longer time as the higher resonance density and the nano-tube density decrease simultaneously during the expansion of the heated nano-tube. While detailed theoretical calculations and computer simulations may be necessary to obtain exact quantitative information, the physical effects are quite well illustrated by taking simple analytical treatment and typical parameters of laser-nano-tube interaction. The observed features make nano-tubes of appropriately chosen inner and outer radii an attractive target for efficient absorption of intense ultra-short laser pulses. It will also be interesting to study the

interaction of nano-tubes with an intense few cycle laser pulse since the hydrodynamic motion is almost frozen in those time scales and the pulse interacts with a solid density plasma. In general, these calculations can also be extended to design efficient carbon nano-tubes based field emitters.

Chapter 9

Near complete absorption in carbon nano-tubes.

The plasma produced from solid targets using an ultra-short laser pulse is a point like, pulsed source of x-rays of ultra-short duration [72, 208]. Such a source can be very useful for applications like mammography [170, 209], phase contrast imaging [210, 211], and radiography [212]. The K_α x-ray line emission from the ultra-short pulse laser produced plasma can provide greatly improved contrast, spatial resolution as well as better dose utilization for mammography applications [213]. Among various targets, molybdenum has an edge over others since its characteristic x-ray emission at 17.5 keV falls in the 17.3-28.5 keV range, which is most optimal wavelength range for mammography [214]. For realizing a compact table top x-ray source, it is necessary to enhance the conversion efficiency of laser into the K_α photons. Among the various processes involved in the absorption of the incident intense laser pulse in the plasma, processes like resonance absorption, JxB heating, and vacuum heating lead to the generation of hot electrons [31, 52, 59]. These hot electrons penetrate the surface layer of cold plasma and interact with the solid core of the target to produce its characteristic x-rays [109, 210]. Increasing the laser intensity is not always useful to increase the K_α flux as the more-energetic electrons produced at higher intensity penetrate deeper into the target and produce x-ray photons deep inside the target, resulting in their re-absorption [109, 210], and increases the size of the source resulting in poor spatial coherence. Moreover, in this case, as the x-rays come from different depths, the pulse duration of the x-rays also increases. Therefore, there is an optimal hot-electron temperature for efficient K_α x-ray conversion, which is roughly 5-6 times the K-shell ionization energy [109, 210]. In view of this, the best way to enhance the K_α emission is to generate more

hot electrons with the desired optimal temperature [109, 210]. One way to achieve this is to utilize the electric field enhancement through resonances in nano-structures, leading to the generation of an increased fraction of hot electrons [72, 76, 87, 177, 202, 215-218]. For this purpose, carbon nano-tubes (CNTs) can be good choice since they have a hollow structure which supports two surface plasmon resonance modes, resulting from the hybridization of the cylindrical cavity plasmon and nano-rod plasmon [219]. It is therefore not very surprising that, as explained earlier in Chapter 8, the CNT plasma supports resonance at two electron densities, and depending on the degree of hollowness, the resonance can be tuned to even close to solid density [220]. A resonance at high density is desirable since if the field enhancement takes place at an instant when the electron density is also high, a larger number of electrons can gain energy from the enhanced field. Unfortunately, this is not the case with planar solid, nano-rod, or cluster targets, where the resonance density is of the order of the critical density (For Ti:sapphire laser, $n_c \approx 1.7 \times 10^{21}/cm^3$). For solids, the resonance takes place at n_c [31], at $2n_c$ for nano-rods [177,202], and at $3n_c$ for clusters [96]. Hence, it may be interesting to use CNT coated on planar Mo target to study laser energy absorption and x-ray emission.

In the Chapter 8, the theoretical aspects of laser nano-tubes interaction and its merits were discussed in detail. We performed experiments with planar target coated with carbon nano-tubes to study the effect of hollow structure in laser energy absorption, x-ray emission, and electric field enhancement. We describe here a comparative study of the laser energy absorption and the hard x-ray emission in the 2-20 keV range from uncoated planar molybdenum, and planar molybdenum coated with CNTs. Near complete energy absorption of intense ultra-short laser pulses is observed in the case of CNT deposited on planar Mo. The enhancement in K_α emission in CNT coated Mo target over planar Mo target is observed to be very sensitive to the

laser intensity. It is also observed that for nano-tubes of a certain degree of hollowness, there exists an optimum laser intensity for maximum K_α x-ray enhancement compared to the uncoated planar target. The results are explained considering the hollow structure of the nano-tube plasma which facilitates resonant electric field enhancement at two plasma electron densities during plasma evolution in time as discussed in Chapter 8. This resonantly enhanced localized field at a density much larger than the critical density n_c leads to highly efficient hot electron generation, which results in enhanced K_α emission.

9.1 Description of the Experiment

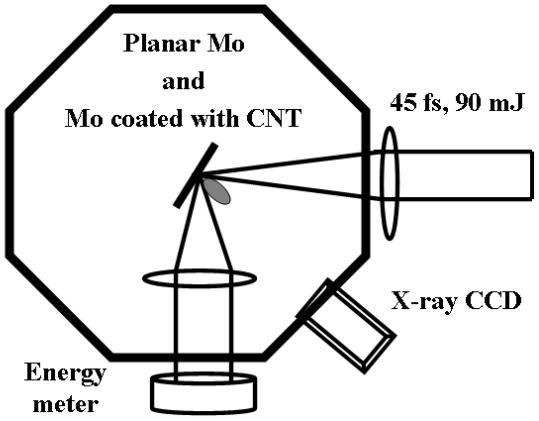

FIG. 9.1: A schematic diagram of the experimental setup

Figure 9.1 shows a schematic diagram of the experimental setup. The plasma was produced by focusing 90 mJ, 45 fs (FWHM) Ti:sapphire laser pulses (λ = 790 nm) on a planar molybdenum with / without pre-deposited 25 μm thick layer of CNTs. Synthesis of carbon nano-tubes was done by cracking of acetylene in presence Fe as catalyst in quartz tube. The substrate material was placed in the central part of the tube, where a temperature of ~ 900^o C was maintained. The p-polarized laser beam was incident on the target at an angle of 45^o with respect to the target normal in the intensity range of ~1.6x10^{16} W/cm^2 to 2.5 x10^{17} W/cm^2. The laser energy absorption was estimated by collecting the reflected laser light using a large aperture

collection lens (to collect specularly reflected as well as diffusely reflected laser light). Diffused scattering of the laser light in other directions was measured to be insignificant. The x-ray spectrum in the 2-20 keV region was recorded using a dispersion-less spectrograph with a 25 μm thick Ni foil (cut-off at 7.9 keV).

9.2 Results

Figure 9.2 shows the transmission electron microscope (TEM, Model : Philips CM200) image of the CNTs. The nano-tubes are clearly seen to be hollow, having an average outer diameter of 30 nm and a degree of hollowness of ~ 0.9 (the degree of hollowness is defined as the ratio of the inner to outer radii of a nano-tube).

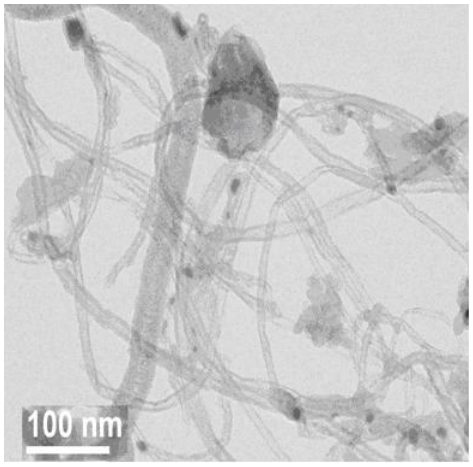

FIG. 9.2: TEM image of the CNTs showing the hollow structure

Figure 9.3a shows the variation of the absorption of the 45 fs laser pulses in the planar Mo target and CNT coated Mo target, in the laser intensity range ~1.6 $x10^{16}$ W/cm^2 to 2.5$x10^{17}$ W/cm^2. A near complete absorption is observed in CNT coated Mo target indicating efficient coupling as compared to the planar Mo. Figure 9.3b shows the hard x-ray emission spectrum from planar Mo and Mo coated with CNTs at a laser pulse intensity of 8 $x10^{16}$ W/cm^2. The

spectrum shows a large enhancement of K_α and bremsstrahlung emission from CNT coated Mo as compared to planar target.

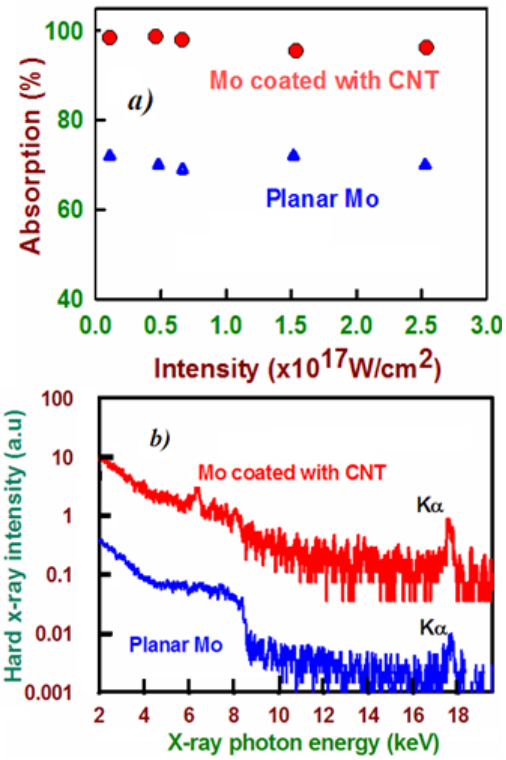

FIG. 9.3: a) Percentage absorption of 45 fs ultra-short laser pulse in planar Mo (solid triangles) and Mo coated with CNTs (solid circles) as a function of the laser intensity; b) Hard x-ray emission spectrum recorded from planar Mo and Mo coated with CNTs, at a laser intensity of ~8x10^{16} W/cm^2

Figure 9.4a shows the intensity of the K_α emission from planar Mo and Mo coated with CNTs, as a function of the laser intensity. It is observed that the K_α emission from CNT coated Mo target is always higher as compared to that from planar Mo. It is important to note here that with increasing laser intensity, the K_α yield from planar Mo keeps on increasing monotonically, with no sign of saturation, unlike the peaking seen in lower and medium Z targets like Al and Ti respectively [221, 222]. This observation eliminates any possibility of re-absorption of the K_α photons generated by the hot electrons penetrating inside the target, even at the highest laser intensity (2.5 x10^{17} W/cm^2) used in our experiments.

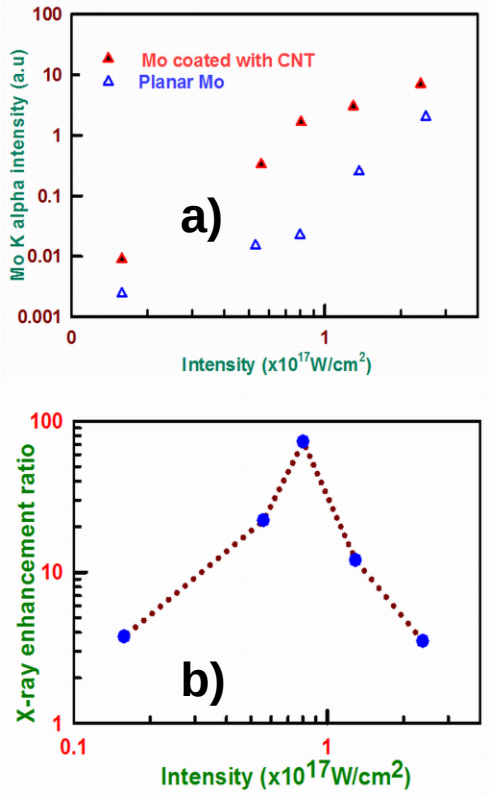

FIG.9.4 : a) K_α generation from planar Mo (hollow triangles) and Mo coated with CNTs (solid triangles) as a function of the laser intensity, b) The enhancement factor of K_α yield from Mo coated with CNT w.r.to planar Mo.

Figure 9.4b shows the enhancement factor of the K_α yield from Mo coated with CNT w.r.to planar Mo. Interestingly, although the absorption was close to 100% in the intensity range used in our experiments, the K_α enhancement from CNT coated target (w.r.to uncoated Mo target) varies drastically with the intensity. The enhancement was only 3.5 times at lower intensity of irradiation of 1.6×10^{16} W/cm^2. As the laser intensity is increased, a sharp increase of x-ray enhancement is observed. The K_α x-ray emission enhancement peaks at an intensity of 8×10^{16} W/cm^2, where the enhancement is ~ 75 times of that obtained from planar Mo. As the laser intensity is increased further, one observes a sharp drop in the enhancement of K_α , and the enhancement decreases to just 3 times at the highest irradiation intensity of 2.5×10^{17} W/cm^2.

Such a sharp enhancement at a particular intensity is indicative of a very efficient hot electron generation process. Such a peak behavior in x-ray enhancement has been also observed recently by Bagchi *et al* using CNT coated Cu target [84]. They studied the hard x-ray bremsstrahlung emission and observed enhancement utilizing the CNTs, but did not discuss the reason for the peak behavior.

9.3 Discussion of the results

To qualitatively understand these observations in Figs 9.3 and 9.4, we determine the electric field and hence the effective laser intensity inside a laser irradiated nano-tubes based on the steps shown in Chapter 8. The laser electric field inside the nano-structure determines the absorption and ionization processes, and hence governs the hot electron generation and the x-ray emission [72, 76, 87, 177, 202]. The electric field enhancement leads to the increase of effective intensity of the laser pulse interacting with the nano-tubes and hence leads to enhancement of the hot electron temperature [72, 76, 87, 177, 202]. It is quite valid to assume that, for an ultra-short pulse of 45 fs duration, the hydrodynamic motion is almost frozen and the nano-tubes geometry is intact during its interaction with the laser. Let the applied instantaneous laser field strength be E_o (the applied intensity I_o), oriented perpendicular to the axis of the nano-tubes of "hollowness" a_o/b_o (where a_o and b_o are the inner and outer radii), and the instantaneous dielectric constant be $\varepsilon = (1- n_e/n_c)$, where n_e is the electron density). The electric field applied at any arbitrary angle with respect to the tube axis can always be resolved in to a parallel and perpendicular component along the axis. As shown in Chapter 8 the field applied parallel to the tube axis does not get modified. The electric field inside the hollow nano-tube (perpendicular to its axis) is calculated using the Laplace equation in cylindrical coordinates neglecting the z variation and under quasi-

static approximation i.e. a_o, $b_o << \lambda$. Applying appropriate boundary conditions, the magnitude of the electric field inside the nano-tube region between a_o and b_o can be calculated to be $E_{in} = \sqrt{A_2^2 + \frac{B_2^2}{r^4} - \frac{2A_2B_2}{r^2}\cos 2\theta}$, where r and θ are the radial and azimuthal cylindrical coordinates, $A_2 = \frac{-2E_0(\varepsilon+1)}{\Delta}$, $B_2 = \frac{-2E_0 a_0^2(\varepsilon-1)}{\Delta}$, $\Delta = (\varepsilon+1)^2 - \left(\frac{a_0}{b_0}\right)^2 (\varepsilon-1)^2$. The root mean square (r.m.s.) electric field enhancement $\left\langle \frac{E_{in}}{E_0} \right\rangle$ can be calculated by taking the spatial average of field as $\frac{1}{\pi(b_0^2 - a_0^2)} \sqrt{\int_0^{2\pi} \int_{a_0}^{b_0} \left(\frac{E_{in}}{E_0}\right)^2 r dr d\theta}$. From this, the r.m.s. intensity enhancement ratio is calculated as $\left\langle \frac{I_{in}}{I_0} \right\rangle = \frac{1}{I_0}\left(A_2^2 + \frac{B_2^2}{a_0^2 b_0^2}\right)$. The electric field is resonantly enhanced when Δ=0, which happens for two value of a_o/b_o i.e. $\frac{a_0}{b_0} = \pm\left(\frac{\varepsilon+1}{\varepsilon-1}\right)$. By using the value of ε = 1- n_e/n_c, the electric field or the effective intensity in the nano-tubes plasma is resonantly enhanced at two densities $n_H = \frac{2n_c}{1-\left(\frac{a_0}{b_0}\right)}$, $n_L = \frac{2n_c}{1+\left(\frac{a_0}{b_0}\right)}$. Figure 9.5a shows the variation of the high and low resonance density with degree of hollowness, where the dashed vertical line is for the CNTs used in our experiments with a_o/b_o =0.9, for which n_H = 20 n_c and n_L =1.05 n_c. It follows from Fig. 9.5a that higher resonance density (n_H) can be increased by choosing a nano-tube of smaller wall thickness. This is in contrast to the case of solid clusters and nano-rods (a_o=0), where the field enhancement occurs only in the vicinity of $3n_c$, and $2n_c$ respectively [96-100, 177, 202]. Figure 9.5b shows the variation of the r.m.s. intensity

enhancement factor of the incident laser intensity inside a CNT (having a degree of hollowness of 0.9) as a function of the electron density. The effective intensity inside nano-tubes shows two peaks at densities mentioned above, but it is the peak corresponding to the high density resonance that governs the hot electron generation more effectively. This is

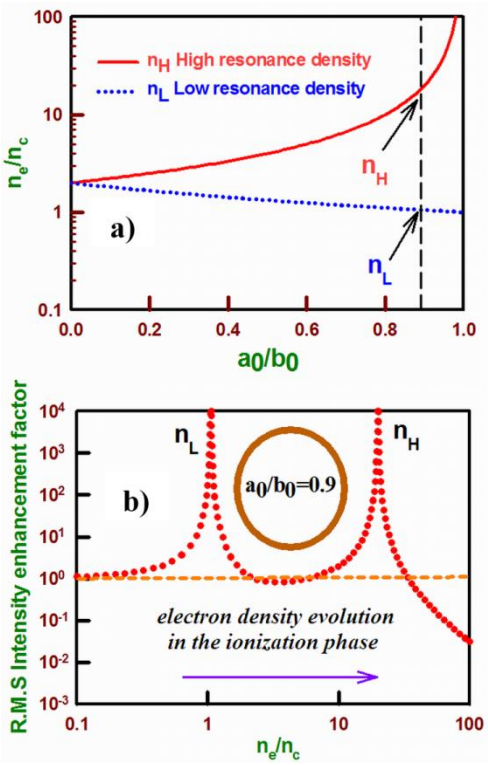

FIG.9.5: a) The variation of high and low resonance density with degree of hollowness, where the dashed vertical line is for the class of CNTs used in our experiments with a_o/b_0 =0.9; b) The r.m.s. intensity enhancement factor inside the hollow nano-tube, compared to the incident intensity of the laser (the inset shows a top view of CNT with a hollowness factor of 0.9).

because, when an intense laser pulse irradiates the CNTs, the plasma is created in the foot of the pulse when the laser intensity exceeds the plasma formation threshold (~10^{14} W/cm^2 for 100 fs pulse) and the plasma density becomes super-critical (> n_c) [194, 200, 201]. Subsequently, as the intensity rises sharply, the electron density also rises because of the intensity dependent

ionization processes like tunnel ionization, optical field ionization, and electron impact ionization [223]. During the ionization phase, the electron density reaches the resonance condition that is determined by the chosen target geometry. It is desirable that for most efficient generation of hot electrons, the high resonance density n_H is achieved at the peak of the laser pulse [96, 97, 177]. If the laser intensity is too low, the electron density generated at the peak falls short of that required for resonance. If the laser intensity is too high, the electron density generated at the peak overshoots the value required for resonance. In both the cases, although the effective intensity is enhanced w.r.to the applied laser intensity, the enhancement is not as strong as when the resonance condition is met, as can be also be seen from Fig. 9.5b. The sharp peaked K_α x-ray emission enhancement at an intensity of $8x10^{16}$ W/cm^2 is probably because in this case, the resonant electron density is reached at the peak of laser pulse, close to the high resonance density $n_H = 20\ n_c$ for the CNTs used in our experiment. In general, it follows that for nano-tubes of a certain degree of hollowness there exists an optimum laser intensity for maximum x-ray enhancement.

Coating CNTs on planar targets is a versatile method which, in principle, should be applicable to any material to enhance the x-ray emission, since the role of the CNTs is to facilitate high absorption and efficient hot electron generation. Taking into consideration the hot electron generation and transport in a material, there exits an optimum intensity and hot electron temperature [109,210] for maximum K_α yield. For materials with higher atomic number (Z), the optimum intensity is higher, and for lower Z materials, the optimum intensity is lower [109]. Consequently, one needs to coat CNTs of greater degree of hollowness on higher Z materials. Since such CNTs have a higher resonance density, at higher intensity of irradiation, the high density resonance may occur closer to the peak of laser pulse, leading to its better absorption.

Similarly, for lower Z materials, lower intensity of irradiation is needed to obtain the optimal K_α generation. Therefore, one has to optimize the laser intensity and the CNT geometry (degree of hollowness) depending on the target whose K_α one is interested in.

Next, it is important to consider the role of the thickness of the CNT layer in this process. A very thick layer of CNTs will inhibit the propagation of the hot electrons generated in the CNTs into the base material and will thereby reduce the x-ray conversion in the base material. Moreover, a thick CNT layer will also attenuate the x-rays produced in the base material. On the other hand, a too thin layer of CNTs will not give rise to sufficient hot electron generation. So one needs to optimize the laser intensity, CNT geometry (degree of hollowness) and CNT layer thickness for different target materials to achieve high x-ray conversion, and this will be studied in future.

To summarize, its observed that near complete energy absorption of intense ultra-short laser pulses is recorded in CNTs deposited on planar molybdenum. The hollow structure of the nano-tube plasma facilitates resonant electric field enhancement at high electron density during the ionization phase of the nano-tubes. This resonance enhancement at a density much larger than the critical density (n_c) leads to highly efficient hot electron generation, which results in enhanced K_α emission. In general, hollow tube targets facilitate more efficient hot electron generation and consequent x-ray emission, and this may be useful as a compact, low cost, table top, ultra-short duration x-ray source.

Chapter 10

Nano-ripple semiconductors as target for ultra-short laser absorption

Surface structuring with lasers is a highly competitive method due to its capability of making fast and easy to implement changes in the structure design [224]. Compared to the picosecond and nanosecond laser pulses, the energy in a femtosecond pulse can be precisely and rapidly deposited in a solid material with fewer thermal effects [225]. Therefore, the femtosecond lasers are widely used in micro-fabrication in transparent materials, metals and semiconductors for applications like modifying the optical properties of the surface [226], improvement of photovoltaic devices by increasing their effective surface area and in turn increasing the response and conversion efficiency [227]. The other applications include modification inside refractive index of bulk materials for fabricating photonic devices, optical data storage, and bio-photonic components [228-230].

Mid-IR femtosecond laser radiation is generally used for the generation of surface ripples, also known as laser-induced periodic surface structures (LIPSS). Various mechanisms have been proposed to explain the nano-ripple formation. Initially, it was thought to be the result of the interference between incident laser light and the scattered light from the surface roughness [231]. However, if this mechanism were to be true, nano-ripple width should always be of the order of the incident laser light wavelength, whereas in many experiments very narrow ripple formation has been observed. For example, Ozkan *et al* [232] found that ripples resulting from 248 nm femtosecond laser irradiation of thin diamond films had a period varying between 50–100 nm. Yasumaru *et al* [233] reported formation of ripple patterns with mean periods of 100–125 and

30–40 nm on TiN and diamond-like carbon after irradiation with 800 and 267 nm femtosecond pulses, respectively. To explain the nano-ripple formation in the case of metals, the surface plasmon created during initial random surface heterogeneities is considered [234]. In dielectrics, the coupling of the electron plasma wave and incident laser explains the observed periodic structure in glass [235]. Other proposed mechanisms for ripple formation are self-organization [236], Coulomb explosion [237], influence of second harmonic generation [238], anisotropic local field enhancement invoking nano-plasmonics [239], etc.

In this chapter, a study of surface nano-ripple formation on different band gap semiconductors is presented. A parametric study of the ripple formation with different laser parameters and ambient media is done with the objective of identifying conditions of forming narrow period ripples. Nano-ripples were formed using a Ti-sapphire laser with 8 mJ energy, 45 fs pulse duration and 800 nm wavelength (1.56 eV) at a fluence in the range of ~ 100 mJ/cm^2 – 1J/cm^2. The effect of the number of laser shots, the angle of incidence, polarisation of the laser, fluence, incident laser wavelength, band gap and ambient medium has been studied. Depending upon the experimental parameters, the nano-ripple sizes varied in the range of $\lambda/9$ to λ. Narrow nano-ripples are formed from wide band gap semiconductors. The width of the nano-ripples also decreases with the laser wavelength and the laser fluence. The observation of high and low spatial frequency ripples in different conditions is explained considering the transient metallic nature of the semiconductor surface on irradiation with intense femtosecond pulses. The surface eventually supports the surface plasmon excitation, which interferes with incident laser light for ripple formation. We attribute the very delicate dependence of ripple period with incident laser parameters to the critical role of electron density. The finding helps identifying suitable band gap

materials and laser parameters for obtaining nano-ripple period considerably small compared to the incident laser wavelength.

10.1 Experimental setup

For studying the nano-ripple formation from ultra-short laser pulse irradiation of semiconductor materials of different band gaps, the following semiconductor materials of narrow (< 1.5 eV, which is the energy of the incident 800 nm photon) band gap: InAs (0.36 eV), GaAs (1.42 eV), InP (1.35eV), and wide (> 1.5 eV) band gap materials like GaP (2.3 eV), GaN (3.4 eV), SiC (3.37 eV), ZnSe (2.82 eV) were used. Multiple laser shots from a Ti-sapphire laser with 8 mJ energy, 45 fs pulse duration, and 800 nm wavelength were focused in air on the semiconductor wafers at a fluence in the range of ~ 100 mJ/cm^2 – 1J/cm^2, i.e. around the plasma formation threshold. Using a BBO crystal, the second harmonic (400 nm) of the 800 nm laser beam was also used to study the influence of the laser wavelength on the ripple formation, while keeping the other parameters same. The effect of the number of laser shots, the angle of incidence, the polarisation of the laser, the fluence, the band gap, and the ambient medium was studied. The spatial features of the laser treated semiconductors were characterized using SEM (Philips XL30CP). The schematic of the experimental setup was already described in chapter 2.

10.2 Experimental results

Figure10.1 shows the surface morphologies resulting from the irradiation of a GaP wafer by femtosecond pulses with two different polarisations and in two different spatial regions. Figure 10.1a shows the formation of spherical nano-particles (~100 nm) with *circularly* polarized laser light, as also reported by several groups [240]. Figure 10.1b shows narrow nano-ripples with

~ 200 nm spacing at the peripheral regions of the laser irradiated spot with *linearly* polarised laser pulses. Figure10.1c shows wider nano-ripples with about 600 nm spacing near the central hot region of the laser irradiated spot. As expected, for linearly polarized light, the nano-ripple orientation was always orthogonal to the laser polarisation [200,201]. Nano-ripple formation was observed with 10-100 shots fired on the semiconductors. It was also observed that number of shots fired on the semiconductor did not have any effect on the ripple period.

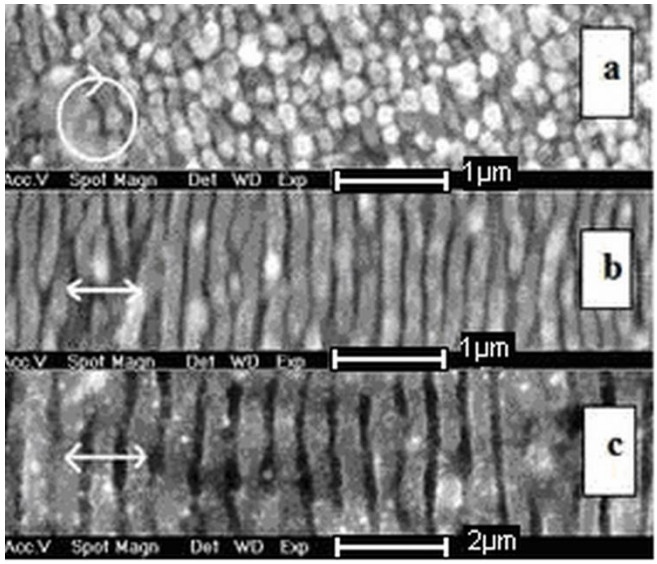

Fig.10.1 : GaP irradiated by 800 nm ultra-short laser pulses, a) with circularly polarised beam, b) and c) linearly polarised beam in two different regions; b) is around the periphery of the irradiated spot (low fluence) and c) is in the central region (high fluence). (The length of the horizontal bar is 1µm in a, b, and 2µm in c)

Figure 10.2 shows the nano-ripple formation using linearly polarised laser pulses in normal incidence. The polarization was rotated using a half wave plate. In all the figures, the rippled grating vectors orient perpendicular to incident laser polarization. In the narrow band gap semiconductors like GaAs and InP, the SEM pictures of the irradiated spot show the spacing to be of the order of 500-600 nm. On the contrary, in wide band gap material like GaN and SiC, the

spacing is of the order of 170-270 nm. Thus, it is observed that, in general, the narrow nano-ripples are formed from material with a wide band gap. This observation of narrow ripple formation in wide band gap semiconductor is consistent with previous reported results by Borowiec *et al* [241], but no explanation of the physical processes involved was given in those experiments.

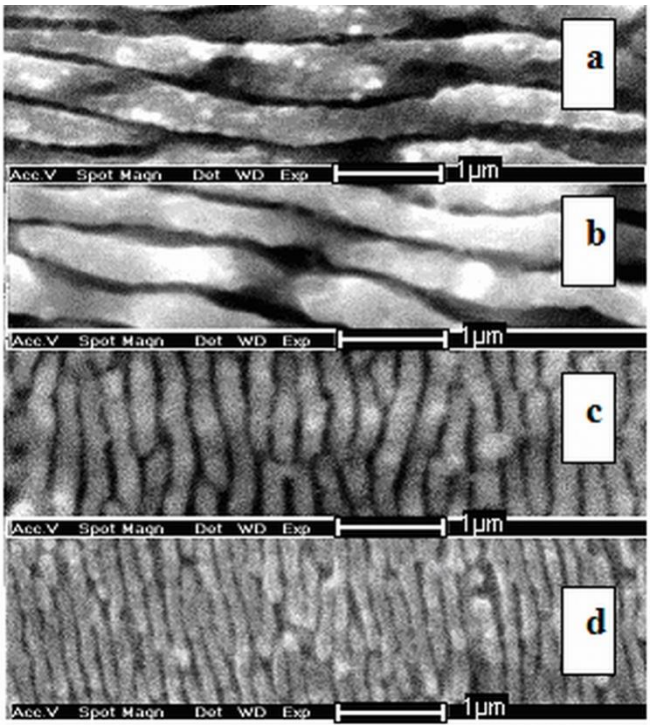

Fig.10.2 : Nano-ripple formation using 800 nm pulses in narrow band gap semiconductors : a) GaAs and b) InP; and in wide band gap semiconductors : c) GaN and d) SiC (The length of the horizontal bar is 1µm in a, b, c and d).

Figure 10.3 shows different micro structure formations using different fluences and ambient conditions for narrow band gap semiconductors like GaAs. In all the figures, the linearly polarised laser was at normal incidence. The SEM picture of the irradiated spot, as seen in Fig.10.3a, shows that, at a high fluence in air, no nano-ripple formation takes place, and only random heterogeneities of a few microns order appear. Figure 10.3b shows the formation of nano-ripples of a typical size of 600 nm, at low fluence (in air). Interestingly, Fig.10.3c shows

formation of nano-holes at high fluence in water. Figure 10.3d shows narrow nano-ripples of 150 nm size in GaAs at low fluence in water. This shows the crucial role of the ambient medium in formation of the nano-ripples. Very narrow nano-ripples are observed in narrow band gap materials like GaAs in water, whereas in air, the corresponding nano-ripple period is of the order of the laser wavelength. Even for a wide band gap material like GaP, which shows narrow nano-ripples of period ~200 nm in air, a narrower period of 150 nm is observed during irradiation in water.

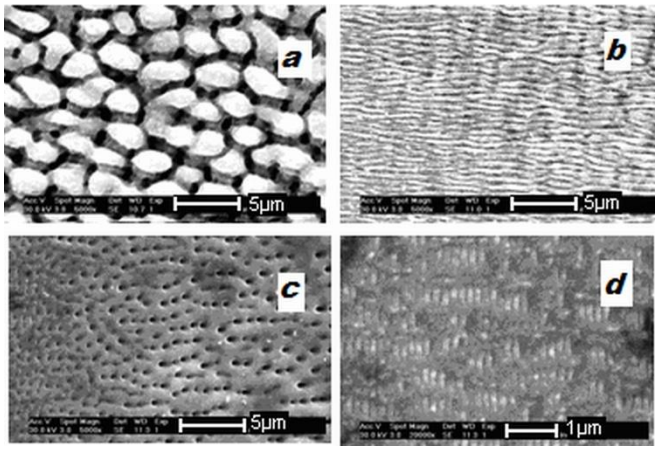

Fig.10.3 : Nano-ripple formation using 800 nm pulses in GaAs : a) at high fluence in air, b) at low fluence in air, c) at high fluence in water, d) at low fluence in water. (The lengths of the horizontal bars correspond to 5µm in a), b) and c), and 1µm in d

Figure 10.4 shows the angular dependence of nano-structure size obtained from narrow (GaAs) and wide (GaP) band gap materials irradiated by 800 nm pulses in water. It was observed that for the narrow band gap (GaAs) semiconductor, the ripple size increased with increasing angle of incidence as shown in Fig. 10.4a. In the case of the wide band gap (GaP) material with increasing angle of incidence the ripple period first increase and becomes constant at higher angles, as shown in Fig.10.4b. It was mentioned earlier in the context of Fig.10.3c that, at high

fluence, nano-holes are formed in GaAs. Figure 10.4c shows that the size of the holes increases with increasing the angle of incidence of the incident p-polarised light.

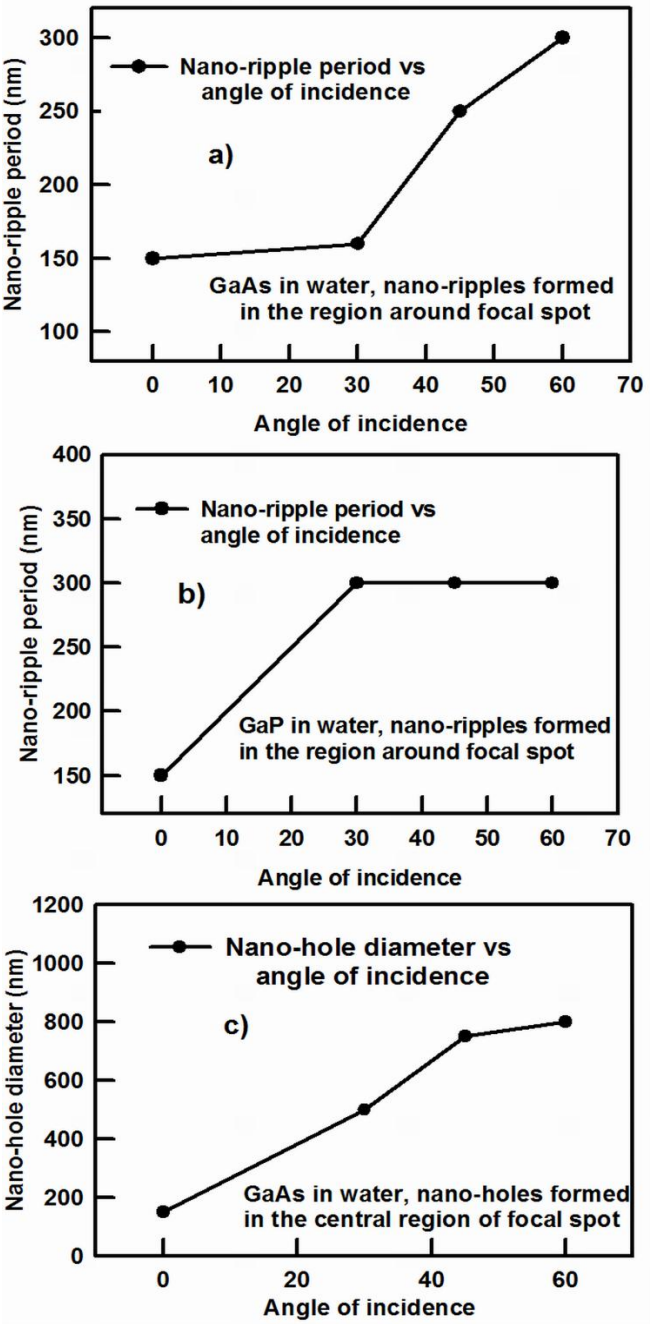

Fig10.4 : Angular dependences of formation of various nano-structures using 800 nm pulses in water :a) Nano-ripple formation in GaAs, b) Nano-ripple formation in GaP, and c) Nano-hole formation in GaAs

In many photonic applications, for example, the two-dimensional photonic crystals and micro diffraction elements, nano / micro holes on the surface of bulk materials are required as the building blocks. Although the mechanism of formation of such structure is still not clear, this process was achieved during irradiation in water medium, thus emphasizing the role of dense surrounding medium in formation of such novel hole structures.

It is commonly accepted that the nano-ripple width is dependent on the wavelength of the incident light. Therefore, to obtain narrow nano-ripples, second harmonic of the fundamental laser radiation is a better choice. Figure 10.5 shows the influence of laser wavelength on nano-ripple formation. In all the figures the rippled grating vectors orient perpendicular to incident laser polarization, which was linear in all the cases. Figures 10.5a and 10.5b show that, in the case of SiC, the use of 400 nm wavelength reduces the ripple period by more than a factor of 2 as compared to the nano-ripples produced by the 800 nm pulses (from 190 nm to about 90 nm). Similarly, for a narrow band gap material like InP also, there is a reduction of ripple period from 620 nm to about 280 nm, as shown in Figs. 10.5c and 10.5d. It may be noted that, for GaP, the ripple period using 400 nm pulse becomes larger than that formed using 800 nm pulses (from 180 nm to about 300 nm).

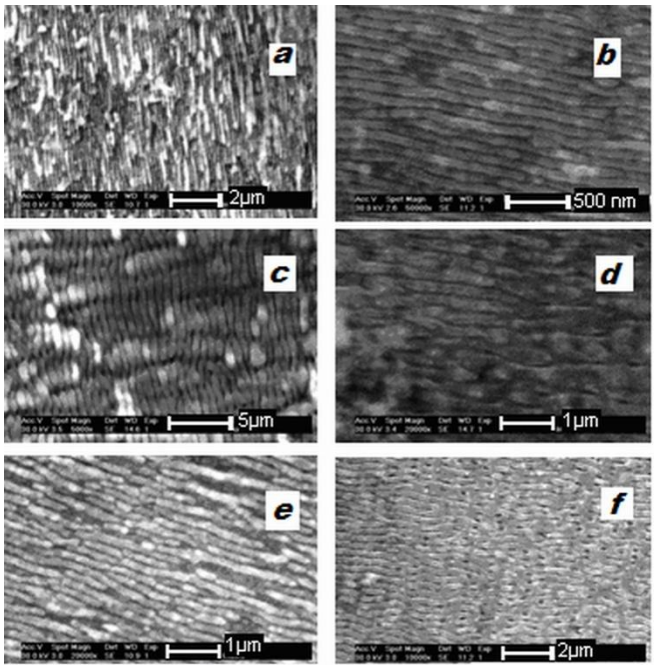

Fig.10.5 : Nano-ripple formation using 800 nm pulses and 400 nm pulses respectively in wide band gap semiconductors : SiC a) and b), GaP e) and f), and in narrow band gap semiconductor InP c) and d). (The length of the horizontal bar is 2µm in a), 500 nm in b), 5µm in c), 1µm in d), 1µm in e), and 2µm in f)).

10.3 Analysis of the experimental observations

The consistent observations regarding the nano-ripple formation are: 1) the ripple period is larger at higher fluence, and 2) the ripple period is large for the materials having band gap narrower than the incident photon energy compared to that for materials having a wider band gap, 3) a denser ambient medium results in the formation of narrower ripple period. We now describe our view on the reasons responsible for the observations made in this experiment. The plausible explanation for all such observation is consistent with the theory that ripple formation is due to excitation of the surface plasmon at the semiconductor surface by the incident laser light with the rough target surface.

The surface plasmon is a well known phenomenon in the context of the metals, which have free electrons for excitation of this longitudinal charge density oscillation. However, in the case of semiconductors the origin of free electrons is because of the excitation of free electrons due to multi-photon ionization by the laser. The typical intensity of 2×10^{12} W/cm^2 is just sufficient to start plasma formation for an ultra-short (45 fs) laser pulse, wherein multi-photon ionization is the dominant process [242]. These laser-generated free electrons give a transient metallic character to the molten surface, which can now support the surface plasmon [200, 201]. During the initial few shots, the surface roughness is enhanced due to irradiation by the high intensity pulses and formation of random nano-structures [243]. The subsequent shots fired on the roughened surface lead to more efficient excitation of surface plasmon [244]. The molten material assumes the shape of a grating which satisfies the relation between wave vectors of the incident laser (which depends on its wavelength, the angle of incidence and the refractive index of the ambient medium) and the surface plasmon (which depends on the electron density of the molten surface). This grating gets frozen once the material cools down as soon as the laser pulse ends giving rise to the observed nano-ripples. The wave vector of this grating satisfies the following relation, as per the momentum conservation [201]

$$G = k_i - k_s \qquad (10.1)$$

where k_i is the wave vector of incident laser, and k_s is the wave vector of surface plasmon. By substituting the expression for *k's* in terms of corresponding wavelengths, and $|G|$ as $2\pi/d$ (where d is the ripple period), one gets the expression for d [201] as

$$d = \frac{\lambda_L}{\frac{\lambda_L}{\lambda_S} \pm \mu \sin\theta} \qquad (10.2)$$

Here λ_L ,λ_s, θ, μ are the incident laser (vacuum) wavelength, surface plasmon wavelength, the incident angle, and the refractive index of the ambient medium. It is clear from equation 10.2 that for normal incidence (i.e. $\theta = 0$) $d = \lambda_s$. Thus, at normal incidence, the ripple period d is equal to the surface plasmon wavelength, which is obtained from its dispersion relation as

$$\lambda_s = \frac{\lambda_L}{\sqrt{\frac{\varepsilon\varepsilon_m}{\varepsilon+\varepsilon_m}}}. \qquad (10.3)$$

Here ε is dielectric constant of the surface plasma created by the intense fs pulse and ε_m is the dielectric constant of the ambient medium (i.e. $\varepsilon_m = \mu^2$; 1 for air and 1.76 for water). Since the multi-photon ionized surface has free electrons, its dielectric constant can be taken similar to a plasma i.e. (neglecting the collision term frequency)

$$\varepsilon = 1 - \frac{n_e}{n_c}, \qquad (10.4)$$

where n_e is the surface plasma free electron density and n_c is the critical density corresponding to the laser wavelength. Putting the expression of ε in the equation 10.3 and then using equation 10.2 one gets for the case of normal incidence

$$d = \frac{\lambda_L}{\sqrt{\frac{\varepsilon_m(1-n_e/n_c)}{\varepsilon_m+(1-n_e/n_c)}}}. \qquad (10.5)$$

From equation 10.5 it is clearly seen that the ripple period is related to the incident laser wavelength, electron density of the surface plasma, and the dielectric constant of the ambient medium. It is also evident from the expression that real values of d will be obtained only if

$$n_e < n_c \quad \text{or} \quad n_e > (\varepsilon_m + 1)n_c. \qquad (10.6)$$

When this condition given by equation 10.6 is not satisfied, the nano-ripples are not formed.

Figure 10.6a shows the variation of nano-ripple period in air and water with electron density plotted using equation 10.5, for 800 nm wavelength. Figure 10.6b shows the corresponding curve for 400 nm wavelength.

A few conclusions can be made from these figures. There exist two branches of solutions for the nano-ripples, one is the super-wavelength nano-ripple and the other is the sub-wavelength nano-ripple. The super wavelength can be formed if the electron density is below the critical density, but such structures are not observed primarily due to two reasons, the first one is that being a low electron density process the plasmon excitation is very weak, and the second one is that the long period structure will have lower groove depth so that any short period structure may overshadow the long period one. The third possible reason could be that at such low fluence, the material simply does not melt to reorganize, thereby precluding any possibility of ripple formation. The sub-wavelength nano-ripples are formed if the electron density is greater than $n_c(\varepsilon_m+1)$. The nano-ripple period is equal to laser wavelength if the electron density is high and a very sharp decrease in the ripple period is observed when the electron density starts approaching $n_c(\varepsilon_m+1)$. If water is the ambient medium, then the nano-ripple period is smaller for the same electron density. Further, the figure also brings out the critical role of electron density in formation of large and narrow ripple formation. Since the electron density-generating surface during femtosecond laser pulse irradiation depends on the laser parameters like fluence and wavelength, a drastic change in the nano-ripple period is expected on a small variation of these parameters.

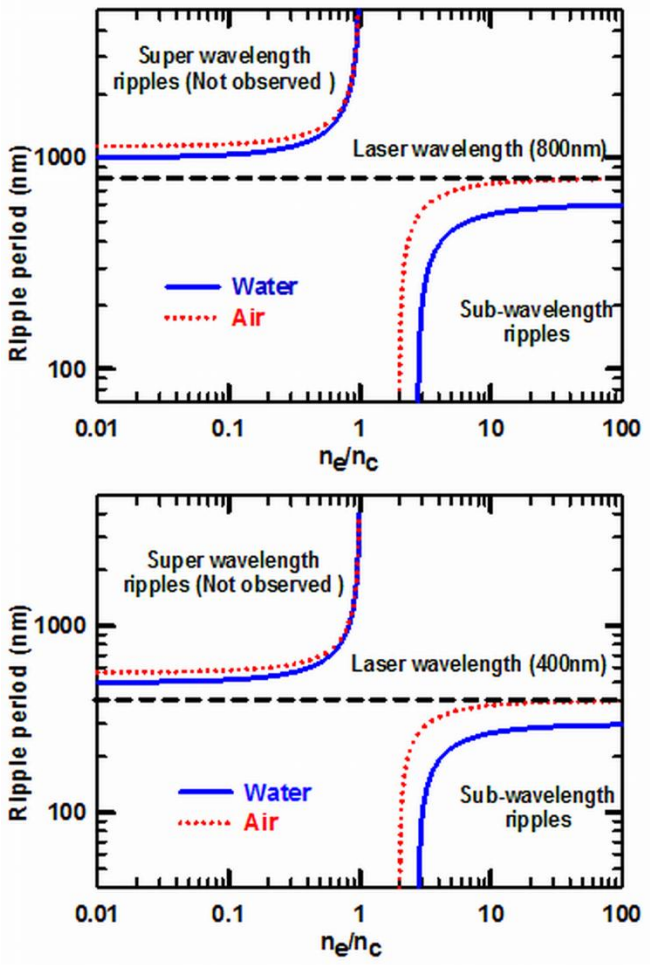

Fig.10.6 : Nano-ripple period as a function of the electron density for air (dotted line) and water (continuous line), using a) 800 nm pulses and b) 400 nm pulses

10.3.1 Ripple width vs. laser fluence

Now we come to the explanation of the experimental observations in terms of the above formulation. The observation from Fig.10.1 regarding narrow ripple of 200 nm width at the periphery of the focal spot and wider 600 nm ripple width in the central hot spot region can be explained as follows. Since the electron density of the laser irradiated surface is proportional to the incident laser fluence, higher intensity of irradiation in the central region of the focal spot will generate a higher electron density [245] leading to formation of wider nano-ripples of 600 nm

spacing, whereas at the region of the edges of focal spot, a lower fluence generates a lower electron density, which leads to a narrower (~ 200 nm) ripple formation. It is also seen from Fig. 10.6 that a slight change in the electron density can cause a drastic change of the ripple period and this explains the observation of the large difference in the ripple period in two spatial regions. The abrupt change in the ripple period is because, as explained earlier, it is very critically dependent on the electron density (see Fig.10.6). At high intensity, ripples slightly smaller than the laser wavelength are formed, and at mid range intensity or lower intensity, the ripple period can become very narrow depending on the free electron density generated on the surface. At very low intensities, no rippling takes place, as explained earlier. Of course, the semiconductor material chosen, its band gap and material breakdown property and irradiation intensity decide the electron density generated.

10.3.2 Ripple width vs. band gap

The main observation that narrow nano-ripples are formed on wide band gap material can also be explained in a similar way. When a femtosecond laser irradiates a narrow band gap material semiconductor surface, more free electrons are likely to be available in comparison to the case if the wide band gap material is irradiated by the same laser. This is because in addition to the multi-photon excitation of electrons, the single photon absorption process will also allow the excitation of free electrons, provided the incident photon energy is larger than the band gap. Therefore, the absorption of the ultra-short pulses in narrow band gap semiconductor material is through a combination of linear and nonlinear absorption process leading to a larger availability of free electrons in the conduction band. Therefore, as observed from Fig.10.2, the ripple period is large (~ 600 nm) in the case of narrow band gap materials, since a higher electron density (n_e

$>> n_c(\varepsilon_m+1)$) leads to formation of larger width nano-ripples. On the other hand, since the generated electron density for wide band gap material is low as single photon absorption is not possible, narrow ripples are formed in this case (provided the incident laser intensity is low).

10.3.3 Ripple width in different ambient

Next, we discuss the nano-ripple formation in GaAs in air and water. The ambient medium has substantial effect on the nano-ripple formation as expected from equation 10.2. This was experimentally was observed by Ganeev *et al* [246] for methanol as the surrounding medium. Our experiments in air and water were carried out at two fluences. At higher fluence, no nano-ripple formation takes place. As seen in Fig.10.3a, only random heterogeneities of few microns order (~ 2.5 μm) appear. At low fluence, sub-wavelength nano-ripples of 600 nm period are formed (Fig.10.3b). Such micron order microstructures have also been observed by Huang *et al*. [247]. They observed that as the laser fluence increases, the ripples become disordered due to the enhancement of the thermal effects. Also, as the laser fluence becomes high, the surface morphology evolves and the degree of ripple irregularity becomes large resulting in the dominant shift of spatial scales of the laser-induced structures from a few hundred nano-meters to a few micrometers. Next, in water, a drastic reduction of the nano-ripple period is recorded from 600 nm in air to about 150 nm in water. Such a reduction in nano-ripple period is expected from Fig.10.6 as already discussed. An interesting observation is that at high fluence irradiation of GaAs in water leads to nano-hole formation. The reason of nano-hole formation is still not understood, although its seems to be like a self organization process due to surface tension relaxation of strained molten GaAs against another liquid (in this case, water). The experiment

was repeated al low fluence for GaP (wide bandwidth material) which shows 200 nm nano-ripple period in air and 150 nm in water.

10.3.4 Ripple width at different incident laser angle

Many groups have done nano-ripple width study with different incident angles of the laser [248, 249]. There are contradictory observations regarding this, as some have reported increase of period with increase in angle of incidence [248], whereas some have shown decrease in the ripple period with angle of incidence [249]. In our experiment, we recorded an overall increase in ripple period with the angle of incidence for GaAs in water. As shown in Fig.10.4 a. GaP in water also shows an increase of ripple period from 150 nm to 300 nm, as the angle is increased from normal incidence to an angle of 30^0. However, the ripple period saturates at larger angles as seen from Fig.10.4b. These trends can be partially explained from equation 10.2 if one takes the "minus" sign. In that case, the denominator decreases in magnitude as the angle of incidence in increased, leading to an increase in the ripple period. Although this explanation holds true for GaAs which shows a continuous increase of ripple period with increasing angle, the same is not correct for GaP where ripple period shows saturation at larger angles. This shows that it is important to consider other factors which contribute to the variation of ripple period with angle of incidence. The most crucial among them is perhaps the electron density of the surface plasma created after irradiation of the semiconductor. The electron density generated, in turn, depends on the laser irradiation conditions (fluence, laser wavelength etc.) [245], material properties (band gap, melting point etc.) [20], and the absorption of laser energy in the material through linear (single photon absorption) and non linear processes (multi-photon absorption). As the angle of incidence is increased, the circular focal spot gets elongated and becomes elliptical, leading to a decrease in

the laser fluence. For example, at an incident angle of 45^{o}, the fluence becomes about 70% of the fluence at normal incidence. Therefore, as the angle is increased, the fluence decreases, resulting in the decrease of electron density of the surface plasma. This should lead to a decrease in the ripple period. However, as the angle of incidence is increased, the laser energy absorption also increases (up to the Brewster angle). The increase in the absorption is because the reflectivity of the *p*-polarized light keeps decreasing as the angle of incidence increases and approaches the Brewster angle. The range of angles covered by us is below the Brewster angle of the semiconductor (the Brewster angle of semiconductors is as high as $70\text{-}80^{o}$). This decreasing reflectivity leads to an enhanced absorption and hence a higher electron density, which should result in generation of larger period ripple. Therefore, resultant ripple period is governed by the above two competing processes of electron generation, one being fluence and the other being absorption. On increasing the angle of incidence, the fluence reduces and less electron generation is expected, but on the other hand, on increasing the angle, more laser light absorption will occur resulting in more electron generation. The relative dominance of the electron generation process viz. laser energy absorption or laser fluence, determines whether as a function of angle the electron density decrease or increase. One can now explain the observation that in the case of GaP the ripple period initially increases and then becomes nearly constant at larger angles (Fig.10.4b). It seems that in our experimental conditions, the laser energy absorption and the laser fluence compete against each other equally. The generated electron density is such that the ripple period becomes constant at higher angles for GaP. The monotonic increase of ripple period with the angle of incidence in the case of GaAs (Fig.10.4a) implies that the electron density in this case is continuously increasing on increasing the angle. This means that electron generation is dominated by absorption process and the fluence has comparatively less influence in the case of

GaAs. Had fluence been the more important parameter, the electron density would be reduced on increasing angle (due to the decrease of fluence), and the nano-ripple period would have decreased. Further, it may be noted that for *s*-polarized light, the period should be independent of the angle of incidence as the magnitude of the laser *k* vector in the direction of the surface plasmon remains unchanged in this case. However, as the angle increases, due to increasing reflectivity (due to *s*-polarization), the absorption of the laser light will keep decreasing with angle, leading to lower electro density and corresponding decrease in ripple period. Interestingly, the nano-holes formed on GaAs (at high laser fluence, in water) also showed increase for the hole diameter for higher angles of incidence (Fig.10.4c). Further experiments are needed to understand their generation mechanism.

10.3.5 Ripple width vs. incident wavelength

The role of the laser wavelength in changing the ripple period is seen from Fig.10.5. As expected from equation 10.5, the ripple period is expected to decrease by a factor of 2 as one goes from fundamental to the second harmonic laser beam, with other conditions remaining the same. This is precisely what is seen in Fig.10.5a for SiC (a wide band gap (3.37 eV) material for both wavelengths) and Fig.10.5b for InP (a narrow band gap (1.35 eV) material for both wavelengths). In both the cases, there is a reduction in the ripple period by a factor of 2 (190 nm to 90 nm and 620 nm to 280 nm). The observation in the case of GaP is just the opposite. Here the ripple period is observed to double (180 nm to 300 nm) instead of becoming half. This is because, GaP has a band gap energy of 2.3 eV, which is wide for 800 nm radiation (~ 1.56 eV), but narrow for 400 nm radiation (~3.12 eV). So, as a wide band gap material, GaP shows a

narrow ripple period (180 nm) for the fundamental (800 nm) and as a narrow band gap material, it shows larger ripple period (300 nm) for the second harmonic radiation (400 nm).

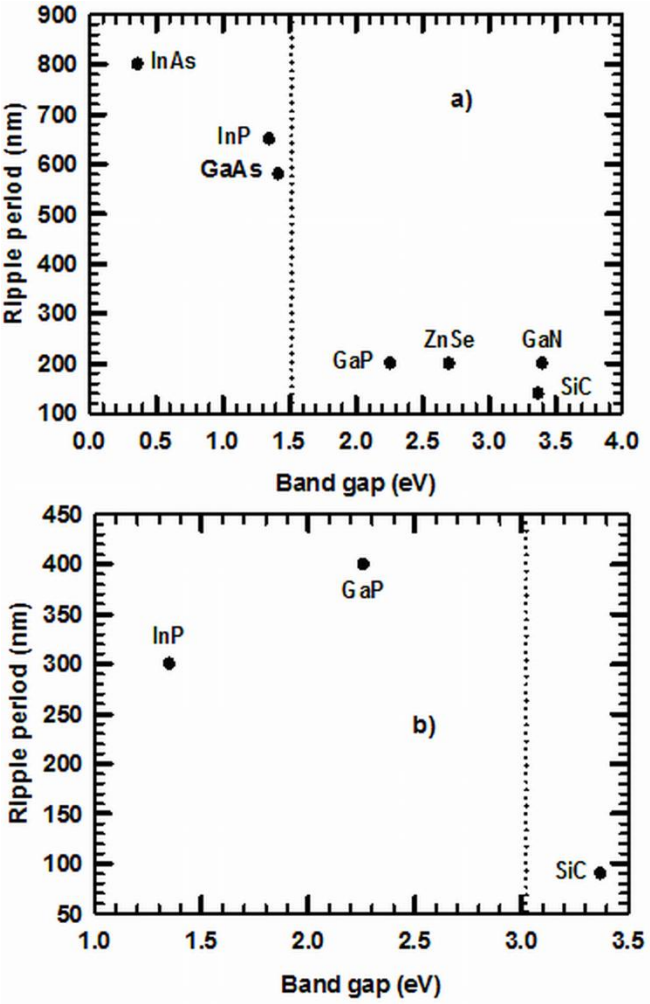

Fig.10.7 : Observed nano-ripple period as a function band gap. The dotted line indicates the incident laser photon energy for a) 800 nm pulses, and b) 400 nm pulses

The above correlation of the band gap with ripple period becomes more obvious in Fig.10.7. The vertical dotted line in Fig.10.7a is the photon energy of the 800 nm laser and for Fig. 10.7b the dotted line represents the photon energy of the 400 nm laser radiation. From these two graphs, it is clear that if the band gap of the semiconductor material is narrower than the incident photon energy, the ripple width formed is slightly less than, but of the order of the laser wavelength. For

the materials having a band gap larger than the energy of the laser photon, the ripple period is much smaller (typically of the order of 1/4th laser wavelength). The reasons for this difference have been already explained earlier in terms of single photon and multiple photon ionization of the molten surface.

10.3.6 Nano-ripples and melting point

Although most of the observations of ripple formation could be explained from the above formulation, there could be other parameters, which are responsible for finer variations of different nano-ripple formation of different materials. We have neglected the material parameters like melting point, conductivity of semiconductors, charge mobility, surface tension and viscosity of the molten material of the surface, which may also be very critical in deciding the resultant structure. For example, melting is one of the primary requirements of restructuring the surface. To see if the melting point plays a deciding role in ripple period, the ripple period has been plotted in Fig.10.8 as a function of melting point for various materials, at a constant laser fluence.

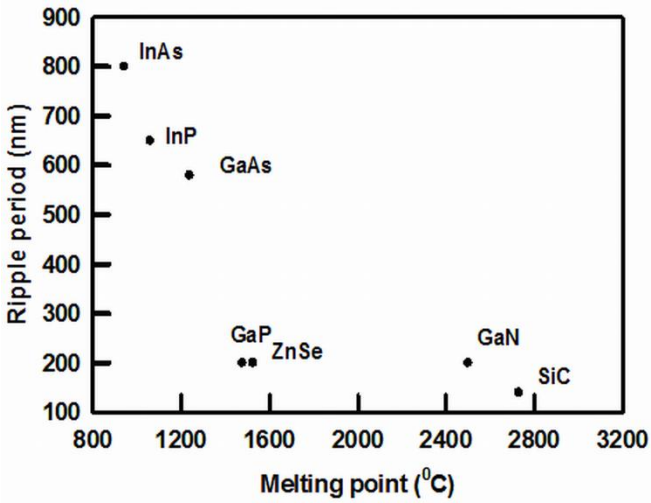

Fig.10.8 : Observed nano-ripple period as a function of melting point for various semiconductors

There is clear trend which shows materials having a high melting point form narrow ripples. Fig.10.8 seen in isolation would give an impression that melting point decided the ripple period. However, when seen with Fig.10.7b for the ripples formed with second harmonic laser beam, it becomes clear that looking at GaP ripple period, it is the band gap (relative to the laser photon energy), which decided the ripple period, and not the melting point, although melting is crucial in nano-ripple formation.

The observations which still need explanation are : 1) formation of nano-islands with circularly polarized light (Fig.10.1a); and 2) formation of nano-holes at high fluence irradiation under water (Fig.10.3 c).

The above studies have shown that, in general, narrow nano-ripples are formed from materials with a wide band gap. The width of the nano-ripples also decreases with the laser wavelength and the laser fluence. Under specific conditions, nano-hole formation is observed over a large area. The ambient medium can further help in narrowing down the ripple period formation. The observations are explained by considering the photo-ionization of the molten semiconductor surface on irradiation with intense femtosecond pulses, which support surface plasmon excitation, which in turn interferes with incident laser light to give rise to the ripple formation. The nano-ripples get frozen due to fast cooling once the laser pulse is over.

It must also be mentioned here that recent experiments have shown grating targets when irradiated with intense laser pulses leads to enhanced absorption, x-ray emission and high energy collimated electrons generation [162, 169, 195, 250]. Nano-ripples resemble grating like surface structure which may also be produced by ultra-short laser pulses on interaction with a solid surface. Properties of nano-ripples depend primarily on the ripple width. One can exploit the surface plasmon excitation in nano-ripples and the electron density at which this excitation will

take place. The surface plasmon excitation can be achieved at solid density from nano-ripples of ripple width of the order of wavelength. Therefore nano-ripples can be another candidate of *in situ* formed nano-structured targets and this possibility has to be explored in future.

Chapter 11

Conclusions and suggestions for future research

In this thesis work a detailed study on ultra-short high intensity laser absorption and x-ray emission from planar targets and various forms of nano-structures, has been carried out. As the absorption of the ultra-short intense laser pulses in smooth planar targets is less, therefore it becomes important to devise new techniques for increasing the laser energy coupling in high density matter. We have identified the conditions for maximizing absorption of intense ultra-short laser pulses in *in situ* formed nano-particles. The absorption was observed to exceed ~70% in silver clusters produced by a sub-ns pre-pulse. The high absorption resulted in an x-ray yield (in the >1 keV region) of ~ 60 μJ/ pulse, which corresponds to a conversion efficiency of 8.5×10^{-2} %. This scheme further led to an order of magnitude enhancement of x-ray emission in the water window spectral region utilizing the *in situ* formed carbon clusters, as compared to planar graphite target. Thus it is demonstrated to be a simple, single step, cost effective method to obtain a high rep-rate nearly debris free x-ray source. A high water window x-ray conversion of 0.54 % /sr of the ultra-short high intensity main pulse was recorded from carbon clusters.

Using various nano-structures like spherical nano-particles, nano-rods, nano-tubes, and nano-holes, high laser energy absorption is demonstrated, with near complete absorption in carbon nano-tubes. The theoretical consideration of nano-particle helped in understanding the role of target geometry on enhancement of electric field, resonances, and dynamics of the laser nano-structure interaction. We predicted analytically multiple resonances in hollow nano-structure, which can facilitate continued occurrence of resonance. As an experimental demonstration of the above prediction, it was shown that very efficient hot electron generation

takes place in carbon nano-tube-coated targets which results in enhanced characteristic K-shell line emission. Hollow target like nano-holes showed that the electric fields enhancement and energy deposition in them is very efficient. The peak of x-ray emission from nano-holes is attributed to the void closure and x-ray peaking time is proportional to the nano-hole diameter. A similar observation was noted from carbon nano-fibers where over an order of magnitude soft x-ray enhancement was recorded. Next, size control of nano-particle is an important aspect as the properties of nano- particles are highly size dependent. Since in the conventional methods, size control is difficult, we have shown that the size of the *in situ* formed nano-particles can be controlled easily by varying the incident laser pulse duration. A study of nano-ripple formation in various band gap semiconductors was also carried to study the dependence of ripple width on incident laser parameters, target material, band gap, and ambient medium. The nano-ripple formation is explained considering the transient metallic nature of the semiconductor surface on irradiation with intense femtosecond pulse which excites surface plasmon leading to the nano-ripple formation. In general, the observations help in identifying various conditions to grow the nano-ripples with controllable ripple period.

An extensive work has been carried on studying the laser interaction with nano-form matter with two different strategies : first forming the nano-targets *in situ* by a portion of laser beam itself, and second using different nano-structures to study effect of shape, size and the structure geometry. Still there are more avenues that need to be explored that can be very exciting and promising as the present work indicates. Enhanced hard x-ray emission from the hollow nano-structures indicates efficient hot electron generation processes taking place in them. The role of target structure in the generation of hot electrons and their subsequent propagation is a point that needs to be explored further. Collimated propagation of charged

particles produced from intense laser fields is a hot topic of research since it is directly related to the solution of problems of beam filamentation faced in fast ignition scheme. Therefore various novel targets have to be explored and designed in future to overcome such problems.

Next, generation of nano-structures in itself is a very interesting field of research and very promising for applications. Our study show that in pulsed laser deposition scheme, the variation of the laser pulse duration is a versatile method to change the size of the cluster. Therefore this opens lot many possibilities of exploring various targets and laser parameters to form clusters. Moreover, it will also be interesting to record the hard and soft x-ray emission from various sized clusters of many materials.

We also did the study on nano-ripple formation and developed an understanding on the mechanism of nano-ripple formation, which helped in controlling the ripple width. This again hints to the possibility of *in situ* forming a ripple or grating like structure by a low intensity ultra-short pulse and then irradiating them with intense laser pulses. By forming ripples of desired period, the surface plasmon can be excited resonantly at solid density by the intense ultra-short laser pulses which may lead to efficient absorption, x-ray emission and hot electron generation.

Bibliography

[1] W. T. Silfvast. "*Laser fundamentals*." Cambridge University Press (2004)

[2] A. K. Ghatak. "Lasers: theory and applications." *New York, Plenum Press* (1981)

[3] H. Joachim, and Bernd Wilhelmi. "Lasers for ultra-short light pulses." (1987). Elsevier Science Pub. Co. Inc.,New York, NY (2008)

[4] D. Strickland and G. Mourou, "Compression of amplified chirped optical pulses", Opt. Commun. **56**, 219 (1985)

[5] V. Yanovsky, V. Chvykov, G. Kalinchenko, P. Rousseau, T. Planchon, T. Matsuoka, A. Maksimchuk et al. "Ultra-high intensity-300-TW laser at 0.1 Hz repetition rate." *Opt. Express* **16**, 2109-2114 (2008)

[6] B. A. Remington, D. Arnett, R. Paul, and H. Takabe, "Modeling astrophysical phenomena in the laboratory with intense lasers." *Science* **284**, 1488-1493 (1999)

[7] M.H. Key, J. C. Adam, K. U. Akli, M. Borghesi, M. H. Chen, R. G. Evans, R. R. Freeman et al. "Fast ignition relevant study of the flux of high intensity laser-generated electrons via a hollow cone into a laser-imploded plasma." *Physics of Plasmas* **15**, 022701 (2008)

[8] G. Mourou, T. Tajima, and S. V. Bulanov, "Optics in the relativistic regime." *Reviews of Modern Physics* **78**, 309 (2006)

[9] S.P.D. Mangles, C. D. Murphy, Z. Najmudin, A. G. R. Thomas, J. L. Collier, A. E. Dangor, E. J. Divall et al. "Monoenergetic beams of relativistic electrons from intense laser–plasma interactions." *Nature* **431**, 535-538 (2004)

[10] V. Malka, S. Fritzler, E. Lefebvre, M-M. Aleonard, F. Burgy, J-P. Chambaret, J.F. Chemin et al. "Electron acceleration by a wake field forced by an intense ultra-short laser pulse." *Science* **298**, 1596-1600 (2002)

[11] L. Willingale, S. P. D. Mangles, P. M. Nilson, R. J. Clarke, A. E. Dangor, M. C. Kaluza, S. Karsch et al. "Collimated multi-MeV ion beams from high-intensity laser interactions with underdense plasma." *Physical review letters* **96**, 245002 (2006)

[12] H. Habara, K. L. Lancaster, S. Karsch, C. D. Murphy, P. A. Norreys, R. G. Evans, M. Borghesi et al. "Ion acceleration from the shock front induced by hole boring in ultra-intense laser-plasma interactions." *Physical Review E* **70**, 046414 (2004)

[13] Ch. Joshi, "The development of laser-and beam-driven plasma accelerators as an experimental field." *Physics of plasmas* **14**,055501 (2007)

[14] B. Dromey, M. Zepf, A. Gopal, K. Lancaster, M. S. Wei, K. Krushelnick, M. Tatarakis et al. "High harmonic generation in the relativistic limit." *Nature physics* **2**, 456-459 (2006)

[15] U. Teubner, C. Wülker, W. Theobald, and E. Förster. "X-ray spectra from high intensity subpicosecond laser produced plasmas." *Physics of Plasmas* **2**, 972 (1995)

[16] C.G. Serbanescu, J. A. Chakera, and R. Fedosejevs. "Efficient K α x-ray source from submillijoule femtosecond laser pulses operated at kilohertz repetition rate." *Review of scientific instruments* **78**, 103502 (2007)

[17] J. Yu, Z. Jiang, J. C. Kieffer, and A. Krol. "Hard x-ray emission in high intensity femtosecond laser-target interaction." *Physics of plasmas* **6**, 1318 (1999)

[18] F.F. Chen, and M. A. Lieberman. *Introduction to plasma physics and controlled fusion/Francis F.* : Plenum Press, New York, 1984, Eliezer, Shalom. *The interaction of high-power lasers with plasmas*. CRC Press (2010.)

[19] M. Dunne, "A high-power laser fusion facility for Europe." *Nature Physics* **2**, 2-5 (2006)

[20] T. Ozaki, R. A. Ganeev, A. Ishizawa, T. Kanai, and H. Kuroda. "Highly directive 18.9 nm nickel-like molybdenum x-ray laser operating at 150 mJ pump energy." *Physical review letters* **89**, 253902 (2002)

[21] Helliwell, John R., and Peter M. Rentzepis, eds. *Time-resolved diffraction*. No. 2. Oxford University Press (1997)

[22] J. Larsson, P.A. Heimann, A. M. Lindenberg, P. J. Schuck, P. H. Bucksbaum, R. W. Lee, H. A. Padmore, J. S. Wark, and R. W. Falcone. "Ultrafast structural changes measured by time-resolved X-ray diffraction." *Applied Physics A: Materials Science & Processing* **66**, 587-591 (1998)

[23] L. Yin, B. J. Albright, B. M. Hegelich, Kevin J. Bowers, K. A. Flippo, T. J. T. Kwan, and J. C. Fernández. "Monoenergetic and GeV ion acceleration from the laser breakout after burner using ultrathin targets." *Physics of plasmas* **14**, 056706 (2007)

[24] N. Hafz, T. M. Jeong, W. Choi, S. K. Lee, K.H. Pae, V. V. Kulagin, J. H. Sung et al. "Stable generation of GeV-class electron beams from self-guided laser–plasma channels." *Nature Photonics* **2**, 571-577 (2008)

[25] P. Zeitoun, G. Faivre, S. Sebban, T. Mocek, A. Hallou, M. Fajardo, D. Aubert et al. "A high-intensity highly coherent soft X-ray femtosecond laser seeded by a high harmonic beam." *Nature* **431**, 426-429 (2004)

[26] P. B. Corkum, "Plasma perspective on strong field multiphoton ionization." *Physical Review Letters* **71**, 1994 (1993)

[27] L. V. Keldysh, "Diagram technique for nonequilibrium processes." *Sov. Phys. JETP* **20**, 1018-1026 (1965)

[28] H. R. Reiss, and V. P. Krainov. "Approximation for a Coulomb-Volkov solution in strong fields." *Physical Review A* **50**, R910 (1994)

[29] A. Scrinzi, M. Geissler, and T. Brabec. "Ionization above the Coulomb barrier." *Physical review letters* **83**, 706 (1999)

[30] P. Gibbon, "*Short pulse laser interactions with matter*" London: Imperial College Press, (2005)

[31] W. L. Kruer, "*The Physics of Laser Plasma Interactions"* Addison-Wesley, New York, 1988)

[32] M. Born and E. Wolf, *Principles of Optics*, fourth edition, Pergamon Press, Oxford (1970)

[33] P. Mulser, "*Theory of Plasma Wave Absorption*, in *Laser Interaction with Atoms, Solids and Plasmas"* Plenum Press, New York, p.383 (1994)

[34] P. Mulser, D. Bauer, and H. Ruhl. "Collisionless laser-energy conversion by anharmonic resonance." *Physical review letters* **101**, 225002 (2008)

[35] K. R. Manes, V. C. Rupert, J. M. Auerbach, P. Lee, and J. E. Swain. "Polarization and angular dependence of 1.06 μm laser-light absorption by planar plasmas." *Phys. Rev. Lett.* **39**, 281(1977)

[36] R. Fedosejevs, R. Ottmann, R. Sigel, G. Kühnle, S. Szatmari, and F. P. Schäfer. "Absorption of femtosecond laser pulses in high-density plasma." *Physical review letters* **64**, 1250 (1990)

[37] P. Mora, "Theoretical model of absorption of laser light by a plasma." *Physics of Fluids* **25**, 1051-1056 (1982)

[38] Garban-Labaune, C., E. Fabre, C. E. Max, R. Fabbro, F. Amiranoff, J. Virmont, M. Weinfeld, and A. Michard. "Effect of laser wavelength and pulse duration on laser-light absorption and back reflection." *Physical Review Letters* **48,** 1018-1021 (1982)

[39] D. F. Price, R. M. More, R. S. Walling, G. Guethlein, R. L. Shepherd, R. E. Stewart, and W. E. White. "Absorption of ultra-short laser pulses by solid targets heated rapidly to temperatures 1–1000 eV." *Physical review letters* **75**, 252 (1995)

[40] D. Riley, L. A. Gizzi, A. J. Mackinnon, S. M. Viana, and O. Willi. "Absorption of high-contrast 12-ps uv laser pulses by solid targets." *Physical Review E* 48, 4855 (1993)

[41] R. Keenan, J. Dunn, P. K. Patel, D. F. Price, R. F. Smith, and V. N. Shlyaptsev. "High-repetition-rate grazing-incidence pumped x-ray laser operating at 18.9 nm." *Physical review letters* **94**, 103901 (2005)

[42] R.P. Godwin, "Absorption in laser-produced plasma experiments: a personal view." *Applied Optics* **18**, 3555-3561 (1979)

[43] J. E. Balmer, and T. P. Donaldson. "Resonance absorption of 1.06 μm laser radiation in laser-generated plasma." *Phys. Rev. Lett.* **39**, 1084 (1977)

[44] O. L. Landen, D. G. Stearns, and E. M. Campbell. "Measurement of the expansion of picosecond laser-produced plasmas using resonance absorption profile spectroscopy." *Physical review letters* **63**, 1475 (1989)

[45] H. M. Milchberg, and R. R. Freeman. "Light absorption in ultra-short scale length plasmas." *JOSA B* 6, 1351-1355 (1989)

[46] D. W. Forslund, J. M. Kindel, K. Lee, E. L. Lindman, and R. L. Morse. "Theory and simulation of resonant absorption in a hot plasma." *Physical Review A* **11**, 679 (1975)

[47] P. P. Rajeev, S. Banerjee, A. S. Sandhu, R. C. Issac, L. C. Tribedi, and G. Ravindra Kumar. "Role of surface roughness in hard-x-ray emission from femtosecond-laser-produced copper plasmas." *Physical Review A* **65**, 052903 (2002)

[48] R. A. Cairns, "Resonant absorption at a rippled critical surface." *Plasma Physics* **20**, 991 (1978)

[49] J. J. Thomson, W. L. Kruer, A. B. Langdon, C. E. Max, and W. C. Mead. "Theoretical interpretation of angle-and polarization-dependent laser light absorption measurements." *Physics of Fluids* **21**, 707 (1978)

[50] M. Borghesi, A. J. MacKinnon, A. R. Bell, R. Gaillard, and O. Willi. "Megagauss magnetic field generation and plasma jet formation on solid targets irradiated by an ultra-intense picosecond laser pulse." *Physical review letters* **81**, 112 (1998)

[51] A. S. Sandhu, A. K. Dharmadhikari, P. P. Rajeev, G. Ravindra Kumar, S. Sengupta, A. Das, and P. K. Kaw. "Laser-generated ultra-short multimegagauss magnetic pulses in plasmas." *Physical review letters* **89**, 225002 (2002)

[52] S.C. Wilks, and W. L. Kruer. "Absorption of ultra-short, ultra-intense laser light by solids and overdense plasmas." *Quantum Electronics, IEEE Journal of* **33**, 1954-1968 (1997)

[53] F. Brunel, "Not-so-resonant, resonant absorption." *Physical Review Letters* **59**, 52 (1987)

[54] M. K. Grimes, Y-S. Lee, A. R. Rundquist, and M. C. Downer. "Experimental identification of "vacuum heating" at femtosecond-laser-irradiated metal surfaces." In *High-Field Science*, 61-72. Springer US, (2000)

[55] L. M. Chen, J. Zhang, Q. L. Dong, H. Teng, T. J. Liang, L. Z. Zhao, and Z. Y. Wei. "Hot electron generation via vacuum heating process in femtosecond laser–solid interactions." *Physics of Plasmas* **8**, 2925 (2001)

[56] P. Gibbon, and A. R. Bell. "Collisionless absorption in sharp-edged plasmas." *Physical review letters* **68**, 1535 (1992)

[57] F. Brunel, "Anomalous absorption of high intensity subpicosecond laser pulses." *Physics of Fluids* **31**, 2714-2719 (1988)

[58] M. Cerchez, R. Jung, J. Osterholz, T. Toncian, O. Willi, P. Mulser, and H. Ruhl. "Absorption of ultra-short laser pulses in strongly overdense targets." *Physical review letters* **100**, 245001 (2008)

[59] Y. Ping, R. Shepherd, B. F. Lasinski, M. Tabak, H. Chen, H. K. Chung, K. B. Fournier et al. "Absorption of short laser pulses on solid targets in the ultrarelativistic regime." *Physical review letters* 100, 085004 (2008)

[60] W.L. Kruer, and K. Estabrook. "J× B heating by very intense laser light." *Physics of Fluids* **28**, 430 (1985)

[61] R. Shepherd, H. Chen, Y. Ping, G. Dyer, S. Wilks, H. Chung, A. Kemp et al. *Short Pulse Laser Absorption and Energy Partition at Relativistic Laser Intensities*. No. UCRL-TR-229579. Lawrence Livermore National Laboratory (LLNL), Livermore, CA, (2007)

[62] W. Wang , J. Liu, Y. Cai, C. Wang, L. Liu, C. Xia, A. Deng et al. "Angular and energy distribution of fast electrons emitted from a solid surface irradiated by femtosecond laser pulses in various conditions." *Physics of Plasmas* **17**, 023108 (2010)

[63] D. F. Cai, Y. Q. Gu, Z. J. Zheng, T. S. Wen, S. T. Chunyu, Z. B. Wang, and X. D. Yang. "Experimental study for angular distribution of the hot electrons generated by femtosecond laser interaction with solid targets." *Physics of Plasmas* 10, 3265 (2003)

[64] M. M. Murnane, H. C. Kapteyn, and R. W. Falcone. "High-density plasmas produced by ultrafast laser pulses." *Physical review letters* **62**, 155 (1989)

[65] M. Borghesi, A. J. Mackinnon, R. Gaillard, O. Willi, and D. Riley. "Absorption of subpicosecond uv laser pulses during interaction with solid targets." *Physical Review E* **60**, 7374 (1999)

[66] T. Feurer, W. Theobald, R. Sauerbrey, I. Uschmann, D. Altenbernd, U. Teubner, P. Gibbon, E. Förster, G. Malka, and J. L. Miquel. "Onset of diffuse reflectivity and fast electron flux inhibition in 528-nm-laser–solid interactions at ultrahigh intensity." *Physical Review E* **56**, 4608 (1997)

[67] A. S. Sandhu, G. R. Kumar, S. Sengupta, A. Das, and P. K. Kaw. "Laser-pulse-induced second-harmonic and hard x-ray emission: role of plasma-wave breaking." *Physical review letters* **95**, 025005 (2005)

[68] A. Hyeyoung, H. Nakano, T. Nishikawa, and N. Uesugi. "Simultaneous measurement of absorption and x-ray emission from preformed plasma generated by ultra-short prepulse." *Japanese Journal of Applied Physics-Part 2 Letters* **35**, L154 (1996)

[69] T. Palchan, S. Peckerand, Z. Henis, S. Eisenmann and A. Zigler, "Efficient coupling of high intensity short laser pulses into snow clusters", *Appl. Phys. Lett.* **90**, 041501, (2007)

[70] G. Kulcsar, D. AlMawlawi, F. W. Bundnik, P. R. Herman, M. Moskovits, L. Zhao, and R. S. Marjoribanks, "Intense picosecond x-ray pulses from laser plasmas by use of nano-structured "Velvet" targets", *Phys. Rev. Lett*. **84**, 5149 (2000)

[71] M. M. Murnane, H. C. Kapteyn, S. P. Gordon, J. Bokor, and E. N. Glytsis, "Efficient coupling of high-intensity subpicosecond laser pulses into solids", *Appl. Phys. Lett.* **62**, 1068, (1993)

[72] M. Krishnamurth, S. Mondal, A. D. Lad, K. Bane, S. Ahmed, V. Narayanan, R. Rajeev et al. "A bright point source of ultra-short hard x-ray pulses using biological cells." *Optics express* **20**, 5754-5761 (2012)

[73] A. Zigler, T. Palchan, N. Bruner, E. Schleifer, S. Eisenmann, M. Botton, Z. Henis, S. A. Pikuz, A. Y. Faenov, Jr., D. Gordon, and P. Sprangle, "5.5-7.5 MeV proton generation by a moderate intensity ultra-short-pulse laser interaction with H_2O nano-wire targets", *Phys. Rev. Lett.* **106**, 134801 (2011)

[74] T. Ditmire, J. Zweiback, V. P. Yanovsky, T. E. Cowan, G. Hays and K. B. Wharton, "Nuclear fusion from explosions of femtosecond laser-heated deuterium clusters", Nature **398**, 489 (1999)

[75] Y. L. Shao, T. Ditmire, J. W. G. Tisch, E. Springate, J. P. Marangos, and M. H. R. Hutchinson, "Multi-keV electron generation in the interaction of intense laser pulses with Xe clusters", *Phys. Rev. Lett.* **77**, 319007 (1996)

[76] P. P. Rajeev, P. Taneja, P. Ayyub, A. S. Sandhu, and G. R. Kumar, "Metal nano-plasmas as bright sources of hard x-ray pulses", *Phys. Rev. Lett.* **90**, 115002 (2003)

[77] S. Kim, J. Jin, Y. J. Kim, I.Y. Park, Y. Kim, and S. W. Kim, "High-harmonic generation by resonant plasmon field enhancement", Nature **453**, 757 (2008).

[78] S. Bagchi, P. P. Kiran, M. K. Bhuyan, S. Bose, P. Ayyub, M. Krishnamurthy, and G. R. Kumar, "Hot ion generation from nano-structured surfaces under intense femtosecond laser irradiation", *Appl. Phys. Lett.* **90**, 141502 (2007)

[79] R. A. Ganeev, L. B. Elouga Bom, J. Abdul-Hadi, M. C. H. Wong, J. P. Brichta, V. R. Bhardwaj, and T. Ozaki, "Higher-order harmonic generation from fullerene by means of the plasma harmonic method", *Phys. Rev. Lett.* **102**, 013903 (2009)

[80] T. Nishikawa, H. Nakano, K. Oguri, N. Uesugi, K. Nishio, and H. Masuda, "Nano-hole-array size dependence of soft x-ray generation enhancement from femtosecond-laser-produced plasma", *J. Appl. Phys.* **96**, 7537 (2004)

[81] T. Nishikawa,H. Nakano, H. Ahn, and N. Uesugi, "X-ray generation enhancement from a laser-produced plasma with a porous silicon target", *Appl. Phys. Lett*. **70**, 1653 (1997)

[82] Z. Zhao, Lihua Cao, Leifeng Cao, J.Wang, W. Huang, W. Jiang, Y. He, Y.Wu, B. Zhu, K. Dong, Y. Ding, B. Zhang, Y. Gu, M. Y. Yu, and X. T. He, "Acceleration and guiding of fast electrons by a nano-brush target", *Phys. Plasmas* **17**, 123108 (2011)

[83] T. Nishikawa, S. Suzuki, Y. Watanabe, O. Zhou, H. Nakano, "Efficient water-window x-ray pulse generation from femtosecond-laser-produced plasma by using a carbon nano-tube target ", *Appl. Phys. B* **78**, 885 (2004)

[84] S. Bagchi, P. P. Kiran, M. K. Bhuyan, M. Krishnamurthy, K. Yang, A.M. Rao, G. R. Kumar, "Bright, low debris, ultra-short hard x-ray table top source using carbon nano-tubes ", *Phys. Plasmas* **18**, 014502 (2011)

[85] Y. Ji, G. Jiang, W.Wu, C. Wang, Y. Gu, and Y. Tang, "Efficient generation and transportation of energetic electrons in a carbon nano-tube array target", *Appl. Phys. Lett*. **96**, 041504 (2010)

[86] Lihua Cao, Y. Gu, Z. Zhao, Leifeng Cao, W. Huang, W. Zhou, H. B. Cai, X. T. He, Wei Yu, and M. Y. Yu, "Control of the hot electrons produced by laser interaction with nano-layered target", *Phys. Plasmas* **17**, 103106 (2010)

[87] P. P. Rajeev, P. Ayyub, S. Bagchi, and G. R. Kumar, "Nano-structures, local fields, and enhanced absorption in intense light-matter interaction ", *Optics Letters* **29**, 22 (2004)

[88] T. Ditmire, R. A. Smith, J. W. G. Tisch, and M. H. R. Hutchinson, "High intensity laser absorption by gases of atomic clusters", *Phys. Rev. Lett.* **78**, 3121 (1997)

[89] B. Ziaja, H. Wabnitz, F. Wang, E. Weckert , and T. Möller, “Energetics, ionization, and expansion dynamics of atomic clusters irradiated with short intense vacuum-ultraviolet pulses”, *Phys. Rev. Lett.* **102**, 205002 (2009)

[90] F. Dorchies, F. Blasco, C. Bonté, T. Caillaud, C. Fourment, and O. Peyrusse, “Observation of subpicosecond x-ray emission from laser-cluster interaction”, *Phys. Rev. Lett.* **100**, 205002 (2008)

[91] A. McPherson, B. D. Thompson, A. B. Borisov, K. Boyer, and C. K. Rhodes, “Multiphoton-induced x-ray emission at 4–5 keV from Xe atoms with multiple core vacancies,” *Nature* **370**, 631 (1994)

[92] O. F. Hagena, and W. Obert. "Cluster formation in expanding supersonic jets: effect of pressure, temperature, nozzle size, and test gas." *The Journal of Chemical Physics* **56**, 1793 (1972)

[93] E. M. Snyder, S. A. Buzza, and A. W. Castleman, “Intense field-matter interactions: multiple ionization of clusters”, *Phys. Rev. Lett*. **77**, 3347 (1996)

[94] U. Saalmann and J. M. Rost, “Ionization of Clusters in Intense Laser Pulses through Collective Electron Dynamics”, *Phys. Rev. Lett*. **91**, 223401 (2003)

[95] T. Ditmire, J. W. G. Tisch, E. Springate, M. B. Mason, N. Hay, R. A. Smith, J. Marangos, and M. H. R. Hutchinson, “High-energy ions produced in explosions of superheated atomic clusters”, *Nature* **386**, 54 (1997)

[96] T. Ditmire, T. Donnelly, A. M. Rubenchik, R. W. Falcone, and M. D. Perry, “Interaction of intense laser pulses with atomic clusters,” *Phys. Rev. A*. **53**, 3379 (1996)

[97] J. Zweiback, T. Ditmire, and M. D. Perry, “Femtosecond time-resolved studies of the dynamics of noble-gas cluster explosions”, *Phys. Rev. A* **59**, R3166 (1999)

[98] H. Singhal, V. Arora, P.A. Naik and P.D. Gupta, "Spectral blue-shifts in laser light scattered from argon-gas cluster plasmas”, *Phys. Rev. A*. **72**, 43201 (2005)

[99] S. Sailaja, R.A. Khan, P.A. Naik, and P.D. Gupta, “Efficient absorption and intense x-ray emission from gas cluster plasmas irradiated by 25 ps laser pulses,” *IEEE Tr. Plasma Sci*. **33**, 1006 (2005)

[100] A. M. Bystrov and V. B. Gildenburg, “ Infrared to ultraviolet light conversion in laser-cluster interactions”, *Phys. Rev. Lett.* **103**, 083401 (2009)

[101] F. Dorchies, T. Caillaud, F. Blasco, C. Bonté, H. Jouin, S. Micheau, B. Pons, and J. Stevefelt, “Investigation of laser-irradiated Ar cluster dynamics from *K*-shell x-ray emission measurements”, *Phys. Rev. E* **71**, 066410 (2005)

[102] Milchberg, H. M., S. J. McNaught, and E. Parra. "Plasma hydrodynamics of the intense laser-cluster interaction." *Physical Review E* **64**, 056402 (2001)

[103] Holkundkar, Amol R., and N. K. Gupta. "Role of radial nonuniformities in the interaction of an intense laser with atomic clusters." *Physics of Plasmas* **15**, 013105 (2008)

[104] Saalmann, Ulf, and Jan-Michael Rost. "Ionization of clusters in intense laser pulses through collective electron dynamics." *Physical review letters* **91**, 223401 (2003)

[105] M. Kundu, and D. Bauer. "Nonlinear resonance absorption in the laser-cluster interaction." *Physical review letters* **96**, 123401 (2006)

[106] P. Mulser, and M. Kanapathipillai. "Collisionless absorption in clusters out of linear resonance." *Physical Review A* **71**, 063201 (2005)

[107] M. Kumar, and V. K. Tripathi. "Nonlinear absorption and harmonic generation of laser in a gas with anharmonic clusters." *Physics of Plasmas* **20**, 023302 (2013)

[108] I.C.E. Turcu and J.B. Dance, "*X-rays from Laser Plasmas"* (New York, Wiley, 1999)

[109] C. Reich, P. Gibbon, I. Uschmann, and E. Förster. "Yield optimization and time structure of femtosecond laser plasma Kα sources." *Physical Review Letters* **84**, 4846 (2000)

[110] D. E. Spence, P. N. Kean, and W. Sibbett, "60-fsec pulse generation from a self-mode-locked Ti:sapphire laser" Optics Letters **16** , 42-44 (1991)

[111] A. Brun. P. Georges, G. Le Saux and F. Satin, "Single-shot characterization of ultra-short light pulses", J. Phys. D: Appl. Phys. **24**, 1225 (1991).

[112] C. Tillman, S. Å. Johansson, B. Erlandsson, M. Grätz, B. Hemdal, A. Almén, S. Mattsson, S. Svanberg" High-resolution spectroscopy of laser-produced plasmas in the photon energy range above 10 keV" *Nucl. Instr. and Meth. A* **394**, 387 (1997)

[113] L. M. Chen, P. Forget, R. Toth, J. C. Kieffer, A. Krol, C. C. Chamberlain, B. X. Hou, J. Nees, and G. Mourou. "High resolution hard x-ray spectroscopy of femtosecond laser-produced plasmas with a CZT detector." *Review of scientific instruments* **74**, 5035-5038 (2003)

[114] C. Stoeckl, W. Theobald, T. C. Sangster, M. H. Key, P. Patel, B. B. Zhang, R. Clarke, S. Karsch, and P. Norreys. "Operation of a single-photon–counting x-ray charge-coupled device camera spectrometer in a petawatt environment." *Review of scientific instruments* **75**, 3705-3707 (2004)

[115] L. Labate., A. Giulietti, D. Giulietti, P. Koster, T. Levato, L. A. Gizzi, F. Zamponi et al. "Novel x-ray multispectral imaging of ultraintense laser plasmas by a single-photon charge coupled device based pinhole camera." *Review of Scientific Instruments* **78**, 103506-103506 (2007)

[116] W. Fullagar, J. Uhlig, M. Walczak, S. Canton, and V. Sundstrom. "The use and characterization of a backilluminated charge-coupled device in investigations of pulsed x-ray and radiation sources." *Review of scientific instruments* **79**, 103302-103302 (2008)

[117] V. Arora, H.S. Vora, J.A. Chakera, M. Tayyab, P.A. Naik, and P.D. Gupta, "Dispersion-less spectrograph for absolute measurement of multi keV x-ray flux from high intensity laser produced plasmas" J. Instrum. **8**, P01010 (2013)

[118] N.M. Ceglio, R. L. Kauffman, A. M. Hawryluk, and H. Medecki. "Time-resolved x-ray transmission grating spectrometer for studying laser-produced plasmas." *Applied optics* **22**, 318-327 (1983)

[119] S. Sailaja, V. Arora, S. R. Kumbahre, P. A. Naik, P.D. Gupta, D. A. Fedin, A. A. Rupasov, and A. S. Shikanov, "A simple XUV transmission grating spectrograph with sub-angstrom resolution for laser–plasma interaction studies" Meas. Sci. Technol. **9**, 1462 (1998)

[120] S. Sailaja , V. Arora, S.R. Kumbhare, P.A. Naik, P.D. Gupta "Study of diffraction efficiency of a free-standing transmission grating in keV spectral region using laser produced plasmas" Optics & Laser Technology **30**, 407 (1998)

[121] U. Kreibig and M. Vollmer, *Optical Properties of Metal Clusters*, Springer Verlag, Berlin (1995)

[122] C. F. Bohren and D. R. Huffman, *Absorption and Scattering of Light by Small Particles,* Wiley, New-York (1998)

[123] G. Mie, Ann. Phys., Lpz. 25, 377 (1908) G. Mie, Beitr¨age zur Optik Tr¨uber Medien, speziell Kolloidaler Metall¨osungen, Ann.Phys., **25**, 377-452 (1908)

[124] P. Taneja, P. Ayyub, and R.Chandra. "Size dependence of the optical spectrum in nanocrystalline silver." *Physical Review B* **65**, 245412 (2002)

[125] R.H Baughman, H., Anvar A. Zakhidov, and Walt A. de Heer. "Carbon nanotubes--the route toward applications." *Science* **297**, 787-792 (2002)

[126] A. S. Edelstein and R. C. Cammarata, *Nanomaterials: Synthesis, Properties and Applications,* Institute of Physics Publishing, Bristol (1996).

[127] M.S. Gudiksen, L. J. Lauhon, J. Wang, D. C. Smith, and C. M. Lieber. "Growth of nanowire superlattice structures for nanoscale photonics and electronics." *Nature* **415**, 617-620 (2002)

[128] C. J. Zhong and M. M. Maye, Adv. Mater. **13**, 1507 (2001).

[129] N. Sano, "Formation of multi-shelled carbon nanoparticles by arc discharge in liquid benzene." *Materials chemistry and physics* 88, 235-238 (2004)

[130] S.L. Stoll, E.G. Gillan, and A.R. Barron, Chem. Vap. Deposition. "Chemical vapor deposition of gallium selenide and indium selenide nanoparticles." **2**, 182 (1996).

[131] S. Banerjee, S. Roy, J.W. Chen, and D. Chakravorty, J. Magn. Mater. "Magnetic properties of oxide-coated iron nanoparticles synthesized by electrodeposition." **219**, 45 (2000).

[132] R.Teghil, L.D.Alessio, A.Santagata, M.Zaccagnino, D.Ferro, and D.Sordelet, "Picosecond and femtosecond pulsed laser ablation and deposition of quasicrystals." Appl. Surf.Sci. **210** 307 (2003).

[133] S. Eliezer, N. Eliaz, E. Grossman, D. Fisher, I. Gouzman, Z. Henis, S. Pecker, Y. Horovitz, M. Fraenkel, S. Maman, and Y. Lereah, "Synthesis of nanoparticles with femtosecond laser pulses." Phys. Rev. B **69**, 144119 (2004).

[134] S. Amoruso, R. Bruzzese, M. Vitiello, N. N. Nedialkov, and P. A. Atanasov, "Experimental and theoretical investigations of femtosecond laser ablation of aluminum in vacuum." J. Appl. Phys. **98**, 044907 (2005).

[135] S. Amoruso, R. Bruzzese, N. Spinelli, R. Velotta, M. Vitiello, X. Wang, G. Ausanio, V. Iannotti, and L.Lanotte, "Generation of silicon nanoparticles via femtosecond laser ablation in vacuum." Appl. Phys. Lett. **84**, 4502 (2004).

[136] S J. Henley, S Mollah, C E. Giusca, and S. R. P. Silva, "Laser-induced self-assembly of iron oxide nanostructures with controllable dimensionality." J. Appl. Phys. **106**, 064309 (2009).

[137] S. K. Das, D. Dufft, A. Rosenfeld, J. Bonse, M.Bock, and R. Grunwald, "Femtosecond-laser-induced quasiperiodic nanostructures on TiO surfaces." J. Appl. Phys. **105**, 084912 (2009).

[138] N. Jiang, D.Su, J. Qiu, and J. C. H. Spence, "On the formation of Na nanoparticles in femtosecond-laser irradiated glasses."J. Appl. Phys. **107**, 064301 (2010).

[139] N. G. Semaltianos, S. Logothetidis, W. Perrie, S. Romani, R. J. Potter, M. Sharp, G. Dearden, and K. G. Watkins, "CdTe nanoparticles synthesized by laser ablation." Appl. Phys. Lett, **95**, 3, 033302 (2009).

[140] A. Y. Vorobyev and Chunlei Guo , "Spectral and polarization responses of femtosecond laser-induced periodic surface structures on metals." J. Appl. Phys. **103**, 043513, (2008).

[141] F. Vidal, T. W. Johnston, S. Laville, O. Barthelemy, M. Chaker, B. Le Drogoff, J. Margot, and M. Sabsabi, "Critical-point phase separation in laser ablation of conductors."Phys. Rev. Lett. **86**, 2573 (2001)**.**

[142] K. Sokolowski-Tinten, J. Bialkowski, A. Cavalleri, D. von der Linde, A. Oparin, J. Meyer-ter-Vehn, and S. I. Anisimov, "Transient states of matter during short pulse laser ablation."Phys. Rev. Lett. **81**, 224 (1998).

[143] D. Perez and L. J. Lewis, "Molecular-dynamics study of ablation of solids under femtosecond laser pulses." Phys. Rev. B **67**, 184102 (2003).

[144] T. E. Glover, "Hydrodynamics of particle formation following femtosecond laser ablation." J. Opt. Soc. Am. B **20**, 125 (2003).

[145] P. Lorazo, L. J. Lewis, and M. Meunier, "Short-pulse laser ablation of solids: from phase explosion to fragmentation." Phys. Rev. Lett. **91**, 225502 (2003)

[146] S. Amoruso, G. Ausanio, R. Bruzzese, L. Lanotte, P. Scardi, M. Vitiello, and X. Wang. "Synthesis of nanocrystal films via femtosecond laser ablation in vacuum." J. Phys. Condens. Matter **18**, L49 (2006)

[147] R. A. Ganeev, A. I. Ryasnyanskiy, U. Chakravarty, P. A. Naik, H. Srivastava, M. K. Tiwari, and P. D. Gupta, "Structural, optical, and nonlinear optical properties of indium nanoparticles prepared by laser ablation." Appl. Phys. B **86**, 337 (2007).

[148] U. Chakravarty, P. A. Naik, S. R. Kumbhare, and P. D. Gupta, "Efficient keV X-ray Generation from Irradiation of in-situ Produced Silver Clusters by Ti: sapphire Laser Pulses." J. Opt. Soc. Korea **13**, 80 (2009).

[149] Mostafa A. El-Sayed, "Small is different: shape-, size-, and composition-dependent properties of some colloidal semiconductor nanocrystals." *Acc. Chem. Res.* **37**, 326 **(**2004).

[150] K. Sturm, S. Fahler, and H. U. Krebs, "Pulsed laser deposition of metals in low pressure inert gas." *Applied surface science* **154**, 462-466 (2000)

[151] S. Amoruso, G. Ausanio, R. Bruzzese, M. Vitiello, and X. Wang, "Femtosecond laser pulse irradiation of solid targets as a general route to nanoparticle formation in a vacuum." Phys. Rev. B **71,** 033406 (2005).

[152] D. Scuderi, O. Albert, D. Moreau, P. P. Pronko, and J. Etchepare, "Interaction of a laser-produced plume with a second time delayed femtosecond pulse."Appl. Phys. Lett. **86**, 071502 (2005).

[153] S. Amoruso, R. Bruzzese, X. Wang, N. N. Nedialkov and P. A. Atanasov, "An analysis of the dependence on photon energy of the process of nanoparticle generation by femtosecond laser ablation in a vacuum." Nanotechnology **18,** 145612 (2007).

[154] R. Hergenröder, M. Miclea and V. Hommes , "Controlling semiconductor nanoparticle size distributions with tailored ultrashort pulses." Nanotechnology **17,** 4065 (2006).

[155] S. Amoruso, G. Ausanio, A. C. Barone, R. Bruzzese, L. Gragnaniello, M. Vitiello, and X. Wang, "Ultrashort laser ablation of solid matter in vacuum: a comparison

between the picosecond and femtosecond regimes." J. Phys. B: Mol. Opt. Phys. **38**, L329 (2005).

[156] E. R. Savinova, E.N. Savinova, and V.N. Parmon, "Copper colloids stabilized by water-soluble polymers: Part II. Their application as catalysts for dihydrogen evolution."J. Mol. Catal. **48,** 231 (1988).

[157] R. Narayanan, and M.A. El-Sayed, "Effect of catalytic activity on the metallic nanoparticle size distribution: electron-transfer reaction between Fe (CN) 6 and thiosulfate ions catalyzed by PVP-platinum nanoparticles." J. Phys. Chem. B **107,** 12416 (2003).

[158] F. Wooten, *Optical Properties of Solids*, Academic Press, San Diego (1972).

[159] D. E. Grady, "Local inertial effects in dynamic fragmentation." J. Appl. Phys. **53**, 322 (1982).

[160] S. Eliezer, N. Eliaz, E. Grossman, D. Fisher, I. Gouzman, Z. Henis, S. Pecker, Y. Horovitz, M. Fraenkel, S. Maman, and Y. Lereah, "Synthesis of nanoparticles with femtosecond laser pulses." Phys. Rev. B **69**, 144119 (2004).

[161] S. P. Gordon, T. Donnelly, A. Sullivan, H. Hamster, and R.W. Falcone, "X rays from microstructured targets heated by femtosecond lasers," *Optics Letters*. **19**, 484-486, (1994).

[162] S. Kahaly, S. K. Yadav, W. M. Wang, S. Sengupta, Z. M. Sheng, A. Das, P. K. Kaw, and G. R. Kumar, "Near-complete absorption of intense ultrashort laser light by sub-λ gratings," *Phys. Rev. Lett.* **101**, 145001 (2008)

[163] T. Ditmire, R. A. Smith, R. S. Marjoribanks, G. Kulcsár, and M. H. R. Hutchinson, "X-ray yields from Xe clusters heated by short pulse high intensity lasers**,**" *Appl. Phys. Lett*. **71,** 166-168, (1997)

[164] R. A. Ganeev , U. Chakravarty, P. A. Naik, H. Srivastava, C. Mukherjee, M. K. Tiwari, R. V. Nandedkar, P. D. Gupta, "Pulsed deposition of metal films and nanoparticles in vacuum using sub-nanosecond laser pulses," *Appl. Optic*s **46**, 1205-1210 (2007)

[165] T. Ditmire, T. Donnelly, R. W. Falcone, M. D. Perry, "Strong x-ray emission from high-temperature plasmas produced by intense irradiation of clusters," *Phys. Rev. Lett*. 75, 3122-3125(1995)

[166] S. Dobosz, M. Lezius, M. Schmidt, P. Meynadier, M. Perdrix, and D. Normand, J. P. Rozet, and D. Vernhet, "Absolute keV photon yields from ultrashort laser-field-induced hot nanoplasmas," *Phys. Rev. A* **56**, R2526-R2529 (1997)

[167] T. Mocek, C. M. Kim, H. J. Shin, D. G. Lee, Y. H. Cha, K. H. Hong, and C. H. Nam, "Enhancement of soft x-ray emission from a cryogenically cooled Ar gas jet irradiated by 25 fs laser pulse," *Appl.Phys. Lett*. **76**, 1819-1821 (2000)

[168] C. Lihua, Y. Gu, Z. Zhao, L. Cao, W. Huang, W. Zhou, X. T. He, W. Yu, and M. Y. Yu. "Enhanced absorption of intense short-pulse laser light by subwavelength nanolayered target." *Physics of Plasmas* **17**, 043103 (2010)

[169] W.M Wang, Z.M. Sheng, and J. Zhang. "A model for the efficient coupling between intense lasers and subwavelength grating targets." *Physics of Plasmas* **15**, 030702 (2008)

[170] A. Krol, A. Ikhlef, J. C. Kieffer, D. A. Bassano, C. C. Chamberlain, Z. Jiang, H. Pepin, and S. C. Prasad. "Laser-based microfocused x-ray source for mammography: Feasibility study." *Medical Physics* **24**, 725 (1997)

[171] J. A. Chakera, S. R. Kumbhare, P. A. Naik, and P. D. Gupta. "Narrow band X-ray emission in the water-window spectral region from a laser heated gold copper mix-Z plasma." *Applied Physics B* **86**, 519-522 (2007)

[172] U. Chakravarty, V. Arora, P.A. Naik, J.A. Chakera J.A, H. Srivastava , A.K. Srivastava, G. D. Verma, S.R. Kumbhare, and P.D. Gupta, "Enhancement of K α emission through efficient hot electron generation in carbon nanotubes on intense laser pulse irradiation." *J. Appl. Phys.*, **112**, 053301 (2012)

[173] S. Amoruso, G. Ausanio, R. Bruzzese, L. Gragnaniello, L. Lanotte, M. Vitiello, and X. Wang, "Characterization of laser ablation of solid targets with near-infrared laser pulses of 100fs and 1ps duration."*Appl. Surf. Sci.* **252**, 4863 (2006)

[174] R. A. Ganeev, C. Hutchison, T. Witting, F. Frank, W. A. Okell, A. Za¨ır, S. Weber, P. V. Redkin, D. Y. Lei, T. Roschuk, S. A. Maier, I. L´opez-Quint´as, M. Martin, M. Castillejo, J .W.G. Tisch and J. P. Marangos, "High-order harmonic generation in graphite plasma plumes using ultrashort laser pulses: a systematic analysis of harmonic radiation and plasma conditions."J. *Phys. B: At. Mol. Opt. Phys.* **45**, 165402 (2012)

[175] Y. Pertot, L. B. Elouga Bom, V. R. Bhardwaj, and T. Ozaki, "Pencil lead plasma for generating multimicrojoule high-order harmonics with a broad spectrum." *Appl. Phys. Lett.* **98**, 101104 (2011)

[176] H. Nakano, T. Nishikawa, and N. Uesugi, "Enhanced K-shell x-ray line emissions from aluminum plasma created by a pair of femtosecond laser pulses." *Appl. Phys. Lett*. **79**, 24 (2001)

[177] U. Chakravarty, P.A. Naik, B.S. Rao, V. Arora, H. Singhal, G.M. Bhalerao, A.K. Sinha, P. Tiwari, and P.D. Gupta, "Enhanced soft X-ray emission from carbon nanofibers irradiated with ultra-short laser pulses." *Appl. Phys. B* **103**, 571 (2011)

[178] Y. Hironaka, Y. Fujimoto, K. G. Nakamura, Ken-ichi Kondo, and M. Yoshida, "Enhancement of hard x-ray emission from a copper target by multiple shots of femtosecond laser pulses."*Appl. Phys. Lett*. **74**, 1645 (1999)

[179] R.Ramis, K. Eidmann, J. Meyer-ter-Vehn, and S. Hüller. "MULTI-fs–A computer code for laser–plasma interaction in the femtosecond regime." *Computer Physics Communications* 183, 637-655 (2012)

[180] S. Amoruso, R. Bruzzese, and X. Wang. "Plume composition control in double pulse ultrafast laser ablation of metals." *Applied Physics Letters* **95**, 251501-251501 (2009)

[181] L.T. Hudson, and J. F. Seely. "Laser-produced X-ray sources." *Radiation Physics and Chemistry* **79**, 132-138 (2010)

[182] T. A. Pikuz, A.Y. Faenov, I. Y. Skobelev, S. V. Gasilov, A. S. Boldarev, V. A. Gasilov, Y. Fukuda et al. "Enhancement of soft x-ray emission from fs laser plasma by using mixture of molecule and atomic gases as cluster jet targets and its application for nanostructure imaging." In *Journal of Physics* IOP*: Conference Series*, **163**, 012106 Publishing, (2009)

[183] J. E. Seres, D. Hochhaus, B. Ecker, D. Zimmer, V. Bagnoud, T. Kuehl, and C. Spielmann. "Laser-driven amplification of soft X-rays by parametric stimulated emission in neutral gases." *Nature Physics* **6**, 455-461 (2010)

[184] D. Altenberndt, U. Teubner, P. Gibbon, E. Forster, P. Audebert, J.P. Geidre, G. Grillon, and A. Antonetti, "Soft x-ray brilliance of femtosecond and picosecond laser-plasmas." J. Phys. B: At. Mol. Opt. Phys. **30,** 3969 (1997)

[185] J. Yanling, G. Jiang, W. Wu, C. Wang, Y. Gu, and Y. Tang. "Efficient generation and transportation of energetic electrons in a carbon nanotube array target." *Applied Physics Letters* **96**, 041504-041504 (2010)

[186] U. Chakravarty, B. S. Rao, V. Arora, A. Upadhyay, H. Singhal, P. A. Naik, J. A. Chakera, C. Mukherjee, and P. D. Gupta. "Enhanced water window x-ray emission from in situ formed carbon clusters irradiated by intense ultra-short laser pulses." *Applied Physics Letters* **103**, 054107-054107 (2013)

[187] G. Chatterjee, P.K Singh, S.Ahmed, A. P. L. Robinson, A. D. Lad, S. Mondal, V. Narayanan et al. "Macroscopic Transport of Mega-ampere Electron Currents in Aligned Carbon-Nanotube Arrays." *Physical Review Letters* **108**, 235005 (2012)

[188] R. Andrews, D. Jacques, A. M. Rao, F. Derbyshire, D. Qian, X. Fan, E. C. Dickey and J. Chen, "Continuous production of aligned carbon nanotubes: a step closer to commercial realization." Chem. Phys. Lett. **303**, 467 (1999).

[189] E. Parra, I. Alexeev, J. Fan, K. Y. Kim, S. J. McNaught, and H. M. Milchberg, "Hydrodynamic time scales for intense laser-heated clusters." J. Opt. Soc. Am. B, **20**, 118 (2003)

[190] G. D. Mahan, "Nanoscale dielectric constants: Dipole summations and the dielectric function in nanowires and quantum dots of cubic materials." Phys. Rev. B. **74**, 033407 (2006).

[191] F. Megi, M. Belkacem, M. A. Bouchene, E. Suraud and G. Zwicknagel, "On the importance of damping phenomena in clusters irradiated by intense laser fields." J. Phys. B. At. Mol. and Opt. Phys. **36**, 273 (2003)

[192] R. C. Issac, G. Vieux, B. Ersfeld, E. Brunetti, S. P. Jamison, J. Gallacher, D. Clark, and D. A. Jaroszynski, "Ultra hard x rays from krypton clusters heated by intense laser fields."Phys. Plasmas **11**, 3491 (2004)

[193] P. Gibbon, and O. N. Rosmej. "Stability of nanostructure targets irradiated by high intensity laser pulses." *Plasma Physics and Controlled Fusion* **49**, 1873 (2007)

[194] P. P. Rajeev S. Sengupta A. Das, P. Taneja, P. Ayyub, P. K. Kaw, andG. R. Kumar, "Laser absorption in short-lived metal and nanoplasmas." Appl. Phys. B, **80**, 1015–1019 (2005)

[195] S. Bagchi, P. Prem Kiran, W.M. Wang, Z. M. Sheng, M. K. Bhuyan, M. Krishnamurthy, and G. Ravindra Kumar. "Surface-plasmon-enhanced MeV ions from femtosecond laser irradiated, periodically modulated surfaces." *Physics of Plasmas* **19**, 030703 (2012)

[196] H. Masuda, and F. Hasegawa, "Self-Ordering of Cell Arrangement of Anodic Porous Alumina Formed in Sulfuric Acid Solution." J. Electrochem. Soc. **144,** L127 (1997)

[197] T. Nishikawa, H. Nakano, N. Uesugi, M. Nakao, and H. Masuda, "Greatly enhanced soft x-ray generation from femtosecond-laser-produced plasma by using a nanohole-alumina target." Appl. Phys. Lett. **75**, 4079 (1999).

[198] J. D. Jackson, in *Classical Electrodynamics*, p.152, second edition, Wiley Eastern Limited, Mumbai (1978)

[199] L. D. Landau and E. M. Lifshitz, in "*Electrodynamics of Continuous Media",* Pergamon, Oxford (1984)

[200] M. Huang, F. L. Zhao, Y. Cheng, N. Xu, and Z. Xu , "Mechanisms of ultrafast laser-induced deep-subwavelength gratings on graphite and diamond." Phys. Rev. B **79**, 125436 (2009).

[201] M. Huang, F. L. Zhao, Y. Cheng, N. Xu, and Z. Xu, "Origin of laser-induced near-subwavelength ripples: interference between surface plasmons and incident laser." ACS Nano **3**, 4062-4070 (2009)

[202] U. Chakravarty, V Arora, J. A. Chakera, P. A. Naik, H. Srivastava, P. Tiwari, A. Srivastava, and P.D Gupta, "X-ray enhancement in a nano-hole target irradiated by intense ultrashort laser pulses*", J. Appl. Phys.* **109**, 053301 (2011)

[203] J. Jha and M. Krishnamurthy, "Collisionless phenomena in heteronuclear clusters ", *Appl. Phys. Lett.* **92**, 191108 (2008)

[204] J. Liu, R. Li, P. Zhu, Z. Xu, and J. Liu, "Modified hydrodynamic model and its application in the investigation of laser-cluster interactions", *Phys. Rev. A* **64**, 033426 (2001)

[205] L. Kim, Eun-mi Lee, S.-J. Cho, J. S. Suh, "Diameter control of carbon nano-tubes by changing the concentration of catalytic metal ion solutions", *Carbon* **43**, 1453 (2005)

[206] K.Y. Kim. I Alexeev, V. Kumarappan, E. Parra,T.Antonsen, T.Taguchi, A. Gupta, and H. M. Milchberg, “Gases of exploding laser-heated cluster nano-plasmas as a nonlinear optical medium”, *Phys. Plasmas* **11**, 2882 (2004)

[207] Y. Liu, Q. Dong, X. Peng,Z. Jin, and J. Zhang, “Soft x-ray emission, angular distribution of hot electrons, and absorption studies of argon clusters in intense laser pulses”, *Phys. Plasmas* **16**, 043301 (2009)

[208] R. Toth, S. Fourmaux, T. Ozaki, M. Servol, and J. C. Kieffer, "Evaluation of ultrafast laser-based hard x-ray sources for phase-contrast imaging."*Phys. Plasmas* **14**, 053506 (2007)

[209] J. C. Kieffer, A. Krol, Z. Jiang, C. C. Chamberlain, E. Scalzetti, and Z. Ichalalene, "Future of laser-based X-ray sources for medical imaging." *Appl. Phys. B: Lasers Opt.* **74**, S75 (2002)

[210] J. A. Chakera, A. Ali, Y. Y. Tsui, and R. Fedosejevs, "A continuous kilohertz Cu Kα source produced by submillijoule femtosecond laser pulses for phase contrast imaging." *Appl. Phys. Lett*. **93**, 261501 (2008)

[211] H. I. Sekiguchi R. Kuroda, M. Yasumoto, H. Toyokawa, M. Koike, K. Yamad, F. Sakai, K. Mori, K. Maruyama, H. Oka, and T. Kimata , "In-line phase-contrast imaging of a biological specimen using a compact laser-Compton scattering-based x-ray source." *Appl. Phys. Lett*. **92**, 131107 (2008)

[212] S.A. Pikuz, O. V. Chefonov, S. V. Gasilov, P. S. Komarov, A. V. Ovchinnikov, I. Yu Skobelev, S. Yu Ashitkov, M. V. Agranat, A. Zigler, and A. Ya Faenov. "Micro-radiography with laser plasma X-ray source operating in air atmosphere." *Laser and Particle Beams: pulse power & high energy densities* **28**, 393-397 (2010)

[213] D. Boschetto, G. Mourou, A. Rousse, A. Mordovanakis, B. Hou, J. Nees, D. Kumah, and R. Clarke. "Spatial coherence properties of a compact and ultrafast laser-produced plasma keV x-ray source." *Applied physics letters* **90**, 011106-011106 (2007)

[214] B. Hou, J. A. Nees, W. Theobald, G. A. Mourou, L. M. Chen, J.C. Kieffer, A. Krol, and C. C. Chamberlain. "Dependence of hard x-ray yield on laser pulse parameters in the wavelength-cubed regime." *Applied Physics Letters* **84**, 2259 (2004)

[215] Z. Zhao, L. Cao, L. Cao, J.Wang, W. Huang, W.Jiang, Y. He et al. "Acceleration and guiding of fast electrons by a nanobrush target." *Physics of Plasmas* **17**, 123108 (2010)

[216] P.K. Singh, G. Chatterjee, A. D. Lad, A. Adak, S. Ahmed, M. Khorasaninejad, M. M. Adachi et al. "Efficient generation and guiding of megaampere relativistic electron current by silicon nanowires." *Applied Physics Letters* **100**, 244104 (2012)

[217] P.K. Singh, I. Chakraborty, G. Chatterjee, A. Adak, A. D. Lad, P. Brijesh, P. Ayyub, and G. Ravindra Kumar. "Enhanced transport of relativistic electrons through nanochannels." *Physical Review Special Topics-Accelerators and Beams* **16**, 063401 (2013)

[218] L. Liao, W. Wu, Y. Gu, W. Zhou, C. Wang, Z. Fu, Xi Yang, and Y. Tang. "Production of collimated MeV electron beam in carbon nanotube array irradiated by super-intense femtosecond laser." Accepted in *Carbon* (2013)

[219] E. Prodan, C. Radloff, N. J. Halas and P. Nordlander, "A hybridization model for the plasmon response of complex nanostructures." *Science* **302**, 419 (2003)

[220] U. Chakravarty, P. A. Naik, and P. D. Gupta. "Electric field enhancement at multiple densities in laser-irradiated nanotube plasma." *Pramana* **79**, 443-456 (2012)

[221] H. Nakano, A.A. Andreev, and J. Limpouch, "Femtosecond X-ray line emission from multilayer targets irradiated by short laser pulses." *Appl. Phys. B: Lasers and Optics* **79**, 469-476, (2004)

[222] V. Arora, H. Singhal, P. A. Naik, and P. D. Gupta, "Conversion efficiency and spectral broadening of the K-α line emitted from planar titanium targets irradiated with ultra-short laser pulses of high intensity." *J. Appl. Phys*. **110**, 083305 (2011)

[223] S. Micheau, H. Jouin, and B. Pons**,** "Modified nanoplasma model for laser-cluster interaction."*Phys. Rev. A* **77**, 053201 (2008)

[224] J. Perrière, É. Millon, and É. Fogarassy, "*Recent Advances in Laser Processing of Materials"*, Elsevier, Amsterdam (2006).

[225] B.N. Chichkov, C. Momma, S. Nolte, F. V. Alvensleben, and A. Tünnermann, "Femtosecond, picosecond and nanosecond laser ablation of solids." *Appl. Phys. A: Mater. Sci. Process*. **63**, 109 (1996).

[226] A. Y. Vorobyev and C. Guo, "Colorizing metals with femtosecond laser pulses."*Appl. Phys. Lett*. **92**, 041914 (2008).

[227] Q. Z. Zhao, F. Ciobanu, S. Malzer, and L. J. Wang , "Enhancement of optical absorption and photocurrent of 6H-SiC by laser surface nanostructuring." *Appl. Phys. Lett.* **91**, 121107 (2007)

[228] K. Minoshima, A. M. Kowalevicz, I. Hartl, E. P. Ippen, and J. G. Fujimoto, "Photonic device fabrication in glass by use of nonlinear materials processing with a femtosecond laser oscillator." *Opt. Lett*. **26**, 1516 (2001).

[229] E. N. Glezer, M. Milosavljevic, L. Huang, R. J. Finlay, T. H. Her, J. P. Callan, and E. Mazur, "Three-dimensional optical storage inside transparent materials."*Opt. Lett*. **21**, 2023 (1996).

[230] T. N. Kim, K. Campbell, A. Groisman, D. Kleinfeld, and C. B. Schaffer, "Femtosecond laser-drilled capillary integrated into a microfluidic device." *Appl. Phys. Lett*. **86**, 201106 (2005).

[231] P. M. Fauchet and A. E. Siegman, "Surface ripples on silicon and gallium arsenide under picosecond laser illumination." *Appl. Phys. Lett*. **40**, 824 (1982).

[232] A. M. Ozkan, A. P. Malshe, T. A. Railkar, W. D. Brown, M. D. Shirk, and P. A. Molian, "Femtosecond laser-induced periodic structure writing on diamond crystals and microclusters." *Appl. Phys. Lett*. **75**, 3716 (1999).

[233] N. Yasumaru, K. Miyazaki, and J. Kiuchi, "Femtosecond-laser-induced nanostructure formed on hard thin films of TiN and DLC." *Appl. Phys. A: Mater. Sci. Process*. **76**, 983 (2003).

[234] H. Raether, "*Surface Plasmons on Smooth and Rough Surfaces and on Gratings"*, Springer-Verlag, Berlin (1988).

[235] Y. Shimotsuma, P. G. Kazansky, J. Qiu, and K. Hirao, "Self-organized nanogratings in glass irradiated by ultrashort light pulses." *Phys Rev. Lett.* **91**, 24 (2003).

[236] J. Reif, F. Costache, M. Henyk, and S. Pandelov, "Ripples revisited: non-classical morphology at the bottom of femtosecond laser ablation craters in transparent dielectrics." *Appl. Surf. Sci*. **197–198**, 891 (2002).

[237] Y. Dong and P. Molian, "Coulomb explosion-induced formation of highly oriented nanoparticles on thin films of 3C–SiC by the femtosecond pulsed laser." *Appl. Phys. Lett*. **84**, 10 (2004).

[238] X.J. Wu, T.Q. Jia, F.L. Zhao, M. Huang, N.S. Xu, H. Kuroda and Z.Z. Xu, "Formation mechanisms of uniform arrays of periodic nanoparticles and nanoripples on 6H-SiC crystal surface induced by femtosecond laser ablation." *Appl. Phys. A: Mater. Sci. Process*. **86**, 491 (2007).

[239] V. R. Bhardwaj, E. Simova, P. P. Rajeev, C. Hnatovsky, R. S. Taylor, D. M. Rayner, and P. B. Corkum, "Optically produced arrays of planar nanostructures inside fused silica." *Phys. Rev. Lett*. **96**, 057404 (2006).

[240] M. Huang, F. Zhao, Y. Cheng, N. Xu, and Z. Xu, "Large area uniform nanostructures fabricated by direct femtosecond laser ablation." *Optics Express* **16**, 19354 (2008).

[241] A. Borowiec and H. K. Haugen, "Subwavelength ripple formation on the surfaces of compound semiconductors irradiated with femtosecond laser pulses." *Appl. Phys. Lett*. **82**, 4462 (2003).

[242] A. C. Tien, S. Backus, H. Kapteyn, M. Murnane, and G. Mourou, "Short-pulse laser damage in transparent materials as a function of pulse duration." *Phys. Rev. Lett*. **82**, 19 (1999).

[243] A.Y. Vorobyev and C. Guo, "Femtosecond laser nanostructuring of metals." *Opt. Express* **14**, 6 (2006).

[244**]** J. E. Sipe, J. F. Young, J. S. Preston, and H. M. van Driel, "Laser-induced periodic surface structure. Theory." *Phys. Rev. B* **27**, 1141 (1983).

[245] S. Sakabe, M. Hashida, S. Tokita, S. Namba, and K. Okamuro, "Mechanism for self-formation of periodic grating structures on a metal surface by a femtosecond laser pulse." *Phys. Rev. B* **79**, 033409 (2009).

[246] R. A. Ganeev, M. Baba, T. Ozaki, and H. Kuroda, "Long-and short-period nanostructure formation on semiconductor surfaces at different ambient conditions."*J. Opt. Soc. Am. B*, **27**, 1077 (2010).

[247] M. Huang, F. Zhao, Y. Cheng, N. Xu, and Z. Xu, "The morphological and optical characteristics of femtosecond laser-induced large-area micro/nanostructures on GaAs, Si, and brass." *Optics Express* **18**, A600 (2010).

[248] J. Wang and C. Guo, "Formation of extraordinarily uniform periodic structures on metals induced by femtosecond laser pulses." *J. Appl. Phys* **100**, 023511 (2006).

[249] Q. Z. Zhao, S. Malzer, and L. J. Wang, "Formation of subwavelength periodic structures on tungsten induced by ultrashort laser pulses."*Optics Letters* **32**, 1932 (2007)

[250] G. Hu, A. Lei, J. Wang, L. Huang, W. Wang, X. Wang, Y. Xu et al. "Enhanced surface acceleration of fast electrons by using subwavelength grating targets." Physics of Plasmas 17, 83102-083102 (2010)